

DISSERTATION

submitted to the

Combined Faculty of Mathematics, Engineering and Natural Sciences

of Heidelberg University, Germany

for the degree of

Doctor of Natural Sciences

Put forward by

Maša Božić-Iven

born in: Valjevo, Serbia

Oral examination: 12 June 2024

NOVEL METHODS FOR NON-CONTRAST PERFUSION MAPPING
IN THE HUMAN MYOCARDIUM USING ARTERIAL SPIN
LABELLING MAGNETIC RESONANCE IMAGING

Referees: Prof. Dr. Lothar R. Schad
Prof. Dr. Leif Schröder

To the kind hearts in science and beyond.

NEUARTIGE METHODEN ZUR KONTRASTMITTELFREIEN PERFUSIONSKARTIERUNG IM MENSCHLICHEN HERZMUSKEL MITHILFE DER ARTERIELLEN SPIN MARKIERUNG MAGNETRESONANZTOMOGRAPHIE

Herkömmliche Methoden der Magnetresonanztomographie (MRT) zur Messung der Herzmuskel-Perfusion und zur Diagnose koronarer Herzkrankheiten benötigen gadoliniumhaltige Kontrastmittel. Diese bergen jedoch das Risiko einer Anreicherung im Körper und sind bei Patienten mit Nierenversagen kontraindiziert. Diese Arbeit befasst sich mit den Herausforderungen der Arteriellen Spin Markierung im Myokard (myoASL, engl. myocardial Arterial Spin Labelling), die eine vielversprechende Methode für kontrastmittelfreie Perfusionsbildgebung ist. Zurzeit ist die klinische Translation dieser Methoden noch durch ein hohes Maß an Messungenauigkeit eingeschränkt. In dieser Arbeit wurden daher drei neuartige Ansätze entwickelt, um den Auswirkungen von physiologischem Rauschen (PR) auf myoASL entgegenzuwirken und die Sensitivität gegenüber Messabweichungen und physiologischen Schwankungen zu minimieren. Zunächst wurde eine verbesserte Quantifizierungsmethode vorgestellt. Diese verringert mithilfe individueller Blut- T_1 -Werte und eines angepassten Referenzbildes die Abhängigkeit der gemessenen Perfusionswerte von der Herzfrequenz und dem Anregungs-Winkel. Danach wurden T_2 -Präparationen für die myoASL-Bildauslese untersucht, die das Myokardsignal und dessen Beitrag zum PR effektiv unterdrücken. Letztendlich wurden Double-Inversion-Recovery-Präparationen untersucht, um Signalschwankungen, die durch eine schwankende Herzfrequenz verursacht werden und eine wesentliche Quelle für PR darstellen, zu unterdrücken. Zusammen verringern diese drei Methoden aufnahmebedingte Messabweichungen und verbessern die Resilienz von myoASL gegenüber physiologischen Schwankungen. Dadurch bieten die entwickelten Techniken praktikable Ansätze, um den potenziellen klinischen Einsatz von myoASL in Zukunft zu verbessern.

NOVEL METHODS FOR NON-CONTRAST PERFUSION MAPPING IN THE HUMAN MYOCARDIUM USING ARTERIAL SPIN LABELLING MAGNETIC RESONANCE IMAGING

Conventional magnetic resonance imaging (MRI) methods for measuring myocardial perfusion and diagnosing coronary artery disease rely on gadolinium-based contrast agents (GBCA). However, GBCAs pose a risk of accumulation in the body and are contraindicated in patients with kidney failure. This thesis addresses the challenges of myocardial Arterial Spin Labelling (myoASL) MRI. MyoASL is a promising candidate for contrast-agent-free perfusion mapping. However, the clinical translation of myoASL is hampered due to high levels of measurement noise. Three novel approaches were developed in this thesis to counteract the effects of physiological noise (PN) in myoASL and reduce its sensitivity to acquisition-related and physiological variations. First, an improved quantification method, incorporating individual blood T_1 values and an adapted baseline acquisition, mitigates the effect of the heart rate and acquisition flip angle on the measured perfusion values. Second, T_2 -prepared myoASL-readouts were introduced, which effectively suppress myocardial signal and reduce the related contributions to the PN. Third, the proposed Double Inversion Recovery preparations substantially reduce signal fluctuations caused by heart rate variability, a major contributor to PN. Together, these techniques alleviate acquisition-related bias and improve the robustness of myoASL against physiological variations. In extension, the developed techniques offer viable approaches to improve the potential clinical use of myoASL in the future.

ACKNOWLEDGMENTS

First and foremost, I would like to thank Prof. Dr. Lothar R. Schad for the opportunity to undertake my PhD under his supervision at the Chair of Computer Assisted Clinical Medicine (CKM). Thank you for offering me the freedom to pursue my scientific goals in collaboration with many researchers across Europe, and your support at every step.

My thanks extend to Prof. Dr. Leif Schröder for being the second referee to this thesis as well as to Prof. Dr. Frank G. Zöllner for his continuous support throughout this project.

I would like to express my gratitude to Dr. Sebastian Weingärtner for his exceptional guidance and mentorship from the very beginning of my PhD journey. Dear Basti, it has been a privilege learning from you and being part of the extraordinary team you have brought together. Thank you for fostering a fantastic research climate and, last but not least, for your terrific bar recommendations around the world.

I am grateful to have had the opportunity to work with Dr. Stanislas Rapacchi, particularly during my research visit at the CRMBM in Marseilles. His brilliant insights, ongoing support, and encouragement have greatly contributed to the results of this work. Stan, I feel fortunate to have been introduced to you. Merci pour tout.

Humble thanks to all volunteers for their participation in our research scans as well as to Ayda, Chiara, Hanna, Kathleen, Maaïke, Markus, Martina, Paulina, Sabine, and Sofija for proofreading parts of this thesis.

My heartfelt thanks go to everyone at CKM, particularly Anne, Christian, Efe, Ingo, Irène, Patrick, Safa, Simon, Steffen and Valerie. Thank you for teaching me the ways around UMM and always making me feel part of the group. This made every trip to the office worthwhile, even when they became scarce towards the end of my PhD. Special thanks to Christian, Ingo and Safa who endured many hours in the scanner bore so I could learn how to properly scan the heart.

I am grateful to Mars Lab and the ImPhys Department at TU Delft for giving me a second scientific home. Especially to Ayda, Chiara, Martina and Paulina: Thank you for being the best girl gang on planet earth and beyond. For the shared projects, the travels, the espresso mar(s)tinis, for your friendship. When science wasn't sciencing, I knew I had you.

I am grateful to my dear friend Sabine for providing the best dinners after long work days, listening to all my PhD worries, and enduring my going MIA around every abstract deadline. Thank you for sharing the highs and lows with me for (almost) exactly 20 years now.

To my parents, Sofija and Markus: Thank you for your unwavering support throughout this journey, for your brave volunteering, and for being there for me in both big and small ways. Most of all, thank you for your love – it is the cornerstone behind all of my achievements.

CONTENTS

| | | |
|-------|------------------------------------------------------------------------------|----|
| 1 | INTRODUCTION | 1 |
| 2 | THEORETICAL BACKGROUND | 7 |
| 2.1 | Physics of NMR | 7 |
| 2.1.1 | Magnetisation formation and dynamics | 7 |
| 2.1.2 | MR signal and relaxation | 10 |
| 2.2 | Image formation | 11 |
| 2.2.1 | k-Space | 12 |
| 2.2.2 | Sequence Building Blocks | 13 |
| 2.3 | Cardiac anatomy and perfusion | 16 |
| 2.3.1 | Fundamental aspects of cardiac anatomy | 16 |
| 2.3.2 | Cardiac perfusion | 18 |
| 2.4 | Assessing cardiac perfusion | 20 |
| 2.4.1 | Detecting and assessing CAD | 20 |
| 2.4.2 | First-pass perfusion cardiac MRI | 23 |
| 2.4.3 | Myocardial Arterial Spin Labelling | 27 |
| 3 | PART I: IMPACT OF PHYSIOLOGICAL AND ACQUISITION PARAMETERS ON MYOCARDIAL ASL | 37 |
| 3.1 | Introduction | 37 |
| 3.2 | Theory | 38 |
| 3.2.1 | ASL signal model | 38 |
| 3.2.2 | Magnetization modulation function | 38 |
| 3.3 | Methods | 42 |
| 3.3.1 | MyoASL sequence | 42 |
| 3.3.2 | Numerical simulations | 43 |
| 3.3.3 | Imaging | 44 |
| 3.4 | Results | 47 |
| 3.4.1 | Phantom results | 48 |
| 3.4.2 | In vivo results | 51 |
| 3.5 | Discussion | 52 |
| 4 | PART II: T_2 -PREPARED MYOCARDIAL ASL | 59 |
| 4.1 | Introduction | 59 |
| 4.2 | Methods | 60 |
| 4.2.1 | Theoretical framework | 60 |
| 4.2.2 | MyoASL sequence and post-processing | 63 |
| 4.2.3 | Simulation experiments | 65 |
| 4.2.4 | Phantom experiments | 66 |
| 4.2.5 | In vivo experiments | 66 |
| 4.3 | Results | 67 |
| 4.3.1 | Simulation experiments | 67 |
| 4.3.2 | Phantom experiments | 69 |
| 4.3.3 | In vivo experiments | 70 |
| 4.4 | Discussion | 71 |
| 5 | PART III: DOUBLE INVERSION RECOVERY MYOCARDIAL ASL | 77 |

| | | |
|-------|---------------------------------------------------------------------------|-----|
| 5.1 | Introduction | 77 |
| 5.2 | Methods | 79 |
| 5.2.1 | Theoretical framework | 79 |
| 5.2.2 | FAIR-myocardial ASL sequence and post-processing | 81 |
| 5.2.3 | Simulation experiments | 81 |
| 5.2.4 | Phantom experiments | 83 |
| 5.2.5 | In vivo experiments | 84 |
| 5.3 | Results | 84 |
| 5.3.1 | Simulation experiments | 84 |
| 5.3.2 | Phantom experiments | 86 |
| 5.3.3 | In vivo experiments | 87 |
| 5.4 | Discussion | 89 |
| 6 | DISCUSSION | 93 |
| 6.1 | Assessing bias in myocardial ASL for ischaemia detection | 95 |
| 6.2 | Assessing precision in myocardial ASL for ischaemia detection | 95 |
| 6.2.1 | Challenges in patient scanning with myocardial ASL | 96 |
| 6.2.2 | Challenges in stress perfusion measurements with myocardial ASL | 96 |
| 6.2.3 | Prior research and novel insights | 97 |
| 6.3 | Non-contrast alternatives to myocardial ASL | 98 |
| 6.4 | Limitations and outlook | 99 |
| 7 | CONCLUSION | 103 |
| I | APPENDIX | 105 |
| A | APPENDIX TO CHAPTER 3 | 107 |
| A.1 | Signal equations for bSSFP and spGRE readout | 107 |
| A.2 | Imaging signal for baseline, control and tag image in FAIR-myocardial ASL | 108 |
| B | APPENDIX TO CHAPTER 4 | 111 |
| B.1 | Free-breathing myocardial ASL | 111 |
| C | PUBLICATIONS | 117 |
| | BIBLIOGRAPHY | 119 |
| | DECLARATION | 141 |

LIST OF FIGURES

| | | |
|-------------|-------------------------------------------------------------------------------------------------------------------------|----|
| Figure 1.1 | Causes of mortality and premature death in Europe. | 2 |
| Figure 2.1 | Proton spin in analogy to a spinning top and a bar magnet. | 8 |
| Figure 2.2 | Orientation of spins in an external magnetic field. | 8 |
| Figure 2.3 | Zeeman effect in proton spins. | 9 |
| Figure 2.4 | MR sequence building blocks. | 13 |
| Figure 2.5 | Schematic illustration of the human heart anatomy. | 17 |
| Figure 2.6 | Impulse response to arterial input and resulting tissue signal curve. | 26 |
| Figure 2.7 | Basic principle of perfusion mapping with myocardial ASL. | 28 |
| Figure 2.8 | Labelling scheme for Flow-sensitive Alternating Inversion Recovery myoASL. | 30 |
| Figure 3.1 | Sequence diagram of the double ECG-gated FAIR-myASL sequence. | 39 |
| Figure 3.2 | Influence of acquisition-related and physiological parameters on the precision and accuracy of FAIR-myASL. | 41 |
| Figure 3.3 | Coefficient of variation of simulated myoASL-MBF as a function of heart rate variability. | 47 |
| Figure 3.4 | Simulated and phantom myoASL-MBF deviation as a function of the control-tag delay. | 48 |
| Figure 3.5 | Phantom myoASL-MBF as a function of acquisition flip angle and matrix size. | 49 |
| Figure 3.6 | Phantom myoASL-MBF as a function of heart rate and blood T_1 . | 50 |
| Figure 3.7 | Simulated myoASL-MBF as a function of acquisition flip angle and matrix size. | 51 |
| Figure 3.8 | Simulated myoASL-MBF as a function of blood T_1 and T_2 relaxation times. | 52 |
| Figure 3.9 | Simulated myoASL-MBF deviation as a function of blood T_1 error. | 53 |
| Figure 3.10 | Simulated myoASL-MBF as a function of heart rate and blood T_1 . | 54 |
| Figure 3.11 | In vivo myoASL-perfusion and physiological noise maps from bSSFP and spGRE readouts. | 55 |
| Figure 3.12 | In vivo mean septal myoASL-MBF with corresponding intra- and inter-subject variability. | 56 |
| Figure 4.1 | Diagram of a T_2 -prepared FAIR-myASL sequence with simulated myocardial and blood signal. | 63 |
| Figure 4.2 | Simulated and phantom signal change due to T_2 -preparations in myocardium and blood as a function of τ_{T_2p} . | 68 |
| Figure 4.3 | Simulated SNR gain with T_2 -prepared FAIR-myASL as a function of T_2 -preparation duration. | 69 |

| | |
|------------|-------------------------------------------------------------------------------------------------------------------------|
| Figure 4.4 | Phantom MBF and PN values with SNR gain relative to conventional FAIR-myoASL as a function of τ_{T2p} . 70 |
| Figure 4.5 | In vivo T_2 map with average perfusion and PN maps for conventional and T_2 -prepared FAIR-myoASL. 71 |
| Figure 4.6 | Mean global MBF, PN and CoV values for conventional and T_2 -prepared FAIR-myoASL. 72 |
| Figure 5.1 | Diagram of a conventional and Double Inversion Recovery (DIR) FAIR-myoASL sequence with simulated myocardial signal. 82 |
| Figure 5.2 | Simulated MBF with conventional FAIR and DIR-labelling as a function of heart rate variability. 85 |
| Figure 5.3 | Simulated PN in conventional FAIR and DIR-labelling as a function of heart rate variability. 86 |
| Figure 5.4 | Simulated SNR gain with DIR FAIR-myoASL as a function of heart rate variability. 87 |
| Figure 5.5 | Phantom MBF, PN, and relative SNR gain for conventional and DIR FAIR-myoASL as a function of heart rate variability. 88 |
| Figure 5.6 | In vivo average perfusion and PN maps for conventional and DIR FAIR-myoASL. 89 |
| Figure 5.7 | Mean global MBF and PN values with corresponding SNR gain for conventional and DIR FAIR-myoASL. 89 |

LIST OF TABLES

| | |
|-----------|------------------------------------------------------------------------------------------|
| Table 3.1 | Sequence parameters of the FAIR-myoASL sequence for phantom and in vivo measurements. 44 |
| Table 4.1 | Sequence parameters of the conventional and T_2 -prepared FAIR-myoASL sequence. 64 |
| Table 5.1 | Sequence parameters of the conventional and DIR-labelled FAIR-myoASL sequence. 81 |

ACRONYMS

| | |
|-----|-------------------------|
| AIF | Arterial Input Function |
| AMS | Acquisition Matrix Size |
| ASL | Arterial Spin Labelling |
| ATT | Arterial Transit Time |

| | |
|--------|-----------------------------------------------------------|
| BIR | B_1 Insensitive Rotation |
| BOLD | Blood Oxygen Level Dependent |
| bSSFP | Balanced Steady-State Free Precession |
| CAD | Coronary Artery Disease |
| CMR | Cardiac Magnetic Resonance (Imaging) |
| CoV | Coefficient of Variation |
| CS | Compressed Sensing |
| CT | Computed Tomography |
| CVD | Cardiovascular Disease |
| DIR | Double Inversion Recovery |
| DS | Degree of Stenosis |
| ECG | Electrocardiogram |
| EMA | European Medicines Agency |
| EPI | Echo-Planar Imaging |
| EPG | Extended Phase Graph |
| ESC | European Society of Cardiology |
| EU | European Union |
| FA | Flip Angle |
| FAIR | Flow-sensitive Alternating Inversion Recovery |
| FDA | US Food and Drug Administration |
| FE | Frequency Encoding |
| FLASH | Fast Low-Angle Shot |
| FFR | Fractional Flow Reserve |
| FOV | Field of View |
| GBCA | Gadolinium-Based Contrast Agent |
| GKM | General Kinetic Model |
| GRE | Gradient Echo |
| GRAPPA | Generalized Auto-calibrating Partial Parallel Acquisition |
| HR | Heart Rate |
| ICA | Invasive Coronary Angiography |

| | |
|--------|---------------------------------------------------------------|
| ISMRM | International Society for Magnetic Resonance in Medicine |
| IVUS | Intra-vascular Ultrasound |
| LGE | Late Gadolinium Enhancement |
| MBF | Myocardial Blood Flow |
| MOLLI | Modified Look-Locker Inversion |
| MMF | Magnetization Modulation Function |
| MRI | Magnetic Resonance Imaging |
| MPR | Myocardial Perfusion Reserve |
| MTT | Mean Transit Time |
| myoASL | Myocardial Arterial Spin Labelling |
| NMR | Nuclear Magnetic Resonance |
| NSF | Nephrogenic Systemic Fibrosis |
| OCT | Optical Coherence Tomography |
| PE | Phase Encoding |
| PET | Positron Emission Tomography |
| PF | Partial Fourier |
| PI | Parallel Imaging |
| PLD | Post-Labeling Delay |
| PN | Physiological Noise |
| PS | Phase-Sensitive |
| PWI | Perfusion-Weighted Image |
| PWS | Perfusion-Weighted Signal |
| ROI | Region of Interest |
| RF | Radio-Frequency |
| RR | R-R interval (time between two successive R-waves on the ECG) |
| SAR | Specific Absorption Rate |
| SASHA | Saturation Recovery Single-Shot Acquisition |
| SE | Spin Echo |
| SENSE | Sensitivity Encoding |
| SPECT | Single-Photon Emission Computed Tomography |

| | |
|--------|--------------------------------------------------|
| spGRE | Spoiled Gradient Echo |
| SNR | Signal-to-Noise Ratio |
| SS | Slice Selection |
| TE | Echo Time |
| TI | Inversion Time |
| TR | Repetition Time |
| VS | Velocity-Selective |
| VS-ASL | Velocity-Selective Arterial Spin Labelling |
| WET | Water suppression Enhanced Through T_1 effects |
| isSD | Inter-Subject Standard Deviation |
| wsSD | Within-Subject Standard Deviation |

INTRODUCTION

Magnetic resonance imaging (MRI) has its origin in an inherently quantum mechanical phenomenon: nuclear magnetic resonance (NMR). The pioneering work of Isidor I. Rabi, who first postulated and experimentally validated NMR in a beam of gaseous lithium chloride in the 1930s [1, 2], set the scene for the development of MRI into one of the cornerstones of modern clinical imaging. This progression was significantly advanced in 1946, when Felix Bloch and Edward M. Purcell independently demonstrated NMR in condensed matter [3–5]. This laid the groundwork for NMR spectroscopy, which to date remains an integral technique for molecular analysis. Despite this rapid initial progress, the translation of NMR into an imaging technology required additional decades of innovation. Already in the early 1950s, Hermann Y. Carr proposed spatially varying magnetic fields for localising magnetisation [6]. Yet, it was not until 1973 that Paul C. Lauterbur [7] and Peter Mansfield [8] published their seminal works, introducing MR image formation via gradient fields. Another fifty years later, MRI offers an extensive range of contrast mechanisms across various anatomies, rendering it an essential part of the modern clinical routine.

Apart from the large number of available contrasts, the non-invasive and non-ionising nature of MRI is one of its main strengths, distinguishing it from other imaging modalities such as computed tomography (CT) or positron emission tomography (PET). MRI is therefore firmly established as the clinical gold standard for evaluating numerous disease entities across the body [9, 10]. However, MR images inherently provide only relative image contrast, unlike CT imaging data, for example, which is obtained in absolute Hounsfield units [11]. Recent developments in MRI research, have triggered a shift towards quantitative MR techniques over the past decade. The primary example is the mapping of the longitudinal and transverse relaxation time, which form an integral part of diagnosing myocardial injury [9]. Other equally relevant quantitative techniques include, among others, blood flow imaging [12], diffusion mapping [13], or fat-fraction quantification [14], all providing access to information otherwise hidden in conventional MRI. Thus, quantitative MRI not only allows for visualising anatomy, but also function, which, in turn, can enable highly informed decision making in complex clinical settings.

Cardiac MR (CMR), i. e. MRI employed for cardiological examinations, has notably benefited from these advancements. Since the first publications on myocardial spectroscopy in the late 1970s [15], CMR has evolved into a multifaceted clinical tool. Its applications range from identifying ischaemic regions of the heart muscle to assessing non-ischaemic cardiomyopathies, such as iron overload [16], cardiac amyloidosis [17], or myocardial inflammation [18, 19]. Providing the capability to evaluate cardiac anatomy, function, and viability, makes CMR indispensable to the diagnosis and management of cardiovascular diseases (CVDs). This is particularly relevant as CVDs constitute the leading cause of death worldwide [20]. Although recent data on mortality rates sug-

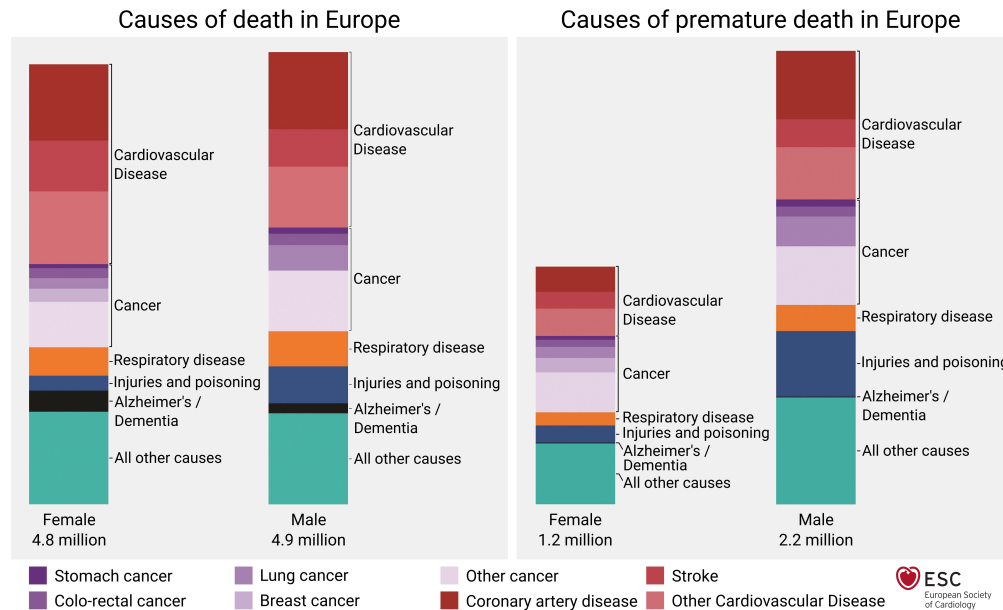


Figure 1.1: Annual mortality and premature death, defined as death before reaching the average expected lifespan, in European Society of Cardiology (ESC) member countries categorised by cause. Cardiovascular Diseases (red) account for approximately one third of premature deaths and remain the leading cause of mortality in Europe. The figure is adapted from the 2021 ESC Cardiovascular Disease Statistics report, based on the December 2019 update of the WHO Mortality Database [21].

gests that cancer has surpassed CVDs in some countries [21], CVDs remain the primary cause of death across Europe¹, accounting for approximately 45 % of deaths and about 30 % of premature deaths [21, 22], as illustrated in Figure 1.1. Furthermore, the CVD-related expenditure of the European Union (EU) was recently estimated to be €282 billion, representing 2 % of its gross domestic product [23]. Thus, addressing CVDs through improved prevention, treatment, and diagnostic techniques, such as CMR, is imperative for reducing their societal and economic impact.

Together with ischaemic stroke, the most common form of CVDs is coronary artery disease (CAD) [21], also known as ischaemic heart disease. It is associated with atherosclerosis of coronary blood vessels which results in reduced coronary blood flow and, in turn, impaired oxygen and nutrient supply to the heart – a condition called myocardial ischaemia. The diagnostic approach to CAD is, thus, to detect obstructive stenoses in the coronary vasculature. Traditionally, coronary angiography has been performed to identify such occlusions. Thereby, a catheter is guided to the coronary vessels in order to distribute a radio-contrast agent required for subsequent X-ray imaging of the region [24]. In addition, nuclear medicine offers a non-invasive alternative for perfusion measurements with cardiac positron emission tomography (PET). Even though it is widely used, PET relies on ionising radiation by intravenous injection of a radionuclide tracer (e. g. ^{15}O) [25].

¹ It should be noted that the geographic and, thus, demographic definition of Europe varies across publications. While Wilkins et al. [22] refer to the member States of the World Health Organization’s European Region, Timmis et al. [21] consider all member states of the European Society of Cardiology in their report, including North-African and Levantine countries.

Without utilising ionising radiation, CMR offers non-invasive alternatives for perfusion imaging. Here, so-called first-pass perfusion and late gadolinium enhancement (LGE) MRI are the clinically most relevant techniques. These techniques are continuing to replace previous gold-standard methods for diagnosing scarring and perfusion defects in the myocardium (heart muscle) as found in CAD [26]. Some anatomical and most functional imaging in CMR can be achieved without the use of exogenous contrast agents. However, most gold-standard procedures for assessing cardiac viability require intravenous administration of contrast-enhancing substances. These particularly include the previously mentioned CMR work-horses LGE and first-pass perfusion imaging, where scarred tissue or areas of norm-perfusion show enhanced signal due to the para-magnetic effect of the contrast agent. Traditionally in CMR, contrast agents are based on the heavy metal gadolinium [27]. These gadolinium-based contrast agents (GBCAs), however, bear the risk of inducing nephrogenic systemic fibrosis in patients with severe kidney failure [28, 29]. Nephrogenic systemic fibrosis describes a multi-organ condition, characterised by scarring of the skin and subcutaneous tissue [30]. Therefore, GBCAs are contraindicated in patients with highly impaired renal function [30]. But, even with healthy renal clearance, the inadvertent accumulation of gadolinium in the body, particularly in certain brain areas, has been reported [31, 32]. This poses a further hindrance for repeated use of gadolinium-enhanced methods in the clinic.

In this regard, so-called arterial spin labelling (ASL) MRI offers a contrast-agent-free alternative for perfusion mapping across various body regions. In ASL, water protons in blood are magnetically labelled, turning the blood itself into an endogenous contrast agent. This method involves acquiring a pair of images in the target area: one with labelled blood flowing into the imaging volume (tag image), and another one without any labelling (control image). By subtracting the control and tag image, the perfusion-related signal can be isolated. Since its first proposal in the early 1990s, ASL has steadily developed into a well-established, commercially available tool for quantifying neurovascular perfusion [33]. In cardiac settings, ASL holds promise for needle-free myocardial perfusion mapping. Recent studies have validated perfusion values obtained in myocardial ASL (myoASL) against those from traditional first-pass perfusion MRI [34, 35] as well as PET-based literature values [36, 37]. Further, myoASL has proven effective in differentiating between myocardial blood flow (MBF) values obtained at stress and rest [35], as well as between normal and ischaemic myocardial segments [34, 35]. Despite these promising results, clinical translation is still hampered mostly due to insufficient reproducibility of myoASL.

To achieve reliable ASL perfusion measurements in the myocardium, several technical challenges need to be overcome. First of all, while the pathway of blood supply to the brain allows relatively straightforward upstream labelling in neurovascular applications of ASL, the complex pathways in the myocardium require a different, more elaborate approach to achieve efficient labelling [38]. Hence, techniques where labelling is global or is not spatially dependent, are preferred. This includes so-called Flow-sensitive Alternating Inversion Recovery (FAIR) or Velocity-Selective ASL (VSASL). Moreover, the signal-to-noise ratio (SNR) is inherently low in ASL, since the signal change be-

tween tagged and control images lies only between 1 % and 8 % [39]. As a result of the low SNR, myoASL imaging is very sensitive to motion, which is highly present in the cardiac region due to both respiration and the heartbeat itself. It has been shown, that physiological noise (PN) – i. e. noise related to metabolic fluctuations, cardiac and respiratory motion – is roughly 3.4 times higher than thermal noise in cardiac ASL measurements [40]. To counteract cardiac motion, the image acquisition in myoASL is commonly triggered via an electrocardiogram (ECG) to occur at a fixed point of the cardiac cycle. In addition, breathing strategies are employed to mitigate undesired respiratory motion, typically by acquiring images during breath-hold or, less often, by instructing the subject to synchronise their breathing to the image readout.

Recognising both the potential and current challenges in myoASL, this thesis is geared towards developing advanced methods for myoASL to enable more robust contrast-agent-free perfusion mapping of the myocardium. Following an introduction to the underlying physics of NMR, the principles of MR image formation, and myocardial perfusion mapping, this thesis is structured into three principal segments. Each part targets a specific aspect of myoASL to optimise its performance:

- I. The investigation of how physiological and acquisition-related parameters affect myoASL perfusion measurements and the development of a correction approach to minimise acquisition-related bias [41].
- II. The development of a myoASL sequence with T_2 -prepared readouts to suppress residual myocardial signal variations and, thus, reduce the physiological noise in myoASL measurements [42].
- III. The development of a Double Inversion Recovery (DIR) approach for mitigating sensitivity to heart rate variations, reducing physiological noise, and improving overall precision in myoASL measurements [43].

The first part of this thesis has been published in [41] and is focused on alleviating biases related to image acquisition in myoASL. The objective of this work is to investigate how physiological and acquisition-related parameters, including the T_1 relaxation time of blood, heart rate, acquisition matrix size, and flip angle, influence perfusion values obtained with myoASL. To that end, two myoASL sequences with balanced steady-state free precession (bSSFP) and spoiled gradient-echo (spGRE) readouts were compared in numerical simulations, phantom experiments, and an in vivo study in nine healthy volunteers. Moreover, we propose an improved MBF calculation to mitigate the dependence on some of the above parameters: First, subject-specific blood T_1 times are used in the quantification model instead of a fixed, literature-based value as employed in previous studies [37, 40, 44, 45]. Second, an additional saturation-prepared baseline is used for spGRE readouts only, to calculate the MBF. Our simulation and phantom results indicate that quantifying the perfusion with subject-specific blood T_1 times can reduce the mild heart-rate-dependence of MBF which occurs when inaccurate blood T_1 times are used. Further, the acquisition flip angle emerged as the strongest factor affecting precision and accuracy in myoASL measurements. However, our results also suggest that, for spGRE readouts, the proposed baseline acquisition in combination with a dedicated

quantification model, can alleviate its confounding effect and lead to increased reproducibility in myoASL.

The second part of this thesis addresses the impact of PN in myoASL originating from myocardial signal variations. This study shifts the focus from external parameters determined by the image readout to noise sources inherent to the individual measurement. As mentioned above, PN can arise from respiratory or cardiac motion and contains signal contributions from both myocardial tissue and blood, just as the myoASL signal itself. Due to the low volume ratio of blood to myocardial tissue, the PN is dominated by myocardial signal variations. Among other causes, these signal variations can stem from incompletely eliminated static tissue components when subtracting the control and tag image in perfusion quantification. Therefore, in this work, we propose applying so-called T_2 -preparation modules immediately prior to the image readout in myoASL sequences. These T_2 -preparation modules introduce signal weighting based on the T_2 relaxation time of the tissue, where longer T_2 times result in stronger imaging signal relative to signal from tissues with shorter T_2 . Due to the much shorter myocardial T_2 time (ca. 45 ms [46]) compared to that of blood (ca. 250 ms [47]), the myocardial signal components are efficiently suppressed in myoASL with T_2 -prepared readouts while only a minor loss in blood signal is incurred. In this study, we investigated the effect of such T_2 -preparations on myoASL in numerical simulations, phantom experiments, and a proof-of-principle in vivo study. Our simulation results indicate that up to a three-fold SNR gain can be achieved with T_2 -prepared readouts compared to conventional myoASL. In vivo, the PN can be reduced by up to 67 % with this method, suggesting an overall improvement of precision in this case. The findings of this study have partially been presented at the 2024 Annual Meeting of the Society for Cardiovascular Magnetic Resonance in London (UK) [42].

The third part of this thesis builds on the findings of the previous part and introduces a novel method for reducing PN in myoASL, specifically targeting the sensitivity to heart rate variations. Labelling and, in turn, perfusion contrast in myoASL is typically achieved using inversion recovery. Thereby, a radio-frequency (RF) pulse is applied which flips the orientation of the longitudinal magnetisation. During the so-called post-labelling delay (PLD) or inversion time (TI) prior to image readout, the (labelled) blood flows into the imaging slice, while the longitudinal magnetisation relaxes to its equilibrium state. Ideally, the static myocardial tissue would cancel out when subtracting the control and tag image. However, changes in the TI between the two images cause different degrees of magnetisation recovery and, thus, residual signal variation in the myocardium. Particularly for myoASL sequences where the TI is determined by the specific heartbeat duration, heart rate variations pose a major source of PN. To address this, we propose so-called Double Inversion Recovery [48] labelling for myoASL in order to reduce the sensitivity to TI changes. Here, the conventional inversion pulse used for labelling is immediately followed by an identical inversion pulse with inverted pulse phase. This flip back ensures near-complete recovery of the stationary myocardial tissue during TI, such that, even in the presence of TI changes, the myocardial signal is effectively eliminated in the MBF calculation. In simulations and phantom experiments we demonstrate that adding a flip-back pulse can compensate for inconsistent my-

ocardial background signal due to heart-rate-dependent changes in TI. Our in vivo study in two healthy volunteers further suggests that Double Inversion Recovery preparations yield substantial reductions in PN and, consequently, an improved signal-to-noise ratio in myoASL measurements. The findings of this study have partially been presented at the 2024 Annual Meeting of the International Society for Magnetic Resonance in Medicine, in Singapore (SG) [43].

THEORETICAL BACKGROUND

The following chapter outlines the theoretical framework necessary to understand the methods developed in this work. The first two sections describe the physical principles of nuclear magnetic resonance (NMR) and image formation in MRI, and have been published in [49] by Frontiers Media¹. To maintain coherence throughout this thesis, slight modifications of the reproduced material were undertaken. Next, the basic principles of cardiac anatomy and blood flow are introduced. The final section briefly covers clinical techniques for evaluating cardiac perfusion, and introduces myocardial Arterial Spin Labelling (myoASL) as the central concept of this work.

2.1 PHYSICS OF NMR

This section aims to provide a brief overview of the physical principles and basic mathematical concepts behind MRI, which is targeted to create the necessary background to understand modern CMR methods. Based on the introduction of the physics of nuclear magnetic resonance and relaxation, image formation and the k-space formalism are discussed. Furthermore, basic building blocks of MRI are introduced, and common cardiac MR sequences are described.

2.1.1 *Magnetisation formation and dynamics*

Magnetic resonance imaging is based on a magnetic property that is intrinsic to certain nuclei, some of which can be found all throughout the human body. Namely, each atomic and subatomic particle possesses an intrinsic quantum mechanical property called spin. Although it does not originate from an actual rotation of the particle, it can be described mathematically as a quantum angular momentum of a spinning sphere, as illustrated in Figure 2.1. As a quantum mechanical quantity, however, the spin can only have a discrete set of states. By convention, the number of spin states is described according to the spin quantum number S with integer or half-integer values, giving rise to $2S + 1$ different spin states. Particles are classified as bosons with integer spins, and fermions with half-integer spins, such as single protons, neutrons and electrons. In MRI, the nucleus of greatest importance can be found in hydrogen atoms (^1H): It comprises only a single proton with $S = \frac{1}{2}$ and, thus, two spin states. These are commonly denoted as $+\frac{1}{2}$ (“spin-up”) and $-\frac{1}{2}$ (“spin-down”). Corresponding to the classical relation between angular momentum and magnetic moment

¹ © 2022 Ismail, Strugnelli, Coletti, Božić-Iven, Weingärtner, Hammernik, Correia and Küstner. Distributed under the terms of the Creative Commons Attribution License (CC BY).

of a rotating charged particle, the spin S is always associated with a magnetic moment μ via the particle-specific gyromagnetic ratio γ :

$$\mu = \gamma S. \quad (2.1)$$

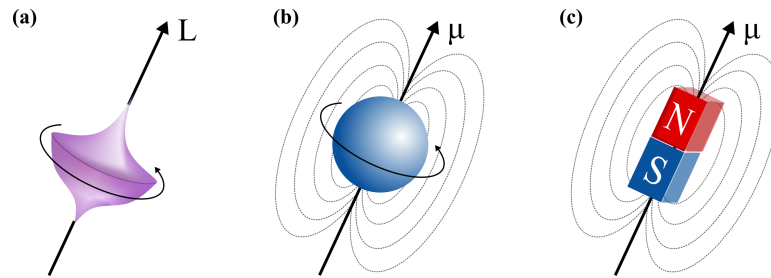


Figure 2.1: A proton with magnetic moment μ (b) can be described in analogy to (a) a spinning top with classical angular momentum L , and (c) a spinning bar magnet with magnetic dipole moment μ . Figure reproduced from [50], courtesy of C. Coletti.

In a proton ensemble, the magnetic moments of the nuclei are randomly orientated unless an external magnetic field \vec{B}_0 is applied. In this case, all particles will align depending on their magnetic moment either parallel (“spin-up”) or anti-parallel (“spin-down”) to the applied field, as depicted in Figure 2.2. Now, spins parallel to the magnetic field are in a lower energy state compared with those in the opposite direction. Hence, the energy levels of the spin states are separated by $\Delta E = \gamma \hbar B_0$, with reduced Planck constant \hbar . This splitting of (nuclear) spin states is also known as the Zeeman effect, named after Pieter Zeeman, who observed it in 1896 as a splitting of optical spectral lines due to a magnetic field.

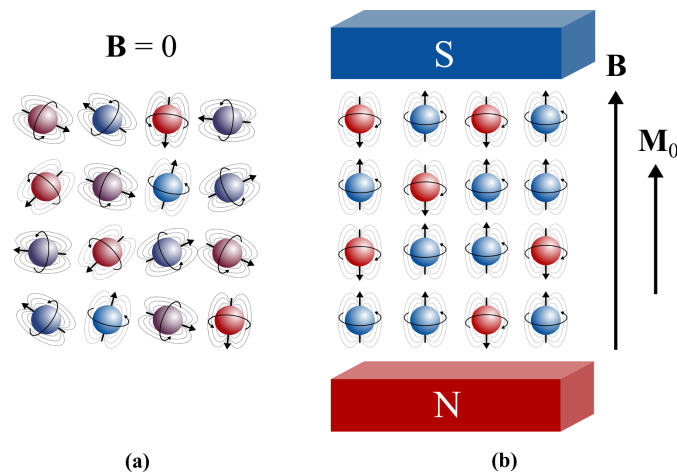


Figure 2.2: (a) Without an external magnetic field, (proton) spins are randomly oriented, (b) whereas in the presence of an external magnetic field \vec{B} , spins align parallel (“spin-up”) or anti-parallel (“spin-down”) to the applied field, creating a net magnetisation \vec{M}_0 oriented along \vec{B} . Figure reproduced from [50], courtesy of C. Coletti.

The number of spins $N(\uparrow)$ and $N(\downarrow)$ in the “spin-up” and “spin-down” state, respectively, follow a Boltzmann distribution:

$$\frac{N(\uparrow)}{N(\downarrow)} = e^{-\Delta E/kT} \quad (2.2)$$

with $\Delta E = E(\uparrow) - E(\downarrow)$. At thermal equilibrium, there is a slight excess of protons in the “spin-up” state due to its lower energy, as shown in Figure 2.3. This can also be shown mathematically by determining the so-called spin polarisation P , i. e. the deviation from an equal distribution of spin states. Using the above Boltzmann distribution one obtains:

$$P = \frac{N(\uparrow) - N(\downarrow)}{N(\uparrow) + N(\downarrow)} = \frac{e^{-\Delta E/kT} - 1}{e^{-\Delta E/kT} + 1} = \tanh\left(-\frac{\Delta E}{2kT}\right). \quad (2.3)$$

Since $\Delta E < 0$, P is positive and so is the difference between spin-up and spin-down states. Due to the angular momentum, the magnetic moment is also associated with a precession around \vec{B}_0 . The rotational frequency of this precession is called the Larmor frequency:

$$\omega_L = \gamma B_0. \quad (2.4)$$

For clinical MRI field strengths (0.5 T-7 T), this frequency is usually found in the radio frequency (RF) range. Thus, the net magnetisation \vec{M} averaged over all protons will be oriented along and precess around \vec{B}_0 .

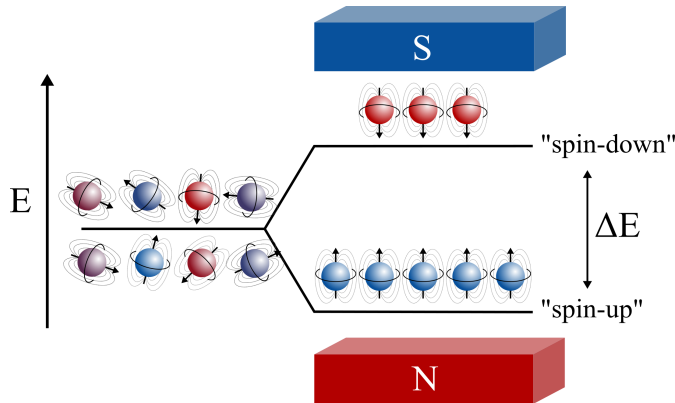


Figure 2.3: Zeeman splitting in an ensemble of spins: Without an external magnetic field, spins are randomly orientated and have the same energy level. If an external field is applied, however, the “spin-up” and “spin-down” states no longer have the same energy level and are separated by an energy gap ΔE . Figure reproduced from [50], courtesy of C. Coletti.

Following the correspondence principle, this net magnetisation \vec{M} and its precession motion can be described with classical mechanics, where the precession dynamics resemble those of a spinning top (Figure 2.1). The net magnetisation \vec{M} can be perturbed if protons are excited from the thermal equilibrium. In the analogy of the spinning top, this would mean tilting its rotation axis to the side. To achieve this, a resonant magnetic field \vec{B}_1 oscillating near ω_L needs to be applied. During this so-called RF pulse, energy will be deposited in the spin system, and some of the protons will flip to the “spin-down” state. Depending on

the duration and strength of the RF pulse, the direction of \vec{M} progressively tips away from \vec{B}_0 leading to a transverse component perpendicular to \vec{B}_0 . Thereby, the polar angle between \vec{M} and \vec{B}_0 is referred to as flip angle. Assuming the initial magnetic field \vec{B}_0 is along the z-axis: Then, the transverse and longitudinal parts of \vec{M} are denoted as \vec{M}_{xy} and \vec{M}_z , respectively. The above described phenomenon is called nuclear magnetic resonance and gives MR imaging its name as the underlying physical principle.

2.1.2 MR signal and relaxation

The precession of \vec{M} leads to an oscillating magnetic field. We can picture the precessing magnetisation as a rotating bar magnet in classical mechanics. This can be detected using a nearby coil where the time-varying magnetic flux induces a measurable electric current via the Faraday-Lenz principle. After the RF pulse has been turned off, the net magnetisation continues to precess around \vec{B}_0 . However, over time, the energy transferred to the system dissipates, and the magnetisation recovers to the thermal equilibrium state \vec{M}_0 . This process is known as longitudinal relaxation and can be described by an exponential growth function with characteristic time T_1

$$M_z(t) = M_{z,eq} - (M_{z,eq} - M_z(0))e^{-\frac{t}{T_1}}. \quad (2.5)$$

Here, $M_z(0) = M_z(t = 0)$ is the flip-angle-dependent initial magnetisation, and $M_{z,0}$ the longitudinal magnetisation at thermal equilibrium.

Besides the regrowth of \vec{M}_z , the transverse magnetisation is subject to an additional relaxation process: The transverse component \vec{M}_{xy} is only preserved if all spins precess with the same frequency, i. e., point to the same direction. But, due to differences in the microscopic environment each spin experiences slightly different magnetic fields. As a result, individual spins precess with slightly different frequencies. Over time, this leads to a dephasing of the spins and a decrease of \vec{M}_{xy} . This is referred to as transverse relaxation and can be modeled by an exponential decay with characteristic decay time T_2 :

$$M_{xy}(t) = M_{xy}(0)e^{-\frac{t}{T_2}} \quad (2.6)$$

In addition, inhomogeneity of the main magnetic field ($\Delta B_{0,i}$) accelerates dephasing and leads to an effective decay time denoted as T_2^* : $\frac{1}{T_2^*} = \frac{1}{T_2} + \gamma \Delta B_{0,i}$. Thus, the actually observed decay time T_2^* is always equal to or shorter than T_2 and usually shorter than T_1 . Both relaxation processes are influenced by the atomic and molecular environment of the proton spins, such as the type, size and motion of the particles. Consequently, different tissue types or pathological tissue changes characteristically influence T_1 and T_2 times. In CMR, for example, the T_1/T_2 times of myocardium and blood at 3 T are 1350/45 ms and around 2000/250 ms, respectively [51]. Together with the proton density, this contributes to the image contrast in MRI.

The above set of equations was first proposed by Felix Bloch to describe the temporal dynamics of \vec{M} , and has accordingly been named Bloch equations [3, 4]. For the evolution of signal intensities, however, this model is less suitable as

it requires solving the individual Bloch equations for all magnetisation vectors. Instead, the so-called Extended Phase Graph (EPG) model has been proposed [52–55], where signal dynamics can be expressed efficiently based on a rotation matrix formalism in the Fourier domain (see section 2.2.1).

2.2 IMAGE FORMATION

Having established the nuclear origin of the MR signal and how it can be manipulated by RF pulses, the next necessary step to image formation is spatially localizing the signal. This is achieved through spatially varying magnetic fields, so-called gradients. As described in Equation (2.4), the precession frequency ω_L of a spin is a function of the magnetic field. Thus, by making the magnetic field a function of the location, spins at different spatial locations will have different resonance frequencies. Although various gradient forms can be applied, linear gradients have proven to be the most useful and, thus, will be assumed in the following. While a linear gradient field is turned on, ω_L becomes a function of the spin position r and the field gradient $\vec{G} = \nabla \vec{B}$:

$$\omega_L(\vec{r}) = \gamma(\vec{B}_0 + \vec{G}) \cdot \vec{r} \quad (2.7)$$

This principle can be used both to select imaging slices within the body as well as to encode positions in-plane within the slice. For simplicity, we will further assume the imaging slice is in the transverse xy -plane. Note, however, that arbitrary acquisition angles can be achieved by using a combination of the x -, y -, and z -gradients for the encoding described below.

Slice selection (SS)

In slice selection, an additional spatially varying magnetic field gradient \vec{G}_z can be applied such that the field strength varies along the z -axis. Thus, the Larmor frequencies of spins will vary along this axis, too: $\omega_L = \gamma(B_0 + G_z z)$. While the additional gradient field is turned on, spins in different xy -planes precess with different frequencies, while spins within the same plane all precess with frequency ω_L . If the excitation RF pulse is chosen to have just the right frequency bandwidth, only spins in the corresponding xy -plane are excited. Accordingly, only in those, a transverse magnetisation will be created.

In-plane frequency encoding (FE)

After selecting a two-dimensional slice, the signal needs to be located within the slice. A gradient \vec{G}_x is applied, such that spins along the x -axis will precess with linearly increasing frequencies. Upon Fourier transforming the signal, each obtained frequency can thereby be connected to a position/pixel on the selected axis, usually the x -axis.

In-plane phase encoding (PE)

To account for the remaining spatial direction, a phase encoding (PE) gradient \vec{G}_y along the y -axis is temporarily applied before the readout. During the

presence of \vec{G}_y , spins along the gradient axis precess with different frequencies. After \vec{G}_y has been turned off, the spins will have accumulated different phases, pointing in different directions, but continue to precess with the same frequency. For one gradient strength, only one phase shift can be achieved. Therefore, multiple PE steps are necessary, which primarily determines the overall scan time. In order to acquire a three-dimensional volume, a second PE gradient along the slice-selection axis can be applied in the same stepwise manner.

2.2.1 k -Space

In the presence of linear gradient fields, the MR signal can be conveniently expressed with so-called k -space formalism. If we consider the precession of \vec{M}_{xy} in the transverse plane, it can be described as

$$M_{xy}(t, \vec{r}) = e^{-i\omega t} M_{xy}^0(\vec{r}), \quad (2.8)$$

with precession frequency $\omega = \gamma B(\vec{r}) = \gamma(\vec{B}_0 + \vec{G}(\vec{r}) \cdot \vec{r})$ (Equation (2.4) and (2.7)). Because the acquired signal is the sum of the magnetisation of all spins in the imaging volume, it can be described as following:

$$S(t) \propto e^{-i\gamma B_0 t} \int e^{-i\gamma \vec{G}(\vec{r}) \cdot \vec{r} t} M_{xy}^0(\vec{r}) d\vec{r} \quad (2.9)$$

The gradient-related frequency contribution can be written in terms of the gradient strengths G_x, G_y and G_z

$$\gamma \vec{G}(\vec{r}) \cdot \vec{r} t = \gamma(G_x x + G_y y + G_z z)t = k_x x + k_y y + k_z z \quad (2.10)$$

with the spatial frequencies k_x, k_y and k_z . If motion is taken into account, \vec{r} becomes a function of time $\vec{r}(t)$. Furthermore, each receiving coil j , i. e. each receiving channel, has a specific sensitivity $c_j(\vec{r})$ to signal from different spatial points. Combining these with the previous equation yields

$$S_j(t) \propto e^{-i\gamma B_0 t} \iiint e^{-i(k_x x + k_y y + k_z z)} c_j(\vec{r}) M_{xy}^0(\vec{r}) dx dy dz. \quad (2.11)$$

Equation (2.11) shows that the measured signal in time domain and the magnetisation in spatial domain are connected via Fourier transformation. As a consequence of this relation, the spatial frequency ($k_{x,y}$) and distance ($\Delta k_{x,y}$) of k -space points are associated with image resolution and size (field-of-view, FOV):

$$FOV_{x/y} = \frac{1}{\Delta k_{x,y}} \text{ and } \Delta x = \frac{1}{k_x}, \Delta y = \frac{1}{k_y} \quad (2.12)$$

The overall scan time is, thus, primarily determined by the number of acquired points in the k -space. In this regard, subsampling techniques offer ways to accelerate image acquisition, as described in [49] and, for a more detailed overview, in [56].

So far, the MR signal has been treated as a continuous function in both space and time. Actual image acquisition, however, is a discretized process characterised by the data sampling rate and image resolution. Hence, the signal model in Equation (2.11) can be discretized as

$$\sigma_j = E_j \vec{\rho} + \vec{\eta}, \tag{2.13}$$

with encoding matrix E_j for coil j , initial transverse magnetisation $\vec{\rho}$, and thermal noise $\vec{\eta}$ [57]. At time point κ and grid point λ , E_j is given by $E_{j,\kappa,\lambda} = c_j(\vec{r})e^{i\Phi(\vec{r}_\lambda, t_\kappa)}$. Neglecting relaxation, the phase factor $\Phi(\vec{r}_\lambda, t_\kappa)$ accounts for phase accumulation due to time-varying magnetic fields.

2.2.2 Sequence Building Blocks

By manipulating the timing and strength of RF-pulses and gradients, a plethora of MR sequences can be constructed. Different pulse sequences differ in their acquisition speed, encoded image information, or to which degree image contrast is affected by differences in proton density, T_1 , $T_2^{(*)}$, or other properties. Cardiac MRI sequences are typically described by components for actual image acquisition and components for preparing the magnetisation. These elements can be understood as building blocks of MRI sequences and the most common ones are presented below. The schematic design of these building blocks is shown in Figure 2.4.

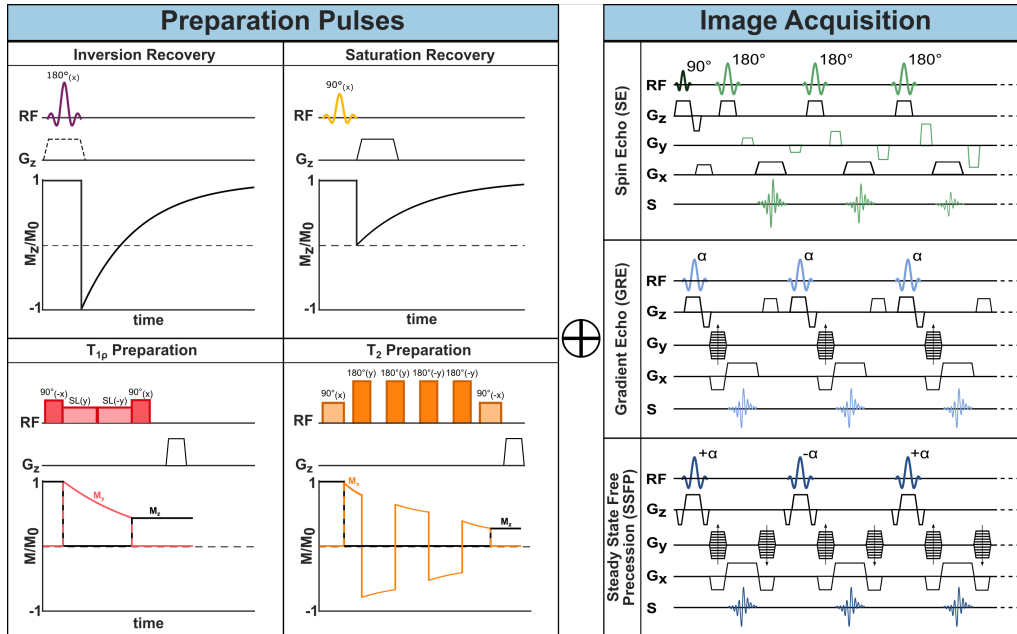


Figure 2.4: MR sequence building blocks: One or more preparatory pulses (left) can be combined with different acquisition sequences (right) to encode the desired information into the imaging data and achieve different image contrasts. Reproduced from [49].

2.2.2.1 Image acquisition methods

Spin Echo (SE)

As described in the previous section, after RF excitation, the net magnetisation is subject to $T_2^{(*)}$ relaxation. Fortunately, part of the dephasing of the transverse magnetisation can be recovered with so-called spin-echo (SE) sequences. In this sequence, a second RF pulse is applied, where the simplest form comprises a 90° excitation and 180° refocusing pulse. After the first excitation, the spins dephase and fan out in the transverse xy -plane. Dephasing caused by temporally invariant field inhomogeneities, however, can be reversed via the second refocusing pulse [58]. Its effect is often described as a pancake-flip: The fan of spins is flipped by 180° around the x - or y -axis, such that the faster spins now move towards instead of away from the slower rotating spins. After a so-called echo time TE, corresponding to twice the time between the two RF pulses, all dephasing caused by static inhomogeneities is rephased and an echo of the signal is created as is depicted in Figure 2.4. This gives the name to the SE sequence. Consequently, the contrast in SE is driven by the T_2 time, which captures the residual dephasing caused by temporally variable factors, such as spin-spin interaction.

Spoiled Gradient Echo (spGRE)

As opposed to SE, so-called gradient echo (GRE) sequences retain not the transverse but the longitudinal magnetisation. They typically require only one RF excitation pulse after which the FE gradient is applied (see Figure 2.4). In GRE, however, the positive FE gradient lobe is preceded by an additional negative lobe. When the areas of the positive and negative lobe are equal, the initially evoked dephasing of spins is reverted – except for T_2^* decay. This creates a signal which is referred to as a gradient echo and gives name to the GRE sequence [59]. In so-called spoiled GRE, the remaining transverse magnetisation is destroyed at the end of each TR cycle. This can be achieved with strong gradients at the end of the TR and results in T_1 weighted imaging [60]. As no additional RF pulses are required, shorter TE and TRs can be achieved in GRE compared to SE, allowing for faster image acquisition. In GRE the echo signal is subject to T_2^* decay as no rephasing of field inhomogeneities is achieved. Therefore, GRE sequences are less robust in presence of field inhomogeneities.

Balanced Steady-State Free Precession (bSSFP)

A third common image acquisition sequence in cardiac settings is the so-called Balanced Steady-State Free Precession (bSSFP). It can be understood as a hybrid between SE and GRE. Starting from a GRE sequence, a train of RF pulses is applied with very short TR ($\ll T_2$) such that the magnetisation never fully recovers between two consecutive RF pulses and a non-zero net magnetisation is present at the next RF pulse. This residual magnetisation contributes to the signal of the following TR. Characteristically for bSSFP, the flip angles are alternated every TR between $+\alpha$ and $-\alpha$, causing the net magnetisation to flip around the z -axis between TRs [61, 62]. This further means that each RF pulse

has both an excitation and refocusing effect on the spins and explains the SE nature of bSSFP sequences. For efficient refocusing of the magnetisation, the gradient moments on all three axes (SS, FE, PE) need to be zero at each TR. This means the areas of positive and negative gradient lobes on each axis must be equal, as shown in Figure 2.4, which is referred to as balanced gradients. The alternating magnetisation progresses through a transient state, and after a certain number of TR cycles \vec{M} reaches a steady-state, that is a stationary amplitude. For $TR \ll T_2$, the contrast in bSSFP sequences is determined by the T_2/T_1 ratio [62]. The main advantage of bSSFP lies in the improved SNR compared with spGRE, due to the recycled transverse magnetisation. However, the scheme is highly sensitive to off-resonances, making it a less common choice for high field strength and rarely useful for ultra-high fields [61].

2.2.2.2 Preparation pulses

Inversion pulses

So-called inversion pulses are 180° RF pulses which can be applied before image acquisition in order to flip the initial magnetisation along the B_0 axis [63]. During the time between inversion and the first imaging RF pulse (inversion time, TI), the longitudinal magnetisation recovers along the B_0 axis towards its equilibrium state as depicted in Figure 2.4. At image acquisition, the degree to which \vec{M} has recovered determines the image contrast, and, thus, induces T_1 weighting. This enhances the image contrast based on T_1 properties, which is of interest in many imaging applications. By adjusting TI, imaging can also be timed to the point when the magnetisation of specific tissues is crossing the zero point, leading to effective signal suppression [63].

Saturation pulses

Intentionally suppressing tissue signal can also be achieved through so-called saturation pulses. These RF pulses flip the magnetisation to the transverse plane. Subsequent spoiler gradients dephase the magnetisation, thereby nulling the signal from the "saturated" spins. The subsequent recovery of longitudinal magnetisation is shown in Figure 2.4. Saturation pulses can be made spatially selective, such that regions in or outside of the image are cancelled out. For instance, artefacts due to through-slice flow can be reduced by applying a saturation pulse upstream parallel to the imaging slice. Furthermore, saturation pulses can be made selective to specific chemical species by adjusting the resonance frequency. The most common example is fat saturation, where RF pulses with carrier frequencies specific to ω_L of fat are applied close to the imaging sequence such that only fat but not water signal is nulled. Creating uniform saturation with common rectangular RF pulses is hindered by their high sensitivity to B_0 and B_1 inhomogeneities. To overcome this limit, adiabatic saturation modules – such as composite [64] or B_1 insensitive rotation (BIR) pulses [65] – have been proposed.

T₂-preparation

T_2 contrast can be induced using so called T_2 -preparations [66, 67]. In a T_2 -preparation, a first 90° excitation pulse is followed by a series of refocusing pulses and, finally, by a 90° flip-back pulse. To induce robust refocusing, the refocusing pulses are separated by a 2τ interval, whereas the interval between the 90° pulses and the refocusing pulses is equal to τ . The total T_2 -preparation time is varied to achieve different echo times. During this time, the refocusing pulses compensate for T_2^* -decay, resulting in a transverse magnetisation decay effectively characterised by the T_2 . The final 90° flip-back pulse brings the remaining transverse magnetisation back to the z axis, encoding T_2 contrast in the longitudinal magnetisation, which is then imaged during acquisition. Several strategies, such as phase cycling following MLEV schemes or using composite pulses, are employed in order to make T_2 -preparations more robust to field inhomogeneities [68, 69].

2.3 CARDIAC ANATOMY AND PERFUSION

In the preceding sections, the physical and technical aspects of MRI have been covered. The following section provides an introduction to cardiac perfusion and how it can be measured with MRI. To understand the blood supply system of the heart, a short introduction on cardiac anatomy and function is given based on [70, 71]. Further, the standard clinical approaches to perfusion measurement, ischaemia detection and diagnosing coronary artery disease (CAD) are briefly outlined. Finally, CMR techniques for perfusion mapping, including first-pass perfusion as well as Arterial Spin Labelling (ASL) MRI, are reviewed.

2.3.1 *Fundamental aspects of cardiac anatomy*

The primary function of the heart is to supply all bodily organs with oxygenated blood via a dual-circulation system: The so-called pulmonary circuit transports deoxygenated blood from the heart to the lungs, which re-saturate it with oxygen and then back to the heart. The second, so-called systemic circuit distributes this freshly oxygenated blood from the heart to all organs in the body, which consume the oxygen, and again back to the heart. To seamlessly accomplish these tasks, the cardiac anatomy follows a distinctive design and features a finely regulated physiology.

Anatomically, the human heart can be divided into a left and right structure. As illustrated in Figure 2.5, each half consists of two separate chambers referred to as the atrium and ventricle. The right chambers receive less oxygenated blood from the organs and pump it to the lungs, while the left chambers receive the re-oxygenated blood from the lungs and pump it to the body. This coupling of the pulmonary and systemic circuit is achieved through a network of blood vessels, connecting the heart with the lungs and the organs. These vessels are categorised as arteries if they transport blood away from the heart or as veins if they transport blood towards the heart. The blood vessels decrease in diameter as they branch out from the heart and reach the organs as so-called capillaries.

The aorta is the largest artery connecting the heart to the organs and measures 2-3 cm in diameter at the aortic root right above the heart [70]. In contrast, the capillary diameter ranges between 5 and 10 μm [70]. For reference, the average diameter of the disk-shaped red blood cells lies between 6 to 8 μm [72].

The movement of blood through the body is achieved via a pumping mechanism driven by the contraction (systole) and relaxation (diastole) of the heart muscle. The two largest veins (lat. *venae cavae*) deliver oxygen-poor blood from the organs to the right atrium and, during relaxation, into the right ventricle. When the heart muscle contracts, blood is pumped from the right ventricle to the lungs via the pulmonary artery. After being re-saturated with oxygen, the blood flows via the pulmonary vein to the left atrium and into the left ventricle once the heart muscle relaxes. With the next contraction, the left ventricle pumps the oxygen-rich blood through the aortic valve and the aorta back to the rest of the body. Once the blood reaches the capillaries, nutrients and oxygen are exchanged, and waste products are cleared from the tissue. Finally, the deoxygenated blood is delivered through the capillaries via increasingly larger veins back to the heart, closing the link between systemic and pulmonary circulation.

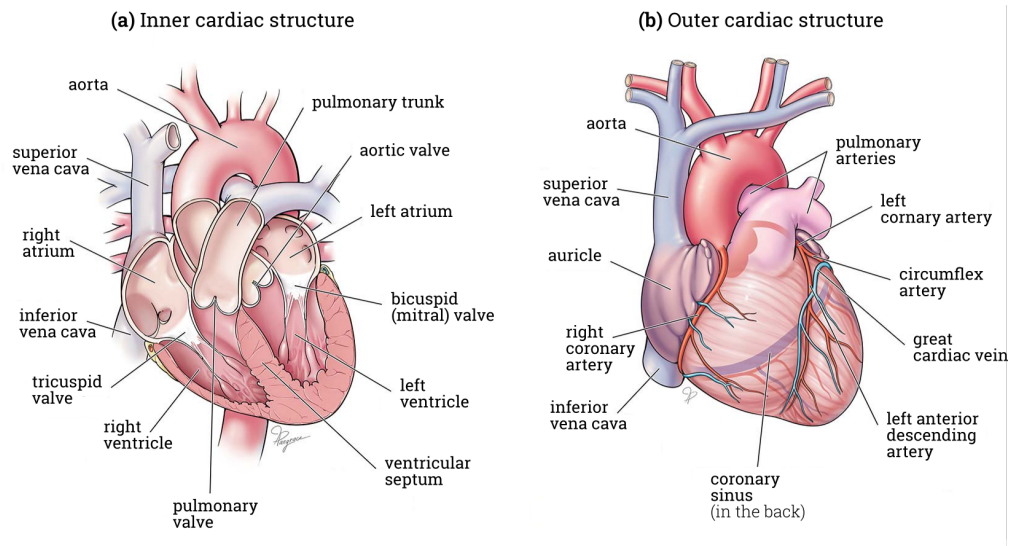


Figure 2.5: (a) Illustration of a cross-sectional view through the human heart. The four cardiac chambers are connected to the lungs and the systemic circulation via a network of large blood vessels. (b) External view of the heart, showing the coronary vessels responsible for blood supply to the heart muscle. Adapted from [73].

The heart and its great vessels are encased by the pericardium, a sac made of fibrous tissue. It consists of two layers, separated by a cavity filled with a lubricating fluid. The inner of the two layers is called epicardium and attaches the pericardium to the actual surface of the heart. It connects the pericardium to the heart muscle (*myocardium*) via a layer of adipose tissue. The endocardium forms the innermost layer of the heart's covering. This sheet of endothelial cells lines not only the internal surfaces of all cardiac chambers but also those of blood vessels, valves and papillary muscles. The myocardium, a so-called striated or striped muscle, performs the contractions that ensure the pumping of the blood. Its muscle cells are arranged in circular and spiral shapes such that

the tension within the chamber during contraction forces the blood to move in one direction towards the respective outlets. The periodic movement of the heart can be largely divided into two phases called systole and diastole. The systole marks the cardiac cycle period during which the myocardium contracts, pushing blood from the left ventricle into the aorta and from the right ventricle into the pulmonary artery. This active phase is followed by the diastole, during which the myocardium relaxes, causing lower pressure within the ventricles relative to the atria and refilling of the ventricles.

To ensure optimal functioning of the pulmonary and systemic circulation at all times, it becomes clear that the various mechanisms require neat regulation. The valves between chambers and blood vessels must operate properly, without obstructions or leakage, to uphold the pressure ratios dictating the blood flow directions. Further, synchronised contraction of individual cardiac muscle cells is required and may not occur irregularly as, for example, in cardiac arrhythmia. Lastly, the myocardial walls around the ventricles need to exert enough force during systole and, equally important, relax enough to allow for adequate refilling during diastole. In order to maintain this intricate orchestration, the heart muscle needs to be sufficiently supplied with blood carrying oxygen and nutrients.

2.3.2 *Cardiac perfusion*

2.3.2.1 *Coronary vasculature*

Contrary to what might be assumed, the heart muscle is not supplied with blood directly from the enclosed ventricles [74]. Apart from the thickness of the myocardium, high blood flow velocities and pressure within the ventricles prevent direct diffusion. Instead, a specific circuit exists within the systemic circulation, which supplies only the heart tissue [75]. This system is formed by a set of arteries and veins that span the cardiac surface in a crown-like shape, as illustrated in Figure 2.5, giving rise to their name as coronary vessels. Right above the aortic valve, two primary coronary arteries arise from the aorta: The right coronary artery winds along a groove between the right atrium and ventricle to the back of the heart. The left coronary artery is very short and bifurcates after a few centimetres into the left descending and left circumflex arteries. While the left descending artery follows the groove between the left and right ventricle, the left circumflex artery winds along the atrioventricular groove to the back of the heart. Akin to the vasculature in other body parts, these three main arteries extend into smaller, dependent vessels and further into a capillary bed, facilitating nutrient and oxygen exchange within the myocardium.

A distinctive characteristic of cardiac perfusion is the clear separation of supply territories by individual coronary vessels. Unlike other organs, there is little to no overlap in blood supply to these regions. Nonetheless, connections between arteries or veins are formed by so-called anastomoses, which offer alternative routes for blood supply or drainage, respectively. These small connecting vessels are observed both within and between coronary perfusion regions [76] and are more pronounced in venous than arterial networks [75]. Anastomoses grow into larger collateral vessels when supplying arteries are damaged

or blocked, for instance, with ageing or in atherosclerosis. By allowing continued blood supply, they can mitigate oxygen shortage and prevent damage to the corresponding supply territories to a certain extent. With increasing severity of arterial lesions, however, the substitute routes provided by collateral vessels are not sufficient to maintain cardiac function [75].

2.3.2.2 Perfusion regulation

Perfusion refers to the local flow of blood through the capillary network and its exchange with the surrounding extracellular space. This physiological process is critical to tissue viability and can be described in analogy to Ohm's law [74]. For both individual vessels and an entire vascular network, the perfusion rate f can be given in units of volume/time as:

$$f = \frac{\Delta P}{R}. \quad (2.14)$$

Here, the pressure difference ΔP between the inlet and outlet of the vessel represents the driving force of the flow. At the same time, flow is impeded by vascular resistance R arising from the friction between moving blood and the vessel wall. The resistance of a cylindrical vessel of length L and radius r , can be described according to Poiseuille's law as:

$$R = \frac{8L\eta}{\pi r^4}, \quad (2.15)$$

with blood viscosity η . Combining Equations (2.14) and (2.15) yields the Hagen-Poiseuille law:

$$f = \frac{\Delta P \pi r^4}{8L\eta} \quad (2.16)$$

Notably, the fourth power dependence on the vessel diameter emphasises its decisive role in regulating vascular flow.

The myocardium at rest is remarkably adept at extracting oxygen from circulating blood, achieving extraction rates of 70 to 80 %. This is in stark contrast to other organs with less efficient oxygen extraction, such as skeletal muscles, which exhibit extraction rates of 30 to 40 % at rest [77, 78]. However, this high baseline extraction capacity also means that during increased demand, the heart cannot substantially enhance oxygen extraction. Instead, the blood flow to heart tissue is increased to meet its metabolic needs. Therefore, the precise regulation of cardiac perfusion is crucial for optimal heart function and, ultimately, the entire body. As per the Hagen-Poiseuille law (Equation (2.16)), the key control variable in coronary perfusion is the vessel diameter. It is adapted by contracting or dilating vessels, mainly arterioles, where the pressure drop is the highest across the human vasculature [74]. This auto-regulation mechanism involves a complex interplay of neural, hormonal, and metabolic processes, all integrated into a single response governing vaso-dilation and constriction.

Another critical parameter in regulating coronary perfusion is the maintenance of the pressure gradient between arteries and the capillaries. The coronary blood flow dynamics are closely tied to the cardiac cycle: During systolic

contraction, the blood flow from the left ventricle into the aorta is highest. Yet, this same contraction paradoxically reduces coronary flow due to the compressive forces exerted on the vessel walls of downstream arterioles, increasing flow resistance. Hence, coronary flow is lowest during systole, an effect known as myocardial extra-vascular contraction [79]. The opposite is the case during diastole, where maximal coronary flow is reached as the myocardium relaxes and vessels are dilated.

2.4 ASSESSING CARDIAC PERFUSION

Due to the critical role of myocardial blood flow (MBF) for optimal cardiac function, even a slight shortage of oxygen leads to symptoms such as chest pain, changes to electrical activity observable via ECG, and alterations to the contractile function [75]. Ischaemia refers to an oxygen deficit caused by diminished blood flow and, if sustained, can result in myocardial infarction, i. e. death of heart muscle cells. In the context of CAD, this critical condition arises due to plaque build-up in the vessel walls, which occludes coronary arteries and limits myocardial perfusion [79]. Such accumulation of fat and cholesterol in the arterial walls, which may calcify with progressing disease, is known as atherosclerosis. Unless collateral vessels exist, atherosclerosis leads to an under-supply of blood to the tissue downstream of the affected vessel depending on the severity of the occlusion. When a patient is suspected or known to have CAD, the diagnostic goal is thus to determine the presence and extent of coronary obstructions, evaluate the myocardium for signs of ischaemia or infarction, and guide therapeutic interventions. The choice of diagnostic procedure depends on the patient's symptoms and medical history, encompassing a spectrum from invasive to non-invasive techniques.

Diagnostic assessments can be performed under resting conditions, during induced stress, or, most often, a combination of both [80, 81]. Here, induced stress refers to increasing oxygen demand in the myocardium in order to prompt an adjustment of coronary perfusion. Hence, the capacity of the heart to increase blood flow through vasodilation is revealed in this hyperaemic state. This enables the identification of conditions in which coronary flow is only partially blocked and myocardial perfusion is preserved by lowering vascular resistance. Namely, when vessels are already at maximum dilation, perfusion cannot be further increased when oxygen demand rises. This inability to elevate MBF under hyperaemic stress, therefore, serves as an essential indicator of underlying vascular pathology [79]. Various stress-inducing methods are available, typically through exercise or pharmacological agents, and are selected based on their compatibility with the chosen diagnostic modality.

2.4.1 *Detecting and assessing CAD*

In the following, both invasive and non-invasive standard techniques for clinical assessment of CAD are presented, based on two recent consensus statements on stenosis [82] and perfusion imaging [81]. Given the aim of this thesis, the emphasis is placed on perfusion rather than stenosis assessment, which gen-

erally relies on distinct contrasts and imaging approaches. In particular, CMR techniques for perfusion imaging are discussed, including first-pass perfusion CMR and myocardial ASL (myoASL).

2.4.1.1 *Invasive diagnostic approaches for CAD*

Invasive coronary angiography (ICA)

As the clinical gold standard for stenosis assessment, Invasive Coronary Angiography (ICA) is based on delivering a contrast agent directly to the coronary arteries. This is achieved via a catheter that is guided to the heart under full or conscious sedation. The contrast agent enhances the visibility of coronary arteries on x-ray imaging and, thus, enables to identify vessels with restricted or blocked blood flow. Although angiographic images are primarily evaluated on a qualitative basis, ICA can also provide quantitative measures, most commonly via the fractional flow reserve (FFR). The FFR is defined as the ratio of maximal blood flow in a stenotic artery to normal maximal blood flow [83]. It is derived from the ratio of distal coronary pressure to the aortic pressure during maximal vasodilatation and is recommended in clinical guidelines for CAD management [84]. It is particularly useful in borderline cases where a decision to proceed with revascularisation cannot be made unambiguously based on angiographic images alone. Moreover, if obstructed vessels are found, ICA can simultaneously guide revascularisation within the same session at the catheterisation laboratory. [81, 82]

Intra-vascular ultrasound and OCT

Intra-vascular ultrasound (IVUS) and optical coherence tomography (OCT) represent alternative catheter-based procedures to assess occlusions in coronary arteries. For IVUS, the catheter probe serves as a regular ultrasound transducer, whereas an OCT probe emits near-infrared light and measures the interference pattern of the back-scattered beams. Although OCT provides the highest spatial resolution, the penetration depth is lower compared to IVUS, which prevents complete evaluation of coronary plaque burden. Overall, IVUS and OCT mainly serve for characterising plaque composition and identifying high-risk plaques, e. g. in stent placement, rather than for direct measurement of cardiac perfusion. [82]

2.4.1.2 *Non-invasive diagnostic approaches for CAD*

Single-photon emission computed tomography (SPECT)

Single-photon emission computed tomography (SPECT) stands as the prevalent non-invasive technique for clinical perfusion imaging. Following intravenous administration, a radio-nuclide tracer accumulates in the myocardium and undergoes γ -decay. Rotating scintillators detect the emitted photons and generate a sinogram that is later reconstructed into a 3D image of the heart, similar to x-ray computed tomography (CT). Because the tracer delivery depends on the regional blood flow, the obtained images are inherently perfusion-weighted

and allow for detecting ischaemic myocardial regions. Historically, absolute measurement of MBF has been limited due to the non-linear uptake properties of traditional SPECT-tracers. Nonetheless, the introduction of new tracers along with advances in imaging technology are bringing SPECT-based MBF quantification within reach, with the goal of wide-spread integration on clinical SPECT systems. [81]

Positron Emission Tomography (PET)

Akin to SPECT, PET perfusion mapping is based on the intravenous injection of a radio-nuclide tracer and subsequent mapping of its activity via γ -photons. However, PET tracers exhibit β^+ instead of γ -decay and, thus, emit positrons, which then recombine with electrons in tissue. This annihilation yields two photons of the same energy being emitted at approximately 180° to each other. These recombination events are registered based on simultaneous detection of two photons at opposite positions of the detector ring. PET-based images are inherently quantitative and allow for absolute measurement of tracer concentration. Together with dynamic imaging during the passage of tracer-bolus and kinetic modelling of the obtained signal, PET can provide accurate MBF values and is thus considered the gold-standard for perfusion quantification. [81]

Computed Tomography (CT)

In combination with an adequate intravenous contrast agent, x-ray CT offers both qualitative and quantitative perfusion imaging. Quantitative analysis, in particular, requires dynamic imaging of the heart during the passage of the contrast agent as well as dedicated quantification algorithms. However, dynamic imaging is associated with high radiation dose and low contrast-to-noise ratio. Despite promising approaches such as low kilovolt (kV) scanning, photon-counting, or energy-selective detectors, cardiac CT remains primarily used for coronary angiography – the non-invasive equivalent of ICA – rather than for perfusion studies in clinical practice. [81]

Echocardiography

Unlike the previous three techniques, cardiac ultrasound or echocardiography does not require ionising radiation and is the predominant modality for assessing cardiac function at the bedside as well as in patients with acute chest pain. Cardiac perfusion can also be evaluated by means of contrast-echocardiography, which uses small, gas-filled spheres called microbubbles as an intravenous contrast agent. Microbubbles are particularly interesting because they remain entirely intra-vascular and do not diffuse into the extra-vascular/inter-cellular space, unlike common contrast agents used in SPECT, PET, CT, or MRI. However, noise and artefacts impair the image quality and, in turn, reproducibility of contrast-echocardiography, which, therefore, remains less frequent in clinical practice. [81]

Cardiac MRI

MRI provides versatile tools for both plaque characterisation and angiography, as well as myocardial ischaemia detection. While the former two applications are widely used in research, their clinical adoption is less advanced compared to the previously described techniques [81]. On the other hand, MR perfusion imaging is more frequently applied, albeit predominantly in expert centres and research settings [49]. Here, so-called first-pass perfusion CMR is most common and is based on monitoring the passage of a previously injected exogenous contrast agent through the coronary vasculature. Compared to ICA or SPECT, first-pass CMR is particularly advantageous for avoiding ionising radiation and in patients with complex disease conditions [81]. Moreover, recent developments towards faster imaging sequences and 3D, whole-heart perfusion mapping continue to improve the utility of first-pass CMR in clinical settings [81]. Despite these benefits and numerous studies establishing a good agreement with standard techniques, a lack of large, randomised clinical trials currently limits wider clinical integration of MR perfusion imaging [12, 81, 85]. The technical details and quantification approaches for first-pass perfusion MRI will be elaborated on in the following.

2.4.2 First-pass perfusion cardiac MRI

2.4.2.1 General principle and imaging sequences

In first-pass perfusion CMR, images of the myocardium are acquired during the first transit of a contrast-agent-bolus, which enhances the blood signal. The most common contrast agents are based on the heavy-metal gadolinium, leveraging its paramagnetic properties. Gadolinium in its free form is highly toxic as it interacts with calcium ion channels [86]. Thus, gadolinium-based contrast agents (GBCAs) are always formulated with highly stable chemical complexes. These so-called chelates bind gadolinium to an organic ligand, neutralising its toxic potential, and result in seven unpaired electrons. As such, when interacting with an external magnetic field, the chelate behaves paramagnetically and amplifies the local magnetic field. In consequence, surrounding hydrogen protons exhibit an increased relaxation rate or, respectively, a decreased relaxation time [27]. Upon intravenous administration, GBCAs circulate through the blood vessels and modify the signal of perfused tissues. In regions with compromised perfusion due to an upstream coronary occlusion, for example, the absence of GBCAs means the signal remains unaltered. To leverage the GBCA-induced shortening of the T_1 relaxation time and amplify the signal in well-perfused tissue, T_1 -weighted imaging sequences are employed, typically single-shot gradient echo (GRE) or balanced steady-state free-precession (bSSFP) [12]. Consequently, this approach yields a perfusion-weighted contrast, with areas of lower GBCAs concentration, indicative of poor perfusion, appearing less intense than well-perfused regions.

In practice, late-gadolinium enhancement (LGE) images are often evaluated alongside first-pass perfusion images [87]. LGE makes use of the contrast agent previously administered for first-pass imaging, but data are acquired follow-

ing a delay, usually about 15 minutes [88]. This waiting interval allows the contrast agent to accumulate in the tissue matrix. In healthy tissue, the contrast agent is swiftly cleared out via diffusion into the venous vasculature. Conversely, in scarred or diseased tissue, wash-out is impaired and contrast agent can accrue in the extra-vascular, extracellular space [89]. This accumulation of GBCAs causes the affected areas to appear brighter in LGE images, providing additional information on the viability of cardiac tissue [89, 90].

2.4.2.2 *Perfusion quantification with first-pass CMR*

The perfusion-dependent contrast variation in first-pass CMR can also be employed for quantitative imaging, which offers incremental prognostic value over qualitative perfusion assessment [91]. In a static image, regions of myocardial tissue with higher perfusion will appear brighter, while those with lower perfusion will appear darker. However, if dynamic imaging is performed during the passage of the contrast-agent-bolus, quantitative parameters can be extracted based on how the signal enhancement changes over time. For the most part, visual interpretations or semi-quantitative measures, like simple enhancement curve properties, remain the backbone of routine clinical reporting [80, 81]. Yet, quantitative perfusion analysis contributes to the overall prognostic value and is particularly beneficial in complex patients because it allows to identify multi-vessel disease and microvascular dysfunction [92, 93]. Full quantification of MBF, however, requires knowledge of the so-called arterial input function (AIF). The AIF characterises the temporal concentration profile of the contrast agent in the bloodstream and accounts for its delivery to the myocardial tissue. Although it is theoretically feasible to extract the AIF from the same imaging data used to monitor the myocardial signal evolution, e. g. from the blood pool signal, this approach is prone to errors due to saturation effects [94]. These occur at high concentrations of GBCA, particularly at the bolus peak, and lead to plateauing of the signal and, in turn, underestimation of the gadolinium concentration.

To mitigate saturation effects when acquiring the AIF, two main strategies exist. In so-called dual-bolus protocols, the contrast agent is administered twice during the imaging session [95]. First, a low-dose bolus is injected, and dynamic images are acquired to derive the AIF from either the blood pool or the proximal aorta. Then, a second, high-concentration bolus is administered in order to acquire the myocardial contrast enhancement curves. Because the concentration ratio of the two boluses is predetermined, the AIF can be scaled accordingly in post-processing to match the myocardial signal. Alternatively, so-called dual-sequence protocols require only a signal contrast injection, but acquire two concurrent images within the same heartbeat [96]: a low-resolution image of the left ventricular blood pool for AIF estimation, followed by a high-resolution image of the myocardial region. The main benefit of dual-bolus over dual-sequence approaches lies in the simplicity of the method [95]. However, it requires precise timing of the two contrast-agent-injections to avoid contamination of the second bolus and increases the gadolinium exposure for the patient [97]. Dual-sequence approaches avoid a second administration of contrast agent and produce high-quality images at the same time, but entail more com-

plex imaging protocols and intricate post-processing compared to dual-bolus methods [97, 98]. The choice of the particular sequence is, therefore, dependent on specific clinical requirements and the expertise of the medical professionals involved.

Having obtained both the AIF and the corresponding myocardial enhancement curve, the aim is to derive either absolute perfusion values or, alternatively, semi-quantitative perfusion metrics. Under ideal conditions with an instantaneous contrast-agent-bolus, the gadolinium influx at the arterioles produces a transient signal increase in downstream tissue, which is proportional to the local perfusion levels. This signal enhancement lasts as long as labelled blood is flowing through the tissue, which is referred to as mean transit time (MTT) and can be determined from first-pass measurements. Given a known or estimated blood volume fraction (V_B), the MBF can be calculated from the MTT in tissue MTT_{tissue} as:

$$MBF = \frac{V_B}{MTT_{tissue}}, \quad (2.17)$$

where the MTT of the arterial input is already subtracted from MTT_{tissue} . But, this relation only holds true in cases where the contrast agent remains confined within the blood vessels. If GBCAs permeate into the extracellular extravascular (i. e. interstitial) space, the observed MTT in tissue exceeds the actual vascular MTT of gadolinium, necessitating adjustments in subsequent quantification [97].

Unlike neurovascular perfusion studies, where the blood-brain-barrier restrains GBCAs to the vasculature, diffusion of GBCAs into the interstitial space is prevalent in cardiac settings [12]. Therefore, myocardial perfusion studies mostly rely on more elaborate MBF estimation methods, which typically involve deconvolution of the myocardial and blood signal. To illustrate why this is necessary, the AIF can be understood as a series of individual impulses that each generate a downstream response in myocardial tissue [97]. The first-pass imaging signal, however, represents the sum of all these myocardial responses, all sharing the same shape scaled according to their respective impulse. This relation between arterial input and measured signal in tissue is illustrated in Figure 2.6. Mathematically, this corresponds to a convolution of the AIF with the myocardial response function, as is illustrated in Figure 2.6.

The specific perfusion quantification methods can be broadly categorised into model-based and model-independent approaches. Model-based quantification mostly relies on two-compartment models for the vascular and interstitial space, which require a predefined set of tissue parameters. Following a deconvolution of the blood and myocardial signal, the model can then be solved for the remaining parameters, such as the MBF [99]. Alternative model-independent approaches directly deconvolve the AIF and myocardial signal curves to obtain the myocardial response function [100]. This is based on the central volume principle, which states that the myocardial response function is equal to the MBF [101]. But, as the deconvolution of the signal enhancement curve is inherently ill-posed, additional constraints on the myocardial response function are required [100]. This is usually achieved by limiting the shape of the myocar-

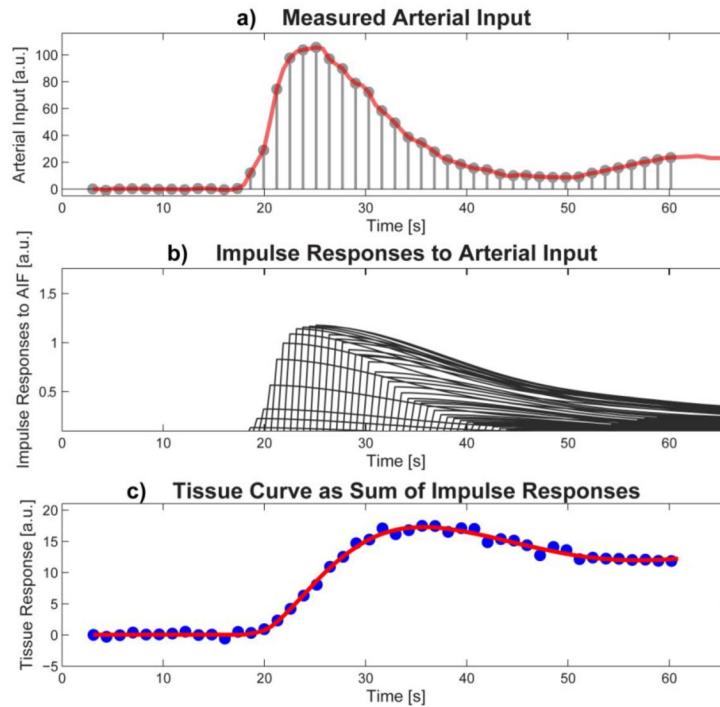


Figure 2.6: (a) The measured arterial input (red) can be understood as a series of individual arterial impulses (black). (b) Over time, each of these impulses leads to a specific downstream response. (c) The measured signal in first-pass perfusion imaging corresponds to the sum of these responses. Reproduced from [97].

dial impulse response to Fermi functions based on observations from simulation experiments. Although computationally demanding, model-independent approaches circumvent the need for defining model parameters, which represent a significant error source in model-based quantification [100].

2.4.2.3 Safety of GBCAs

The clinical utility of MR perfusion imaging as a non-ionising alternative, and particularly the added value of quantitative perfusion metrics, is limited due to the required use of GBCAs. Notably, the administration of GBCAs in patients with severe renal impairment has been directly associated with the incidence of nephrogenic system fibrosis (NSF) [28, 30]. The vast majority of patients develop NSF a few months after exposure to GBCAs and present with thickened skin, joint shortening, and potentially life-threatening fibrosis of internal organs [30]. While the exact pathophysiology is not fully understood, the specific chelate-type of the GBCAs is known to affect the risk of NSF onset [29]. Owing to regulatory measures and adjusted formulation of GBCAs, the incidence of NSF has thus been substantially reduced [102]. Nonetheless, after an initial report of accumulation of GBCAs in brain tissue [31], it is known today that all bodily tissues retain gadolinium after GBCA use, even in subjects with healthy kidney function [32]. Therefore, safety concerns regarding GBCAs usage persist across all patient populations.

In the wake of these safety issues, alternative candidates for contrast enhancement have gained attraction, among which mainly ferumoxytol. This iron-oxide based agent was initially approved for treating iron deficiency in patients with chronic kidney failure [103]. But, as a paramagnetic substance, ferumoxytol affects the MR signal similar to conventional GBCAs. Despite its potential for MR perfusion imaging and angiography, the off-label use of ferumoxytol as a contrast agent is controversial. The US Food and Drug Administration (FDA) issued the most severe safety warning for ferumoxytol in 2015, following severe and sometimes fatal incidents upon its use as a contrast agent [104]. The FDA restricts the use of ferumoxytol only to instances, where the potential benefits outweigh its risks, while the European Medicines Agency (EMA) fully suspended its use in the EU [105]. The EMA further warns that ferumoxytol may be retained in the body and alter the MR signal up to three months after initial administration. Studies have further found ferumoxytol to have higher rates of adverse and severe adverse events compared to GBCAs [106]. In conclusion, enhancing the accessibility of MR perfusion imaging and leveraging its non-invasive, non-ionising nature requires the development of new contrast agents with improved safety profiles or alternative imaging techniques, which eliminate the need for contrast agents altogether.

2.4.3 Myocardial Arterial Spin Labelling

MRI offers an alternative technique known as Arterial Spin Labelling (ASL) to quantify perfusion without exogenous contrast agents like GBCAs. Instead, magnetically labelled blood acts as an endogenous contrast agent in ASL. Moreover, ASL facilitates a more straightforward MBF quantification than first-pass CMR or nuclear imaging techniques, as the imaging signal can be made directly proportional to the perfusion rate [107, 108]. Originally, ASL was developed for neurovascular perfusion mapping and has become a well-established clinical method for neurological studies over the past three decades [33, 107]. Although ASL has been explored early on for various anatomies such as the lungs [109] or placenta [110, 111], the most notable success outside the brain was achieved for kidney perfusion [112]. However, most extra-cranial ASL methods remain limited to research, often as a result of application-specific, technical challenges [113]. This is particularly true for myocardial ASL (myoASL), where high physiological noise (PN) levels and respiratory and cardiac motion limit clinical translation. Nonetheless, the advancements achieved in myoASL over the years suggest its potential as a contrast-agent-free alternative to traditional first-pass perfusion CMR.

More specifically, myoASL has proven efficient for measuring MBF values in healthy subjects that agree with those obtained from gold-standard methods such as PET [114]. Studies in a porcine model further validated the accuracy of myoASL measurements, demonstrating a close match between myoASL-based perfusion values and those obtained using radio-labelled microspheres [115]. Additionally, several studies in healthy individuals have demonstrated the sensitivity of myoASL to perfusion changes induced by exercise [40, 116, 117] or pharmacological stress (i. e. vasodilation) [118–120]. In clinical studies, myoASL

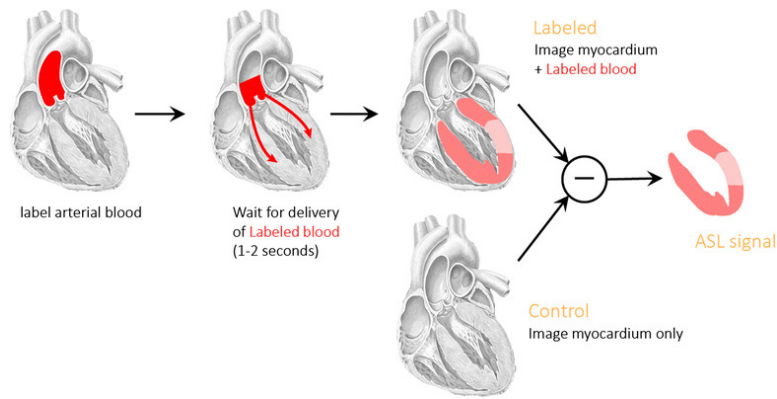


Figure 2.7: Schematic illustration of the basic principle of perfusion mapping with myocardial arterial spin labelling (ASL). The perfusion-related signal can be extracted by subtracting two separately acquired images: a tag image with labelled blood (top) and a control image without (bottom). Reproduced from [38].

showed potential for detecting reduced myocardial perfusion reserve – defined as the ratio of MBF under stress versus at rest – in patients with single-vessel CAD [120]. Moreover, in cohorts with known or suspected CAD, myoASL allowed for differentiating between healthy and ischaemic myocardial regions, in agreement with semi-quantitative first-pass perfusion measures [45]. Finally, ischaemic myocardial regions identified using myoASL were shown to correspond with concurrent findings from ICA in patients with confirmed CAD [35].

The fundamental principle underlying most ASL sequences involves the acquisition of two images with differing blood contrast, usually one with magnetically labelled blood and one without any labelling. Throughout this work, these two images will be referred to as tag and control image, respectively. Ideally, the contrast of static tissue will be identical in control and tag image such that one can isolate the perfusion-related signal by subtracting the two images, as illustrated in Figure 2.7. Due to the low SNR in ASL, perfusion values or maps are typically obtained as an average across multiple pairs of control and tag images. In the following, the common myoASL sequences are described in terms of labelling schemes and image readouts, as well as methods for quantifying myocardial blood flow.

2.4.3.1 Labelling techniques

Several approaches exist to achieve magnetic labelling of the blood, a process that is notably more challenging in the heart compared to the brain. Whereas the brain is supplied by one main vessel on each side of the neck – the carotid and vertebral arteries – the intricate cardiac anatomy and vascular structure complicate direct labelling in the heart. Although inversion of blood at the aortic root was successfully demonstrated in human hearts [121], upstream labelling remains substantially harder to achieve than in the brain. Therefore, two main approaches have been explored in human myoASL: velocity-selective labelling (VS-myASL) and Flow-sensitive Alternating Inversion Recovery labelling (FAIR-myASL).

VS-my α ASL

In VS-my α ASL, spins in the blood are labelled based on their velocity instead of their location, such that the label is created directly in the imaging volume – a hallmark of VS-ASL compared to other labelling approaches. This concept was first proposed for ASL in the brain to alleviate confounding effects of slow blood flow and long transit times [122]. The essence of VS-labelling lies in encoding velocity information of the spins into the longitudinal magnetisation and, thus, the imaging signal. This is achieved by first flipping the spins into the transverse plane and then applying bipolar gradients to induce spin dephasing depending on their velocity. Namely, the accumulated net phase of a spin moving at constant velocity v through a linear gradient of constant strength G is given by:

$$\phi_{net} = \gamma G \int_0^{\Delta t} x(t) dt = \gamma G \int_0^{\Delta t} vt dt = \gamma G v \Delta t^2 \quad (2.18)$$

with gradient duration Δt and gyromagnetic ratio γ . Upon a flip-back to the longitudinal axis, the longitudinal magnetisation M_z for a spin with velocity v then becomes:

$$M_z = M_0 \delta_{sat} \cos(\gamma v G \Delta t^2), \quad (2.19)$$

where δ_{sat} is the saturation efficiency of the RF pulses. Assuming laminar flow with a uniform velocity distribution between 0 and v_{max} , the mean magnetisation can be expressed as

$$\bar{M}_z = \frac{M_0 \delta_{sat}}{v_{max}} \int_0^{v_{max}} \cos(\gamma v G \Delta t^2) dv = M_0 \delta_{sat} \text{sinc}(\gamma v G \Delta t^2). \quad (2.20)$$

Based on the first zero-crossing of M_z in this velocity profile, a cut-off velocity v_c can be specified, above which spins are effectively dephased. Experimentally, this velocity threshold is realised by adjusting the gradient shape, strength, and duration. Combined with imaging that captures only spins with velocities below v_c , this approach selectively enhances signals from decelerating blood spins. Through careful selection of v_c , effective elimination of signal from static tissue and venous blood, which accelerates transiting from tissue to veins, can be accomplished. The velocity selection of the image readout can be implemented via bipolar readout gradients or additional VS-pulses prior to imaging. Despite its broader application in neurovascular ASL studies [123], VS-labelling is rarely used in the myocardium [124, 125].

FAIR-my α ASL

The vast majority of my α ASL studies resorts to FAIR-labelling [126] to create endogenous blood contrast. Here, magnetic labelling is achieved by inverting the spins of inflowing blood before the imaging readout. More specifically, inversion pulses are applied in an alternating fashion either globally across the entire imaging volume (non-selective) or to the imaging slice only (slice-selective) as illustrated in Figure 2.8 [126]. To ensure thorough inversion, mainly adiabatic

Flow-sensitive Alternating Inversion Recovery

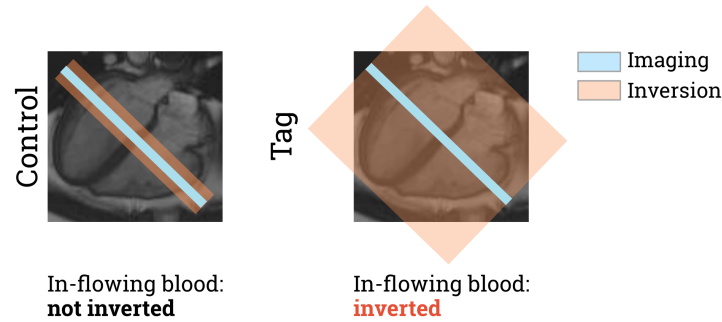


Figure 2.8: In Flow-sensitive Alternating Inversion Recovery (FAIR) myoASL, slice-selective (left) and non-selective (right) inversion pulses are applied in an alternating fashion to achieve perfusion contrast. As a consequence, blood flowing into the imaging volume is native/non-inverted in control acquisitions and inverted in tag acquisitions, respectively. Adapted from [38].

hyperbolic-secant pulses are used and the width of the slice-selective inversion slab is usually set to three times that of the actual imaging slice [40, 116]. Following a defined waiting period after the labelling pulse, known as post-labelling delay (PLD) or inversion time (TI), imaging is performed. In the control image, the slice-selective pulse allows non-inverted spins to replace the previously inverted ones within the imaging volume. Due to the fast cardiac blood flow compared to the typical labelling slab width, it can be assumed that, during TI , most blood spins are replaced in the imaging slice. In the tag image, on the other hand, the non-selective labelling leads to inverted spins flowing into the imaging volume, reducing the average longitudinal magnetisation compared to the control image proportionally to the perfusion rate [108].

To ensure full magnetisation recovery between images and avoid signal contamination, control and tag images are acquired with a delay period of typically 6 seconds, further referred to as control-tag-delay. Although the static myocardial tissue is also inverted in the FAIR-images, as shown in Figure 2.8, the contrast should be identical between the images such that the static tissue signal can be eliminated by subtraction. Thus, the difference between the control and tag image yields a perfusion-weighted image from which the MBF can be quantified directly. Further, acquiring FAIR-images at multiple delay times allows for concurrent estimation of MBF and arterial transit time (ATT), representing the duration necessary for the labelled blood to reach the imaging slice.

2.4.3.2 *Imaging readouts*

Given the high motion sensitivity of myoASL, rapid image acquisition within a cardiac cycle is crucial to ensure adequate image quality. The predominant acquisition sequence in myoASL for this purpose is snapshot bSSFP, as commonly employed in CMR owing to its short acquisition duration and good signal efficiency. In this context, "snapshot" denotes an imaging process where all k-space lines are acquired in a single heartbeat. Recently, snapshot echo-planar imaging (EPI) has been introduced for myoASL [127], offering the potential for

multi-slice acquisitions and sufficient coverage of coronary territories, as recommended by the American Heart Association [128]. Its susceptibility to cardiac motion as well as B_0 inhomogeneities, however, is currently restricting the use of EPI primarily to research settings.

To further reduce the acquisition window, several acceleration strategies have been proposed, including Parallel Imaging (PI), Partial Fourier (PF) and Compressed Sensing (CS) techniques. In particular, the use of image-domain based Sensitivity Encoding (SENSE) [129] with bSSFP readouts showed markedly reduced PN while maintaining comparable MBF values to conventional bSSFP readouts [37, 117]. The majority of studies, however, resort to GRAPPA (Generalized Auto-calibrating Partial Parallel Acquisition), the k-space equivalent of SENSE, [36, 127, 130], often in tandem with PF acquisitions [116, 127, 131]. A recent investigation has also explored the utility of CS for myoASL, demonstrating comparable perfusion values to SENSE-accelerated bSSFP acquisition [44].

2.4.3.3 ECG gating and breathing strategies

Due to the inherently low SNR, myoASL is particularly susceptible to cardiac and respiratory motion and, thus, requires appropriate control strategies. To mitigate cardiac motion, ECG gating to the mid-diastole, the most quiescent phase of the cardiac cycle, is widely adopted as the standard approach [36, 40, 115]. However, systolic myoASL acquisitions have also been proposed due to the increased perfusion signal and reduced PN [44]. Further, cardiac gating techniques in myoASL can generally be divided into single and double ECG-gating. In single ECG-gating, only the inversion pulses are synchronised to a specific cardiac phase, and the image acquisition occurs after a fixed, preset TI [45]. Alternatively, in double ECG gating, both inversion and image readout can be gated to the same cardiac phase, rendering the TI dependent on the heart rate [115, 130]. Heart rate variations affect both approaches, albeit in different ways: The fixed TI in single ECG gating maintains consistent inversion recovery across all images without being influenced by the heart rate. At the same time, a varying cardiac phase at the time of readout can also lead to discrepancies in the alignment of myocardial regions in the control and tag image. Double ECG gating, on the other hand, provides consistent overlap of the myocardial regions by gating the image readout to the same cardiac phase in every heartbeat [115]. In turn, the resulting TI variations need to be taken into account for accurate estimation of the MBF.

The employed breathing strategies vary across studies and can be categorised into breath-held acquisitions [37, 40, 44, 118, 119, 124, 127], synchronised breathing [45, 115], and free-breathing acquisitions [36, 116, 121]. Breath-holding is the most prevalent method due to its simplicity and minimal post-processing requirements and involves subjects holding their breath during image acquisition. Typically, both control and tag image are acquired together at end-exhalation, which results in 10 to 15 seconds long breath-holds due to the added control-tag delay [40]. Synchronised breathing is a slightly modified approach where subjects are trained to coordinate their breathing with the rhythm of myoASL image acquisitions. Allowing the subject to breathe freely during the control-

tag-delay reduces the need for prolonged breath-holds to brief intervals of about two heartbeats coinciding with each image acquisition [45, 115]. Because multiple averages of control-tag pairs need to be acquired, both breath-holding and synchronised breathing can often be challenging. Especially in elderly subjects or those with limited pulmonary function, having to repeatedly perform long breath-holds can be an obstacle. However, even healthy subjects can have difficulties in maintaining consistent breath-holds, such that free-breathing approaches have been proposed [116, 121]. To that end, images are acquired continuously during normal breathing and later selected for the desired respiratory phase [36, 121]. To avoid extensive post-processing, respiratory navigators can be employed, which track the position of the diaphragm and trigger image acquisition only when the diaphragm position is within a preset acceptance window. As it requires a dedicated sequence setup and may extend scan times due to low acceptance rates, only a minority of studies have employed this approach so far [116].

2.4.3.4 Quantification of MBF

The relatively straightforward dependence of the myoASL signal on MBF is one of its key advantages compared particularly to first-pass perfusion imaging. Several models are available to convert the myoASL signal into absolute values of perfusion. For the purpose of this overview, these approaches will be broadly categorised into three groups: those based on apparent T_1 variations, those based on image intensity, and those combining intensity-based modelling with parameter fitting. The choice of quantification model is closely linked to the chosen myoASL sequence because the imaging signal is directly dependent on the scheme of labelling and readout pulses. In this work, a FAIR-myASL sequence is used for all experiments; therefore, the main focus of this section will be on the corresponding intensity-based quantification techniques. However, for the sake of completeness, a brief overview of the apparent T_1 and combined models will also be provided.

Apparent T_1 -based approach

In an early application of ASL in the brain, Detre et al. introduced a theoretical framework which allowed to determine perfusion values based on changes in the T_1 relaxation time of tissue [107]. Specifically, the in- and outflow of labelled blood spins are considered to introduce flow-dependent terms to the Bloch equation for the longitudinal tissue magnetisation. Assuming that the magnetisation of spins in venous outflow is identical to that in tissue, the Bloch equation yields an additional relaxation term when solved for the arterial label delivery. This results in an observed, or apparent, T_1 time of tissue (T_1^*), which decreases with increasing flow rate f :

$$\frac{1}{T_1^*} = \frac{1}{T_1} + \frac{f}{\lambda}. \quad (2.21)$$

Here, the blood-tissue water partition coefficient λ quantifies the equilibrium distribution of water molecules (spins) between blood and tissue and is ex-

pressed as $\lambda = \frac{\text{spins per g of tissue}}{\text{spins per ml of blood}}$. This framework was later extended to cardiac ASL in animal models [132, 133] and, eventually, adapted for studies in the human heart [119]. With alternating selective and non-selective labelling, for instance FAIR [134], myocardial perfusion can thus be quantified for known values of T_1^* and T_1 in blood ($T_{1,B}$) [119]:

$$MBF = \frac{\lambda}{T_{1,B}} \left(\frac{T_{1,ns}}{T_{1,ss}} - 1 \right). \quad (2.22)$$

Here, $T_{1,ns}$ and $T_{1,ss}$ refer to relaxation times obtained from non-selective and slice-selective labelling, respectively. The estimation of these T_1 values requires fitting the imaging signal to a T_1 recovery curve sampled at multiple time points. This essentially resembles conventional T_1 mapping methods, where multiple images are acquired after a single inversion pulse with varying TI to enable accurate curve-fitting [135]. Look and Locker introduced this approach to accelerate the otherwise time-consuming process of performing separate inversion preparations for each image interspersed with long delays for magnetisation recovery [135]. In cardiac settings, the Modified Look-Locker Inversion (MOLLI) scheme prevails and is characterised by ECG-gated images acquired within a single heartbeat [136]. In analogy to MOLLI, Look-Locker-FAIR was initially proposed for myoASL in a rodent model [39] and has since been successfully applied for perfusion quantification in human myocardium [134, 137].

Combined approach

The first study on FAIR-myASL in humans also introduced a novel method to quantify MBF by combining an intensity-based model with inversion recovery fitting [115]. Instead of a multi-delay acquisition, however, Poncelet et al. used double ECG-gating to acquire multiple control and tag images with the same TI of one heartbeat. They derived an MBF model by solving the modified Bloch equation described in [107] for an arterial input function $c(t) = \delta_{inv} \frac{M_{0,B}}{\lambda} e^{-t/T_{1,B}}$. Here, $M_{0,B}$ denotes the equilibrium magnetisation of spins in the blood, and $\delta_{inv} = 1 - \cos(\alpha_{inv})$ is the inversion efficiency for an inversion flip angle α_{inv} . Then, the resulting magnetisation difference between selective and non-selective inversions yields:

$$\Delta M(t) = \delta_{inv} M_{0,B} f \frac{e^{-t/T_1^*} - e^{-t/T_{1,B}}}{1/T_{1,B} - 1/T_1^*} \quad (2.23)$$

Considering typical physiological values for f and λ , the central premise is that the perfusion-induced reduction of T_1 is negligible. It follows that $\frac{fT_1}{\lambda} \ll 1$, which permits a power series expansion of the exponential terms in Equation (2.23). Together with the assumption of a comparable T_1 in blood and myocardium, the model for ΔM at inversion time TI further simplifies to:

$$\Delta M(TI) = \delta_{inv} \frac{M_{0,B}}{\lambda} f T I e^{-\frac{TI}{T_{1,B}}}. \quad (2.24)$$

In a second step, they proposed a correction approach to account for the TI variability induced by double ECG-gating. To that end, the image signal for

both control and tag data was fitted separately to a three-point inversion recovery model ($S(TI) = M_0(1 - \delta_{inv}e^{-TI/T_1})$). This allowed for estimating the input parameters – M_0 , T_1 , and δ_{inv} – as well as for interpolating the control and tag signal to the mean inversion time \overline{TI} . Finally, the MBF was calculated based on Equation (2.24) as:

$$MBF = \frac{\lambda(\overline{I_C} - \overline{I_T})}{\delta_{inv}M_0\overline{TI}e^{-\overline{TI}/T_{1,ns}}}, \quad (2.25)$$

where $\overline{I_C} - \overline{I_T}$ is the interpolated signal difference between control and tag, and $T_{1,B}$ is derived from non-selective inversions. Bar a few works [116, 131], ensuing studies have often implemented single rather than double ECG gating, diminishing the need for TI corrections, or have transitioned towards a fully intensity-based approach, as described in the following.

Intensity-based approach

Today, most myoASL studies resort fully to an intensity-based model similar to the one introduced by Poncelet et al. [115]. The approach was initially proposed by Kim et al. [126] to quantify cerebral blood flow from FAIR-ASL data and has subsequently been adapted for different labelling strategies. In 1998, Buxton et al. published a detailed derivation of a general kinetic model for ASL based on single-compartment kinetics such that systematic quantification errors could be investigated. Thereby, they also laid the theoretical foundation for future myoASL-based MBF quantification such that the model is today widely known as Buxton's General Kinetic Model (GKM). In their work, Buxton et al. developed a model which is applicable to any ASL sequence, which acquires two images with different blood contrast. This model is independent of the labelling scheme and reduces to other published models when appropriate assumptions are made. The GKM itself is based on two central assumptions:

1. Off-resonance and magnetic transfer effects are constant for the tag and control image, such that the longitudinal tissue magnetisation is identical in control and tag settings.
2. Two sets of spins are considered based on their location at the time of labelling: tissue spins in the imaging voxel and labelled arterial blood spins, eventually travelling towards the voxel.

In combination, this means that the difference in the net magnetisation only depends on the amount of spins delivered by arterial blood flow to the voxel. Further, at any given time t , the amount of labelled magnetisation in the voxel depends only on the history of arterial input, the rate of venous clearance, and longitudinal relaxation. For each of these parameters, a function can then be defined:

- $c(t)$: The arterial delivery function $c(t)$ describes the normalised concentration of labelled arterial blood spins arriving at the voxel. For ASL sequences such as FAIR, where labelling is applied in a pulsed rather than continuous fashion, the labelled bolus is considered to travel via uniform

plug flow. This means that labelled blood arrives only after an initial delay, the ATT, and is uniformly labelled for a certain duration τ . For inversion-based labelling, such as in FAIR, $c(t)$ can thus be understood as a rectangular function:

$$c(t) = \frac{M_B(t) - M_{0,B}}{M_{0,B}} = \begin{cases} \delta_{inv} e^{-t/T_{1,B}} & ATT < t < ATT + \tau \\ 0 & \text{else} \end{cases}, \quad (2.26)$$

with equilibrium blood magnetisation $M_{0,B}$, and inversion efficiency δ_{inv} .

- $r(t)$: The residue function $r(t)$ represents the fraction of labelled spins that arrived at a time t' and are still in the voxel at time t . Moreover, the water exchange between blood and tissue is described by single-compartment kinetics, leading to a constant ratio of spin concentrations in tissue to venous blood. The proportionality constant is given by the blood-tissue water partition coefficient λ . Consequently, the residue function can be expressed as $r(t) = e^{-\frac{ft}{\lambda}}$, where f is the perfusion in units of ml/g/min.
- $m(t)$: This relaxation function describes the mono-exponential T_1 recovery of labelled spins. It is assumed that labelled water spins relax with $T_{1,B}$ as long as they are in the blood vessels and with $T_{1,M}$ as soon as they enter (myocardial) tissue. With the premise that water is extracted fully and immediately upon arrival in tissue, the relaxation function is: $m(t) = e^{-\frac{t}{T_{1,M}}}$.

Under constant physiological conditions in tissue, the difference in magnetisation between control and tag image can then be defined as the sum over all magnetisation, which arrived at the voxel at the ATT and is still present at time t :

$$\begin{aligned} \Delta M(t) &= \delta_{inv} M_{0,B} f \int_0^t c(t') r(t-t') m(t-t') dt' = \\ &= \begin{cases} 0 & 0 < t < ATT \\ \delta_{inv} M_{0,B} f (t-ATT) e^{-\frac{t}{T_{1,B}}} q(t) & ATT < t < ATT + \tau \\ \delta_{inv} M_{0,B} f \tau e^{-\frac{t}{T_{1,B}}} q(t) & ATT + \tau < t \end{cases} \quad (2.27) \end{aligned}$$

The dimensionless factor $q(t)$ combines effects due to different relaxation times and venous clearance:

$$q_p(t) = \begin{cases} \frac{e^{kt}(e^{-kATT} - e^{-kt})}{k(t-ATT)}, & \text{if } \Delta t < t < \Delta t + \tau \\ \frac{e^{kt}(e^{-kATT} - e^{-k(\tau+ATT)})}{k\tau} & \text{if } t > \Delta t + \tau \end{cases}. \quad (2.28)$$

with

$$k = \frac{1}{T_{1,B}} - \left(\frac{1}{T_{1,M}} + \frac{f}{\lambda} \right) = \frac{1}{T_{1,B}} - \frac{1}{T_1^*} \quad (2.29)$$

The GKM illustrates that, while the signal difference is directly proportional to the MBF, it also exhibits a non-linear dependence via $q_p(t)$ due to the apparent T_1 relaxation effects, as previously noted by Detre et al. [107]. However, for early times t , $q_p(t)$ remains constant at a value close to 1. Only at later times and if T_1^* substantially differs from T_1 , does $q_p(t)$ affect the magnetisation. Considering that normal values for MBF range between 0.7 and 2.5 ml/g/min [114] and λ is approximately 1 ml/g [138, 139], the perfusion-related term in Equation (2.21) becomes $\frac{f}{\lambda} \ll 1$, and $q(t)$ can be neglected. This aligns with the central assumption from Poncelet et al. [115] that perfusion-related changes in T_1 are minimal. For FAIR-labelling in the myocardium, ATT-related effects are also considered negligible due to fast coronary blood flow and short distances within the labelling slab [115, 140]. As a result, the relation given in Equation (2.27) for a given inversion time TI simplifies to:

$$MBF = \frac{\lambda \Delta M}{\delta_{inv} M_{0,B} T I e^{-TI/T_{1,B}}} \quad (2.30)$$

This relation reproduces and further streamlines the model presented in [115], avoiding the need for signal parameter fitting to determine T_1 . Instead, parameters such as $T_{1,B}$ and δ_{inv} are derived from literature, while M_0 is typically obtained from an additional unlabelled baseline image. To correct for potential TI variations in double ECG-gated FAIR-myocardial ASL, instead of relying on inversion-recovery-fits, recent studies have normalised the control and tag signals using individual TI values as measured via ECG [44].

Thus, the key argument underlying all intensity-based modelling is that a small perfusion-induced change in T_1 translates to a stronger difference in magnetisation between control and tag settings. To illustrate this consideration, we can consider an average voxel T_1 of 1500 ms and typical physiological values for MBF and λ as given above. This results in a relative change in T_1 of roughly 2 % (using Equation (2.21)), whereas the associated signal difference relative to the equilibrium magnetisation amounts to 5 to 10 %, depending on the inversion efficiency. Therefore, even minor deviations in T_1 measurements have a large impact on the estimated MBF if apparent T_1 or combined approaches are used for quantification. In comparison, intensity-based strategies eliminate the susceptibility to inaccurate curve-fitting by relying on predetermined model parameters, but require estimated or literature values for quantifying MBF. A comprehensive overview and comparison of quantification models for single and double ECG-gated FAIR-myocardial ASL can be found in [131].

IMPROVED REPRODUCIBILITY FOR MYOCARDIAL ASL: IMPACT OF PHYSIOLOGICAL AND ACQUISITION PARAMETERS

The results of this chapter have been published in [41] by John Wiley & Sons ¹. The material is reproduced here with minor modifications to maintain consistency and coherence throughout this thesis.

3.1 INTRODUCTION

First-pass myocardial perfusion with cardiac MR (CMR) is widely used as the clinical gold standard for non-invasive assessment of myocardial ischemia [12, 141–143]. However, the need for exogenous, gadolinium based contrast agents (GBCAs), limits the clinical applicability of first-pass perfusion MRI. Since gadolinium is cleared from the body almost exclusively through the kidneys [144, 145], GBCAs are contraindicated in patients with renal dysfunction [145]. Additionally, concerns have been raised about gadolinium accumulation in the brain following the repeated use of GBCAs, even in combination with healthy renal clearance [31, 32].

Arterial Spin Labeling (ASL) offers a contrast-agent-free alternative for perfusion measurements, using magnetically labeled blood as an endogenous contrast [107, 146]. ASL has been well established in neurovascular applications and has steadily gained importance in quantifying cerebral blood flow over the last decades [147, 148]. In cardiac applications, promising results have been achieved with myocardial ASL (myoASL): Reported myoASL-based myocardial blood flow (MBF) values were in agreement with reference values from positron emission tomography (PET) gold standard measurements [40]. Moreover, myoASL has shown to be sensitive to perfusion changes induced by either vasodilatory stress or when comparing normal and ischemic myocardial segments [35]. However, due to a low signal-to-noise ratio, insufficient reproducibility and robustness have hampered more wide-spread clinical translation of myoASL thus far [38].

Typically, multiple pairs of tag and control images are acquired in an ASL measurement. In tag images magnetically labeled blood is flowing into the imaging volume, while no labeling is applied for control images. Subtracting tag from control yields perfusion weighted images, which can then be used to quantify the MBF [40, 108, 115]. With signal differences between tag and control images of 1 % to 8 % [39], myoASL is rendered very sensitive to physiological signal variations, such as those caused by cardiac or respiratory motion. This physiological noise was found to be the dominant noise source in myoASL [40]. However, its ratio to thermal noise is highly dependent on the choice of imaging

¹ © 2023 The Authors. Magnetic Resonance in Medicine published by Wiley Periodicals LLC on behalf of International Society for Magnetic Resonance in Medicine.

readout and acquisition parameters [149]. In myoASL the perfusion weighted signal is most commonly acquired using snapshot image readouts, where all k-space lines are acquired in a single heart-beat. To obtain quantitative MBF, however, the perfusion weighted signal is modeled only based on the effects of the labeling preparation [108]. As the imaging pulses perturb the magnetization signal, the image contrast can still be dependent on parameters related to image readout. This can cause a number of factors, including sequence parameters such as the acquisition flip angle or physiological parameters such as the heart rate variability, to affect the precision and bias of ASL measurements.

The objective of this study is to investigate the effect of physiological and acquisition-related parameters on the bias and precision of quantitative myoASL measurements. Simulation and phantom experiments are used to evaluate the relative contribution of various confounders in balanced steady-state free precession (bSSFP) and spoiled gradient-echo (spGRE) based myoASL. Next, we propose an improved MBF calculation approach to alleviate some of those confounders, to reduce the bias, and, potentially in extension, help to improve the reproducibility of Flow-sensitive Alternating Inversion Recovery (FAIR) myoASL. Namely, subject-specific blood T_1 relaxation times and, for spGRE readouts only, additional saturation-prepared baseline acquisitions are used to calculate MBF. Finally, the repeatability of myoASL with and without corrections is studied in healthy volunteers.

3.2 THEORY

3.2.1 ASL signal model

MBF quantification in myoASL is most commonly based on Buxton's general kinetic model (GKM) [108]. In the GKM, the difference between control and tag signal is modeled based on the transport of inverted magnetization into the imaging volume with arterial blood. The present work focuses on a FAIR-ASL sequence (Figure 3.1), for which the GKM can be derived as:

$$MBF = \frac{\lambda(I_C - I_T)}{\delta I_{BL} T I e^{-TI/T_{1,B}}}, \quad (3.1)$$

with control (I_C), tag (I_T), and baseline signal (I_{BL}), inversion time TI , inversion efficiency $\delta = 1 - \cos(\alpha_{inv})$, blood-water partition coefficient $\lambda = 1ml/g$ [138, 139], and blood T_1 relaxation time $T_{1,B}$. Due to the substantially faster flow in the heart compared to other anatomies, the labeling slab is considered to be small relative to the fast flow in coronary arteries during the TI [115]. Therefore, as previously applied in cardiac ASL [37, 115], in the present work it has been decided to neglect the effect of the ATT in the model as a first approximation.

3.2.2 Magnetization modulation function

Imaging in myoASL has been previously proposed with bSSFP or spGRE snapshot readouts. These readouts lead to a significant modulation of the magnetiza-

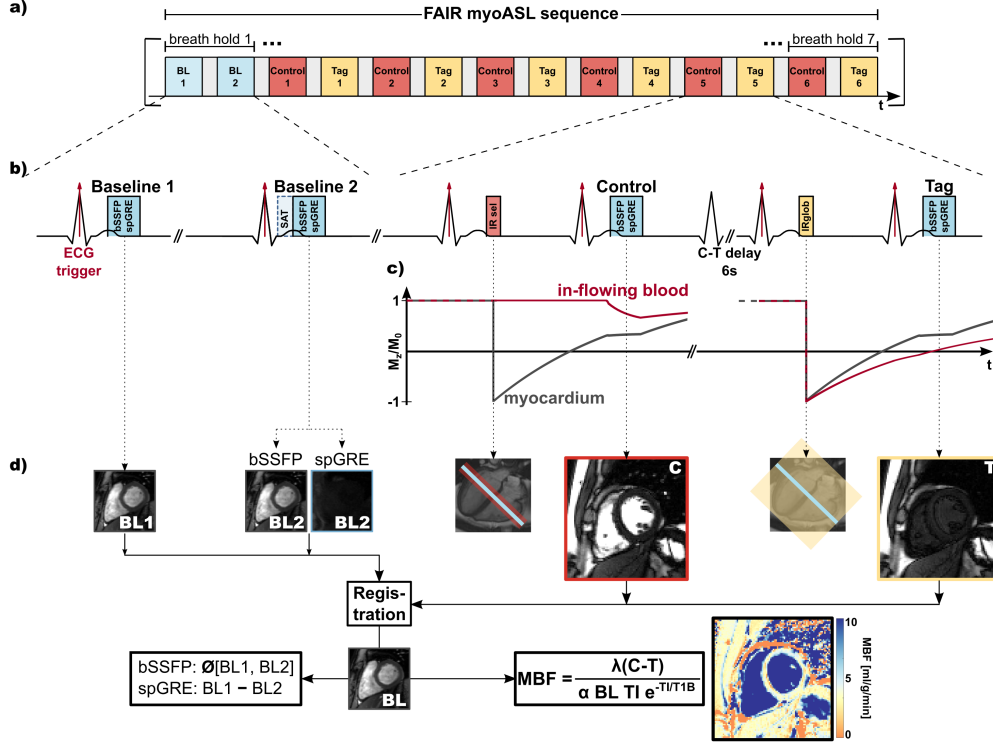


Figure 3.1: (a), (b) Sequence diagram of the FAIR-myocardial ASL sequence and (d) processing pipeline used in this study. (c) Temporal evolution of the longitudinal magnetization after an initial inversion pulse and during the imaging readout in the subsequent heart-beat.

tion, which is expressed as a magnetization modulation function (MMF, f_{MMF}) throughout this work.

The signal equations for bSSFP and spGRE readouts are provided in Appendix A.1. They can be simplified in the form of a general affine linear model for the MMF:

$$f_{MMF}(x) = Ax + B. \quad (3.2)$$

Here, the coefficients A and B depend on the acquisition parameters as well as T_1 and T_2 , while $x = M_z(t_0)$ represents the initial magnetization immediately prior to the readout. Due to the low systolic coronary blood-flow [74, 150], in- and out-flow effects during the image readout were considered negligible and, thus, were not explicitly considered in the MMF. Based on the MMFs in the appendix (Equations (A.1), (A.5)), A and B are given as

$$A = \begin{cases} \sin\left(\frac{\alpha}{2}\right)(E_1 \cos^2\left(\frac{\alpha}{2}\right) + E_2 \sin^2\left(\frac{\alpha}{2}\right))^n & , \text{ bSSFP} \\ \rho \cos^n(\alpha) E_1^{n-1} & , \text{ spGRE} \end{cases} \quad (3.3)$$

and

$$B = \begin{cases} (1 - (E_1 \cos^2(\frac{\alpha}{2}) + E_2 \sin^2(\frac{\alpha}{2}))^n) M_{ss} & , \text{bSSFP} \\ \frac{1 - (\cos(\alpha)E_1)^{n-1}}{1 - \cos(\alpha)E_1} (1 - E_1) \cos(\alpha) \rho M_{z,eq} & , \text{spGRE} \end{cases} \quad (3.4)$$

with $E_{1/2} = e^{-TR/T_{1/2}}$, proton density ρ , steady-state and equilibrium longitudinal magnetization M_{ss} and $M_{z,eq}$, flip angle (FA) α , and n applied imaging pulses.

FAIR-myASL sequence

In a FAIR-myASL measurement, the imaging signal can be modeled with blood (I_B) and myocardial contributions (I_M) weighted by the blood-volume-fraction V_B and its complement $V_M = 1 - V_B$, respectively. Due to differences in the relaxation times [151, 152], the coefficients A_M and A_B in the MMF (Equations (3.3), (3.4)) differ between I_B and I_M .

Using the approach of Buxton's GKM (Equation (3.1)) and the image signals as derived in the appendix (Equations (A.8) - (A.15)), the ratio of control, tag, and baseline signal can be given as:

$$\frac{I_C - I_T}{I_{BL}} = \frac{V_B f_{in} A_B (x_B^+ - x_B^-)}{V_M (A_M x_M^+ + B_M) + V_B (A_B x_B^+ + B_B)}. \quad (3.5)$$

This relation only yields the unbiased, true perfusion rate f_{in} , in the case of $A_B = A_M = 1$ and $B_B = B_M = 0$ which is implicitly assumed in Buxton's GKM. In an experimental setting, however, this condition is not met due to the long echo trains ($n \gg 1$) in particular for snapshot readouts. Hence, the obtained perfusion rate is confounded by acquisition parameters such as the FA and the acquisition matrix size (AMS), which determines the number of imaging pulses applied prior to the k-space center.

Precision and accuracy in FAIR-myASL

Three types of error metrics [153] can be distinguished when considering MBF quantification: Repeatability and reproducibility are measures of precision, where repeatability is mainly influenced by physiological noise, while reproducibility relates to variability on longer time scales, as well as between systems and set-ups. Bias, as the third metric, relates to the accuracy of the measurement, i. e. systematic deviations intrinsic to the measurement, such as sequence parameters. Bias stemming from uncorrected confounders is a common source of lack of reproducibility [153]. These quantities can be influenced by several physiological and acquisition-related factors. Figure 3.2 illustrates the interdependencies for a selection of parameters relevant to this study, namely: heart rate variations, $T_{1,B}$, acquisition FA, and AMS. A varying heart rate can involve changes in the coronary blood flow [154], which represents a major source of physiological noise and strongly affects repeatability and reproducibility. At the same time, myASL measurements can be confounded by changes in the sequence timing as a result of varying RR durations (Figure 3.2). Thus, MBF

values obtained at different RR intervals are subject to different biases. If the RR duration changes among control-tag pairs, this compromises repeatability. If the average RR duration changes across measurements or subjects, this compromises reproducibility or imparts bias. Further, the value of $T_{1,B}$ depends on numerous factors – such as hematocrit[155, 156], iron levels[157, 158], and water intake[159, 160]. These might change over longer periods of time and, consequently, alter the MBF bias and affect reproducibility. Finally, flow effects in FAIR-myASL experiments can lead to a modulation in the magnetization transfer function, due to the replacement of spins in the imaging slice. This can impart bias and compromise reproducibility as elaborated on above. Regarding sequence parameters, different prescribed FA values in separate measurements impart different biases, which compromise reproducibility. Further, the B_1^+ field distribution depends on the subject and their positioning[161, 162], which can induce additional bias and impair reproducibility. Further, residual motion through the inhomogeneous B_1^+ field distribution can lead to short-term variations of the induced bias. This affects the repeatability, but the contribution can be considered small due to the likely presence of prospective motion correction.

| | repeatability (short term) | reproducibility (long-term) | bias (systematic) |
|------------------------------------------|-------------------------------|--------------------------------|----------------------|
| acquisition matrix size | none | high | high |
| flip angle (FA) prescribed FA | none | low | high |
| flip angle (FA) B_1^+ inhomogeneity | low | high | high |
| heart rate | high | high | high |
| blood T_1 | none | low* | high |
| blood flow** | low | low | low |

*depending on the time scale of the observation

**blood flow is the measurand and as such induces a bias profile rather than confounding the measurement

Figure 3.2: Various sequence-related (acquisition flip angle and matrix size) and physiological parameters (heart rate, blood T_1 , blood flow) influence the FAIR-myASL measurement in terms of precision (repeatability, reproducibility) and accuracy (bias). The different factors manifest as different types of MBF errors depending on their respective time scale. Parameters affected by the proposed correction approach are framed in red.

Saturation-baseline

As apparent from Equation (3.5), eliminating the coefficients B_B and B_M from the image signal can reduce the dependence on acquisition parameters. This can be achieved with the acquisition of an additional saturation prepared baseline image ($I_{BL,Sat}$), such that the signal only represents the imaging readout and not the magnetization history anymore. To this end, a saturation pre-pulse immediately prior to the baseline image can be used. Assuming perfect saturation, the initial magnetization of both myocardium and blood can be considered to be zero ($x_M = x_B = 0$) for the saturation-baseline signal. If the signal difference between the saturation and original baseline (see Equation (A.16)) is used instead of the original baseline signal in Equation (3.5), the ratio of control and tag image becomes

$$\begin{aligned} \frac{I_C - I_T}{I_{BL} - I_{BL,Sat}} &= \frac{V_B f_{in} A_B (x_B^+ - x_B^-)}{V_M A_M x_M^+ + V_B A_B x_B^+} = \\ &= \frac{V_B f_{in} (x_B^+ - x_B^-)}{V_M \frac{A_M}{A_B} x_M^+ + V_B x_B^+}. \end{aligned} \quad (3.6)$$

Due to the different MMFs, this leads to different factors $\frac{A_M}{A_B}$ in Equation (3.6) for the two readout types:

$$\frac{A_M}{A_B} = \begin{cases} \left(\frac{E_{1,M} \cos^2(\frac{\alpha}{2}) + E_{2,M} \sin^2(\frac{\alpha}{2})}{E_{1,B} \cos^2(\frac{\alpha}{2}) + E_{2,B} \sin^2(\frac{\alpha}{2})} \right)^n, & \text{bSSFP} \\ e^{-(n-1) \cdot TR \cdot (\frac{1}{T_{1,M}} - \frac{1}{T_{1,B}})}, & \text{spGRE} \end{cases} \quad (3.7)$$

Notably the use of the saturation-baseline eliminates the FA dependence for the case of spGRE readout and the only residual acquisition-parameter-related influence is given by the AMS (n). With bSSFP readout, however, the signal ratio remains both FA and AMS dependent as the transverse magnetization contributes to the readout signal at each TR .

3.3 METHODS

3.3.1 MyoASL sequence

Based on the considerations above, a double ECG-triggered FAIR-ASL sequence building on the design by Do et al. [37, 130] is proposed. As depicted in Figure 3.1, non-labeled control and labeled tag images are acquired in an alternating fashion. For the control image, a spatially selective, adiabatic inversion pulse is applied in one heartbeat. The image acquisition is performed in the subsequent heartbeat during the same cardiac phase. To ensure consistent inversion within the imaging slice, the inversion slab is chosen three times as thick as the imaging slice. Following a 6 s long delay, the tag image is acquired in the same fashion but using a non-selective adiabatic inversion pulse. Each myoASL measurement comprised six pairs of control and tag images, referred to as individual scans, using either bSSFP or spGRE readouts.

Additionally in each measurement, a pair of baseline images was acquired without preceding inversion pulses. For bSSFP readouts, both baseline images are acquired without any preparation pulses, while for spGRE an additional saturation pre-pulse is added immediately prior to the readout of the second baseline image.

Post-processing of images including MBF quantification and statistical analysis was performed in MATLAB (MathWorks, Natick, MA, USA). The MBF was quantified using Buxton's GKM as described in Equation (3.1). For bSSFP-based MBF calculation, the baseline signal I_{BL} corresponds to the average of the two baseline images. With spGRE readout, the saturation-baseline image $I_{BL,sat}$ is subtracted from the original one and the difference image is used as the baseline value in MBF calculations as given in Equation (3.6). As shown in Equation (3.7), this saturation-baseline correction does not eliminate FA dependencies in bSSFP readouts and is therefore not applied for those. The double ECG-triggering of both labeling pulses and image readouts leads to a variable, heart rate dependent TI . For MBF calculation, TI was evaluated using either individual TIs , an average inversion time \overline{TI} for each control-tag pair, or a global TI averaged per sequence.

In previous studies on cardiac ASL, $T_{1,B}$ was set to a fixed, literature based value between 1650 and 1700 ms [37, 40, 44, 163]. To avoid discrepancies with the actual T_1 , subject-specific T_1 relaxation times are used in a second quantification method. In summary, perfusion values were calculated in four different modes depending on the readout:

- bSSFP readout with conventional, uncorrected MBF calculation (fix $T_{1,B}$, no saturation-baseline)
- bSSFP readout with corrected MBF calculation (measured individual $T_{1,B}$, no saturation-baseline)
- spGRE readout with conventional, uncorrected MBF calculation (fix $T_{1,B}$, no saturation-baseline)
- spGRE readout with corrected MBF calculation (measured individual $T_{1,B}$ and saturation-baseline)

Based on previous FAIR-myoASL studies [40, 130, 163], the uncorrected MBF calculation from bSSFP-images is considered as the reference configuration throughout the remainder of this work.

3.3.2 Numerical simulations

To assess the effect of physiological and acquisition-related parameters on myoASL-based MBF values, the FAIR-myoASL sequence was numerically simulated using Bloch equation simulations. All numerical simulations were performed in MATLAB. Both, bSSFP and spGRE readouts were simulated. If not indicated otherwise, general sequence parameters in simulation were: ramp-up pulses 10/0 (bSSFP/spGRE), FA 50°/35° (bSSFP/spGRE), 100 readout pulses ($n = 50$), 100 % inversion efficiency, 6 s control-tag delay. To simulate the effect of flow during TI , a blood volume fraction of 0.14 [164] and a blood

| Experiment | FA (°) | | TE / TR (ms) | | Matrix size | FOV (mm ²) | HR (bpm) | Resolution / slice thickness | Partial Fourier / GRAPPA rate |
|----------------------|--------|--------|--------------|---------|------------------------|------------------------|----------|-----------------------------------|-------------------------------|
| | bSSFP | spGRE | bSSFP | spGRE | | | | | |
| Phantom - Varying HR | 70 | 15 | 1.6/3.3 | 3.3/6.3 | 160 x 160 | 280 x 280 | 40 - 120 | 1.7 x 1.7 mm ² 8 mm | 6/8 R = 2 |
| Phantom - Varying FA | 1 - 80 | 1 - 40 | 1.6/3.3 | 3.3/6.3 | 160 x 160 208 x 208 | 280 x 280 364 x 364 | 60 | | |
| In vivo | 70 | 18 | 1.2/2.4 | 1.9/2.9 | 154 x 192 | 272 x 340 | n/a | | |

Abbreviations: FA: flip angle; FOV: field of view; GRAPPA, Generalized Auto-calibrating Partially Parallel Acquisition; HR: heart rate; TE: echo time; TR: repetition time

Table 3.1: Sequence parameters of the FAIR-myocardial ASL sequence with bSSFP and spoiled GRE readouts for phantom and in vivo measurements. All imaging was performed with Partial Fourier (6/8) and GRAPPA rate of 2.

replacement/in-flow rate of 0.29 1/s were simulated, resulting in an effective MBF input value of 2.4 ml/g/min. The assumed in-flow rate corresponds to about 4 ml/s for a myocardial blood volume of 15 ml (about 10 % of the left-ventricular mass [165, 166]). Other physiological parameters were simulated as: HR 60 bpm, blood T_1/T_2 relaxation times at 3 T of 2000 ms/250 ms, and myocardial T_1/T_2 relaxation times of 1460 ms/45 ms [151, 152], unless otherwise specified.

To simulate the effect of in-flow during TI and to obtain the control and tag signal, the inverted and native signal of blood and myocardium were combined according to Eqs. (A.13) and (A.14). The conventional and saturation-baseline signal (in spGRE) were calculated using Equation (A.15).

Three simulation experiments were performed to investigate the effect of physiological and acquisition parameters, respectively. For the first set of simulated myoASL-MBF data, a FA range of 1° - 80° in bSSFP and 1° - 40° in spGRE was simulated for AMSs between 100 and 220. For the second data set, the HR was varied between 40 and 120 bpm (RR duration 500 - 1500 ms) and different combinations of representative T_1/T_2 relaxation times corresponding to those of the selected phantom vials were used. For the third simulation experiment, the control-tag delay was varied between 6 and 12 s with fixed physiological and sequence parameters as described above.

3.3.3 Imaging

All imaging was performed at 3 T. In all experiments, a WET saturation pulse [167, 168] has been used for preparation of the saturation-baseline. The detailed sequence parameters for all experiments are provided in Table 3.1.

3.3.3.1 Phantom experiments

A phantom comprising 13 NiCl₂-doped agarose vials submerged in agarose gel was used, with T_1 relaxation times ranging between 1100 and 2500 ms and T_2 relaxation times between 50 and 170 ms. For further evaluation, five vials with relaxation times in the physiological range were selected. Phantom experiments were performed at 3 T (Magnetom Skyra, Siemens Healthineers, Erlangen, Ger-

many). The FAIR-myASL sequence was used with the acquisition parameters provided in Table 3.1.

As in the numerical simulations, three sets of experiments were performed. First, phantom data was acquired for both readout types for a range of FAs in bSSFP and spGRE with two matrix sizes (i. e. with different AMS). Further, images were acquired with varying simulated HR which resulted in varying TI and, lastly, with fixed HR, FA and AMS for control-tag delays between 6 and 12 s.

The perfusion weighted signal was generated in the same manner as for numerical simulations. Prior to further processing, the signal polarity had been restored based on the recovery curves obtained with different TIs [136]. Following Equations (A.13) - (A.15), the control, tag and baseline signals were generated from the image signal of different vials, which was obtained from manually drawn ROIs. The inverted signal contributions to I_C and I_T were taken from the selective and non-selective inversion recovery, respectively. For the myocardial signal, a vial with T_1/T_2 relaxation time of 1460 ms/45 ms was used. The blood signal was taken from four different vials with T_1 relaxation times of 1770 - 2300 ms and T_2 relaxation times of 45 - 124 ms. The image phase was used to restore the signal polarity for all vials prior to summation.

3.3.3.2 *In vivo experiments*

The present study was approved by the local institutional review board and written informed consent was obtained from all participants prior to examination. Nine healthy subjects (3 female, 6 male, 36 ± 8 years) with no history or current symptoms of cardiovascular disease were included in this study. The *in vivo* scans were performed at 3 T (Magnetom Prisma, Siemens Healthineers, Erlangen, Germany).

MOLLI [136] T_1 maps were acquired in each subject to obtain blood T_1 ($T_{1,B}$) times in the corrected MBF calculation. In the individual T_1 maps, an ROI was manually drawn in the left ventricle and $T_{1,B}$ was determined as the mean value across all pixels within this ROI. For FAIR-myASL, labeling and imaging were placed in the systole for increased perfusion signal [44]. The detailed imaging parameters are given in Table 3.1. In six out of the nine subjects, two repetitions of two FAIR-myASL sequences (bSSFP and spGRE) were acquired. Images were acquired during 12-16 s long breath-holds, depending on the subject's heart rate, with one image pair (baseline/control-tag) per breath-hold.

Each FAIR-myASL sequence consisted of seven breath-holds: one for the baseline images and six for the six control-tag image pairs. The bSSFP and spGRE data sets were group-wise registered for each subject [169]. Subsequently, control-tag pairs subject to ECG mis-triggering or a difference in TI larger than approximately 120 ms were excluded prior to image analysis. For each subject, the myocardium as well as a septal ROI were segmented manually [170]. Pixel-wise perfusion maps and segment-wise septal MBF were obtained using uncorrected calculation in bSSFP and spGRE as well as corrected spGRE calculation as described above. Global MBF values are reported as the mean MBF across the myocardial ROI and across all control-tag image pairs in each repe-

tition. Mean septal MBF values are reported as the septal MBF averaged across all control-tag image pairs.

3.3.3.3 Statistical analysis

In simulation and phantom experiments, the correlation of MBF with HR and FA was assessed using Spearman's correlation, respectively. To further evaluate the HR and FA dependence, slope and intercept values were obtained from a linear regression of simulation and phantom MBF. Moreover, the relative MBF error ($\frac{MBF_{phantom} - MBF_{true}}{MBF_{true}}$) was compared across the calculation modes using a Friedman test for group-wise comparison, followed by a Wilcoxon signed-rank test for pair-wise comparison. For in vivo septal MBF and each readout-calculation combination, the intra-subject variability within a measurement $\bar{\sigma}_p$ was calculated as the physiological noise (PN) averaged across all subjects:

$$\bar{\sigma}_p = \frac{1}{N_S} \sum_{j=1}^{N_S} PN_j, \quad (3.8)$$

with number of subjects $N_S = 9$. The PN for each repetition m with $N_{CT}^{j,m}$ control-tag image pairs is obtained as [40]

$$\begin{aligned} PN_{j,m} &= \frac{1}{\sqrt{N_{CT}^{j,m}}} \sigma(MBF_{j,m})_{N_{CT}^{j,m}} \\ &= \sqrt{\frac{\sum_{i=1}^{N_{CT}^{j,m}} (MBF_{i,j,m} - \overline{MBF}_{j,m})^2}{N_{CT}^{j,m} (N_{CT}^{j,m} - 1)}} \end{aligned} \quad (3.9)$$

The mean between-measurement, intra-subject variability \overline{wsSD} of each sequence was defined as the difference in mean MBF from the two repetitions scaled by $\sqrt{2}$ and averaged over the corresponding sub-cohort ($N_S = 6$) [153]:

$$\begin{aligned} \overline{wsSD} &= \frac{\sum_{j=1}^{N_S} wsSD_j}{N_S} \\ wsSD_j &= \frac{|\overline{MBF}_{j,1} - \overline{MBF}_{j,2}|}{\sqrt{2}} \end{aligned} \quad (3.10)$$

Lastly, the inter-subject variability $isSD$ was evaluated as the standard deviation across the individual mean MBF values:

$$\begin{aligned} isSD &= \sqrt{\frac{\sum_{j=1}^{N_S} (\overline{MBF}_j - \overline{MBF})^2}{N_S - 1}} \\ \overline{MBF} &= \frac{1}{N_S} \sum_{j=1}^{N_S} \overline{MBF}_j \end{aligned} \quad (3.11)$$

In subjects with multiple repetitions, only MBF data from the first repetition has been used to obtain $\bar{\sigma}_p$ and $isSD$. The intra- and inter-subject variability were

compared across the calculation modes using a Friedman test for group-wise comparison, followed by a Wilcoxon signed-rank test for pair-wise comparison. A significance level of 0.05 was used in all statistical tests.

3.4 RESULTS

Simulated perfusion showed negligible differences whether calculated with individual TIs , an average inversion time \overline{TI} for each control/tag pair, or a global TI averaged per sequence as shown in Figure 3.3. Therefore, in all further phantom and in vivo measurements MBF was calculated with a pairwise averaged \overline{TI} for each control/tag pair. While differently evaluated TIs in MBF calculation led only to small changes in the MBF deviation, the HR variability appeared as a major confounder in myoASL-MBF.

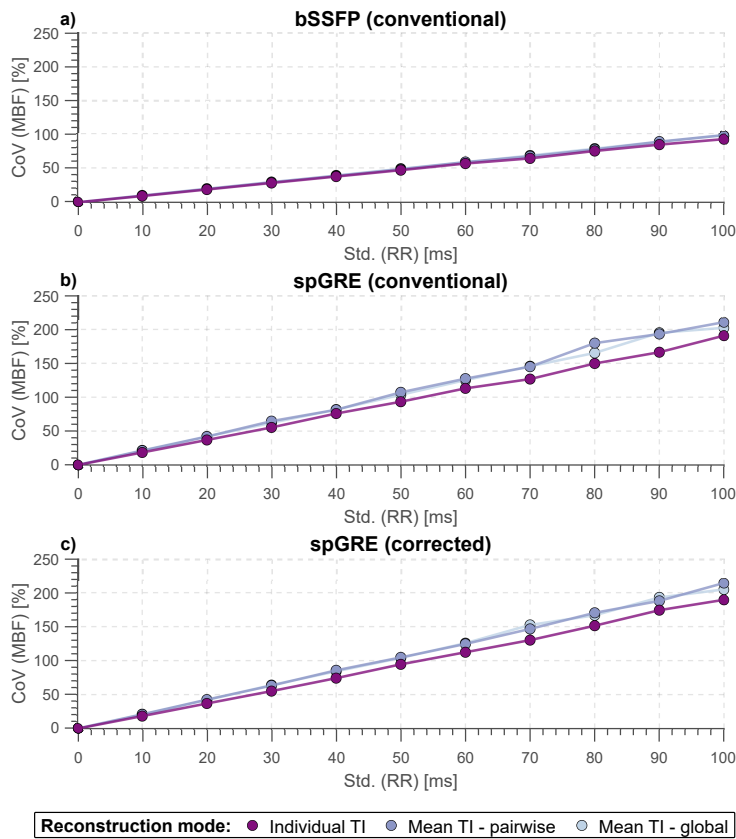


Figure 3.3: Coefficient of variation of simulated myoASL-MBF from (a) uncorrected bSSFP and (b) spGRE readouts as well as corrected spGRE readouts as a function of simulated heart rate variability. Calculating bSSFP-based MBF with a pairwise inversion time (\overline{TI}) for each control/tag pair leads to negligible differences compared to using individual TIs . For spGRE readout, MBF deviations increase by 10 % when pairwise or globally averaged \overline{TI} instead of individual TIs are used in MBF quantification. (c) Moreover, the proposed correction does not lead to a substantial increase in MBF deviations compared to the uncorrected case.

The following phantom results are shown for all four combinations of readout and MBF calculation. Here, corrected calculation in bSSFP refers to using individual $T_{1,B}$ values, but no saturation-baseline which is only applied for sp-

GRE as explained in the Methods section. The relative error in simulated and phantom MBF for varying control-tag delays is shown in Figure 3.4. For uncorrected as well as corrected calculations, the MBF values from bSSFP and spGRE readouts were largely constant over the range of applied control tag delays. The difference in MBF between a 6 s long delay and the steady state was $< 2.2\%$ / $< 6.0\%$ (bSSFP/spGRE) in simulations and $< 4.8\%$ / $< 3.8\%$ (bSSFP/spGRE) in phantom experiments. Thus, a control-tag delay of 6 s was chosen for all further experiments.

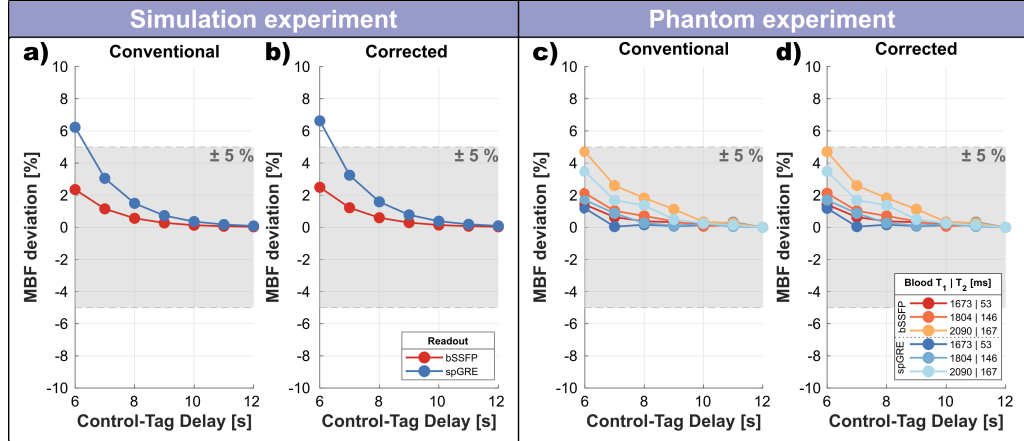


Figure 3.4: Relative MBF deviation from the asymptotic MBF (very long control-tag delay " ∞ ") as a function of the control-tag delay for bSSFP and spGRE readout, from (a), (b) simulation and (c), (d) phantom experiments. MBF was calculated with (a), (c) fixed and (b), (d) individual blood T_1 ($T_{1,B}$). Additionally, for corrected spGRE (d), the saturation-baseline approach as proposed in this work was used in MBF calculation. Simulated MBF deviation decreases with increasing delay and reaches 0% at about 10 s (simulated $T_{1,B}$: 1900 ms). In phantom, MBF deviation reaches 0% from delays of about 9 s for all readout/quantification combinations and for all phantom vials (i. e. $T_{1,B}$ values). In phantom, the difference between a 6 s long delay and the steady state was $< 4\%$ in bSSFP and $< 5\%$ in spGRE readouts, such that a control-tag delay of 6 s was chosen.

3.4.1 Phantom results

Flip angle

Figure 3.5 shows the phantom MBF plotted against the acquisition FA for two different AMSs. In uncorrected bSSFP, phantom MBF increased with increasing FA for all vials ($0.73 < R^2 < 0.86$, slope: 0.01-0.02) except one (T_1/T_2 of 1770/45 ms), where MBF was underestimated with increasing FA ($R^2 = 1$, slope: -0.004). For all vials, longer AMS resulted in increased MBF values. This FA dependence remained for bSSFP readout when MBF was calculated with $T_{1,B}$ -correction ($0.73 < R^2 < 1$). In uncorrected spGRE, MBF values correlated strongly with FA ($0.82 < R^2 < 1$). Phantom MBF decreased with increasing FA and was lower for longer AMS for all vials, with linear slopes of -0.017 to -0.027. Using corrected calculation, spGRE-based MBF stayed largely constant around 2.48 ml/g/min up to about 25° from where it decreased slightly to 2.14 ml/g/min ($0.27 < R^2 < 1$, slope: -0.006 - -0.010). For all vials, group-

wise comparison revealed a significant difference in relative MBF error among the compared readout-calculation combinations ($p < 0.05$). With fully corrected calculation in spGRE-readouts, the relative MBF error was significantly reduced compared to uncorrected spGRE ($p < 0.05$) in all vials and showed a small, non-statistically significant reduction compared to uncorrected bSSFP ($0.05 < p < 0.25$) in all vials except one ($p = 0.74/0.84$ for AMS 120/256, T_1/T_2 of 1865/82 ms). Thus, the saturation-baseline approach was used for the correction of spGRE readouts in the remainder of this work.

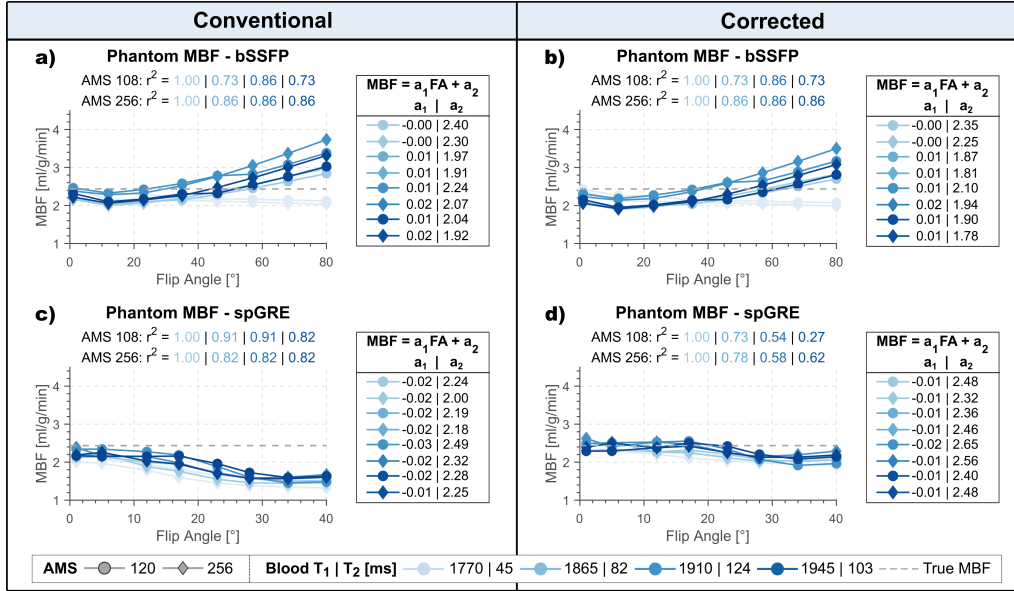


Figure 3.5: Phantom myoASL-MBF from bSSFP and spoiled GRE (spGRE) readouts. Myocardial blood flow (MBF) was calculated with (a), (c) fixed and (b), (d) individual blood T_1 ($T_{1,B}$). Additionally, for corrected spGRE (d), the saturation-baseline approach as proposed in this work was used in MBF calculation. MBF is shown as a function of acquisition flip angle (FA) for two acquisition matrix sizes (AMS) and four phantom vials (i. e. different blood T_1 and T_2). The slope (a_1) and intercept (a_2) for each vial are obtained from linear regression. Across all vials, a strong FA dependence of bSSFP- and spGRE-based MBF is observed and this effect is exacerbated for larger AMS. When the proposed correction is used in spGRE readouts, the FA dependence is alleviated over the range of acquired FAs.

Heart rate

Phantom based MBF values from different vials are plotted as a function of simulated HR in Figure 3.6. If an incorrect $T_{1,B}$ was used for quantification, phantom MBF shows a weak dependency on the HR (on average 0.01 ml/g/min per 100 ms change in RR). This effect was more pronounced with larger difference between actual and quantification $T_{1,B}$ (1700 ms). Significant differences in relative MBF error were observed among the three readout-calculation combinations when examined through group-wise comparison ($p < 0.05$). When the correct $T_{1,B}$ was used, the relative MBF error was significantly reduced compared to uncorrected MBF calculation ($p < 0.05$) and MBF values were largely constant with HR for both readout types ($0.03 < R^2 < 0.21/0.30 < R^2 < 0.64$ bSSFP-

P/spGRE). A bias in MBF of 0.43/0.16 ml/g/min (bSSFP/spGRE) remained across the different T_1/T_2 values.

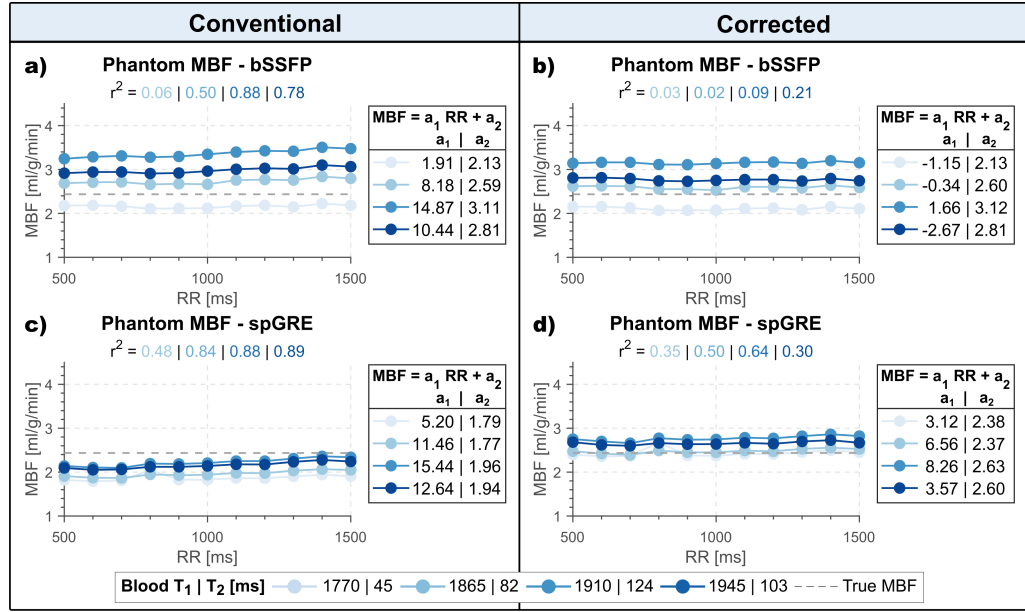


Figure 3.6: Phantom myoASL-MBF from (a), (b) bSSFP and (c), (d) spGRE readout. MBF was calculated with (a), (c) fixed and (b), (d) individual blood T_1 ($T_{1,B}$). Additionally, for corrected spGRE (d), the saturation-baseline approach as proposed in this work was used in MBF calculation. MBF is plotted against the simulated heart rate (HR) for four phantom vials corresponding to different blood T_1 ($T_{1,B}$) and T_2 relaxation times. The slope (a_1) and intercept (a_2) for each vial are obtained from linear regression. Phantom MBF from both readouts shows an HR dependence if the $T_{1,B}$ used in quantification differs from the true (vial) $T_{1,B}$. The HR dependence is significantly reduced when MBF is calculated with true $T_{1,B}$ as proposed in this work. Differences between the different vials remains for corrected bSSFP due to the differences in T_2 relaxation times.

Simulated MBF from bSSFP-readouts was overestimated with increasing FA and AMS whether calculated with or without individual $T_{1,B}$ (slope: 0.02-0.06, $R^2 = 1$), as depicted in Figure 3.7. For the case of uncorrected spGRE, MBF was largely constant up to FAs of about 5° , and was increasingly underestimated with FA increasing beyond 5° (slope: -(0.08-0.07), $R^2 = 1$). With fully corrected calculation, spGRE-based MBF was largely constant over the entire range of FAs (AMS 120: slope 0.0, $0.0 < R^2 < 0.30$; AMS 256: slope 0.0-0.01, $0.11 < R^2 < 0.44$).

As shown in Figure 3.8, simulated spGRE-based MBF was constant over the range of simulated blood T_2 values, while bSSFP-based MBF showed a strong non-linear relation. MBF obtained with bSSFP and spGRE readouts showed a moderate dependence on $T_{1,B}$, which is eliminated when calculated with the correct $T_{1,B}$. Increasing measurement errors in $T_{1,B}$ led to increasing MBF errors (approximately 3 % per 100ms) for all four combinations of readout and calculation mode (Figure 3.9). Further, if an inaccurate $T_{1,B}$ is used in quantification, MBF shows a weak HR dependence in both readouts, as illustrated in Figure 3.10, which is alleviated when calculated with true $T_{1,B}$.

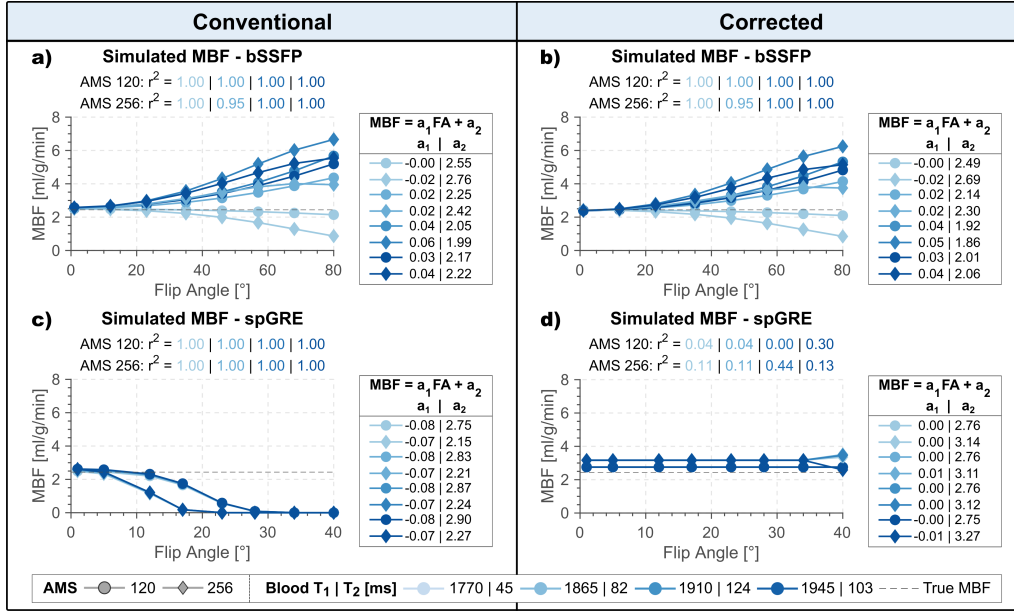


Figure 3.7: Simulated myoASL-MBF from (a), (b) bSSFP and (c), (d) spGRE readout. MBF was calculated with (a), (c) fixed and (b), (d) individual blood T_1 ($T_{1,B}$). Additionally, for corrected spGRE (d), the saturation-baseline approach as proposed in this work was used in MBF calculation. MBF is shown as a function of acquisition flip angle (FA) for two acquisition matrix sizes (AMS). The slope (a_1) and intercept (a_2) are obtained from linear regression. A strong dependence of bSSFP- and spGRE-based MBF on FA is observed which is enhanced for larger AMS. Using the proposed correction eliminates the FA dependence for spGRE readouts.

3.4.2 In vivo results

Based on the relatively mild effect of $T_{1,B}$ compared to the FA on simulated and phantom MBF, in vivo results from bSSFP readouts are presented with uncorrected MBF calculation only. Over all subjects, mean blood $T_{1,B}$ was 1860 ± 68 ms and the HR ranged from 47 to 72 bpm. Perfusion maps and corresponding PN maps of the myocardium are shown for two representative subjects in Figure 3.11. For uncorrected bSSFP, mean global MBF \pm PN were 3.05 ± 0.76 ml/g/min and 0.75 ± 0.34 ml/g/min for the two subjects, respectively. In spGRE, global MBF was $3.14 \pm 1.52 / 2.63 \pm 1.36$ ml/g/min (subject 1/2) with uncorrected and $1.98 \pm 0.96 / 1.67 \pm 0.87$ ml/g/min (subject 1/2) with fully corrected calculation. In visual assessment, uncorrected bSSFP-based maps appeared more homogeneous compared to uncorrected spGRE-based maps. With corrected MBF calculation, however, the image quality of spGRE-based perfusion maps was improved compared to the uncorrected spGRE-maps and visually comparable to the conventional bSSFP approach.

The intra-subject variability within ($\overline{\sigma_p}$) and between measurements (\overline{wsSD}) as well as the inter-subject variability ($isSD$) based on septal MBF are displayed in Figure 3.12 for the three different combinations of readout and MBF calculation. In group-wise comparison, $\overline{\sigma_p}$ and \overline{wsSD} showed significant differences among the three combinations of readout and calculation mode ($p < 0.05$). Mean within-measurement, intra-subject variability was lower in uncorrected bSSFP (0.61 ml/g/min) than in uncorrected spGRE (0.90 ml/g/min, $p = 0.30$).

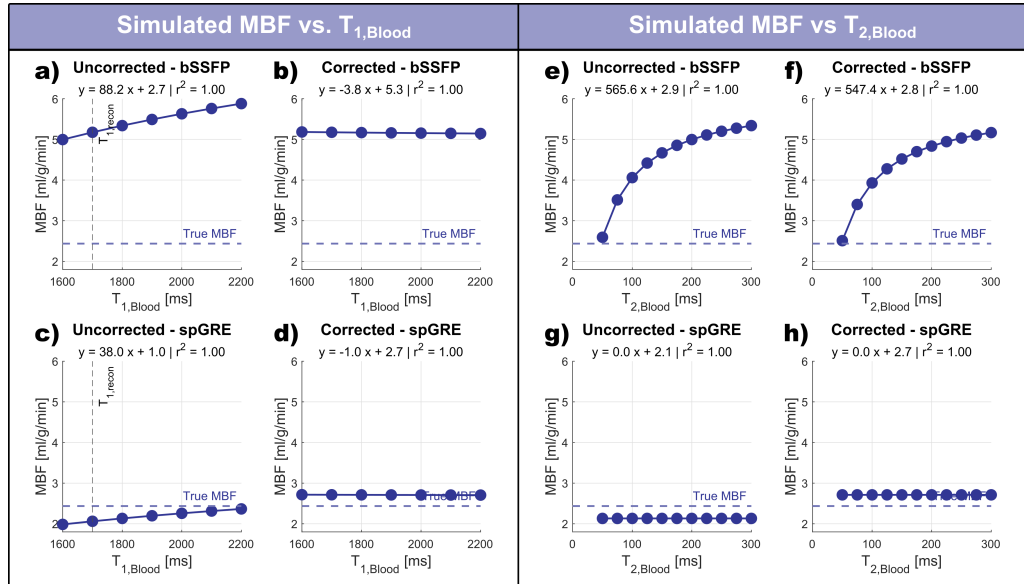


Figure 3.8: Simulated myoASL-MBF as a function of blood (a)-(d) T_1 and (e)-(g) T_2 relaxation times from (a), (b), (e), (f) bSSFP and (c), (d), (g), (h) spGRE readouts. MBF was calculated with (a), (c), (e), (g) fixed and (b), (d), (f), (h) individual blood T_1 ($T_{1,B}$). Additionally, for corrected spGRE (d), (h), the saturation-baseline approach as proposed in this work was used in MBF calculation. Simulated MBF increased with increasing blood T_1 for uncorrected bSSFP and spGRE readouts. When the proposed correction was used, MBF from both readouts decreased slightly with increasing T_1 due to the effect of the long acquisition matrix size in snapshot readout. For both quantification methods, bSSFP-based MBF strongly increased with increasing blood T_2 , while spGRE-based MBF was constant over the range of simulated T_2 values.

The mean within-measurement, intra-subject variability in corrected spGRE-based MBF calculation (0.60 ml/g/min) was on par with uncorrected bSSFP ($p = 0.73$). Uncorrected bSSFP showed lower \overline{wsSD} (0.58 ml/g/min, $p = 0.44$) and $isSD$ (1.49 ml/g/min) compared to uncorrected spGRE (0.74 and 1.92 ml/g/min, respectively). However, when spGRE-MBF was calculated with individual $T_{1,B}$ and saturation-baseline, \overline{wsSD} was reduced compared to uncorrected spGRE by 40 % ($p < 0.05$) and showed a slight but not significant reduction compared to uncorrected bSSFP 22 % ($p = 1.0$). With fully corrected MBF quantification, the $isSD$ of spGRE-MBF was reduced compared to uncorrected bSSFP/spGRE by 13 %/33 %, respectively.

3.5 DISCUSSION

In this work, we investigated how physiological and acquisition-related parameters affect FAIR-myASL based MBF measurements, when bSSFP or spGRE readouts are used. Our simulation and phantom experiments suggest that, out of the investigated parameters, the acquisition flip angle (FA) has the strongest effect on the MBF and may cause spurious MBF deviations. Through an adapted baseline acquisition this effect can be mitigated for spGRE readouts. Furthermore, inaccurate blood T_1 relaxation times in the MBF calculation led to a mild HR dependence which can be reduced if calculated with individual

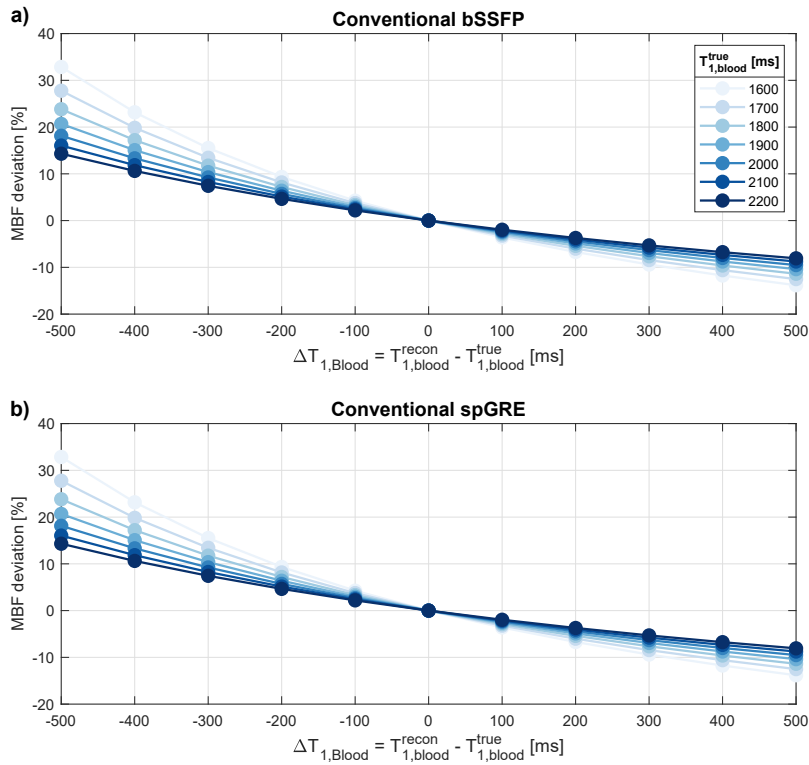


Figure 3.9: Simulated myoASL-MBF deviation as a function of the measurement error of blood T_1 ($T_{1,B}$) for a range of $T_{1,B}$ values. If $T_{1,B}$ is quantified incorrectly, an error of approximately 3 % per 100 ms of blood $T_{1,B}$ deviation in MBF is accrued with conventional (uncorrected) MBF calculation for both (a) bSSFP and (b) spGRE readouts.

$T_{1,B}$. Using both approaches, spGRE-MBF measurements with increased reproducibility have been obtained.

This study uses the Buxton general kinetic model which is a common choice with cardiac FAIR-ASL [37, 40, 115]. However, several simplifications are made when applying this kinetic model. Importantly, the arterial transit time (ATT) effect is considered to be negligible due to the relatively small size of the labeling slab compared to the relatively fast flow in the coronary arteries. However, ATT is known to be a major confounder to accurate perfusion measurements in other anatomies [171], and the validity of this simplification in cardiac applications warrants thorough investigation. Alternative approaches, such as saturation pre-conditioning of the signal preceding the bolus edge [172], or velocity selective labeling [124, 125], where labeling and imaging volumes coincide, are promising for mitigating this confounder. Furthermore, measurements, with multiple post-labeling delays may allow for joint quantification of the ATT to fully correct for this effect [116]. These approaches and the metrological characterization of the impact of ATT on FAIR-based cardiac ASL quantification remain an important topic of future studies.

In this study, imaging is performed during systole, when blood flow is minimal [74, 150], resulting in less than 1 % of spins being exchanged throughout the imaging readout. Consequently, the magnetization modulation function (MMF) is only very weakly affected by flow and spin-exchange during the acquisition readout. However, in approaches that involve extended imaging readouts dur-

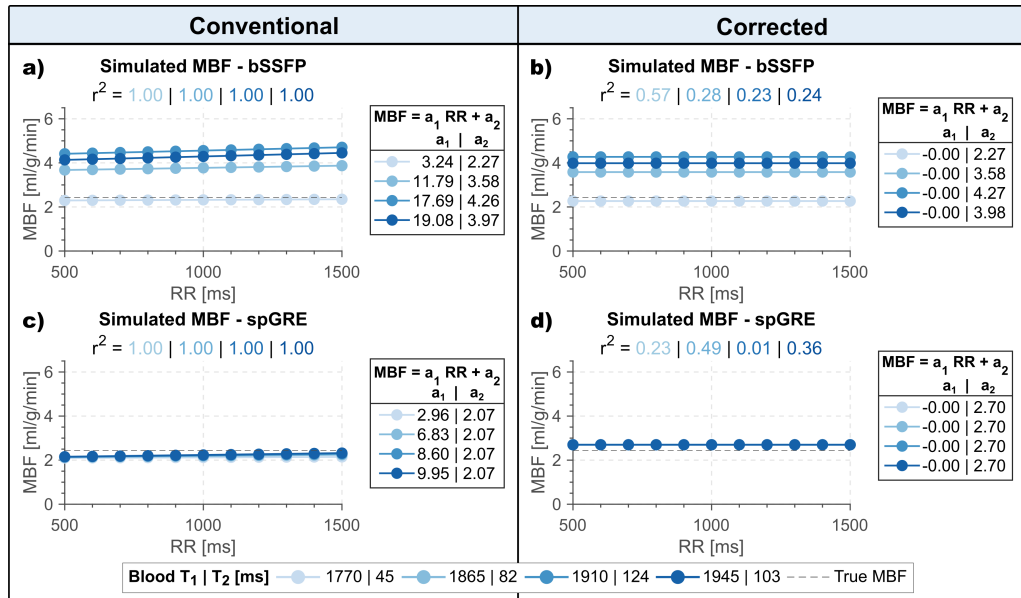


Figure 3.10: Simulated myoASL-MBF from (a), (b) bSSFP and (c), (d) spGRE readout. MBF was reconstructed with (a), (c) fixed and (b), (d) individual blood T_1 ($T_{1,B}$). Additionally, for corrected spGRE (d), the saturation-baseline approach as proposed in this work was used in reconstruction. MBF is shown as a function of heart rate (HR) for different blood T_1 ($T_{1,B}$) and T_2 relaxation times. The slope (a_1) and intercept (a_2) are obtained from linear regression. If an inaccurate $T_{1,B}$ is used in reconstruction, MBF shows an HR dependence in both readouts. This is alleviated when MBF is reconstructed with true $T_{1,B}$ as proposed in this work.

ing diastole or continuous imaging readouts, like "cine-ASL" [173], the in-flow effect becomes more relevant. Recently proposed numerical models aim to capture this phenomenon [174], offering a promising avenue for future research in cardiac ASL. Additionally, the proposed correction scheme assumes that the MMF is identical for baseline, control and tag acquisitions. While this is a common assumption in all ASL techniques [108], differences in MMF among those images may be caused by factors such as changes in the in-flow rate during the readout or changes in the effective FA. To that end, repeating baseline acquisitions throughout the measurement may be useful to minimize the resulting variability in perfusion calculation.

The acquisition FA was identified as a strong confounder in simulated and phantom myoASL-MBF measurements. In both simulation and phantom experiments, bSSFP-based MBF increased with increasing FA while spGRE-based MBF decreased with increasing FA, when conventionally calculated. As a result of the increased number in applied RF pulses, the effect of the imaging readout is exacerbated for larger AMS used in a snapshot readout. These results are especially relevant in view of the high B_1^+ variability across the myocardial region. Particularly at $3 T_1$, variations of up to 50 % of the nominal FA have been observed [162]. In order to alleviate this FA dependence, we proposed an adapted baseline acquisition and MBF calculation for spGRE readouts using an additional saturation-baseline image. Due to the nature of the MMF in bSSFP, this approach can only correct for FA effects with spGRE readouts. However, in this case, the FA dependence is fully eliminated in simulated MBF and

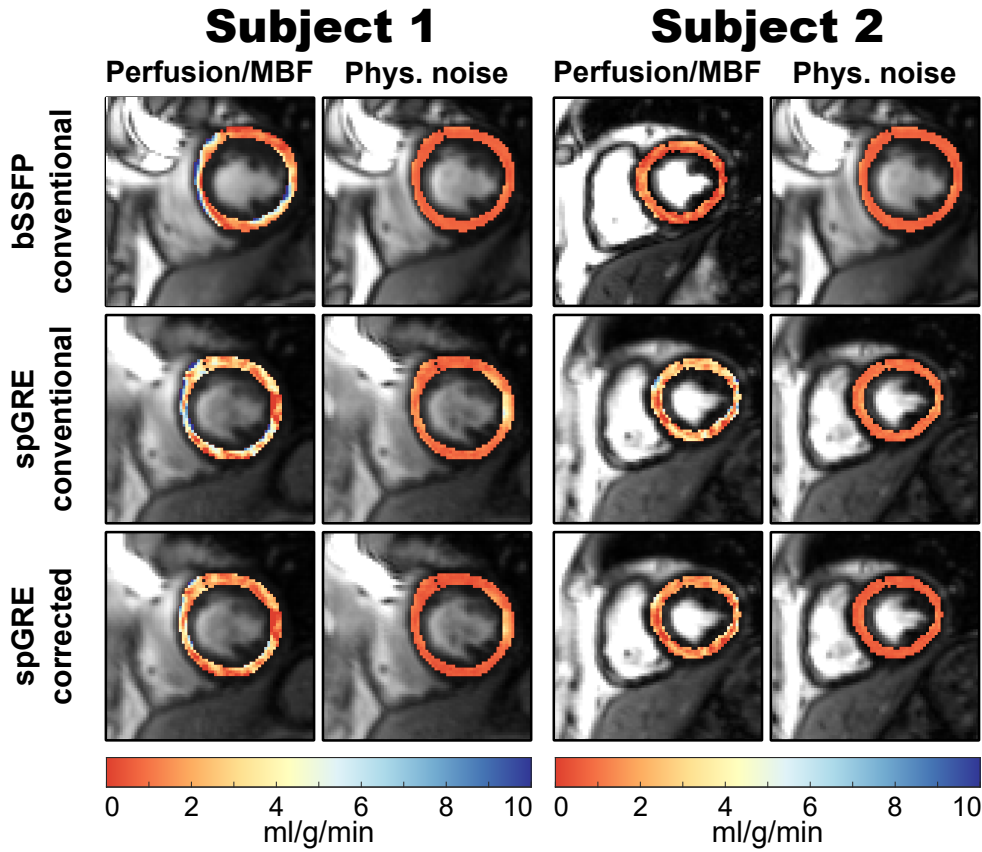


Figure 3.11: MyoASL-perfusion and physiological noise (PN) maps for two representative subjects. For uncorrected bSSFP/spGRE readouts, mean global myocardial blood flow (MBF) \pm PN was $3.05 \pm 0.76 / 3.14 \pm 1.52$ ml/g/min in subject 1 and $0.75 \pm 0.34 / 2.63 \pm 1.36$ ml/g/min in subject 2. Uncorrected bSSFP-maps appear visually more homogeneous and show lower PN across the myocardium compared to uncorrected spGRE-maps. With the proposed correction, however, spGRE-maps were on par with uncorrected bSSFP-maps showing improved image quality and reduced PN compared to uncorrected spGRE. Mean global MBF \pm PN in this case was 1.98 ± 0.96 ml/g/min in subject 1 and 1.67 ± 0.87 ml/g/min in subject 2.

substantially reduced in phantom experiments, potentially alleviating a major acquisition-related confounder.

Perfusion values were comparable between bSSFP and spGRE readouts in simulation and phantom experiments. However, bSSFP-based MBF showed a larger variability with blood T_1/T_2 relaxation times compared to spGRE due to the T_2 dependence of the bSSFP readout signal. Our simulation and phantom results further show that a mismatch between true and quantification $T_{1,B}$ may render myoASL-MBF mildly dependent on HR. Cardiac ASL has previously been reported in the literature with intra-subject variability between 7.5 % [130] and 28 % [44]. In the present study, those values ranged between 26 % and 39 %. Thus, acquisition-related factors, such as FA and AMS, can have a relevant impact on the measurement error in cardiac ASL (up to 60 % of MBF). HR-related factors, on the other hand, were found to be mostly negligible in our results (up to 2 % of MBF). As a result, the effect of using individual $T_{1,B}$ to alleviate the HR dependence is less noticeable in visual assessment compared to using the saturation-baseline for FA correction. Nonetheless, in light of the prevalence of

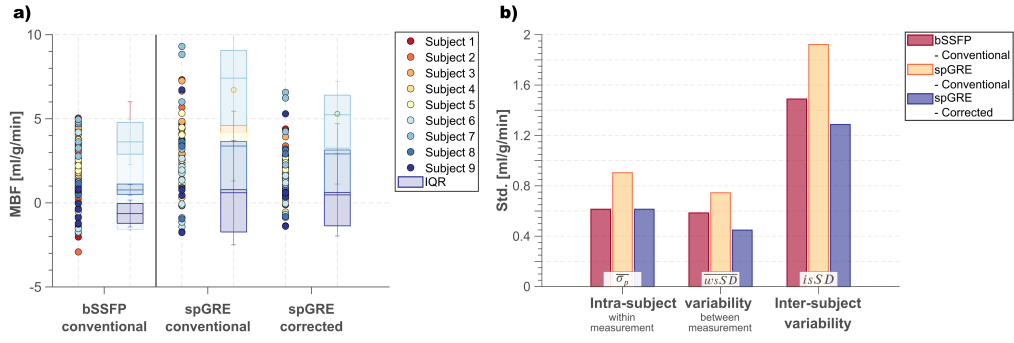


Figure 3.12: (a) In vivo septal myoASL-MBF for all acquired control-tag pairs and all nine subjects. With uncorrected calculation, myocardial blood flow (MBF) from spGRE readouts showed larger variation compared to bSSFP-based MBF. When MBF was calculated with the proposed correction, however, the spread in spGRE-MBF values was reduced compared to both uncorrected bSSFP and spGRE. (b) This is also reflected in the mean intra-subject variability within and between measurements as well as inter-subject variability: With the proposed correction, spGRE readouts show improved reproducibility compared to uncorrected spGRE and are comparable to uncorrected bSSFP.

T_1 mapping in clinical practice [9], individual $T_{1,B}$ values can easily be obtained in common CMR examinations, and can often be incorporated without adding extra scans to the protocol.

In vivo, mean global MBF values from uncorrected bSSFP readout (2.10 ± 0.95 ml/g/min) agreed with previously reported PET-based resting MBF (0.74 – 2.43 ml/g/min [114]). Compared to the reported MBF at rest in healthy subjects as obtained from first-pass perfusion MRI (0.62 ± 0.13 to 1.24 ± 0.19 ml/g/min [98, 175]), the observed myoASL-MBF values were elevated across all readout and calculation mode combinations. However, previous studies using myoASL reported values between 0.7 and 2.7 ml/g/min [36, 37, 40, 130] for global resting MBF. Those values are comparable to the obtained results using the bSSFP readout with uncorrected MBF calculation across all but one subject. Compared to the previously reported range for myoASL-based MBF, uncorrected spGRE-based MBF values were elevated (2.59 ± 1.37 ml/g/min). When calculated with the correction, however, spGRE-based MBF (0.54 – 2.59 ml/g/min) was generally in line with this range and comparable to uncorrected bSSFP. The lowest observed perfusion values ranged at the lower end of MBF values reported in first-pass perfusion literature (0.62 to 1.24 ml/g/min) [175].

With uncorrected calculation, spGRE-based MBF showed higher PN, intra- and inter-subject variability compared to bSSFP-based MBF. This is in agreement with previous findings which demonstrate lower SNR and temporal SNR in cardiac imaging with spGRE snap shot imaging compared to bSSFP readout [149]. Calculating spGRE-based perfusion with the proposed correction tended to improve precision: Both intra-subject variability and average PN from corrected spGRE readouts were on par with uncorrected bSSFP-based values, while simultaneously providing reduced sensitivity to FA-related effects. Similarly, the corrected spGRE approach resulted in less inter-subject variability compared to both uncorrected bSSFP and spGRE.

Nonetheless, variability in those measurements remains high. This is likely due to physiological noise, caused by temporal fluctuations of the blood flow. Changes in the heart rate can further induce timing variations within a control tag-pair potentially impairing the variability if not accounted for. Lastly, residual motion after registration, such as caused by beat-to-beat variability or inconsistent breath-holds, might add to the uncertainty in perfusion values. Further sequence development, such as free-breathing or motion-corrected acquisitions, and research into advanced post-processing are warranted to address these sources of variability. With respect to diagnosis of myocardial ischemia, stress MBF cut-off values ranged between 0.91 and 1.86 ml/g/min [176, 177], with stress MBF values in healthy volunteers of 1.97 up to 4.5 ml/g/min [175]. Thus an effect size of about 55 % can be expected. The inter-subject variability obtained in the present work, promises only moderate detection of those changes. Thus, further reduction of the variability in FAIR-myASL remains crucial for achieving diagnostic confidence as required in the clinic.

As it is common to ECG gated acquisitions, excessive heart rate variability in combination with inadequate gating windows can lead to imaging in different effective cardiac phases[178]. Thus, in double ECG-gated FAIR-myASL, this effect can lead to incongruence between the control and tag image. Due to the relatively stable duration of the systole compared to the diastole[179], however, recent studies suggest that systolic FAIR-myASL can offer higher robustness to such timing issues[44]. Future studies in targeted cohorts, such as patients suffering from cardiac arrhythmia, are warranted to further investigate the suitability of systolic cardiac ASL in the clinic.

In the proposed work the correction was derived for the case of a FAIR-ASL sequence. However, the proposed saturation-baseline approach does not depend on the labeling mode and is applicable to other ASL schemes such as velocity [124] or acceleration selective ASL [180]. In fact, Zhang et al. proposed a similar approach to account for magnetization saturation in Look-Locker FAIR-myASL (LL-FAIR) [181] using multivariate regression to eliminate the T_1 error. However, the performance was not compared to conventional fitting approaches and the proposed method was not explored in other myASL sequences.

This study has several limitations. Current FAIR-myASL methods generally do not allow for extensive myocardial coverage since large inversion slabs can lead to increasing, non-negligible transit delays[116, 140]. Velocity selective labeling may allow for larger myocardial coverage as it is largely insensitive to transit delays, albeit with potential sensitivity to residual motion[124, 125]. Future studies applying the proposed MBF calculation to velocity-selective ASL are warranted. The FAIR-myASL sequence was acquired in healthy subjects at rest only and no stress perfusion has been obtained. Repeatability, as assessed by back-to-back scanning, presents only a subset of the factors influencing reproducibility or intra-subject variability in a clinical setting. Further, the reproducibility and sensitivity of the corrected FAIR-myASL approach remain to be evaluated in patients with myocardial pathology. Due to the relatively small number of subjects included in this proof-of-principle study, larger studies assessing precision in a clinical set-up or reproducibility over more extended time periods or different scan settings are warranted and would also allow for

increased statistical power in comparing the uncorrected and corrected MBF calculation in bSSFP and spGRE readout. In this study, individual $T_{1,B}$ were obtained with MOLLI T_1 -mapping, which is known to underestimate T_1 [152, 182]. This could lead to inaccurate $T_{1,B}$ and, as shown in the results, impair the effectiveness of the proposed MBF calculation with individual $T_{1,B}$ to reduce the HR dependence of myoASL-MBF. To that end, saturation based T_1 mapping sequences can be used in future work [183].

MYOCARDIUM SIGNAL SUPPRESSION WITH T_2 -PREPARATIONS FOR REDUCED PHYSIOLOGICAL NOISE IN MYOCARDIAL ASL

The results in this chapter have been partially presented at *CMR 2024*, the 26th Annual Scientific Sessions of the Society for Cardiovascular Magnetic Resonance in London (UK) [42].

4.1 INTRODUCTION

As previously described, myoASL has emerged as a promising alternative to conventional first-pass perfusion CMR that relies on exogenous contrast agents. Instead, myoASL utilises magnetically labelled blood as an endogenous tracer, allowing to quantify myocardial perfusion and detect perfusion alterations related to coronary occlusions [35, 45]. This is particularly advantageous in view of the safety concerns attributed to gadolinium-based contrast agents (GBCAs), which have been linked to the onset of nephrogenic system fibrosis [28, 29] and inadvertent gadolinium accumulation in the body [32], limiting clinical applicability of first-pass perfusion CMR. Despite the potential of myoASL in this regard, the inherently low signal-to-noise ratio (SNR) impairs its robustness and hampers widespread clinical translation. While Part I of this thesis mainly addressed acquisition-related biases in myoASL, this chapter focuses on reducing physiological noise (PN) arising from myocardial signal fluctuations in double ECG-gated FAIR-myASL.

In myoASL, the noise profile is governed by physiological rather than thermal noise [40]. Due to the low blood-volume fraction, myocardial signal fluctuations prevail in physiological noise (PN) and can stem from uncorrected motion or variations in the heart rate. In this context, double ECG-gated FAIR-myASL is particularly susceptible to heart rate variations because both labelling and acquisition are triggered to the same cardiac phase. Thus, changes in the heart rate lead to a variable TI and inconsistent inversion recovery of the signal across the FAIR images. In consequence, static tissue components do not cancel out in the subtraction of control and tag images, and confound the accurate estimation of myocardial perfusion using Buxton's General Kinetic Model (GKM) ([108], see Section 2.4.3.4).

To address the challenges of PN in (myocardial) ASL, background suppression strategies offer a potential solution. These are generally recommended for neurovascular applications of ASL [33], but their adoption for myoASL remains limited. Background suppression aims at enhancing the overall SNR levels by reducing confounding background signals without impairing the perfusion-related ASL signal. In the context of myoASL, a number of studies applied a combination of slice-selective saturation and non-selective inversion pulses between labelling and image readout in combination with FAIR-labelling [184,

185]. Akin to background suppression strategies used for ASL in the brain [186], the additional inversion pulses are timed so that the myocardial background signal reaches the zero-crossing at the time of the image readout. However, these approaches suppress only a specific range of T_1 relaxation times, determined by the pulse timing, and are susceptible to HR variations, which somewhat limits their effectiveness in reducing PN [185].

In this work, we explore the use of conventional T_2 -preparations [187] to suppress the myocardial signal. T_2 -preparations are commonly employed in CMR to induce T_2 image-weighting and map myocardial T_2 times, which can aid in the assessment of myocardial inflammation and oedema [19, 87]. Such T_2 -preparations suppress the signal from all tissue, but the amount of attenuation depends on the tissue-specific T_2 time and the resulting T_2 -dependent exponential weighting factor. Thus, as a result of the substantially shorter myocardial T_2 time compared to blood [46, 47], the myocardial signal is heavily suppressed whereas the blood signal, responsible for the perfusion-contrast, is only minimally affected. In consequence, this selective suppression can reduce myocardial contributions to PN and may improve overall SNR in myoASL.

The aim of this study is, therefore, to investigate the use of T_2 -preparations to suppress PN originating from myocardial signal in a free-breathing, respiratory-navigated FAIR-myocardial ASL sequence. We conducted simulation and phantom experiments to evaluate the effect of the T_2 -preparations on the myoASL signal as well as on the PN based on random heart rate variations. Furthermore, in a proof-of-concept in vivo study, we compared the PN in a conventional and two T_2 -prepared FAIR-myocardial ASL sequences, with preparation durations of respectively 40 and 80 ms, to assess their efficacy in improving robustness of FAIR-myocardial ASL.

4.2 METHODS

4.2.1 Theoretical framework

4.2.1.1 Conventional myoASL

In conventional FAIR-myocardial ASL, the control image signal I_C is a combination of myocardial and blood signal contributions I_M and I_B , respectively:

$$\begin{aligned} I_C &= I_{M,C} + I_{B,C} = \\ &= V_M(A_M x_{M,C}^- + B_M) + \\ &+ V_B(f_{in}(A_B x_{B,C}^+ + B_B) + (1 - f_{in})(A_B x_{B,C}^- + B_B)) = \\ &= V_M(A_M x_{M,C}^- + B_M) + V_B(f_{in} A_B (x_{B,C}^+ - x_{B,C}^-) + (A_B x_{B,C}^- + B_B)) \quad (4.1) \end{aligned}$$

with blood-volume-fraction $V_B = 1 - V_M$, and in-flow rate f_{in} . The coefficients A and B , as defined earlier in Section 3.2.2, depend on the acquisition param-

eters as well as the tissue relaxation times. The initial magnetisation prior to readout x can be given as

$$x^+ = M_{z,eq} \quad (4.2)$$

$$x^- = M_{z,eq} \cdot \left(1 - \delta_{inv} e^{-\frac{TI}{T_1}}\right), \quad (4.3)$$

with equilibrium magnetisation $M_{z,eq}$, inversion time TI , longitudinal relaxation time T_1 , and inversion efficiency $\delta_{inv} = 1 - \cos(\alpha_{inv})$. Likewise, the tag image signal yields:

$$I_T = I_{M,T} + I_{B,T} = V_M(A_M x_{M,T}^- + B_M) + V_B(A_B x_{B,T}^- + B_B). \quad (4.4)$$

Then, the signal difference between control and tag signal can be derived as

$$\begin{aligned} \Delta I = I_C - I_T &= (I_{M,C} - I_{M,T}) + (I_{B,C} - I_{B,T}) = \\ &= V_M A_M (x_{M,C}^- - x_{M,T}^-) \quad + \quad \{\text{I:} = \Delta I_M \\ &+ V_B A_B (x_{B,C}^- - x_{B,T}^-) \quad + \quad \{\text{II:} = \Delta I_B \\ &+ V_B A_B f_{in} (x_{B,C}^+ - x_{B,C}^-). \quad \{\text{III:} \propto \text{MBF} \end{aligned} \quad (4.5)$$

The first two terms, ΔI_M and ΔI_B , depend on the difference in TI between control and tag image and disappear if the TI is identical for control and tag ($\Delta TI = 0$). If, however, $\Delta TI \neq 0$, these terms confound the perfusion-weighted signal given in term (III). This can lead to inaccurate myocardial blood flow (MBF) values as obtained from Buxton's GKM [108], introduced in Section 2.4.3.4:

$$MBF_{estim} = \frac{\lambda(I_C - I_T)}{\delta_{inv} I_{BL} T I e^{-\frac{TI}{T_{1,B}}}}, \quad (4.6)$$

with blood-water partition coefficient λ and baseline image signal I_{BL} . The baseline signal in a conventional FAIR-myocardial ASL sequence is given by

$$I_{BL} = V_M(A_M x_M^+ + B_M) + V_B(A_B x_B^+ + B_B). \quad (4.7)$$

Combining this with Equations (4.6) and (4.2) yields for the MBF quantification:

$$MBF_{estim} \propto \frac{I_C - I_T}{I_{BL}} = \frac{\Delta I_M + \Delta I_B + V_B A_B f_{in} M_{z,eq} \delta_{inv} e^{-\frac{TI}{T_{1,B}}}}{V_M(A_M x_M^+ + B_M) + V_B(A_B x_B^+ + B_B)}. \quad (4.8)$$

Only for the case of $A_M = A_B = 1$ and $B_M = B_B = 0$, as is implicitly assumed in Buxton's GKM, and for $\Delta I_M = \Delta I_B = 0$, the estimated MBF value matches the actual perfusion rate.

4.2.1.2 T_2 -prepared FAIR-myocardial ASL

When a non-selective T_2 -preparation module of duration τ_{T2p} is applied immediately prior to the readout, the myocardial and blood signal contributions

are weighted by a T_2 -dependent factor $e_M = e^{-\tau_{T2p}/T_{2,M}}$ and $e_B = e^{-\tau_{T2p}/T_{2,B}}$, respectively. The control and tag signal then become:

$$I_C^{T2p} = V_M(A_M e_M x_{M,C}^- + B_M) + V_B(f_{in} A_B e_B (x_{B,C}^+ - x_{B,C}^-) + (A_B e_B x_{B,C}^- + B_B)), \quad (4.9)$$

$$I_T^{T2p} = V_M(A_M e_M x_{M,T}^- + B_M) + V_B(A_B e_B x_{B,C}^- + B_B). \quad (4.10)$$

Notably, the myoASL signal in control and tag settings is suppressed by the T_2 -weighting. However, given that T_2 relaxation times in myocardium (ca. 45 ms [46]) are much shorter compared to blood (ca. 250 ms [47]), the myocardial signal contributions are more strongly suppressed. Based on this, the signal difference between control and tag image yields:

$$\begin{aligned} \Delta I_{T2p} = I_C^{T2p} - I_T^{T2p} &= V_M A_M e_M (x_{M,C}^- - x_{M,T}^-) + \text{I: } = e_M \Delta I_M \\ &+ V_B A_B e_B (x_{B,C}^- - x_{B,T}^-) + \text{II: } = e_B \Delta I_B \\ &+ V_B A_B e_B f_{in} (x_{B,C}^+ - x_{B,C}^-). \quad \text{III: } \propto e_B M B F \end{aligned} \quad (4.11)$$

The potential noise terms ΔI_M and ΔI_B are now also weighted by the respective T_2 -preparation factors e_M and e_B and the myocardial signal fluctuations are effectively suppressed due to the short $T_{2,M}$ [46]. Further, any other terms contributing to PN – i. e. due to cardiac or respiratory motion or fluctuations in the blood-flow itself – will be weighted by the same T_2 -dependent factors.

4.2.1.3 SNR considerations in FAIR-myASL

The SNR of the perfusion-weighted signal is given by the ratio of the expected value ($\mu_{I_C-I_T}$) and standard deviation ($\sigma_{I_C-I_T}$) of the control-tag signal difference

$$SNR = \frac{\mu_{I_C-I_T}}{\sigma_{I_C-I_T}} = \frac{V_B A_B \overline{f_{in}} \delta_{inv} e^{-\frac{\overline{TI}}{T_{1,B}}}}{\sigma_{tot}}. \quad (4.12)$$

with the mean perfusion rate $\overline{f_{in}}$ and inversion time \overline{TI} averaged across the control and tag acquisition. The total noise of the measurement $\sigma_{tot} = \sigma_{th} + \sigma_{pn}$ can be described as a sum of thermal noise σ_{th} and PN σ_{pn} .

In this regard, the additional T_2 -preparation can reduce the contribution of PN if an adequate preparation duration τ_{T2p} is chosen. Assuming constant thermal background noise, the SNR for a T_2 -prepared FAIR-myASL sequence can be estimated as

$$SNR_{T2p} = \frac{\mu_{I_C-I_T}^{T2p}}{\sigma_{I_C-I_T}^{T2p}} = \frac{V_B A_B e_B \overline{f_{in}} \delta_{inv} e^{-\frac{\overline{TI}}{T_{1,B}}}}{\sigma_{th} + \sigma_{pn}^{T2p}}. \quad (4.13)$$

From Equations (4.5) and (4.11), the PN can be described as a sum of myocardial and blood components:

$$\sigma_{pn} = \sigma_M + \sigma_B \quad \text{conventional} \quad (4.14)$$

$$\sigma_{pn}^{T2p} = e_M \sigma_M + e_B \sigma_B \quad T_2\text{-prepared} \quad (4.15)$$

It follows then for the ratio of the SNR of T_2 -prepared relative to conventional FAIR-myoASL sequence:

$$\frac{SNR_{T2p}}{SNR} = \frac{e_B(\sigma_{th} + \sigma_{pn})}{\sigma_{th} + \sigma_{pn}^{T2p}} = \frac{e_B(\sigma_{th} + \sigma_M + \sigma_B)}{\sigma_{th} + e_M \sigma_M + e_B \sigma_B} \quad (4.16)$$

Considering that $\tau_{T2p} > 0$, it holds that $0 < e_{M/B} < 1$ for both myocardium and blood, such that the potentially confounding noise terms can be reduced compared to a conventional FAIR-myoASL acquisition when an adequate τ_{T2p} is chosen.

4.2.2 MyoASL sequence and post-processing

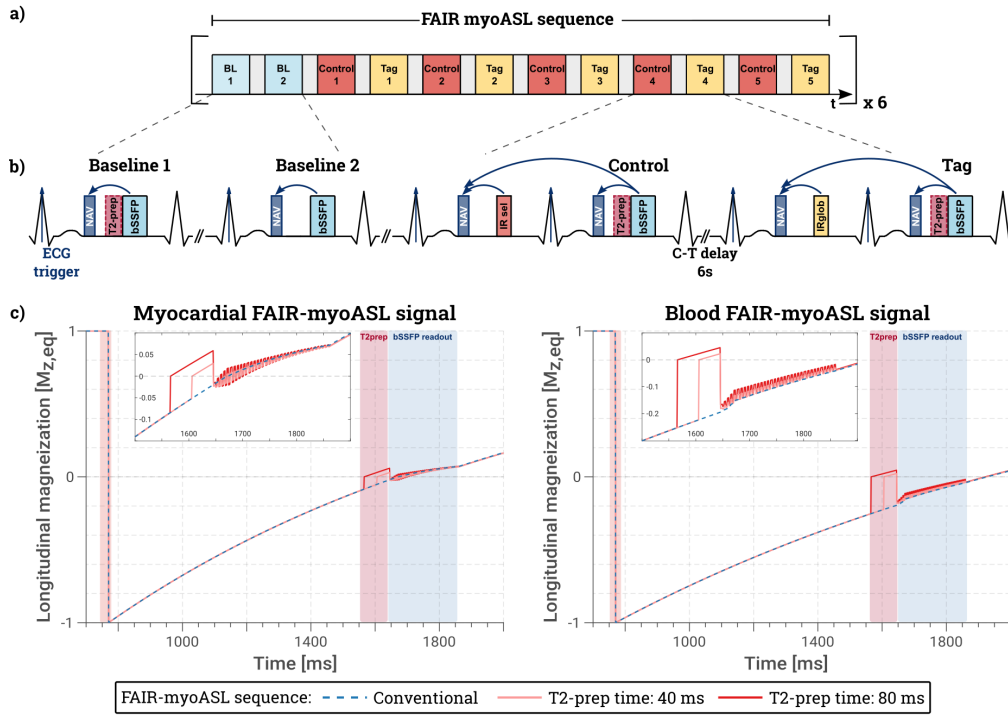


Figure 4.1: (a) Diagram of the double ECG-gated, respiratory-navigated FAIR-myoASL sequence. (b) After a selective/global inversion pulse, control/tag images are acquired only if both the current and preceding navigator are accepted. (c) Magnitisation recovery following the FAIR inversion, and an additional T_2 -preparation with $\tau_{T2p}=40\text{ms}/80\text{ms}$ to increase the blood-myocardium contrast.

Based on our previously published work [41], a double ECG-triggered FAIR-myoASL sequence with bSSFP readout was used for all experiments. In addition to this conventional FAIR-myoASL sequence, a T_2 -prepared sequence was

implemented, where T_2 -preparations were applied immediately before the readout of all images as depicted in Figure 4.1. Adiabatic T_2 -preparation pulses optimised for cardiac applications [187], consisting of rectangular tip-down and tip-up pulses combined with B_1 -insensitive refocusing pulses (BIR-1), were used as provided by the vendor. All imaging was performed at 3 T (Magnetom Skyra, Siemens Healthineers, Erlangen, Germany) with detailed sequence parameters as provided in Table 4.1. The post-processing of myoASL data was performed in MATLAB (MathWorks, Natick, MA, USA) and MBF was quantified using Buxton's GKM [108] as given in Equation (4.6). As proposed in our earlier work [41], measured values for the T_1 relaxation time of blood were used in phantom and in vivo experiments to quantify perfusion.

| Experiment | FA (°) | TE/TR (ms) | Matrix size | FOV (mm ²) | Voxel size (mm ³) |
|------------|--------|------------|-------------|------------------------|-------------------------------|
| Phantom | 60 | 1.68/3.36 | 168 × 176 | 300 × 300 | 1.7 × 1.7 × 8.0 |
| In vivo | 60 | 1.70/3.4 | 170 × 208 | 341 × 291 | 1.6 × 1.6 × 8.0 |

Abbreviations: FA: flip angle; FOV: field of view; TE: echo time; TR: repetition time

Table 4.1: Sequence parameters of the FAIR-myASL sequence for phantom and in vivo measurements were identical for conventional and T_2 -prepared readouts. All imaging was performed with Partial Fourier (6/8) and Generalized Auto-calibrating Partially Parallel Acquisition (GRAPPA) rate of 2.

4.2.2.1 Correction for signal decay during τ_{T2p}

As illustrated in Equation (4.11), T_2 -prepared readouts also affect the perfusion-weighted signal and need to be corrected for when calculating MBF. Assuming zero noise ($\Delta I_M = \Delta I_B = 0$), the ratio of the estimated MBF value with and without T_2 -preparation is proportional to the ratio of the conventional and T_2 -prepared baseline signal:

$$\begin{aligned}
 \frac{MBF_{T2p}}{MBF} &= \frac{V_B f_{in} e_B \delta_{inv} M_{z,eq} e^{\frac{-TI}{T_{1,B}}}}{BL_{T2p}} \cdot \frac{BL}{V_B f_{in} \delta_{inv} M_{z,eq} e^{\frac{-TI}{T_{1,B}}}} = \\
 &= e_B \frac{BL}{BL_{T2p}} = \\
 &= e_B \frac{V_M (A_M x_M^+ + B_M) + V_B (A_B x_B^+ + B_B)}{V_M (A_M e_M x_M^+ + B_M) + V_B (A_B e_B x_B^+ + B_B)}. \quad (4.17)
 \end{aligned}$$

Ignoring readout effects ($A_M = A_B = 1$, $B_M = B_B = 0$), the ratio can be estimated as

$$\begin{aligned}
 \frac{MBF_{T2p}}{MBF} &= \frac{e_B M_{z,eq} (V_M + V_B)}{M_{z,eq} (V_B e_B + V_M e_M)} = \frac{e_B}{V_B e_B + V_M e_M} = \\
 &= \frac{1}{V_B + (1 - V_B) e_M / e_B}. \quad (4.18)
 \end{aligned}$$

If the timing of the readout (k-space centre) is unchanged with added T_2 -preparations, an additional factor of $e^{\tau_{T2p}/T_{1,B}}$ needs to be included to account for the shorter inversion recovery period compared with a conventional sequence.

4.2.3 Simulation experiments

To assess how T_2 -preparations influence MBF and PN in FAIR-myASL, numerical, Bloch-equation-based simulations were performed using MATLAB. Both conventional and T_2 -prepared sequences were simulated following the same design described in Section 3.3.2. Unless otherwise specified, general simulation parameters for the myASL sequence with bSSFP readout were as follows: 10 ramp-up pulses, FA 60° , 60 readout pulses (k-space centre at $n_{RF} = 30$), TE/TR 1.55 ms/3.1 ms, 100 % inversion efficiency, and a control-tag delay of 6 s. These parameters are chosen according to the acquisition parameters in the phantom study. A blood volume fraction of 0.14 [164] and a blood replacement/in-flow rate of 0.29 1/s were simulated, resulting in an effective MBF input value of 2.4 ml/g/min. Other physiological parameters were simulated as: HR 60 bpm, blood T_1/T_2 relaxation times at 3 T of 1700 ms/210 ms, and myocardial T_1/T_2 relaxation times of 1300 ms/60 ms [151, 152], if not indicated otherwise.

The myASL signal was simulated over a range of preparation durations τ_{T2p} from 0 to 500 ms. Here, 0 ms corresponds to the conventional myASL sequence without T_2 -preparations. To mimic PN as caused by fluctuations in TI , the duration of the simulated RR interval was varied randomly between control and tag acquisitions. To that end, zero-mean Gaussian noise was added to the simulated RR duration with a standard deviation σ_{RR} of 100 ms in agreement with observed heart rate variability in vivo [188–190]. Furthermore, thermal fluctuations of the imaging signal were modelled as constant zero-mean Gaussian noise. These simulations were repeated $n = 1000$ times to determine an average SNR and its standard deviation σ_{SNR} as a function of the T_2 -preparation duration.

In addition, the simulations were carried out across four different ratios of physiological to thermal noise (1.0, 1.6, 2.6, and 6.3), in line with expected ratios for myASL in vivo [40]. This was achieved by varying the degree of thermal noise for a constant σ_{RR} of 100 ms. The specific noise ratio for each scenario was calculated based on the conventional, unprepared myASL sequence as:

$$\frac{\sigma_{pn}}{\sigma_{th}} = \frac{\sigma_{tot} - \sigma_{th}}{\sigma_{th}}. \quad (4.19)$$

Here, the mean total noise σ_{tot} was determined from the standard deviation across the control-tag pairs and averaged over the number of repetitions (n). The thermal noise was calculated in the same manner but for a fixed heart rate, i. e. $\sigma_{RR} = 0$.

Then, for each preparation duration and noise ratio, the SNR was calculated according to Equation (4.12) as

$$SNR = \frac{\overline{MBF}}{\sigma_{MBF}} = \frac{\sum_{j=1}^{N_{CT}} MBF_j}{\sigma_{MBF}^{N_{CT}}} \quad (4.20)$$

where $N_{CT} = 6$ is the number of control-tag pairs. $\sigma_{MBF}^{N_{CT}}$ is calculated as the standard deviation of MBF across the control-tag pairs. Finally, the SNR gain was determined relative to the SNR of the unprepared, conventional sequence: $\Delta SNR = SNR_{T_2prep} / SNR_{conv}$.

4.2.4 Phantom experiments

To further evaluate the efficacy of T_2 -prepared FAIR-myocardial ASL readouts, experiments were conducted using a phantom comprising 20 NiCl₂-doped agarose vials submerged in agarose gel. The T_1 relaxation times ranged between 300 and 2500 ms and the T_2 relaxation times between 40 and 170 ms, mimicking the relevant physiological range for CMR [51, 151]. For subsequent evaluation, two vials were chosen with T_1/T_2 relaxation times corresponding to those in the myocardium (1362 ms/55 ms) [51] and blood (1965 ms/167 ms) [47, 152], respectively. In addition to a conventional FAIR-myocardial ASL sequence, T_2 -prepared FAIR-myocardial ASL sequences with τ_{T_2p} ranging from 30 to 200 ms were acquired. Each sequence comprised three control-tag image pairs as well as a pair of baseline images. Each FAIR-myocardial ASL sequence was then repeated with different simulated RR intervals between 900 and 1100 ms, in increments of 25 ms.

To simulate the image-to-image heart rate variability of in vivo cardiac imaging, a new data set was synthesised from the acquired phantom data as follows. For 30 control-tag pairs, corresponding to the six sequence repetitions in vivo, an array of random RR interval durations was simulated based on a zero-mean Gaussian distribution between 900 and 1000 ms. Then, for a predefined standard deviation σ_{RR} ranging between 0 and 100 ms, the RR durations were matched to the acquired ones and images were drawn accordingly. To ensure the presence of thermal noise, a different control or tag image was chosen randomly from the available set per RR interval. This process was repeated 1000 times for each acquired FAIR-myocardial ASL sequence, resulting in a dataset containing 30 control-tag image pairs and a corresponding baseline image for each T_2 -preparation strategy/ τ_{T_2p} , each level of heart rate variability σ_{RR} , and each repetition. The subsequent MBF simulation was based on the scheme outlined in the previous chapter (see Section 3.3.3.1).

4.2.5 In vivo experiments

As a proof-of-concept, one healthy volunteer (male, 29 years) was included in the study, which was approved by the local institutional review board. Written consent was obtained from the participant prior to examination.

In total, three myocardial ASL sequences were acquired: conventional and T_2 -prepared with preparation durations of 40 ms and 80 ms, respectively. Each sequence consisted of two baseline images and five control-tag image pairs and was repeated six/four times for $\tau_{T_2p} = 40$ ms/ $\tau_{T_2p} = 80$ ms in a randomised order. Additionally, T_1 and T_2 mapping sequences were acquired using MOLLI [136] and T_2 -prepared snapshot Fast Low-Angle Shot (FLASH) [191], respectively. An individual $T_{1,B}$ value for MBF calculation was determined from a manually drawn ROI in the left-ventricular blood pool. Prior to MBF quantifi-

cation, all myoASL images were registered group-wise [169], and the signal polarity was restored using phase-sensitive (PS) reconstruction [192, 193]. The left-ventricular myocardium was segmented manually [128], and in vivo PN was calculated pixel- and segment-wise based on the definition in Chapter 3, Equation (3.9). Finally, for each sequence, the global coefficient of variation (CoV) was individually determined for each repetition and then averaged across all repetitions.

4.2.5.1 Free-breathing acquisitions and PS reconstruction

For this in vivo study, we combined free-breathing, dual-respiratory-navigated image acquisition with PS reconstruction, as published in [193]. This approach is briefly outlined in the following, while the original publication including a detailed discussion is reproduced in Appendix B.

Due to the low SNR, multiple averages of myoASL acquisitions are needed to ensure sufficient accuracy. As discussed in Section 2.4.3.3, this typically requires tedious averaging over multiple breath-holds. While free-breathing myoASL acquisition have been proposed [163], they often require retrospective image selection, which may lead to excessive scan times. Therefore, in this study, in vivo scans were performed in free-breathing with a dual respiratory navigator to increase scan time efficiency and improve patient-comfort. To that end, a pencil-beam navigator placed at the liver dome was played prior to both inversion and image acquisitions. The acquisitions were accepted only when both consecutive navigators were valid in order to ensure that FAIR-images are acquired upon successful inversion. This dual-heartbeat navigation also led to matching slice-selective inversion and excitation in control images. Baseline images were conventionally navigated within a single heartbeat.

In addition, a PS image reconstruction was implemented for myoASL images. Namely, due to the long T_1 relaxation times in myocardium and blood relative to the TI in FAIR-myocardial [47, 152], the magnetisation could be negative at the time of the image readout. Depending on the tissue T_1 and the heart rate, which determines the TI in double ECG-gated FAIR-myocardial, the distorted image contrast may then lead to inaccurate MBF estimation. Hence, we performed a PS reconstruction to restore the signal polarity and image contrast. To this end, both magnitude and phase of the FAIR-myocardial images were acquired. Subsequently, the phase difference between inversion-prepared and unprepared images was unwrapped and rounded to 0 or π to extract the signal polarity, as previously described [192].

4.3 RESULTS

4.3.1 Simulation experiments

The effect of T_2 -preparations on the simulated myoASL signal for both myocardium and blood is illustrated in Figure 4.2. When no inversion labelling was applied, the native myocardial and blood signal continuously decreased with increasing T_2 -preparation duration. Compared to signals derived from conventional myoASL, T_2 -preparations resulted in a signal reduction of up to

77 % in blood and up to 94 % in myocardium at $\tau_{T_2p}=200$ ms. For inversion-prepared magnetisation, the blood signal was continuously reduced with increasing T_2 -preparation time, reaching a reduction of 18 % at $\tau_{T_2p}=200$ ms. The myocardial inversion recovery signal first decreased and then plateaued at about 90 % of the initial signal for τ_{T_2p} between 30 ms and 80 ms. Beyond this range, T_2 -preparations lead to a progressive reduction of the myocardial signal, up to of 41 % at $\tau_{T_2p}=200$ ms.

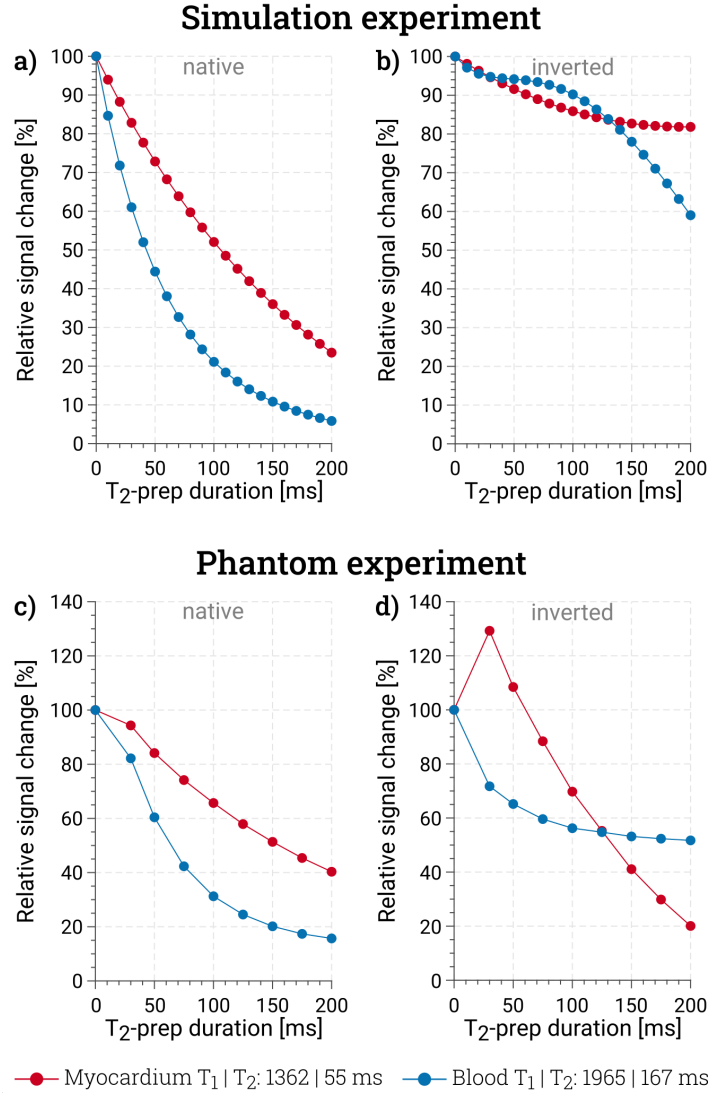


Figure 4.2: For a simulated RR interval of 1000 ms and a range of preparation times (τ_{T_2p}), the signal change as induced by a T_2 -preparation is shown for myocardium (blue) and blood (red) relative to unprepared signal ($\tau_{T_2p}=0$). In (a), (b) simulation and (c), (d), phantom experiments, T_2 -preparations were applied to (a), (c) equilibrium magnetisation and (b), (d) after inversion recovery. Notably, the signal reduction was more pronounced for myocardium than blood due to the shorter T_2 time.

The relative difference in simulated SNR achieved with T_2 -prepared myoASL-sequences is shown in Figure 4.3. Compared to the conventional myoASL sequence, the SNR gain using T_2 -prepared readouts varied with the duration of the applied T_2 -preparation. Overall, for longer preparation duration, the

SNR gain increased until reaching a broad peak and then decreased towards zero. The optimal T_2 -preparation duration corresponding to the maximum SNR gain, increased with higher simulated ratios of physiological to thermal noise present during the measurement. Further, the maximum achievable SNR gain was higher for larger ratios of physiological to thermal noise. For equal magnitude of thermal and physiological noise, the SNR was improved on average by a factor of 1.4 using T_2 -preparations of 60 to 80 ms. Whereas, for a physiological to thermal noise ratio of 6.3, up to a three-fold increase in SNR was achieved for T_2 -preparation of 150 to 200 ms.

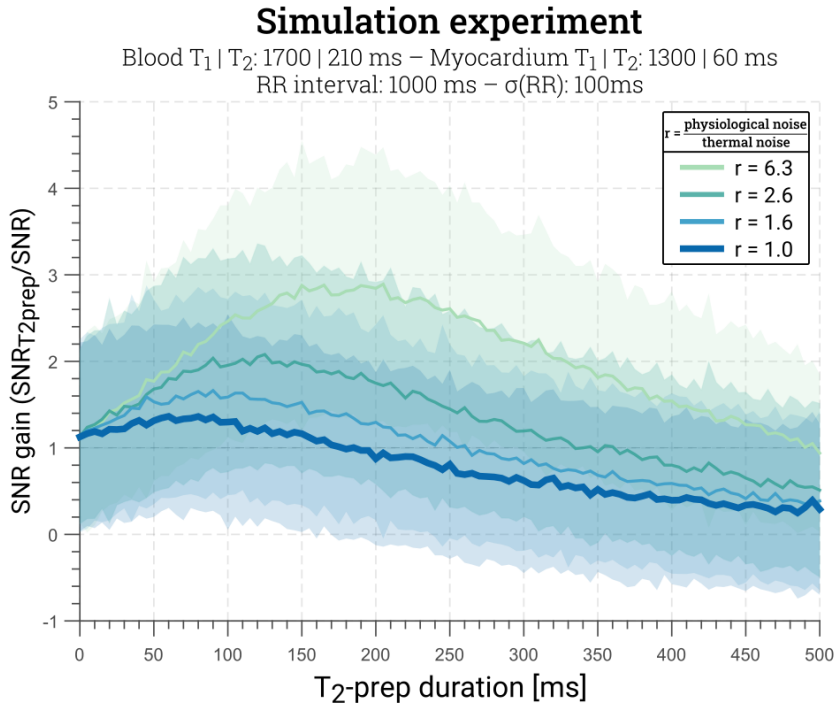


Figure 4.3: Relative SNR gain with T_2 -prepared readouts compared to a conventional FAIR-myocardial ASL sequence for a range of preparation times (τ_{T_2p}) from simulation experiments. The τ_{T_2p} , at which the SNR gain is maximised, increased with increasing simulated ratio of physiological and thermal noise.

4.3.2 Phantom experiments

The relative myocardial and blood signal change upon applying T_2 -preparations in phantom experiments is depicted in Figure 4.2. When no inversion labelling was employed, a continuous decrease of both myocardial and blood signal was observed with increasing duration of T_2 -preparations. At the longest acquired preparation time τ_{T_2p} of 200 ms, the blood and myocardial signal were reduced by 60 % and 84 %, respectively. For the case of inversion-prepared magnetisation, the myocardial signal decreased continuously as the T_2 -preparation duration increased, with a maximum reduction of 48 %. After an initial increase at $\tau_{T_2p}=30$ ms, the blood signal continuously decreased with increasing τ_{T_2p} beyond this point, reaching a maximum reduction of 80 %. It is to be noted that the range of sampled τ_{T_2p} values was shorter in phantom than in simulation ex-

periments, resulting in the corresponding data points being positioned before the simulated peak SNR gain, illustrated in Figure 4.3.

Figure 4.4 shows the perfusion and corresponding noise values obtained from the synthetic phantom dataset for a range of T_2 -preparation durations τ_{T_2p} . Without correction for decay during the preparation, MBF values increased with longer T_2 -preparations and plateaued for values of τ_{T_2p} above approximately 150 ms. For all levels of modelled PN, the simulated noise decreased continuously with the τ_{T_2p} and levelled off at τ_{T_2p} above 150 ms. Moreover, the overall noise increased with higher heart rate variability that models higher levels of PN. In comparison to conventional FAIR-myocardial ASL, the SNR gain grew with longer τ_{T_2p} across all simulated heart rate variabilities. At T_2 -preparations of 200 ms, the SNR gain decreased sharply for $\sigma_{RR} = 25$ ms, whereas it slightly levelled off for higher σ_{RR} .

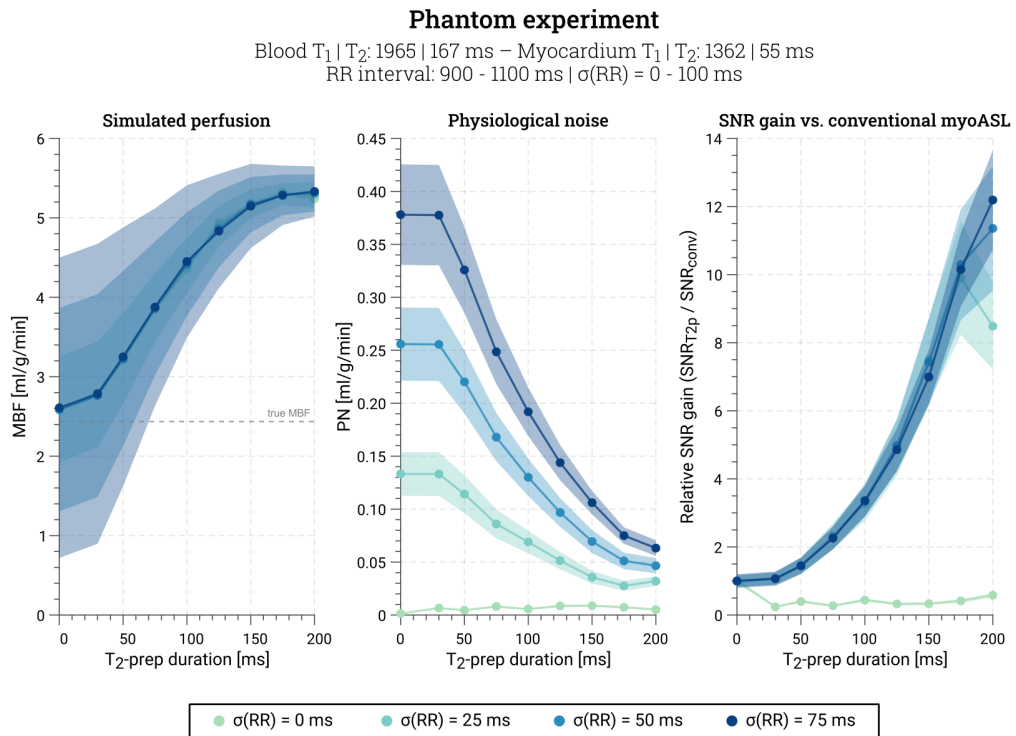


Figure 4.4: (a) Myocardial blood flow (MBF), (b) physiological noise (PN), and (c) relative SNR gain obtained from phantom experiments. Data is shown as a function of the T_2 -preparation time (τ_{T_2p}) for a range of simulated heart rate variation levels. The PN was calculated as the standard deviation across control-tag pairs randomly combined from acquisitions at different heart rates. MBF values were not corrected for decay during τ_{T_2p} and increased with increasing preparation durations. However, lower PN and higher SNR were achieved for T_2 -prepared compared to conventional myoASL-readouts.

4.3.3 *In vivo* experiments

The T_1 and T_2 values averaged across the left-ventricular blood pool ROI were 1819 ± 32 ms and 109 ± 10 ms, respectively. For myocardial tissue, mean T_1 time was estimated as 1189 ± 39 ms, and mean T_2 time was 37 ± 3 ms. The average

perfusion and associated PN maps are presented in Figure 4.5 for all three acquired FAIR-myocardial ASL (myoASL) sequences. The MBF maps appeared visually homogeneous across the three acquisition strategies, with comparable image quality between conventional and T_2 -prepared sequences. However, PN maps globally exhibited lower values for data acquired with T_2 -preparations compared to those from conventional FAIR-myocardial ASL acquisitions.

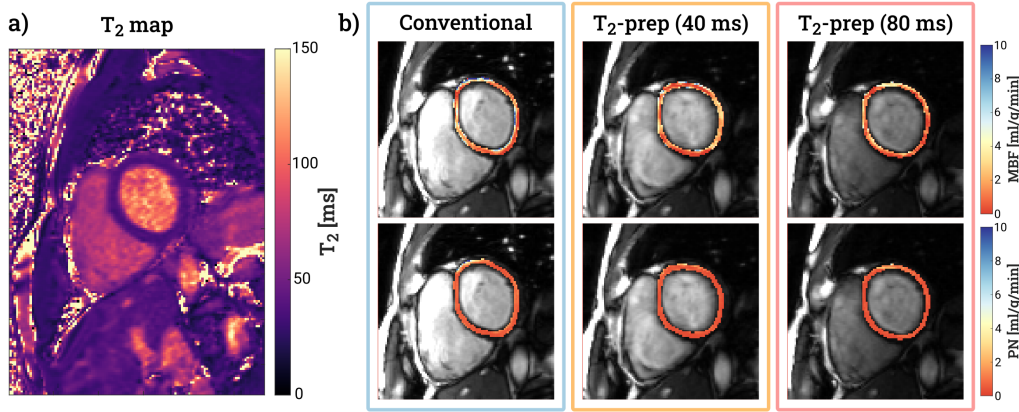


Figure 4.5: (a) In vivo T_2 map in short-axis view. The respective values for the mean $T_2 \pm \text{SD}$ in myocardium and blood were 37 ± 3 ms and 109 ± 10 ms. (b) Average in vivo myoASL-MBF maps: Using T_2 -preparations with $\tau_{T_2p} = 40$ ms/80 ms (orange/red), comparable image quality to conventional FAIR-myocardial ASL (blue) is achieved.

For the three acquired myoASL sequences, the mean global MBF alongside the corresponding PN and CoV are displayed in Figure 4.6. The mean global MBF \pm PN was 2.79 ± 1.01 ml/g/min for the conventional myoASL sequence. When T_2 -prepared readouts were used, mean global MBF \pm PN was 2.02 ± 0.51 ml/g/min for $\tau_{T_2p} = 40$ ms and 1.29 ± 0.38 ml/g/min for $\tau_{T_2p} = 80$ ms. Thus, the PN across the 6 control-tag pairs was reduced on average by 55 % and 67 % using a T_2 -preparation with $\tau_{T_2p} = 40$ ms and 80 ms, respectively. Data obtained from conventional FAIR-myocardial ASL, showed a mean CoV of 36 ± 26 %, which was reduced on average by 26 % / 34 % with T_2 -prepared readouts of $\tau_{T_2p} = 40$ ms/80 ms to 27 ± 14 % / 24 ± 14 %.

4.4 DISCUSSION

In this study, we investigated the use of T_2 -prepared readouts for reducing physiological noise (PN) and enhancing the signal-to-noise-ratio (SNR) in Flow-sensitive Alternating Inversion Recovery (FAIR) myocardial Arterial Spin Labelling (myoASL). Our simulation results indicate that, by suppressing myocardial signal, T_2 -preparations can improve the SNR of FAIR-myocardial ASL-based myocardial blood flow (MBF) measurements compared to using a conventional FAIR-myocardial ASL sequence. The gain in SNR further depends on the T_2 -preparation duration as well as the ratio of physiological to thermal noise. When T_2 -prepared readouts were used in vivo, perfusion values comparable to conventional FAIR-myocardial ASL but with reduced levels of PN were achieved.

In our simulation and phantom studies, we observed that the T_2 -preparations suppress both myocardial and blood contributions to the FAIR-myocardial ASL sig-

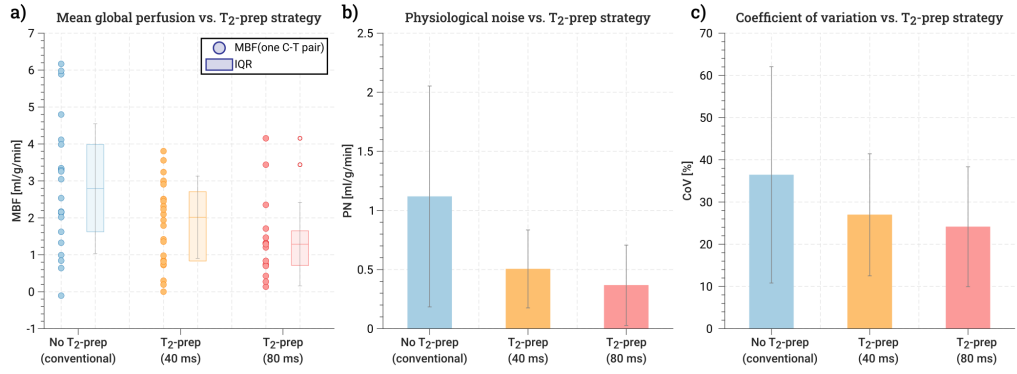


Figure 4.6: (a) In vivo mean global MBF values for all acquired control-tag pairs, (b) average physiological noise (PN), and (c) coefficient of variation (CoV) across the six/four ($\tau_{T2p} = 40\text{ ms} / \tau_{T2p} = 80\text{ ms}$) repetitions of the respective FAIR-myocardial ASL sequence. Compared to conventional FAIR-myocardial ASL, the average PN across the 6 repetitions was reduced by 55 %/67 % and the average CoV by 26 %/34 % when a 40 ms/80 ms long T₂-preparation is used.

nal. Owing to the substantially shorter myocardial T_2 relaxation times [46, 47], however, the myocardial signal is more strongly suppressed than that of blood. Therefore, a T₂-preparation duration can be chosen which enhances the contrast between blood and myocardium when control and tag signal are subtracted for MBF calculation using Buxton’s General Kinetic Model (GKM) [108].

In this context, background suppression methods, similar to those applied in neurovascular ASL [186], have been investigated to alleviate PN in FAIR-myocardial ASL [184, 185]. These techniques typically involve the application of a saturation pulse immediately after FAIR-labelling, succeeded by one or more non-selective inversion pulses after a designated TI . By carefully timing the additional inversions, background signal from static myocardial tissue with specific T_1 values can be nulled at the point of image readout [184, 185]. Similar to the proposed T₂-prepared readouts, they attenuate a wide range of noise contributions. However, potential mistiming of the additional inversion pulses may compromise the PN reduction in the presence of a variable heart rate [185].

Primarily, as suggested by our simulation and phantom experiments, T₂-prepared readouts can mitigate myocardial signal fluctuations induced by variable inversion times (TI) between control and tag images. Given that PN is predominantly influenced by myocardial signal, such myocardial background suppression can lead to an overall reduction of noise in FAIR-myocardial ASL. This is particularly beneficial for double ECG-gated FAIR-myocardial ASL, where the TI is heart-rate dependent and represents a major source of PN.

However, the utility of T₂-preparations in FAIR-myocardial ASL extends beyond TI -related noise. They target any residual myocardial or blood signal in the perfusion-weighted image, for example as a result of uncorrected in-plane or through-plane motion. This renders the proposed approach also appealing for single ECG-gated FAIR-myocardial ASL, where TI is constant but PN still poses a major limitation and a reduction could elicit an improvement in SNR [40]. Furthermore, T₂-prepared readouts can be applied to various labelling schemes in myocardial ASL other than FAIR. This includes Look-Locker-FAIR acquisitions [134, 137] as well as steady-pulsed myocardial ASL [121] where blood is labelled at the aor-

tic root. Both methods rely on MBF quantification based on apparent T_1 times (see Section 2.4.3.4) and, thus, would require incorporating an exponential T_2 -weighting factor in the signal model.

Further, our simulation and phantom experiments suggest that the preparation duration as well as the ratio of thermal to physiological noise determine the SNR gain achievable with T_2 -preparations. Longer T_2 -preparations correlate with stronger suppression of myocardial and blood signals, reduced PN, and, ultimately, elevated SNR. However, our simulations also indicate that overly extended preparation times limit the SNR gain compared to conventional myoASL, as the PN is suppressed below the level of constant thermal noise. In our phantom experiments, this drop in SNR gain was not observed, likely because the sampled preparation durations were shorter, and, thus, data points were collected before reaching the SNR peak. Additionally, higher ratios of physiological to thermal noise require longer T_2 -preparations to attain peak SNR gains, but also result in increased magnitude of the peak SNR gain. This underscores the fact that T_2 -preparations influence PN exclusively, without affecting the thermal background noise.

Finally, the differential effect of T_2 -prepared readouts on blood and myocardial tissue may also introduce residual bias in the estimated MBF values, depending on the ratio of myocardial and blood T_2 time as well as the T_2 -preparation duration. Because the T_2 time can generally be considered stable over the time scales of a FAIR-myASL acquisition, this effect remains uniform across individual perfusion maps. Yet, MBF values from disparate acquisitions, potentially employing different T_2 -preparation times, may lack comparability. Therefore, T_2 -preparations might impart bias and compromise reproducibility of FAIR-myASL if not accounted for. Similar to the readout effects discussed in the previous chapter [41], however, these discrepancies can be mitigated by modelling the T_2 -dependence of the estimated MBF. Implementing a correction factor for T_2 -preparations, such as the one applied in this work, can alleviate the bias in perfusion estimates. Nonetheless, the variability of T_2 times between and within individuals introduces a dependence on the accuracy of myocardial and, in particular, blood T_2 time, which can vary in myocardial pathologies [9, 194] as well as with iron or hydration levels among others [195]. The efficacy of the specific correction factor used in this work is further undermined due to the fact that the (non-linear) influence of the bSSFP-readout is omitted, which might be improved with linear readout strategies.

In vivo, perfusion values obtained with the conventional FAIR-myASL sequence (2.79 ± 1.01 ml/g/min) were slightly elevated compared to previously reported PET-based MBF values (0.74-2.43 ml/g/min)[114], and those obtained from first-pass perfusion CMR (0.62-1.24 ml/g/min)[98, 175]. MBF values derived from T_2 -prepared FAIR-myASL acquisitions (2.02 ± 0.51 ml/g/min for $\tau_{T_2p}=40$ ms and 1.29 ± 0.38 ml/g/min for $\tau_{T_2p}=80$ ms) aligned more closely with those reported in PET-based literature [114]. While the perfusion values for $\tau_{T_2p}=40$ ms remained slightly higher compared to those based on first-pass perfusion CMR, MBF values for $\tau_{T_2p}=80$ ms were found to be more congruent. In comparison with perfusion values reported in other myoASL studies, however, the MBF obtained from all three acquired sequences in our study were in agreement with the reported range (0.7-2.7 l/g/min) [36, 37, 40, 130].

In our in vivo study, we compared two T_2 -prepared FAIR-myocardial ASL sequences with T_2 -preparation durations of 40 ms and 80 ms, respectively. While both sequences demonstrated a reduction in PN above 50 % relative to the conventional FAIR-myocardial ASL sequence, a more pronounced decrease was observed for $\tau_{T_2p}=80$ ms (67 %) compared to 40 ms (55 %). These findings are in agreement with our simulation results, which indicated an optimal SNR gain at preparation durations around 100 ms for physiological to thermal noise ratios of approximately 3.0, as previously reported for in vivo FAIR-myocardial ASL [40]. In the context of myocardial ischaemia diagnosis, an inadequate perfusion increase under stress conditions signals underlying perfusion anomalies as elaborated on in Section 2.4.1. Stress MBF thresholds identified in first-pass perfusion CMR range from 0.91 to 1.86 ml/g/min [176, 177], whereas stress MBF in healthy individuals was reported between 1.97 and 4.5 ml/g/min [175], reflecting an effect size of roughly 55 %. The average CoV of 36 % in conventional acquisitions was reduced to 27 %/24 % when using T_2 -preparations ($\tau_{T_2p}=40$ ms/80 ms), which highlights the potential of the proposed approach to facilitate an improved detection of pathological perfusion changes with FAIR-myocardial ASL.

The chosen T_2 -preparation is a pulse module specifically optimised for robust performance in the presence of high B_0 and B_1 inhomogeneities encountered in cardiac imaging at high field strengths [187]. Thereby, high resilience to field inhomogeneities and cardiac motion is achieved via multiple adiabatic refocusing pulses. However, these impose high specific absorption rates (SAR) [196] and may pose a limiting factor for T_2 -prepared FAIR-myocardial ASL at high field strengths, particularly in combination with the high flip angles required for bSSFP. Besides, T_2 -preparations preceding the image readout prolong the acquisition time. Especially in the presence of high heart rates, i.e. short RR intervals, the T_2 -preparation module combined with snapshot readout might exceed the window of the quiescent diastolic phase. This is particularly accentuated for extended preparation durations in the range of 100 ms to 150 ms, which were identified in our simulations as most effective for suppressing myocardial signal fluctuations at the expected levels of physiological noise [40].

This study has several limitations. To calculate the MBF from Buxton's GKM, individual $T_{1,B}$ values obtained with MOLLI T_1 -mapping were used in this work. Due to the tendency of MOLLI to underestimate T_1 values [152, 182], this approach might give rise to inaccurate $T_{1,B}$ in the quantification model and potentially lead to overestimation of the MBF values, as discussed in the previous chapter. While saturation-based T_1 -mapping techniques such as SASHA [183] might offer a remedy, the widespread availability of MOLLI on clinical MR systems renders it a more accessible option. Furthermore, as a proof-of-concept study, our in vivo experiments allowed only a limited evaluation of the effect of T_2 -prepared readouts on the reproducibility of FAIR-myocardial ASL. A larger study cohort could allow the assessment of its influence on both between-measurement, intra-subject variability as well as inter-subject variability.

In this study, T_2 -prepared readouts have proven effective in mitigating PN and improving SNR in FAIR-myocardial ASL. However, their impact on the bias in estimated MBF values represents a significant limitation to this technique. This issue highlights the need for alternative strategies, which maintain sufficiently

accurate MBF values while also addressing the high PN levels in myoASL. To that end, the third chapter of this thesis introduces a novel approach for FAIR-myASL based on double inversion recovery labelling. This method may provide a more balanced solution to reduce PN in FAIR-myASL without introducing additional biases on the derived perfusion values, as will be described in the following chapter.

DOUBLE INVERSION RECOVERY IN MYOCARDIAL ASL FOR REDUCED PHYSIOLOGICAL NOISE

The results in this chapter have been partially published at the 2024 Annual Meeting of the International Society for Magnetic Resonance in Medicine (ISMRM) in Singapore (SG) [43], and at the 16th Annual Meeting of the ISMRM Benelux chapter in s’Hertogenbosch (NL).

5.1 INTRODUCTION

Myocardial Arterial Spin Labelling (myoASL) offers a potential alternative for cardiac perfusion mapping without the need for exogenous contrast agents. The current clinical gold standard, first-pass perfusion MRI, relies on gadolinium-based tracers to enhance blood contrast. However, inadvertent gadolinium accumulation in the body [31] and the risk of inducing nephrogenic systemic fibrosis [29] limit the repeatability and applicability of this method [197]. MyoASL is instead based on magnetically labelling the hydrogen nuclei spins within the blood. Two images are acquired in myoASL: a tag image with magnetically labelled blood and a control image without. The difference between the two is known as perfusion-weighted image (PWI) as it is related to the perfusion rate [108, 115]. Flow-sensitive Alternating Inversion Recovery (FAIR) preparations are most commonly used in myoASL due to their overall robustness to motion and independence of the vessel geometry [115, 126]. In FAIR-labelling, magnetisation inversion is applied in a first heartbeat, followed by an imaging readout in the next heartbeat. In an alternating fashion the magnetisation inversion is either performed slice-selectively, producing a control image as non-inverted spins flow into the imaging slice, or non-selectively, producing a tag image as inverted spins flow in. The difference between the alternating images generates the perfusion-weighted contrast [115].

MyoASL was proven to be sensitive to differences between myocardial blood flow (MBF) values obtained at stress and rest [35], as well as between normal and ischaemic myocardial segments [34, 35]. However, despite accumulating evidence suggesting its potential clinical utility, broad adoption of myoASL methods in clinical settings remains limited. This primarily stems from a lack of reproducibility and robustness of myoASL-based perfusion quantification, which is largely due to its inherently low signal-to-noise ratio (SNR): The perfusion-related signal change in myoASL generally ranges between 1 % and 8 % for typical physiological values of MBF between 0.5 ml/g/min and 4.0 ml/g/min [39]. The predominant source of noise in myoASL has been identified as physiological noise (PN) rather than thermal noise [40]. This physiological noise can stem from uncorrected cardiac or respiratory motion and physiological variations in the heart or perfusion rate itself.

Two main ECG-gating strategies are employed in FAIR-myocardial ASL to mitigate the impact of cardiac motion. In so-called single ECG-gating, only the inversion pulse is synchronised with the cardiac rhythm, while the image is acquired after a preset, fixed inversion time (TI) [116]. However, variations in the heart rate (HR) can shift the timing of the image readout within the cardiac cycle, leading to major signal variability and poor myocardial image quality. Alternatively, double ECG-gating can be employed. Here, both the inversion pulse and the subsequent image readout are triggered to the same cardiac phase in order to ensure sufficient overlap of the myocardial region in the control and tag images [40, 115]. In turn, this approach leads to a variable TI as a function of the HR, which poses an additional source of PN. While the signal of static myocardial tissue is assumed to cancel out in the subtraction of control and tag images, differences in TI between these acquisitions result in disparate levels of inversion recovery. This mismatch causes a residual signal after subtraction, which manifests as measurement noise.

To address this issue, background suppression techniques have been proposed for FAIR-myocardial ASL. This can be achieved by preceding the FAIR-labelling with a slice-selective saturation pulse [36, 116], which allows for faster recovery of the myocardial background signal. However, static tissue signal may not fully recover during the TI , particularly for higher HR. Alternatively, one or more non-selective inversion pulses can be added between FAIR-labelling and image readout [184, 185]. The additional pulse(s) are timed such that the myocardial signal is nulled at the time of readout. This, however, renders the approach sensitive to mistiming in the presence of a variable HR. Therefore, both approaches remain prone to PN contributions related to TI variability, which may compromise their effectiveness for double ECG-gated FAIR-myocardial ASL.

In this work, we propose the use of additional inversion pulses immediately after the FAIR-labelling. This approach is similar to so-called double-inversion recovery (DIR) black-blood preparations, which are designed to maximise blood-myocardium contrast in cardiovascular MR (CMR) [48, 198]. A second inversion pulse of opposite phase directly after FAIR-labelling restores the magnetisation within the static myocardial tissue. This facilitates near-complete signal recovery before the imaging readout and effective cancellation of the myocardial signal in the subtraction. We investigate the potential of this approach to reduce PN originating from variable TI and to mitigate the sensitivity of double ECG-gated FAIR-myocardial ASL to HR variations. Simulation and phantom experiments are performed to compare the accuracy and SNR achieved with DIR-preparations to conventional, single FAIR-labelling. Finally, we evaluate the effectiveness of DIR-labelling to reduce PN and improve SNR relative to conventional FAIR-myocardial ASL in healthy subjects.

5.2 METHODS

5.2.1 Theoretical framework

In FAIR-myASL, perfusion values are commonly estimated using Buxton's General Kinetic Model (GKM) [108]. Here, the MBF is directly proportional to the difference of control (I_C) and tag signal (I_T):

$$MBF = \frac{\lambda(I_C - I_T)}{\delta_{inv} I_{BL}} T I e^{\frac{-TI}{T_{1,B}}}, \quad (5.1)$$

with baseline image signal I_{BL} , blood-water partition coefficient $\lambda = 1.0$ ml/g [138, 139], inversion efficiency $\delta_{inv} = 1 - \cos(\alpha_{inv})$, inversion time TI , and blood T_1 relaxation time $T_{1,B}$. As detailed in Section 4.2, the difference between control and tag signal in FAIR-myASL can be derived as:

$$\begin{aligned} \Delta I = I_C - I_T &= V_M A_M (x_{M,C}^- - x_{M,T}^-) + \quad \{\text{I: } \Delta I_M \\ &+ V_B A_B (x_{B,C}^- - x_{B,T}^-) \quad + \quad \{\text{II: } \Delta I_B \\ &+ V_B A_B f_{in} (x_{B,C}^+ - x_{B,C}^-). \quad \{\text{III: } \propto MBF \end{aligned} \quad (5.2)$$

with blood-volume fraction $V_B = 1 - V_M$ and myocardial-volume fraction V_M . The acquisition coefficients A_M and A_B depend on the respective relaxation times in the myocardium and blood as well as the acquisition parameters of the myASL image readout. The initial magnetisation x prior to readout can be given as

$$x^+ = M_{z,eq} \quad (5.3)$$

$$x^- = M_{z,eq} \cdot (1 - (1 - \cos(\alpha_{inv})) e^{\frac{-TI}{T_1}}), \quad (5.4)$$

for native and inversion-prepared signals, respectively.

The respective noise terms ΔI_M and ΔI_B from myocardial and blood contributions depend on the difference in TI between control and tag image ΔTI . Assuming that other sources of discrepancy between control and tag signal are negligible, ΔI_M and ΔI_B are zero only if $\Delta TI = 0$. If $\Delta TI \neq 0$, however, ΔI_M and ΔI_B act as additional error terms in the calculation of perfusion values in the GKM using Equation (5.1). This is particularly relevant in double ECG-gated myoASL, where both labelling and image readout are triggered to occur in the same cardiac phase, rendering the TI heart-rate-dependent. A varying duration of the RR interval between control and tag images thus leads to $\Delta TI \neq 0$ and an incomplete elimination of the background signals ΔI_M and ΔI_B in Equation (5.2).

The influence of changes in the HR can be mitigated by applying a second inversion pulse immediately after the FAIR-labelling, referred to as Double Inversion Recovery (DIR) labelling. As depicted in Figure 5.1, the reinversion ensures near-complete recovery of the stationary myocardial tissue during TI . Thus, even in the presence of TI changes, the myocardial signal effectively cancels out in the subtraction of control and tag image.

The reinversion pulses can be either slice-selective or non-selective, but need to be consistent across control and tag acquisitions to preserve the perfusion-induced contrast. Throughout the remainder of this work, FAIR combined with slice-selective reinversion will be referred to as "selective DIR" and, respectively, as "non-selective DIR" with non-selective reinversion. When slice-selective reinversion pulses are applied, the magnetisation of both static tissue and blood within the imaging volume is inverted twice. Hence, the initial magnetisation prior to readout with slice-selective DIR-preparations becomes:

$$x'^+ = M_{z,eq} \cdot (1 - 2(1 - \cos(\alpha_{inv}))^2) e^{-\frac{TI}{T_1}}, \quad (5.5)$$

The signal of in-flowing blood, however, is not affected by the additional slice-selective pulse. Based on this, the signal difference between control and tag image can be given as:

$$\begin{aligned} \Delta I_{SS} = I_C^{SS} - I_T^{SS} = & V_M A_M (x'_{M,C}{}^+ - x'_{M,T}{}^+) + \quad \{\text{I:} = \Delta I'_M \\ & + V_B A_B (x'_{B,C}{}^+ - x'_{B,T}{}^+) \quad + \quad \{\text{II:} = \Delta I'_B \\ & + V_B A_B f_{in} (x'_{B,C}{}^+ - x_{B,C}^-). \quad \{\text{III:} \propto MBF \end{aligned} \quad (5.6)$$

If, instead, non-selective reinversion pulses are used, spins within the imaging volume undergo double inversion, resulting in the same magnetisation prior to readout as seen with slice-selective reinversion pulses (Equation (5.5)). However, non-selective reinversion pulses also affect blood spins outside the imaging volume. A selective FAIR-preparation combined with a non-selective reinversion causes inverted blood spins to flow into the imaging slice. With non-selective FAIR-preparation, the non-selective reinversion leads to in-flowing blood spins being inverted twice. Thus, compared to a conventional FAIR-preparation, non-selective DIR-labelling leads to a swapping of control and tag images: The control setting is defined as non-selective FAIR-labelling combined with non-selective reinversion. The tag setting then corresponds to the case of selective FAIR-labelling followed by non-selective reinversion. With these considerations in mind, the difference between control and tag image for non-selective DIR yields:

$$\begin{aligned} \Delta I_{NS} = I_C^{NS} - I_T^{NS} = & V_M A_M (x'_{M,C}{}^+ - x'_{M,T}{}^+) + \quad \{\text{I:} = \Delta I'_M \\ & + V_B A_B (x'_{B,C}{}^+ - x'_{B,T}{}^+) \quad + \quad \{\text{II:} = \Delta I'_B \\ & + V_B A_B f_{in} (x'_{B,C}{}^+ - x_{B,C}^-). \quad \{\text{III:} \propto MBF \end{aligned} \quad (5.7)$$

While the noise terms $\Delta I'_M$ and $\Delta I'_B$ remain the same as for selective reinversion pulses (Equation (5.6)), the perfusion-weighted signal is modified with non-selective DIR-labelling. Instead of the native blood signal x_B^+ , the perfusion-weighted signal now contains the twice inverted blood signal $x_B'^+$. In consequence, an additional dependence on the inversion and reinversion efficiency is introduced to the estimated perfusion values.

5.2.2 FAIR-myocardial ASL sequence and post-processing

In this study, a double ECG-gated FAIR-myocardial ASL sequence with bSSFP readout, based on our previously published design [41] described in Chapter 3, was used as reference for all experiments. Alongside the reference method, two FAIR-myocardial ASL sequences with DIR-preparations were implemented. Here, the FAIR-labelling pulses were immediately followed by either a slice-selective or non-selective inversion pulse with inverted pulse phase [48, 198], as illustrated in Figure 5.1. All imaging was performed at 3 T (Magnetom Skyra, Siemens Healthineers, Erlangen, Germany). FAIR-labelling as well as selective and non-selective reinversion were achieved using hyperbolic secant pulses. A complete list of sequence parameters is provided in Table 5.1. The post-processing of imaging including the quantification of myocardial ASL-MBF based on Buxton’s GKM as described above [108] was performed in MATLAB (MathWorks, Natick, MA, USA). Individual blood T_1 relaxation times were measured and used in the quantification to mitigate the HR dependence of MBF values as discussed in Chapter 3 [41].

| Experiment | FA (°) | TE/TR (ms) | Matrix size | FOV (mm ²) | Voxel size (mm ³) |
|------------|--------|------------|-------------|------------------------|-------------------------------|
| Phantom | 70 | 1.68/3.36 | 176 × 176 | 300 × 300 | 1.7 × 1.7 × 8.0 |
| In vivo | 70 | 1.63/3.26 | 170 × 208 | 341 × 291 | 1.9 × 1.9 × 8.0 |

Abbreviations: FA, flip angle; FOV, field of view; TE, echo time; TR repetition time

Table 5.1: Sequence parameters of the FAIR-myocardial ASL sequence for phantom and in vivo measurements were identical for conventional and DIR FAIR-labelling. All imaging was performed with Partial Fourier (6/8) and Generalized Auto-Calibrating Partially Parallel Acquisition (GRAPPA) rate of 2.

5.2.3 Simulation experiments

To assess the effect of the selective or non-selective reinversion pulses on the SNR in FAIR-myocardial ASL, Bloch-equation-based numerical simulations were performed using MATLAB. Following the design described in Chapter 3, perfusion values were estimated from simulated myocardial ASL-signal under three different labelling conditions: conventional FAIR as well as selective and non-selective DIR, as described above. Unless otherwise specified, general simulation parameters were as follows: FA 60°, TE/TR 1.55 ms/3.1 ms, and a control-tag delay of 6 s. Imaging readout was simulated based on a single RF pulse and without ramp-up pulses, to eliminate its potential influence on the perfusion values [41]. A blood-volume fraction V_B of 0.14 [164] and a blood replacement/in-flow rate of 0.29 1/s were simulated, resulting in an effective MBF input value of 2.4 ml/g/min. Other physiological parameters were simulated as: HR 60 bpm, blood T_1/T_2 relaxation times at 3 T of 2000 ms/250 ms, and myocardial T_1/T_2 relaxation times of 1400 ms/45 ms [151, 152], if not indicated otherwise.

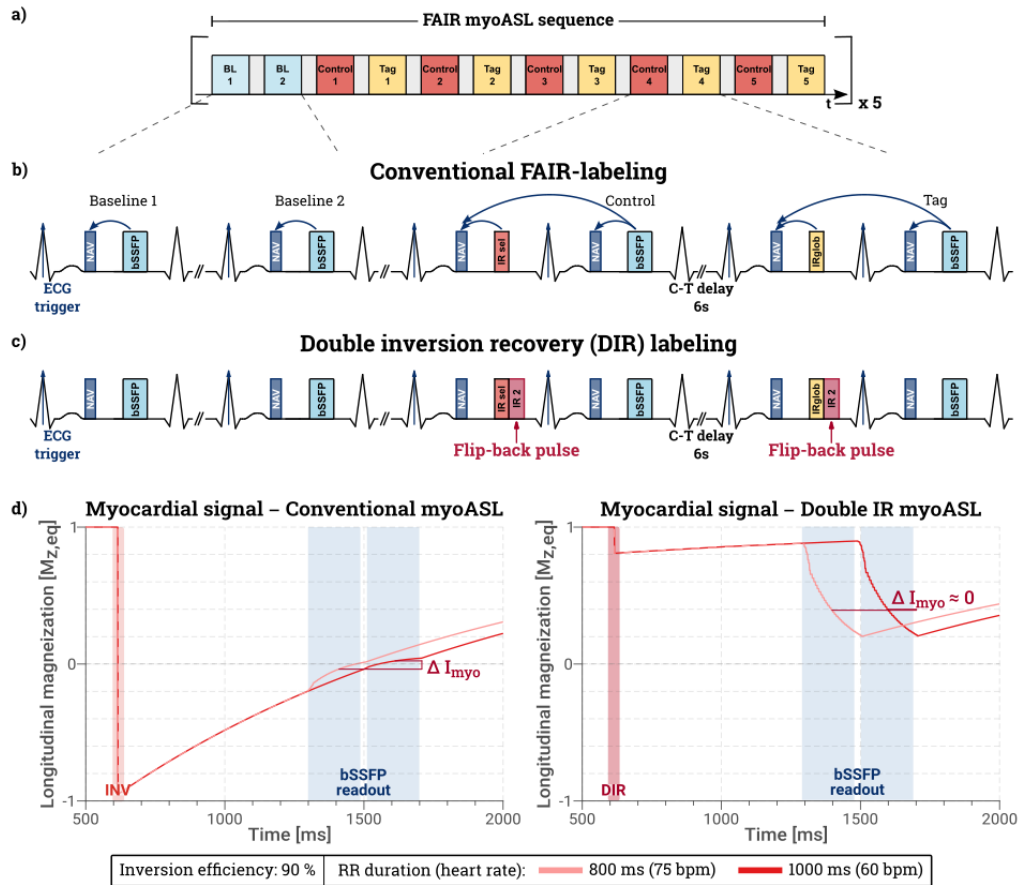


Figure 5.1: (a) Diagram of the double ECG-gated, respiratory-navigated FAIR myocardial ASL sequence. After a selective/global inversion pulse, control/tag images are acquired during mid-diastole, with a 6s delay between images. (b) Images are acquired only if both the current and preceding navigator are accepted. (c) For Double Inversion Recovery (DIR) preparations, a reinversion pulse is added right after the FAIR-labelling pulses. (d) For heart rate variations, residual myocardial signal is substantially reduced with DIR (right) compared to single inversion (left).

To assess the PN caused by variations in TI , the myoASL signal was simulated for six control-tag pairs with randomly varying RR interval durations for all three labelling strategies. Zero-mean Gaussian noise was added to the simulated RR interval duration with a standard deviation σ_{RR} ranging from 0 ms to 250 ms (CoV: 0 % - 25 %), in line with HR variabilities observed in vivo [188–190]. Additional thermal noise was modelled as constant zero-mean Gaussian noise. The standard deviation of the thermal noise was chosen such that the ratio of physiological to thermal noise, as defined in Equation (4.19), ranged between 0 and 6 across the range of simulated RR variability [40]. All simulations were repeated $n = 1000$ times per setting to determine an average $SNR \pm \sigma_{SNR}$ as a function of HR variability. Four data sets were generated in total, with different inversion efficiencies (δ_{inv}) between 85 % and 100 %. The correlation of the PN with the HR variability (σ_{RR}) was evaluated using Spearman’s correlation. Slope and intercept values were obtained from a linear regression of simulated PN values and are reported with a 95 % confidence interval.

5.2.4 Phantom experiments

Phantom experiments were conducted to further evaluate the influence of DIR-labelling on the MBF values and PN of FAIR-myASL. The phantom comprised 20 NiCl₂-doped agarose vials submerged in agarose gel, with T_1 relaxation times between 300 and 2500 ms and T_2 relaxation times between 40 and 170 ms. The two vials with T_1/T_2 relaxation times closest to that of myocardial tissue (1370 ms/60 ms) [51] and blood (2090 ms/160 ms)[47, 152], respectively, were selected for further processing. Each of the three FAIR-myASL sequences (conventional, selective DIR, and non-selective DIR-labelling) acquired three control-tag image pairs and one pair of baseline images. The phantom acquisitions were repeated for a range of simulated RR interval durations, spanning 600 ms to 1200 ms in increments of 50 ms.

To mimic the HR variability between in vivo cardiac acquisitions, a new data set was synthesised from the acquired phantom data. To that end, a series of random RR interval durations was generated for 25 control-tag pairs to match the five sequence repetitions in vivo. The specific RR interval durations were simulated based on a zero-mean Gaussian distribution between 600 and 1200 ms. For a predefined range of standard deviations ($\sigma_{RR} = 0-100$ ms), the simulated RR durations were then matched to the ones acquired in the experiment, and phantom images were drawn accordingly. A different control or tag image was chosen randomly from the available set for each RR interval to incorporate thermal noise. This procedure was repeated 100 times for each acquired FAIR-myASL sequence, resulting in a dataset containing 25 control-tag image pairs and a corresponding baseline image for every labelling strategy, level of HR variability σ_{RR} , and repetition. Subsequently, the MBF was simulated based on our previous framework [41], as described in Section 3.3.3.1 of this thesis. Similar to the numerical simulations, the correlation between the obtained PN and the HR variability (σ_{RR}) was evaluated using Spearman’s correlation. Slope and intercept values were obtained from a linear regression of phantom PN values and are reported with a 95 % confidence interval.

5.2.5 *In vivo experiments*

Two healthy volunteers (1 male, 1 female, 30.5 ± 3.5 years) without history or current symptoms of cardiovascular disease were included in this study. The present study was approved by the local institutional review board, and written informed consent was obtained from all participants prior to examination. In vivo myoASL imaging was performed at rest in free-breathing acquisitions with a dual-respiratory navigator [193]. Dual respiratory navigation included playing a pencil-beam navigator placed at the liver dome prior to both labelling and image readout. Images were acquired only when both consecutive navigators were within the pre-defined acceptance window. This ensures that FAIR-images are acquired only upon successful inversion and that sufficient overlap between the selective inversion slab and the excitation slice is achieved.

As in the simulation and phantom experiments, three myoASL sequences were acquired in total: conventional myoASL with single FAIR-labelling, and two DIR-prepared myoASL sequences, using slice-selective and non-selective reinversion pulses, respectively. Each of the three sequences comprised five control-tag pairs and two baseline images. All scans were repeated five times in randomised order to assess repeatability. Additionally, a Modified Look-Locker Inversion recovery (MOLLI) [136] T_1 -mapping sequence was acquired to determine individual blood T_1 relaxation times for MBF calculation [41]. Manual segmentation of left-ventricular myocardium and blood pool ROIs was performed prior to evaluating MBF using Buxton's GKM [108]. The corresponding PN values were calculated in a pixel- and segment-wise manner using the definition given in Equation (3.9). Finally, the relative SNR gain compared to conventional FAIR-myASL was determined for both DIR-strategies as:

$$\Delta SNR = \frac{SNR_{DIR}}{SNR_{conv}} = \frac{\mu_{MBF_{DIR}}}{\sigma_{MBF_{DIR}}} \cdot \left(\frac{\mu_{MBF_{conv}}}{\sigma_{MBF_{conv}}} \right)^{-1} \quad (5.8)$$

with mean μ_{MBF} and standard deviation σ_{MBF} of the MBF obtained across the five control-tag pairs acquired in each repetition.

5.3 RESULTS

5.3.1 *Simulation experiments*

Figure 5.2 depicts the MBF values obtained from simulations with conventional FAIR and DIR-myASL. Across the range of simulated HR variability σ_{RR} and inversion efficiency, the simulated MBF values remained largely constant at 2.4 ml/g/min for FAIR ($0.04 < R^2 < 0.06$, $-0.03 [-0.11, 0.06] < \text{slope [CI]} < 0.03 [-0.05, 0.11]$, $p < 0.001$) and selective DIR-preparations ($0.07 < R^2 < 0.71$, $-0.03 [-0.04, 0.03] < \text{slope [CI]} < -0.01 [-0.03, 0.04]$, $p < 0.001$). Non-selective DIR-labelling resulted in slightly lower perfusion values, around 1.9 ml/g/min ($R^2 = 0.11$, CI: [1.82, 1.91], $p < 0.001$) at 85 % inversion efficiency, but remained almost constant across the all simulated HR variabilities ($0.11 < R^2 < 0.49$, $-0.03 [-0.04, -0.02] < \text{slope [CI]} < 0.02 [-0.05, 0.01]$, $0.001 < p < 0.20$). The differences in MBF between

non-selective and selective DIR-labelling were reduced with improved inversion efficiency and there was no difference for perfect inversion.

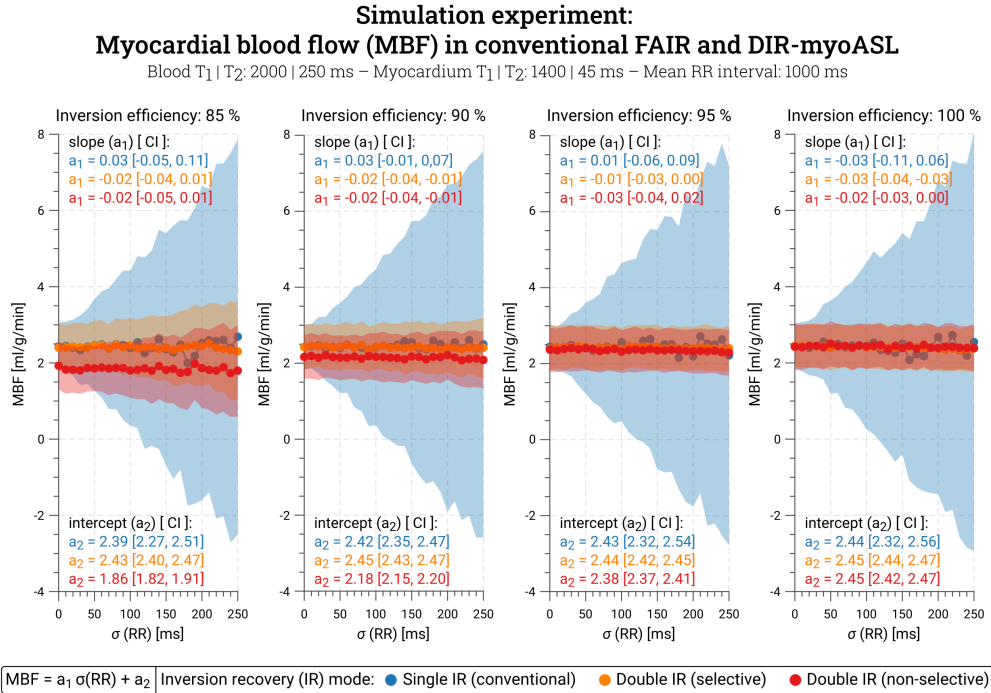


Figure 5.2: Simulated myocardial blood flow (MBF) obtained with double inversion recovery (DIR; orange, red) and a conventional FAIR-myASL sequence (blue). The MBF is shown as a function of the simulated heart rate variability σ_{RR} . The linear regression slope (a_1 , in units of $\frac{1}{100 \text{ ms}}$) and intercept (a_2) are reported with the corresponding 95 % confidence interval (CI). The MBF is largely constant over the range of simulated σ_{RR} (slope: -0.03-0.03 across all sequences), showing larger fluctuations for conventional compared to DIR labelling. Non-selective reinversion pulses lead to decreasing perfusion values for lower inversion efficiencies (intercept: 1.86-2.45).

Figure 5.3 shows the PN, determined as the standard deviation of simulated perfusion values, as a function of simulated HR variability σ_{RR} . The slope as obtained from linear regression analysis is given in units of $\frac{1}{100 \text{ ms}}$. For conventional FAIR-myASL, PN increased with increasing σ_{RR} across all levels of inversion efficiency ($R^2=1$, 4.43 [4.29, 4.56] < slope [CI] < 4.48 [4.35, 4.62], $p < 0.001$). However, for selective and non-selective DIR-labelling, the correlation of PN with HR variability progressively decreased as inversion efficiency increased. At 85 % inversion efficiency, the regression slope was 0.63 ($R^2=1.0$, CI: [0.57, 0.67], $p < 0.001$) with selective and 0.62 ($R^2=0.99$, CI: [0.56, 0.67], $p < 0.001$) with non-selective reinversion pulses. While at 100 % inversion efficiency, PN remained largely constant both with selective ($R^2=0.03$, slope: 0.01 , CI: [0.00, 0.03], $p=0.07$) and non-selective reinversion pulses ($R^2=0.34$, slope: 0.03 , CI: [0.01, 0.04], $p < 0.001$). Overall, PN values were nearly identical when comparing selective and non-selective DIR-preparations.

The simulated gain in SNR relative to conventional FAIR-ASL is illustrated as a function of HR variability (σ_{RR}) in Figure 5.4. With increasing HR variability, the SNR gain achieved with selective and non-selective DIR-labelling continuously increased across all levels of inversion efficiency. At the lowest

simulated inversion efficiency (85 %), however, the SNR gain plateaued around 3.78 with selective and at around 2.95 with non-selective DIR-labelling when the HR variability surpassed approximately 150 ms. In general, greater inversion efficiencies led to higher SNR gains for both selective and non-selective DIR-labelling compared to conventional FAIR-myocardial ASL. The linear regression slope in units of $\frac{1}{100 \text{ ms}}$ increased for selective DIR-labelling from 1.24 ($R^2=0.83$, CI: [1.00, 1.49], $p<0.001$) at 85 % inversion efficiency to 3.22 ($R^2=0.98$, CI: [2.99, 3.45], $p<0.001$) at 100 % inversion efficiency. The corresponding values for non-selective DIR-labelling were 0.98 ($R^2=0.85$, CI: [0.81, 1.16], $p<0.001$) and 3.19 ($R^2=0.97$, CI: [2.94, 3.44], $p<0.001$) at 85 % and 100 % inversion efficiency, respectively. Relative to single FAIR-labelling, the SNR increased up to 9.5 and 9.3 times with selective and non-selective DIR-labelling, respectively, across all simulated inversion efficiencies and levels of HR variability.

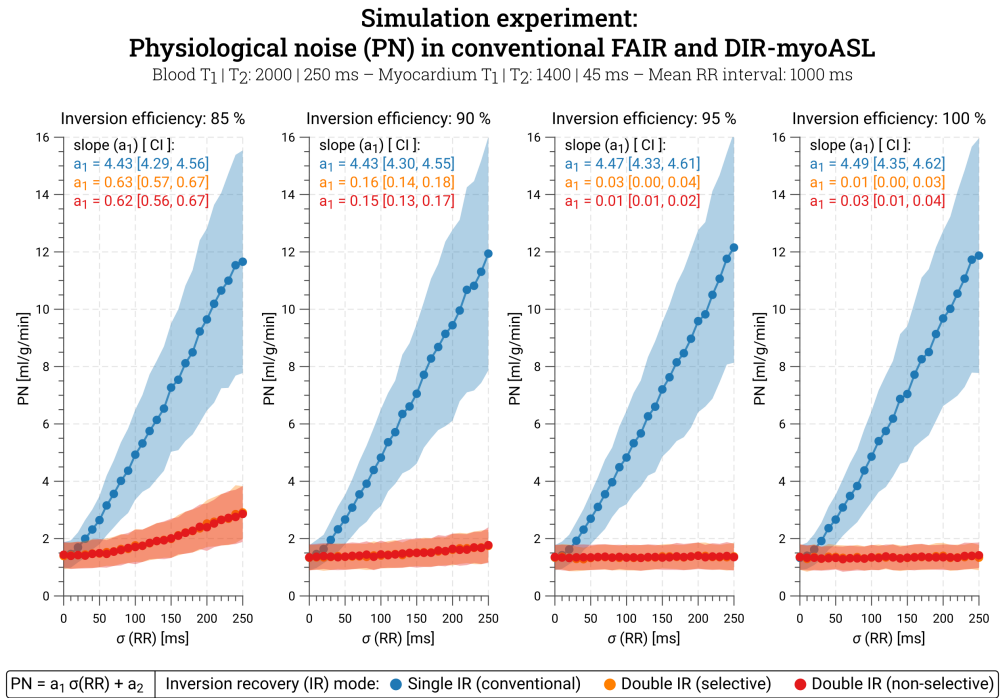


Figure 5.3: Physiological noise (PN) determined as the standard deviation of simulated perfusion values obtained with double inversion recovery (DIR; orange, red) and a conventional FAIR-myocardial ASL sequence (blue). PN is shown as a function of the simulated heart rate variability σ_{RR} . The linear regression slope (a_1) is reported with the corresponding 95 % confidence interval (CI) in units of $\frac{1}{100 \text{ ms}}$. With DIR-labelling the PN increases slightly with increasing σ_{RR} ($0.03 < R^2 < 0.99$, slope: 0.01-0.63 for both DIR-inversions) at low inversion efficiencies, whereas for conventional myoASL PN shows a much stronger increase with σ_{RR} ($R^2=1.0$, slope: 4.43-4.49).

5.3.2 Phantom experiments

In phantom experiments the average MBF values remained largely constant at around 3.3 ml/g/min ($0.45 < R^2 < 0.88$, -0.08 [-0.15, -0.02] < slope [CI] < 0.02 [0.01, 0.02], $p < 0.05$) over the range of simulated HR variability for all three myoASL sequences, as illustrated in Figure 5.5. However, the PN progressively

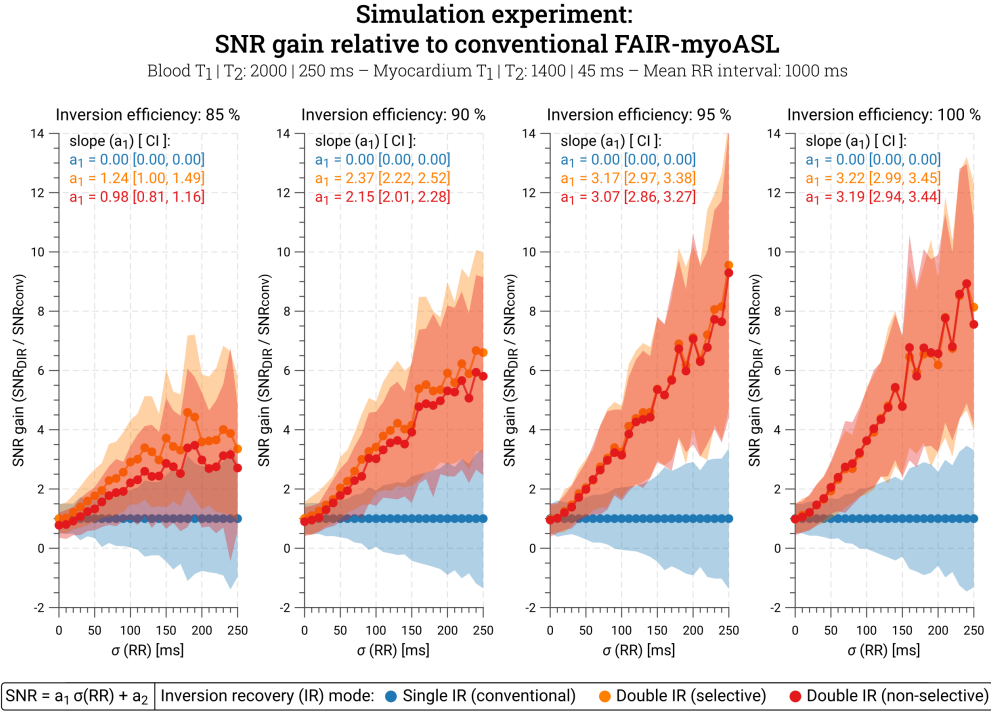


Figure 5.4: Relative SNR gain with double inversion recovery (orange, red) compared to a conventional FAIR-myASL sequence (blue) in simulation experiments. The SNR gain is shown as a function of the simulated heart rate variability that models the physiological noise. The linear regression slope (a_1) is reported with the corresponding 95 % confidence interval (CI) in units of $\frac{1}{100 \text{ ms}}$. The SNR gain increases with increasing simulated ratio of physiological and thermal noise as well as with higher inversion efficiency ($0.83 < R^2 < 0.98 / 0.85 < R^2 < 0.97$, slope: 1.24-3.22/0.98-3.19 for selective/non-selective DIR).

increased with higher HR variability: For conventional FAIR-preparations, the PN reached up to 1.7 ml/g/min ($R^2=1.0$, slope: 0.67, CI: [0.63, 0.71], $p < 0.001$), while the maximum PN for both selective and non-selective DIR-labelling was 0.15 ml/g/min ($R^2=1.0$, slope: 0.06, CI: [0.05, 0.06], $p < 0.001$). In comparison to single FAIR-labelling, the relative SNR gain with DIR-preparations slightly increased from 10.2 to 12.0 both with selective ($R^2=0.15$, slope: 0.04, CI: [-0.57, 0.65], $p=0.88$) and non-selective reinversions ($R^2=0.68$, slope: 0.61, CI: [0.27, 0.94], $p < 0.001$). With non-selective DIR-labelling, the relative SNR gain was on average 5 % lower compared to selective DIR-labelling, but the difference decreased for higher HR variabilities. Over the entire range of simulated HR variability, the average SNR in DIR-prepared myASL increased by up to 13.4 times when selective and 10.8 times when non-selective reinversion pulses were used.

5.3.3 *In vivo* experiments

Figure 5.6 shows the control, tag, and baseline images obtained *in vivo* alongside the resulting MBF and PN maps for one representative subject. In visual assessment, perfusion maps obtained with DIR-labelling showed improved image quality compared to those obtained with conventional FAIR-myASL. More-

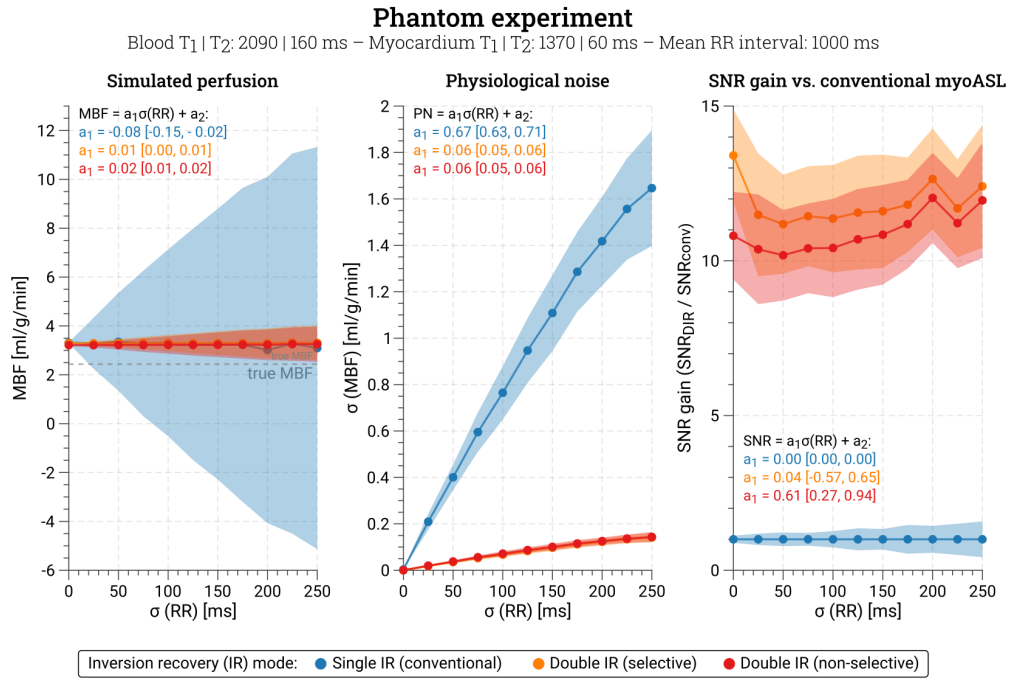


Figure 5.5: (a) Myocardial blood flow (MBF), (b) physiological noise (PN), and (c) relative SNR gain obtained from phantom experiments. Data is shown as a function of the heart rate (HR) variability for conventional (blue), selective (orange), and non-selective (red) double inversion labelling. The linear regression slopes (a_1) are reported with the corresponding 95 % confidence interval (CI) in units of $\frac{1}{100 \text{ ms}}$. PN was induced by combining control and tag images acquired at different HR, and the PN was then calculated as the standard deviation across control-tag pairs. With comparable MBF values, lower PN and higher SNR were achieved for double inversion preparations compared to conventional labelling.

over, PN maps showed overall lower values for DIR-labelling relative to conventional FAIR, particularly in the inferior and inferoseptal regions.

For each acquired myoASL sequence, mean global MBF is shown in Figure 5.7 per acquired control-tag pair in all subjects, together with the average PN and SNR gain relative to conventional FAIR-myocardial ASL. The average blood T_1 relaxation time across all subjects was 1846 ± 13 ms. Averaged over all acquisitions of the conventional FAIR-myocardial ASL sequence, the mean $\text{RR} \pm \sigma_{\text{RR}}$ ranged between 779 ± 57 ms and 1153 ± 38 ms across all subjects. With DIR-labelling, mean $\text{RR} \pm \sigma_{\text{RR}}$ ranged from 783 ± 38 ms to 1151 ± 35 ms for selective reinversion pulses, and from 793 ± 31 ms to 1129 ± 45 ms for non-selective pulses.

Using conventional FAIR-labelling, the in vivo mean global $\text{MBF} \pm \text{PN}$ was 2.47 ± 1.06 ml/g/min averaged across all subjects. With DIR-preparations, mean $\text{MBF} \pm \text{PN}$ was 1.60 ± 0.31 ml/g/min for selective reinversion pulses and 2.07 ± 0.75 ml/g/min for non-selective reinversion pulses. In addition, Figure 5.7 shows the corresponding PN and CoV values averaged across all subjects and the five repetitions of each sequence. The average PN across all subjects was reduced by 66 ± 14 % for selective and 44 ± 27 % for non-selective DIR-preparations, respectively. The average coefficient of variability was 64 % for conventional FAIR-myocardial ASL and 43 %/27 % for selective/non-selective DIR-labelling.

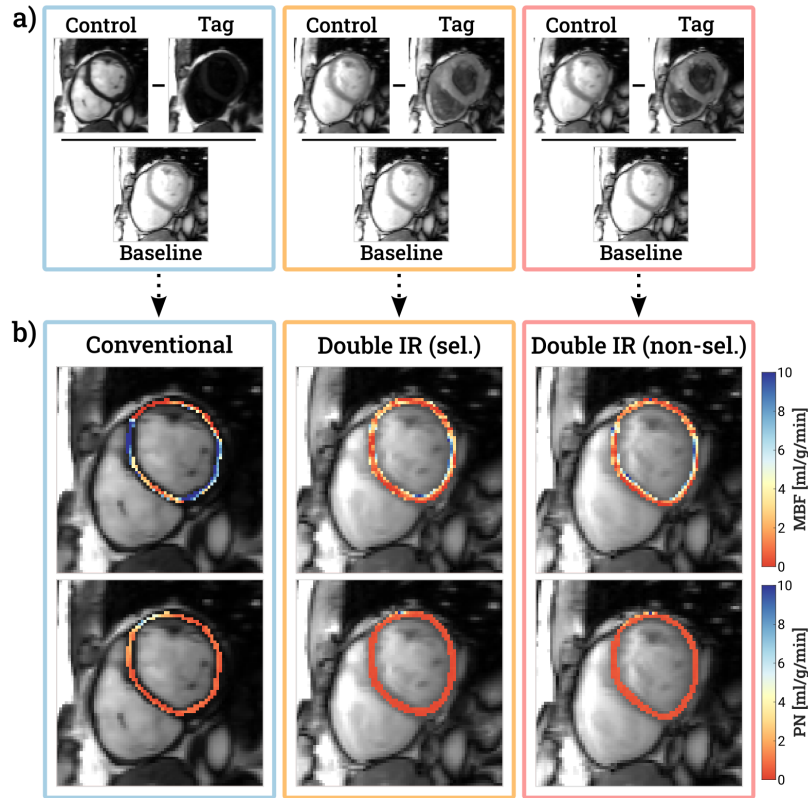


Figure 5.6: (a) Representative control, tag, and baseline images for conventional FAIR-myocardial ASL (blue) as well as double inversion recovery (DIR) labelling with selective (orange) and non-selective (red) reinversion pulses. (b) Resulting in vivo perfusion (top) and physiological noise (PN) maps (bottom). Improved map quality and lower PN levels were achieved with DIR labelling compared to the conventional sequence.

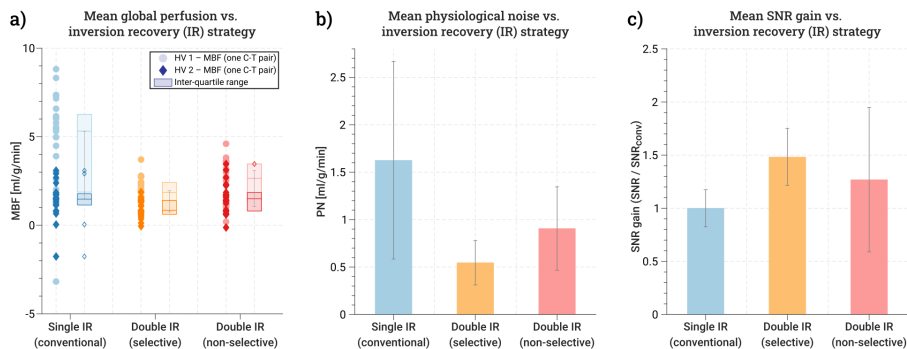


Figure 5.7: (a) In vivo global myocardial ASL-MBF for all acquired control-tag pairs. Values for the two subjects are depicted with lighter and darker shades of the colours corresponding to the three acquired sequences. (b) When double inversion recovery (DIR) preparations were used, the average physiological noise was reduced by 66 % for selective and 42 % for non-selective reinversion pulses compared to conventional myocardial ASL. (c) Relative to conventional myocardial ASL the SNR increased 1.35 ± 0.27 times and 1.27 ± 0.68 with selective and non-selective DIR-preparations, respectively.

5.4 DISCUSSION

In this study, we investigated the use of Double Inversion Recovery (DIR) labelling in double ECG-gated myocardial ASL to reduce physiological noise (PN) re-

lated to heart rate (HR) variations. Reinversion immediately after the FAIR-preparation allows for near-complete signal recovery of static tissue. This facilitates effective cancellation of the background signal in the subtraction and mitigates signal fluctuations stemming from differences in the signal relaxation of control and tag acquisitions. In simulations and phantom, both DIR variations, using either a selective or non-selective reinversion pulse, demonstrated reduced PN and increased SNR compared to conventional FAIR-labelling. In vivo, the proposed DIR-approaches yielded comparable perfusion values to conventional FAIR-myocardial ASL, but with significantly higher reproducibility and lower PN.

In simulation and phantom experiments, the observed myocardial blood flow (MBF) values were largely comparable between single FAIR-labelling and DIR-labelling across the range of simulated HR variability. In phantom, a residual bias in MBF values relative to the input perfusion rate was observed across all sequences due to imaging readout effects [41], as elaborated in Chapter 3. In vivo, mean global MBF for all three labelling strategies was generally in line with perfusion values reported in PET literature (0.74-2.43 ml/g/min) [114]. Compared to reported perfusion values from first-pass perfusion CMR (0.62-1.24 ml/g/min) [98, 175], the MBF values for selective DIR-labelling were in agreement, while those obtained with conventional FAIR and non-selective DIR-labelling were slightly elevated. Further, MBF estimates from all three investigated sequences agreed with perfusion values reported in previous studies using myocardial ASL (0.7-2.7 l/g/min) [36, 37, 40, 130].

In simulation and phantom experiments, DIR-labelling achieved a substantially reduced PN and up to a 11-fold SNR gain compared with conventional FAIR-myocardial ASL. When simulated with perfect inversion efficiency, DIR-preparations fully eliminated the measurement noise originating from variations in the inversion time (TI). Simulations suggest that residual variability is observed with imperfect inversion efficiency in the DIR-preparations. Our phantom and simulation results indicate that PN from TI variation accounts for a substantial fraction of the overall measurement noise. After adjusting for the simulated thermal noise (ca. 0.7 ml/g/min), a simulated RR variability of 50 ms resulted in a net PN of 1.7 ml/g/min, representing approximately 70 % of the total measurement noise. Given that a level of HR variability of around 100 ms can be expected for in vivo imaging [188, 189], variations in TI can likely be considered the largest contributor to PN in double ECG-gated FAIR-myocardial ASL.

The PN levels observed in the in vivo experiments were comparable to the range reported in earlier myocardial ASL-studies [36, 37, 40, 130]. Compared with conventional FAIR-myocardial ASL, the PN was reduced on average by 66 % with selective and 44 % with non-selective DIR-preparations, where the PN relative to mean MBF was on average 19 % for selective and 36 % for non-selective reinversions, respectively. Compared to an anticipated reduction in stress MBF of about 55 % in CAD [175-177], the proposed DIR-method may thus improve detection of perfusion defects with FAIR-myocardial ASL.

With DIR-preparations, the choice between slice-selective and non-selective reinversion pulses affects the estimated MBF and associated PN. In our simulations, the perfusion values were found to be lower with non-selective than with selective reinversion pulses at low inversion efficiencies. With non-selective rein-

version the blood entering the imaging slice is inverted twice. Hence, the control signal in blood is a function of the inversion/reinversion efficiency, as opposed to single FAIR-labelling, where inflowing blood remains unaltered. Consequently, non-selective DIR-preparations introduce an additional noise term to the perfusion-weighted signal compared to their slice-selective counterpart and the conventional FAIR-labelling. Therefore, slice-selective DIR-preparations demonstrate superior SNR performance at low inversion efficiencies. When applied *in vivo*, slice-selective DIR-labelling also led to lower PN levels and slightly higher SNR improvement than non-selective DIR-labelling. However, lower perfusion values were observed with slice-selective than with non-selective reinversions, likely as a result of reduced non-zero-mean contributions to the PN.

In our study, adiabatic hyperbolic secant pulses were used to ensure consistent inversion across the imaging volume due to their resilience against B_0 and B_1 field inhomogeneities [199]. Nonetheless, the effectiveness of these pulses can be compromised by factors such as non-uniform slice profile and $T_{1\rho}$ relaxation during the adiabatic pulse itself [200], resulting in imperfect inversions. While poor inversion efficiency affects conventional FAIR-ASL, its effects are exacerbated in DIR due to the reinversion. Besides, the efficiency of the inversion and reinversion pulse can be further reduced due to magnetisation transfer effects, leading to signal saturation. Thus, careful adjustment of the parameters is warranted to ensure ideal inversion efficiency in myoASL. As our results indicate, this can be an effective measure to minimise the effects of HR variability and further reduce PN.

The proposed DIR-preparations specifically target contributions to PN arising from HR-induced TI variability. Previously proposed background suppression techniques used additional non-selective inversions between FAIR-labelling and image acquisition to null overall myocardial signal at the time of readout [184, 185]. Similarly, our previous strategy using T_2 -prepared readouts effectively suppresses myocardial signal fluctuations relative to the blood signal. In comparison, the proposed DIR-labelling mitigates signal fluctuations related to TI variability more directly. Previous studies have also proposed the addition of pre-saturation pulses immediately before the FAIR labelling [36, 116]. By ensuring a more complete recovery of myocardial background signal during TI , this approach addresses TI variability as a source of similar to the DIR-labelling proposed in this work. However, additional reinversion pulses can achieve full signal recovery faster, even in the presence of imperfect inversion/reinversion efficiency. Our results indicate that successfully suppressing signal fluctuations caused by TI variability greatly reduces PN. Thus, the proposed DIR-labelling technique proved very effective in achieving overall higher SNR. Approaches to mitigate residual signal fluctuations in the perfusion-weighted signal can in principle be combined with overall background suppression. Therefore, a combination of both approaches warrants further investigation.

Another approach to reduce the effect of TI variability on perfusion quantification with Buxton's General Kinetic Model (GKM) [108] is to incorporate separate TI values for the weighting of the control and tag image within the quantification model [44]. This straightforward approach requires only the recording of individual TI values for each acquisition. However, our previous results

(Chapter 3) indicate that this quantification method yields only a marginal reduction in MBF variation relative to employing an averaged T_I within the GKM. Moreover, this T_I correction predominantly accounts for the recovery of blood signal, since Buxton's GKM considers exclusively the T_1 relaxation in blood. The compensation of signal fluctuation in the myocardium remains incomplete due to the difference in T_1 values between myocardium and blood at 3 T [152]. Nonetheless, the proposed T_I correction approach is complimentary to many acquisition-based strategies. Thus, it can also be combined with the proposed DIR-labelling to further reduce the sensitivity of double ECG-gated FAIR-myASL to a varying HR.

This study has several limitations. MOLLI T_1 -mapping [136], from which blood T_1 values were obtained for in vivo MBF quantification, is known to underestimate T_1 values. Alternatively, saturation-based methods, such as saturation recovery single-shot acquisition (SASHA) [183], could offer a solution to this potential confounding factor, albeit its availability on clinically MR systems remains limited compared to MOLLI. Regarding the accuracy of perfusion values, the MBF quantification might further benefit from estimating the effective inversion efficiency attained in the specific experiments. The current study investigated the use of DIR-prepared FAIR-myASL in healthy subjects at rest only. Particularly in view of translation to clinical settings, additional evaluation of the proposed method is required in patients with myocardial pathology, where arrhythmia is a common comorbidity [201, 202]. Moreover, a broader participant cohort would provide a deeper understanding of the robustness of DIR-labelling and allow for improved statistical comparison to conventional FAIR-myASL.

DISCUSSION

In this work, we addressed the challenges of quantifying myocardial perfusion without contrast agents using Arterial Spin Labelling (ASL) MRI. First-pass perfusion imaging, the clinical gold-standard for perfusion assessment with MRI [12, 81], necessitates the use of gadolinium-based contrast agents (GBCAs), which limit its repeatability and applicability due to risk of gadolinium retention [31, 32] and inducing nephrogenic systemic fibrosis [28, 29]. Myocardial ASL (myoASL) relies on magnetically labelled blood as an endogenous contrast agent and promises a safer, repeatable alternative for evaluating myocardial blood flow (MBF) [45, 115]. However, inherently low signal-to-noise ratios persist as a major challenge and are dominated by physiological fluctuations [40, 149]. To combat the effects of physiological noise (PN) in myoASL, three novel approaches were developed in this work: an improved MBF quantification method combining an adapted baseline-acquisition with subject-specific blood T_1 values; T_2 -prepared readouts for myocardial background suppression; and Double Inversion Recovery preparations for reducing PN related to a varying heart rate. These methods will be briefly summarised and discussed in the following sections.

The first part of this thesis investigated how acquisition-related and physiological parameters influence the bias and precision of perfusion values obtained with myoASL. The assessed parameters included the T_1 relaxation time of blood ($T_{1,B}$), heart rate (HR), acquisition matrix size, and the acquisition flip angle (FA). For this purpose, we implemented two Flow-sensitive Alternating Inversion recovery (FAIR) myoASL sequences with balanced Steady-State Free Precession (bSSFP) and spoiled Gradient Echo (spGRE) readouts, respectively. The sequences were assessed in numerical simulations as well as phantom and in vivo experiments. The perfusion quantification was based on Buxton's General Kinetic Model (GKM) [108], which is most widely used in cardiac FAIR-myASL studies [115, 131]. Among the examined physiological parameters, $T_{1,B}$ emerged as the key influencing factor in our simulation and phantom results: The use of inaccurate $T_{1,B}$ values for perfusion calculation in the GKM led to a mild but significant HR dependence of estimated MBF values, which was mitigated if individual $T_{1,B}$ values were used for calculation.

The strongest confounding effect, however, was identified for the acquisition FA. While a 100 ms deviation in $T_{1,B}$ led to a 3 % change in MBF, an average MBF change of 7 % for bSSFP and 9 % for spGRE readouts was accrued for every 10° change in FA. The deviation in MBF was exacerbated for long trains of RF excitation pulses, for example in the case of the widely used snapshot readouts. This dependence is directly related to the perfusion quantification using Buxton's GKM, which does not account for modulations of the magnetisation during the image readout. Therefore, we proposed a saturation-baseline acquisition combined with an adapted perfusion calculation, to alleviate the influence of the acquisition FA. Due to the nature of the magnetisation mo-

dulation function, this correction approach is not applicable to bSSFP readouts. Yet, it fully eliminated the FA dependence in spGRE readouts in numerical simulations, and showed potential for reducing variability of in vivo perfusion estimates.

In the remainder of this thesis, we focused on the primary sources of physiological noise (PN) in myoASL, starting with PN related to variations of the myocardial background signal. A key contributor to these signal fluctuations is the incomplete elimination of static myocardial tissue during subtraction of control and tag signals in Buxton's GKM. To mitigate this, we introduced T_2 -prepared readouts for FAIR-myASL, leveraging the stark difference in transverse relaxation time (T_2) between myocardium and blood to selectively suppress the overall myocardial signal. The use of T_2 -preparations substantially improved the signal-to-noise ratio (SNR) in simulations and phantom experiments, achieving up to a 67 % reduction of in vivo PN relative to conventional FAIR-myASL. However, while T_2 -preparations effectively reduce myocardial background fluctuations irrespective of their origin, they introduce a T_2 -dependent bias to the estimated perfusion values, potentially compromising the accuracy of FAIR-myASL.

In the final part of this thesis, we approached the issue of PN in FAIR-myASL from a different angle by specifically targeting PN caused by variations in the inversion time (TI). Namely, HR-induced TI variability represents a major source of PN in double ECG-gated FAIR-myASL, as identified in our simulations. Thus, we developed Double Inversion Recovery (DIR) labelling for myoASL, similar to black-blood imaging techniques in CMR [48, 198]. A reinversion pulse added immediately after FAIR-labelling allows for almost complete signal recovery during TI , thus alleviating the susceptibility of FAIR-myASL measurements to HR variations. Compared to single FAIR-labelling, our studies have demonstrated an average 11-fold SNR gain with DIR-labelling in simulations, accompanied by a notable PN reduction in vivo of up to 66 %. Importantly, although achieving full signal recovery with DIR-labelling strongly depends on the inversion/reinversion efficiency, the obtained MBF values were largely comparable with conventional FAIR-myASL. Hence, DIR-labelling emerges as a promising technique to enhance myoASL-SNR without compromising bias, and to improve reproducibility of double ECG-gated FAIR-myASL, even in the presence of high HR variability.

This thesis introduced novel methods to address various factors that influence the bias and noise profiles in myoASL, laying the groundwork for its potential use as a non-contrast alternative to first-pass CMR. Central to this attempt, is the capability of myoASL to reliably measure MBF and detect relevant perfusion defects in cardiovascular diseases (CVDs). Thus, the technical validation of myoASL as a quantitative MR technique is prerequisite to its clinical translation and entails the consideration of two main aspects: bias and precision [153]. The following sections will discuss the effectiveness of the proposed methods in fulfilling these criteria and their potential contribution to the diagnostic toolkit provided by CMR.

6.1 ASSESSING BIAS IN MYOASL FOR ISCHAEMIA DETECTION

The assessment of ischaemia in coronary artery disease (CAD) mainly relies on comparing the myocardial perfusion reserve (MPR), i. e. the ratio of stress to resting perfusion, across different myocardial regions [203, 204]. This approach is best suited for identifying ischaemic areas of the myocardium when the stenosis is confined to a single coronary vessel and ischaemia is restricted to the corresponding supply territory. If, however, multiple arteries are affected by plaque, the entire myocardium often exhibits globally reduced blood flow. Such diffuse perfusion reduction is also observed in microvascular dysfunction, which is characterised by impaired coronary microcirculation rather than stenotic arteries [92]. In such scenarios, absolute quantification of MBF and the comparison against established reference or threshold values become crucial for clinical evaluation [81, 91]. Early studies in a porcine model, have validated perfusion values derived from FAIR-myocardial ASL against those measured with radio-labelled microspheres [115]. Although direct validation against gold-standard methods like PET in human subjects is limited due to the necessary exposure to ionising radiation and contrast agents, good correlation to PET-based literature values has been reported throughout myocardial ASL literature [36, 40].

In vivo applications of myocardial ASL, particularly with FAIR-labelling, most often resort to Buxton's GKM for quantifying myocardial perfusion owing to its straightforward computational approach [131]. In this work, however, we identified that the GKM fails to account for the modification of magnetisation, which occurs during the image readout. As a consequence, parameters related to the image readout, including the acquisition matrix size and FA, impart major bias to myocardial ASL-based perfusion values. This issue is particularly relevant for snapshot readouts, which sample all k-space points in a single acquisition and are the most common choice in cardiac imaging. The impact of the acquisition parameter choice substantially compromises the reproducibility and comparability of MBF values from different myocardial ASL measurements. Ultimately, without appropriate corrections, this is a major limitation for establishing reference MBF values in healthy subjects and defining diagnostic cut-off values in myocardial pathologies.

6.2 ASSESSING PRECISION IN MYOASL FOR ISCHAEMIA DETECTION

To be clinically useful the sensitivity of myocardial ASL-based perfusion mapping needs to compare favourably with the effect size of the specific cardiac pathology in question. Regarding coronary artery disease (CAD), the predominant form of CVDs, the extent of regional perfusion reduction depends on the number and severity of coronary stenoses [176]. In first-pass perfusion literature, stress MBF in stenotic territories showed a 20 % decrease compared to unaffected territories and a 25 % decrease relative to the global MBF in individuals without CAD [205]. Further, Knott et al. compared stress perfusion between healthy myocardium and territories affected by varying degrees of stenosis (DS), as identified by invasive coronary angiography (ICA) [176]. Relative to values in healthy subjects, the stress perfusion was found to decrease with in-

creasing DS: The reduction in regional stress MBF ranged from approximately 30 % for vessels with DS < 50 % to about 60 % for DS > 70 %. They further report an optimal cut-off value for diagnosing endocardial ischaemia at 1.3 ml/g/min, representing an effect size of 55 % compared to stress perfusion in healthy volunteers.

6.2.1 *Challenges in patient scanning with myoASL*

Patients with CAD or heart failure often present with atrial fibrillation, the most prevalent form of cardiac arrhythmia [201, 202]. This condition leads to difficulties in CMR imaging, especially in myoASL, as arrhythmia interferes with prospective ECG-triggering. The result is often overall impaired image quality due to cardiac motion during image readout in shortened heartbeats [178]. For double ECG-gated myoASL techniques, the highly irregular heartbeat poses an additional challenge as it causes increased *TI* variability. This work has identified signal fluctuations due to variable *TI* between control and tag images as the main source of PN in double ECG-gated FAIR-myASL. To tackle this issue, DIR-preparations have been introduced for FAIR-myASL, which promise substantially improved PN levels and, thus, should be further evaluated.

Due to the impaired cardiac function, patients often commonly present with shortness of breath. This is further exacerbated under pharmacological stress, rendering breath-hold acquisitions often infeasible. At the same time, myoASL requires tedious averaging over multiple breath-holds to ensure sufficient precision of estimated MBF values. Free-breathing myoASL sequences alleviate this additional burden, but typically involve the acquisition of an increased number of imaging data which are retrospectively sorted. In comparison, respiratory navigated sequences require less repeated acquisitions and, thus, may improve scan time efficiency. Thus, we introduced dual respiratory navigated free-breathing myoASL acquisitions, to improve patient comfort while maintaining scan time efficiency. For this purpose, a pencil-beam navigator was played prior to both labelling and image acquisitions, and myoASL images were only acquired when both consecutive navigators were within the gating window. In vivo, perfusion values obtained with navigated acquisitions were comparable to those obtained with conventional breath-holding. However, navigator gating achieves shorter scan times and improved subject comfort. The method was therefore adopted in all our further studies and holds promise for application of FAIR-myASL in patient populations.

6.2.2 *Challenges in stress perfusion measurements with myoASL*

Given the essential role of stress perfusion testing in the diagnostic routine for CAD, myoASL needs to provide accurate and precise perfusion estimates, both at rest and under induced stress, in clinically acceptable scan times. Various options are available for inducing hyperaemic stress during perfusion imaging. Because MR-compatible hardware is costly and exercise is more complex to perform [206], pharmacological stress agents have become generally preferred in CMR. Vasodilatory substances like adenosine are commonly employed and

cause widening of the blood vessels through the relaxation of smooth muscles in the artery walls [207]. For patients with respiratory conditions, where vasodilation is contra-indicated, dobutamine serves as a viable alternative. It mimics the physiological effects of exercise more accurately by increasing the HR and myocardial contractility [207]. Nevertheless, stress testing poses numerous challenges for myoASL-based perfusion mapping, including an increased and potentially more variable HR as well as intensified patient movement due to discomfort during the procedure.

First of all, the enhanced oxygen demand induced by pharmacological stress agents typically coincides with an increased HR. In adenosine-based stress protocols, for example, an HR increase of at least 10 bpm is regarded as an indicator of an adequate vasodilatory response [208]. The resulting shortening of RR intervals, however, necessitates the use of rapid imaging sequences like bSSFP. Nonetheless, an insufficient quiescent period or inadequate gating may still compromise image quality in myoASL. Moreover, additional sources of PN may compromise the precision of myoASL measurements. For instance, patients tend to move more as they experience increasing discomfort during pharmacological stress [209, 210]. This may lead to artefacts and complicate motion correction, especially if the movement is severe or occurs through the imaging plane. Furthermore, stress agents can only be administered for a limited duration due to safety concerns [208, 211]. This confines the stress window to 2 to 6 min and restricts the scan time available for perfusion mapping. Consequently, the number of averages that can be acquired for myoASL is limited, and the amplified PN cannot be compensated for by enhancing the SNR through extended averaging. This highlights the need for efficient acquisition strategies for myoASL within the constrained time frame of pharmacological stress testing.

6.2.3 *Prior research and novel insights*

The sensitivity of myoASL to stress-induced perfusion changes has been established in studies on healthy volunteers using both vasodilatory stress-agents [119, 120, 212] as well as non-pharmacologic stressors including exercise [117] and isometric hand-grip [40, 116]: Stress MBF measured with FAIR-myASL was found to be significantly increased compared to rest MBF and to be consistent with PET-based literature, when vasodilatory agents were used [119, 120, 212]. With isometric hand-grip [116], leg elevation [40], and in-bore ergometer exercise [117], the observed perfusion increase relative to resting perfusion was lower than with pharmacologic stress. However, myoASL-measurements during induced stress showed decreased SNR compared to those performed at rest, with relative PN of 42 % during stress and 26 % at rest [117].

Nevertheless, the effectiveness of myoASL in clinical settings has also been demonstrated. Previous studies evaluated MPR values derived from FAIR-myASL in patients with suspected CAD, who additionally underwent ICA [35, 45, 120]. A statistically significant reduction in MPR has been found in patients with single-vessel CAD between anterior and posterior myocardial wall [120], as well as between normal and the most ischaemic myocardial segments [35].

Further, myoASL-based MPR correlated with values obtained from first-pass perfusion CMR and showed significant differences between normal and abnormal myocardial segments. These included ischaemic and infarcted regions as identified by ICA and late-gadolinium enhancement (LGE), respectively [45]. However, MPR values showed larger standard deviations when obtained from FAIR-myASL compared to first-pass perfusion CMR [45] and to SPECT-based literature values [35].

In this work, relative PN levels, expressed as a coefficient of variation (CoV), ranged between 36 % and 43 % for conventional FAIR-myASL. Considering an anticipated effect size in CAD between 20 and 60 % as mentioned above, this level of noise might only allow for detection of the most severe perfusion defects. Although prior research has validated the utility of myoASL for stress-rest comparisons in healthy volunteers, a simultaneous decrease in SNR has been observed for stress perfusion mapping. Importantly, induced stress in healthy subjects typically leads to an increase in myocardial blood flow, causing an amplified perfusion signal in myoASL. This is not the case in patients with perfusion defects, where, even with a constant PN, a decreased SNR can be expected. Hence, the challenges associated with stress-testing may reduce the overall sensitivity of myoASL to pathological perfusion changes.

Background suppression techniques are topical to achieve the necessary sensitivity in myoASL in this context. In this work T_2 -prepared readouts were proposed to effectively suppress myocardial background fluctuations such that a substantial reduction in PN was achieved. This, in turn, may lead to improved SNR of myoASL under stress conditions. Such background suppression methods mitigate a wide range of noise contributions by attenuating the overall signal. However, our results show that the T_2 -prepared readouts introduce an additional T_2 -dependence on MBF values which may limit their applicability for accurate perfusion quantification. On the other hand, the introduced DIR-preparations for FAIR-myASL target fluctuations in the perfusion-weighted signal stemming from variations in TI . While less effective against other contributions to measurement noise, DIR-labelling substantially reduced PN relative to conventional double ECG-gated FAIR-myASL, where TI variability represents the major source of PN. DIR-prepared acquisitions resulted in relative PN levels of 19 %, which promises an improved sensitivity to less severe perfusion changes, e. g. in minimally constricted vessels or across different myocardial territories. Nonetheless, the proposed methods remain to be evaluated in patient populations with myocardial pathology, and residual sources of physiological noise need to be addressed to enable detection of subtle perfusion changes.

6.3 NON-CONTRAST ALTERNATIVES TO MYOASL

The field of CMR is pursuing a collective effort to reduce or, ideally, eliminate the use of GBCAs and move towards fully contrast-agent-free protocols. Quantitative MRI, most notably parametric mapping techniques, has emerged as an essential part of this endeavour, encompassing a comprehensive set of myocardial assessment techniques. Prominent examples are myocardial T_1 and T_2 mapping, which gained clinical importance in diagnosing acute myocardial injury,

acute myocarditis, and iron overload, among others [9, 213]. While contrast-based LGE remains the clinical standard for evaluating myocardial scarring and fibrosis [87], non-contrast alternatives to LGE are a hot topic of research. Novel contrast mechanisms, such as T_1 relaxation in the rotating frame ($T_{1\rho}$) are investigated, due to their sensitivity to slow molecular processes and have been successfully applied in patients [214, 215]. Within this general context, myoASL presents a promising alternative for non-contrast perfusion assessment. Despite all limitations, it could provide a method for assessing severe ischaemia or long-term monitoring after revascularisation therapy, as it allows for repeated measurements.

Taking a wider view, the adequacy of perfusion imaging, and myoSAL in particular, as a method for assessing ischaemia remains an open question. The success of revascularisation of coronary arteries is highly dependent on the haemodynamic significance of the stenosis and is, thus, recommended only in presence of ischaemia [216]. However, the relationship between stenosis, its impact on haemodynamics, and ischaemia is not always unequivocal as MBF can be maintained via collateral vessels or metabolic adaptation [75]. It is therefore beneficial to consider the exact meaning of ischaemia as an undersupply of oxygen relative to the demand in tissue. To adequately evaluate myocardial ischaemia in this sense, the measurement contrast should be indicative of the balance between oxygen supply and demand in the myocardium. In (cardiac) MRI, deoxygenated haemoglobin in the capillaries exerts a paramagnetic effect on surrounding hydrogen spins, leading to reduced T_2 and T_2^* relaxation times [217, 218]. This is known as the blood-oxygen level dependent (BOLD) effect and can be used to derive the oxygen-extraction fraction [219]. Providing a quantitative measure of tissue oxygenation, this may allow for more direct evaluation of myocardial ischaemia compared to perfusion metrics alone. Comparative studies between BOLD-CMR and standard perfusion modalities like first-pass perfusion CMR or PET, have shown that hypo-perfused and de-oxygenated myocardial segments do not necessarily overlap [220, 221]. Regarding non-contrast protocols, combined use of myoASL and BOLD during a single adenosine-infusion has been demonstrated in healthy volunteers [212]. While this approach leverages the additional information contained in the BOLD-response, it remains to be validated in larger cohorts of healthy subjects and patients. Moreover, imaging oxygenation with BOLD-CMR is limited by inherently low SNR, long acquisition times, and its sensitivity to B_0 inhomogeneity and susceptibility artefacts. Despite these challenges, BOLD-CMR remains a promising candidate for accurate ischaemia detection and, alongside myoASL, a compelling route towards advancing non-contrast CMR diagnostics.

6.4 LIMITATIONS AND OUTLOOK

Buxton's GKM became the current workhorse for quantifying perfusion with myoASL, and beyond, as it provides a simple, analytical model, which facilitates an intuitive apprehension of the signal dynamics in myoASL. However, as shown in this work, accurate estimation of MBF with the GKM values becomes less straightforward with extended imaging readouts and variable inversion

times – scenarios frequently encountered in myoASL. The former issue mainly arises from the fact that the influence of the image readout on magnetisation is not taken into account in the model. In this regard, however, neither effects due to off-resonance, magnetisation transfer, nor flow during the imaging readout are considered in the GKM [174]. Therefore, future work should include a thorough theoretical re-evaluation of perfusion quantification to improve the bias and reproducibility of (FAIR-)myoASL.

However, the most decisive aspect for further adoption and clinical translation of myoASL remains the management of high noise levels caused by PN. Strategies for improving SNR may be categorised into two larger groups: Those suppressing or eliminating the sources of signal fluctuations all together or, alternatively, those reducing acquisition time to allow for more extensive averaging. In terms of mitigating noise, both background suppression methods as well as new labelling approaches, such as those introduced in this work, remain to be validated in larger cohorts and, especially, in patients to evaluate their clinical utility. Regarding scan time acceleration, undersampling approaches such as compressed-sensing have been explored for FAIR-myASL [44]. Yet, a significant portion of the acquisition time is typically allocated to the delay between control and tag images to ensure complete magnetisation recovery. As shown in our study, control-tag delays below 6 s lead to accrual of MBF deviations above 5 %. However, in an approach similar to transient state techniques [222], the control-tag delay could be fully eliminated. Instead, the myoASL acquisitions would be simulated for a range of physiological parameters and perfusion values would be estimated through dictionary mapping of the obtained signal. Such ASL-fingerprinting approaches have been explored in cerebral blood flow mapping [223, 224] and were recently applied to the assessment of ischaemic stroke [225]. Equivalent approaches in the heart may offer reduced scan times but would require generating subject-specific dictionaries due to the high sensitivity of cardiac imaging to HR variations.

Enhancing the SNR in myoASL is intrinsically connected to increasing its spatial coverage. Currently, FAIR-myASL only allows for single-slice acquisitions and is not compatible with multi-slice acquisitions due to non-negligible arterial transit time (ATT) delays in large labelling slabs [40]. Consequently, the sequential acquisition of multiple slices, covering all relevant coronary territories, extends scan times beyond what is typically feasible in clinical settings. However, accelerated imaging techniques might reduce the scan time for serial slice-acquisitions to clinically acceptable limits, thereby expanding spatial coverage in FAIR-myASL.

Moreover, alternative labelling approaches, such as velocity-selective (VS) labelling [124] can be utilised for efficient myoASL that is robust against ATT effects. By creating the label within the imaging volume itself, VS-labelling can theoretically provide an advantage in cardiac pathologies, where coronary flow is slowed down, ATT is prolonged and the label delivery is delayed in turn [124]. However, the increased movement of the heart as well as the geometry of coronary vessels, require careful adjustment of the velocity encoding direction, cut-off velocity, and TI in cardiac applications. Otherwise, myoASL signal may easily be confounded by intravascular signal and spurious labelling of moving spins in myocardial tissue [124]. An initial study on VS-labelling in the human

heart revealed comparable MBF values to those derived from FAIR-myocardial ASL, albeit with a three times lower SNR in the former. This reduction in SNR can be attributed to reduced myocardial ASL signal with saturation instead of inversion-based labelling as well as signal loss due to T_2 -decay during the VS-preparation. Improved design of VS-pulses, however, have yielded a sharper velocity-profile and improved SNR on par with FAIR-myocardial ASL [125], promising a more enhanced resilience of VS-labelling in cardiac settings.

Despite the inherent challenges, myocardial ASL holds promise as a valuable tool for assessing myocardial health and making perfusion assessment more accessible to patients with contra-indications to GBCAs. With the advanced methods proposed in this work and anticipated future developments, myocardial ASL may become part of a comprehensive, non-contrast toolbox within CMR alongside other quantitative MRI techniques like parametric mapping. In combination with these, myocardial ASL could provide complementary insights into perfusion and ischaemic conditions, facilitating a more extensive assessment of myocardial function.

CONCLUSION

In this work, novel Arterial Spin Labelling (ASL) methods have been developed for non-contrast mapping of myocardial perfusion with magnetic resonance imaging (MRI). Measuring myocardial blood flow (MBF) and detecting perfusion anomalies are central to the diagnosis of coronary artery disease (CAD). Considering the high health and socio-economic burden of cardiovascular diseases (CVDs), reliable diagnosis can support the management of CVDs. In the context of identifying CAD, cardiac perfusion MRI offers an essential diagnostic and prognostic tool. However, the safety concerns attributed to the required gadolinium-based contrast agents limit the clinical applicability of conventional perfusion CMR. As a non-contrast alternative, myocardial ASL (myoASL) relies on magnetically labelled blood as an endogenous tracer, showing promise in quantifying MBF and detecting perfusion defects. However, a lack of reproducibility and robustness hamper the broader clinical translation of myoASL, mainly due to inherently low signal-to-noise ratios (SNR). Therefore, three advanced methods for Flow-sensitive Alternating Inversion Recovery (FAIR)-labelled myoASL were developed and investigated in this thesis to improve its robustness against variable acquisition and physiological parameters.

First, the influence of acquisition-related and physiological parameters on the estimated perfusion values and the physiological noise (PN) in FAIR-myocardial ASL has been investigated. Inaccurate blood T_1 relaxation times in perfusion quantification were found to induce a mild heart rate dependence on myoASL-based MBF values, which can be mitigated if accurate, subject-specific values for the blood T_1 are used. Moreover, the acquisition flip angle emerged as the strongest influencing factor, which may impair reproducibility and impart bias on perfusion estimates in FAIR-myocardial ASL. However, the proposed saturation-baseline approach for spoiled GRE readouts can compensate for the confounding effect of the flip angle. Thus, the proposed quantification corrections can reduce variations in measured MBF and improve the reproducibility of FAIR-myocardial ASL against acquisition parameters. These findings are particularly relevant in view of the potential definition of reference MBF values in healthy myocardium and diagnostic thresholds for patient populations.

Next, the focus was placed on addressing different sources of PN in free-breathing, respiratory-navigated FAIR-myocardial ASL. First, PN originating from fluctuations in the myocardial background signal was addressed. To that end, T_2 -prepared readouts have been introduced for FAIR-myocardial ASL. By suppressing the myocardial background relative to the perfusion-related blood signal, a substantial reduction in PN and improvement in SNR were achieved both in simulations and phantom experiments, as well as in vivo. At the same time, T_2 -prepared readouts introduced a T_2 dependence to the estimated MBF values, which would require modelling or correction to preserve the accuracy of MBF values. Nonetheless, T_2 -prepared readouts target a broad range of PN sources and can be combined with any type of labelling strategy. Thus, they hold a

potential benefit for reducing the impact of PN in myoASL techniques even beyond FAIR-labelling.

In a final step, approaching the issue of PN from a different angle, Double Inversion Recovery (DIR) preparations were developed for FAIR-myocardial ASL to reduce PN contributions related to heart rate variability. With reinversion pulses added immediately after the FAIR-labelling, the static myocardial signal can recover almost entirely prior to image acquisition and signal differences caused by variable inversion times were reduced. In simulation and phantom experiments, DIR-labelling thus led to an average 10-fold SNR gain relative to conventional myoASL with single FAIR-labelling. Further, in vivo perfusion values based on DIR were comparable to conventional FAIR-myocardial ASL, but showed up to a 66 % reduction in PN. This potentially offers significant clinical value, as it yields relative noise levels below the anticipated effect size of perfusion defects in CAD.

In summary, three novel approaches for FAIR-myocardial ASL have been proposed and evaluated in this thesis. The relevant confounding factors related to image acquisition and physiological parameters have been identified. Furthermore, dedicated correction approaches and strategies to mitigate major contributions to PN have been developed. Combining these methods enables FAIR-myocardial ASL measurements that are more robust against physiological fluctuations and provide perfusion estimates with reduced acquisition-related bias. However, several challenges to the wider adoption of FAIR-myocardial ASL remain, primarily due to residual bias and PN limiting the measurement sensitivity. Future research should thus focus on advanced noise reduction techniques to manage remaining sources of PN and efficient acquisition strategies for improved SNR performance to further enhance the applicability of myoASL. This may help to promote a broader clinical translation of myoASL and establish it as a part of a general non-contrast CMR toolbox for examining myocardial health.

Part I

APPENDIX

APPENDIX TO CHAPTER 3

A.1 SIGNAL EQUATIONS FOR BSSFP AND SPGRE READOUT

bSSFP readout

The MMF for a bSSFP readout can be expressed via the transient state magnetization as described by Scheffler [226]. For a readout with flip angle (FA) α and an $\frac{\alpha}{2}$ -preparation pulse, the magnetization vector after the k -th RF pulse can be given as [226]:

$$\mathbf{M}(k) = (\sin(\frac{\alpha}{2})\mathbf{M}_0 - \mathbf{M}_{ss})\lambda_1^k + \mathbf{M}_{ss} , \quad (\text{A.1})$$

with initial magnetization \mathbf{M}_0 , steady state magnetization $M_{ss} = \rho \frac{\sqrt{E_2}(1-E_1)\sin(\alpha)}{1-(E_1-E_2)\cos(\alpha)-E_1E_2}$, proton density ρ , coefficients $E_{1/2} = e^{-TR/T_{1/2}}$, and the eigenvalue λ_1 :

$$\begin{aligned} \lambda_1 &= \cos(\alpha)(E_1 - E_2) + \sqrt{\cos^2(\alpha)(E_1 - E_2)^2 + 4E_1E_2} \\ &\approx E_1 \cos^2(\frac{\alpha}{2}) + E_2 \sin^2(\frac{\alpha}{2}) . \end{aligned} \quad (\text{A.2})$$

With $x = M_z(t_0)$ the MMF becomes:

$$f_{MMF}^{bSSFP}(x) = \sin(\frac{\alpha}{2})\lambda_1^k x + (1 - \lambda_1^k)M_{ss} \quad (\text{A.3})$$

spGRE readout

Similarly, the MMF for a spGRE readout can be derived based on the Bloch equations. After a first RF pulse with FA α at t_0 and a second after a repetition time TR , the longitudinal magnetization $M_z(t_0 + TR)$ is given by

$$M_z(t_0 + TR) = \cos^2(\alpha)E_1M_z(t_0) + \cos(\alpha)(1 - E_1)M_{z,eq} , \quad (\text{A.4})$$

with initial magnetization $M_z(t_0)$ and equilibrium magnetization $M_{z,eq}$. After k RF pulses, the longitudinal magnetization yields

$$\begin{aligned} M_z(k) &= \cos^k(\alpha)E_1^{-(k-1)}M_z(t_0) + \\ &+ \left(\sum_{i=0}^{k-2} (\cos(\alpha)E_1)^{-i} \right) \cos(\alpha)(1 - E_1) . \end{aligned} \quad (\text{A.5})$$

and the MMF for spGRE can be given as

$$\begin{aligned} f_{MMF}^{spGRE}(x) &= \cos^k(\alpha)E_1^{-(k-1)}x + \\ &+ \frac{1 - (\cos(\alpha)E_1)^{k-1}}{1 - \cos(\alpha)E_1} (1 - E_1) \cos(\alpha) \rho M_{z,eq} . \end{aligned} \quad (\text{A.6})$$

A.2 IMAGING SIGNAL FOR BASELINE, CONTROL AND TAG IMAGE IN FAIR-MYOASL

In both, control and tag images, the myocardium is inverted in the imaging slice and recovers with $T_{1,M}$ during the time TI preceding the imaging readout. Using Equation (3.2), the myocardial signal contribution can, thus, be expressed as

$$I_M = V_M(A_M x_M^- + B_M), \quad (\text{A.7})$$

where $x_M^- = M_{z,eq}(1 - (1 - \cos(\alpha_{inv}))e^{-TI/T_{1,M}})$, with inversion flip angle α_{inv} .

The blood signal, however, differs between the two settings. After the slice-selective inversion in the control image, non-inverted blood flows into the imaging slice with in-flow rate f_{in} giving rise to the signal contribution

$$I_{C,B}^+ = V_B f_{in}(A_B x_B^+ + B_B), \quad (\text{A.8})$$

with $x_B^+ = 1$. At the same time outflow of the initially inverted blood occurs with the same rate f_{in} , such that the remaining non-inverted blood contributes to the signal with

$$I_{C,B}^- = V_B(1 - f_{in})(A_B x_B^- + B_B), \quad (\text{A.9})$$

where $x_B^- = M_{z,eq}(1 - (1 - \cos(\alpha_{inv}))e^{-TI/T_{1,B}})$. Combining Eqs. (A.8) and (A.9) the full contribution of blood signal to the control image yields:

$$I_{C,B} = V_B(f_{in}(A_B x_B^+ + B_B) + (1 - f_{in})(A_B x_B^- + B_B)). \quad (\text{A.10})$$

In tag images, the in-flowing blood is also inverted due to the non-selective inversion, and can be expressed as

$$I_{T,B} = V_B(A_B x_B^- + B_B). \quad (\text{A.11})$$

Finally, in the case of the baseline image, neither myocardium nor blood is inverted ($x_M^+ = x_B^+ = 1$):

$$\begin{aligned} I_{BL,B} &= V_B(A_B x_B^+ + B_B) \\ I_{M,BL} &= V_M(A_M x_M^+ + B_M) \end{aligned} \quad (\text{A.12})$$

Combining the signal contributions from Eqs. (A.7)-(A.12), yields the following signal equations for the control (I_C), tag (I_T), and baseline signal (I_{BL}) in FAIR-myASL:

$$\begin{aligned} I_C &= I_M + I_{C,B} = \\ &= V_M(A_M x_M^- + B_M) \\ &\quad + V_B(f_{in}(A_B x_B^+ + B_B) + (1 - f_{in})(A_B x_B^- + B_B)) , \end{aligned} \quad (\text{A.13})$$

$$\begin{aligned} I_T &= I_M + I_{T,B} = \\ &= V_M(A_M x_M^- + B_M) + V_B(A_B x_B^- + B_B) , \end{aligned} \quad (\text{A.14})$$

$$\begin{aligned} I_{BL} &= I_{M,BL} + I_{BL,B} = \\ &= V_M(A_M x_M^+ + B_M) + V_B(A_B x_B^+ + B_B) . \end{aligned} \quad (\text{A.15})$$

Subtracting this saturation-baseline from the original baseline image yields

$$\begin{aligned} I_{BL} - I_{BL,Sat} &= V_M(A_M x_M^+ + B_M) + V_B(A_B x_B^+ + B_B) \\ &\quad - (V_M(A_M \cdot 0 + B_M) + V_B(A_B \cdot 0 + B_B)) = \\ &= V_M A_M x_M^+ + V_B A_B x_B^+ . \end{aligned} \quad (\text{A.16})$$

B.1 RESPIRATORY NAVIGATED FREE-BREATHING MYOCARDIAL ARTERIAL SPIN LABELING (ASL) WITH PHASE SENSITIVE RECONSTRUCTION

The following findings have been presented at the 2023 Annual Meeting of the International Society for Magnetic Resonance in Medicine, in Toronto (CA), and the corresponding conference abstract is reproduced here.

B.1.1 *Synopsis*

Myocardial arterial spin labeling (myoASL) holds promise for needle-free myocardial blood flow (MBF) quantification but requires tedious averaging over multiple breath-holds. Here, free-breathing myoASL was implemented with dual-navigator gating, both with bSSFP and spoiled GRE readout. Images were processed using individual blood T_1 and inversion time correction as well as a phase-sensitive (PS) image reconstruction. Phantom results showed PS reconstruction to reduce MBF variations for short RR and T_1 values. MBF values were comparable with breath-held myoASL and on par with the literature. Ultimately, this can enable faster myoASL acquisitions with improved patient comfort.

B.1.2 *Introduction*

First-pass perfusion imaging is the clinical gold standard for detecting myocardial ischemia and quantifying myocardial perfusion [12]. However, it requires the use of exogenous contrast agents limiting its repeated use. Arterial spin labelling (ASL) can provide a promising alternative based on magnetically labelled blood as endogenous tracer. Due to low signal-to-noise ratios and high physiological noise levels [40], however, multiple averages are needed to ensure sufficient accuracy. While myocardial ASL (myoASL) has mostly been performed during breath-holds [37, 40], free-breathing, retrospectively gated myoASL has recently been demonstrated [163]. However, retrospective image selection may lead to excessive scan times. In this work, we propose a respiratory navigated free-breathing myoASL sequence with increased scan time efficiency and noise performance, using phase-sensitive myoASL image reconstruction.

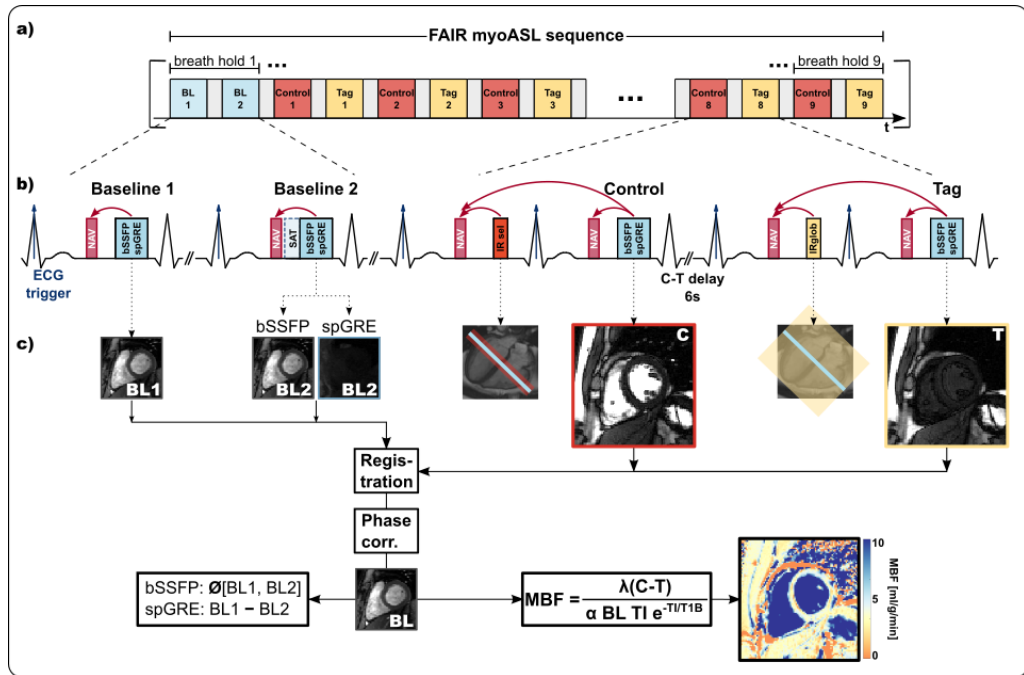


Figure B.1: (a) Diagram of the double ECG-gated FAIR myocardial ASL sequence. Control/Tag images are acquired after a selective/global inversion pulse during mid-diastole, with a 6 s delay in between. (b) In free-breathing, images are acquired only if both current and preceding navigators (before inversion) were accepted. (c) Registered control and tag images are phase corrected and processed with a baseline image to obtain myocardial blood flow values.

B.1.3 Methods

FAIR-myocardial ASL sequence

Imaging was performed on a 3 T scanner (Magnetom Vida, Siemens Healthineers, Erlangen, Germany). For all measurements, a double ECG-gated Flow-sensitive Alternating Inversion Recovery (FAIR) ASL sequence [37] was implemented (Figure B.1). For the free-breathing sequence, as shown in Figure B.1b, a pencil-beam navigator placed at the liver dome was played prior to both inversion and image acquisitions. To ensure that images are acquired only upon successful inversion, FAIR images were accepted only when both consecutive navigators were valid. This dual-heartbeat navigation also led to matching slice-selective inversion and excitation in control images. Baseline images were conventionally navigated within a single heartbeat.

Phantom and in vivo measurements

Data was acquired both with bSSFP and spoiled GRE (spGRE) readout. In phantom, two control-tag image pairs were acquired with a 6 s delay between the two images. Phantom experiments were performed with varying simulated RR intervals in a NiCl₂-doped agarose phantom. In vivo images of 4 healthy subjects (1 female, 3 male, 35±4.8 years) were obtained in 12-15s long breath-holds per image pair depending on the heart rate (scan duration ca. 3 min) as well as in free-breathing (scan duration ca. 2-3 min). For each of the four combinations

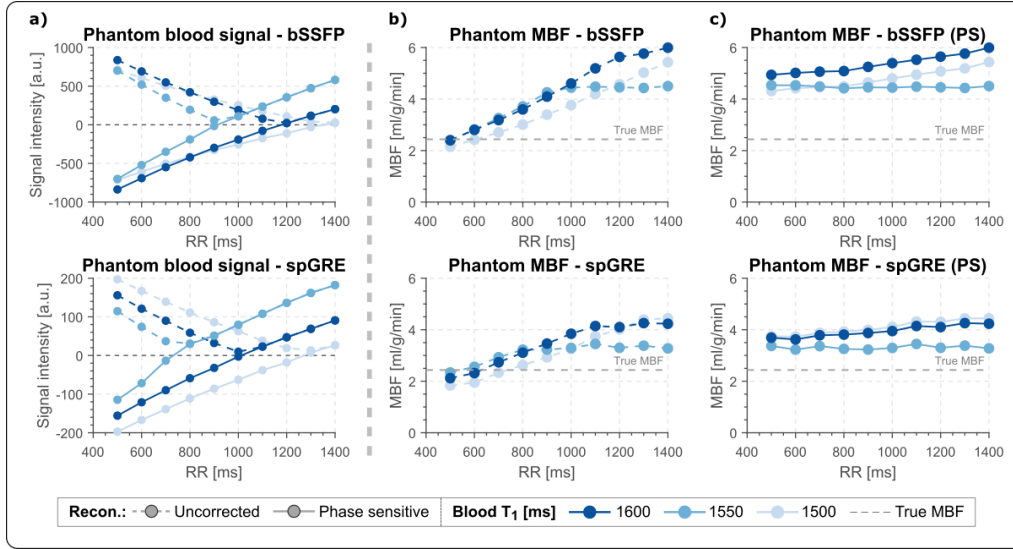


Figure B.2: Phantom (a) blood signal and (b), (c) MBF vs. heart rate with and without phase correction for different phantom vials. (a) Short RR intervals lead to short effective inversion times, such that the blood signal is still negative. The point of the zero-crossing varies with readout type and T_1 values. (b) Computing the MBF with the signal magnitude only leads to errors for RR intervals below this zero-crossing point. (c) With phase sensitive reconstruction, this error is mitigated.

of readout and breathing strategy, eight control-tag pairs were acquired with a 6 s delay. In phantom and in vivo, two baseline images (no inversion) were acquired with bSSFP, while with spGRE one of the two was directly preceded by a WET saturation pulse (“saturated baseline”, Sat-BL) to compensate for the effect of the imaging readout [227, 228]. All images were acquired with $1.6 \times 1.6 \times 8 \text{ mm}^3$ voxel size, TE 1.36/1.97 ms, TR 3.6/4.3 ms, and FA $60^\circ/17^\circ$ (bSSFP/spGRE), GRAPPA 2 and Partial Fourier (6/8). MOLLI [136] was used for T_1 mapping in phantom and in vivo.

Data analysis

In vivo image pairs with inconsistent inversion times (TI) were excluded, before registering the images group-wise [169]. Phase-sensitive (PS) reconstruction was performed to restore the signal polarity and image contrast. To this end, the phase difference was unwrapped and rounded to 0 or π to extract the signal polarity [192]. Pixel- and segment-wise myocardial blood flow (MBF) were reconstructed using individual blood T_1 and a Sat-BL correction as previously described [108, 227, 228].

B.1.4 Results

Phantom MBF values are underestimated and vary with the RR duration, when no signal polarity correction is used (Figure B.2). The inflection point occurs at longer RR intervals/TIs for longer T_1 values and, also for spGRE compared to bSSFP. With PS reconstruction the MBF is largely constant over the range of simulated heart rates. Uncorrected images of a representative subject depict a

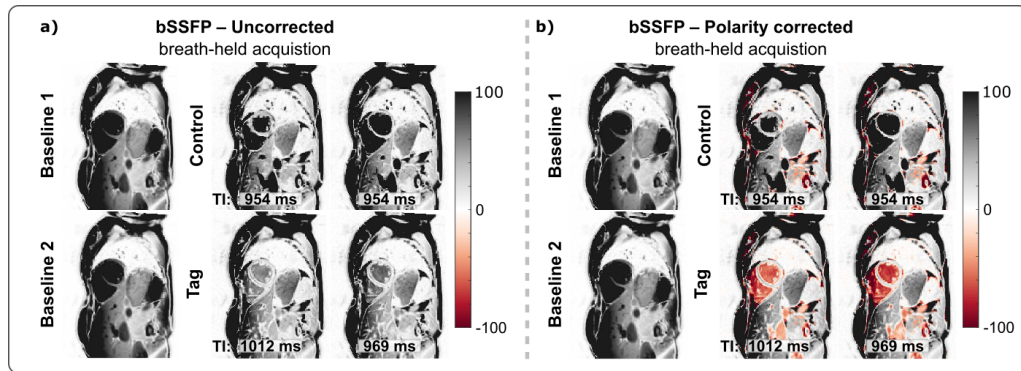


Figure B.3: ASL baseline images and two control (top) and tag (bottom) image pairs from one representative subject **(a)** without and **(b)** with phase correction. Images were acquired with bSSFP readout in breath-held acquisitions. **(a)** Due to the low RR interval in this subject, the blood pool appears brighter in uncorrected images. **(b)** With phase correction, the signal polarity and image contrast are restored. (Baseline signal values were rescaled to range from -300 to 300 for improved contrast.)

bright blood pool (Figure B.3a), indicating that the readout occurred before the inflection point of the blood signal due to a high heart rate (short RR duration and TI). The polarity corrected (Figure B.3b) images show a dark blood pool and restored image contrast. In vivo MBF maps show visually homogeneous values throughout the myocardium, with comparable physiological noise between bSSFP and spGRE (Figure B.4). Mean septal MBF per subject ranged between 1.25/2.53 and 3.48/5.70 ml/g/min (bSSFP/spGRE), as shown in Figure B.5, with a reduced number of outliers using phase-sensitive reconstruction in some subjects.

B.1.5 Discussion

In this work we evaluate a free-breathing myocardial ASL sequence, using navigator gating and phase-sensitive reconstruction. Homogeneous MBF map quality is achieved during free-breathing. Phase-sensitive reconstruction is shown to reduce the number of outliers in some subjects. As a result of short RR intervals, i.e. short TIs, the magnetization can be negative at the time of the image readout depending on the tissue T_1 . The distorted image contrast can then lead to inaccurate MBF quantification. Phase-sensitive reconstructions were shown to mitigate this effect in phantom. A residual phantom MBF deviation was observed due to the impact of the image readout. Phantom as well as in vivo MBF matched previously reported perfusion values [37, 40, 163]. Respiratory navigation generally yielded shorter scan times than breath-held acquisitions, while MBF maps were comparable for the two breathing strategies. Our in vivo data further suggest that the use of phase-sensitive reconstruction may reduce the number of outliers obtained during the MBF measurement.

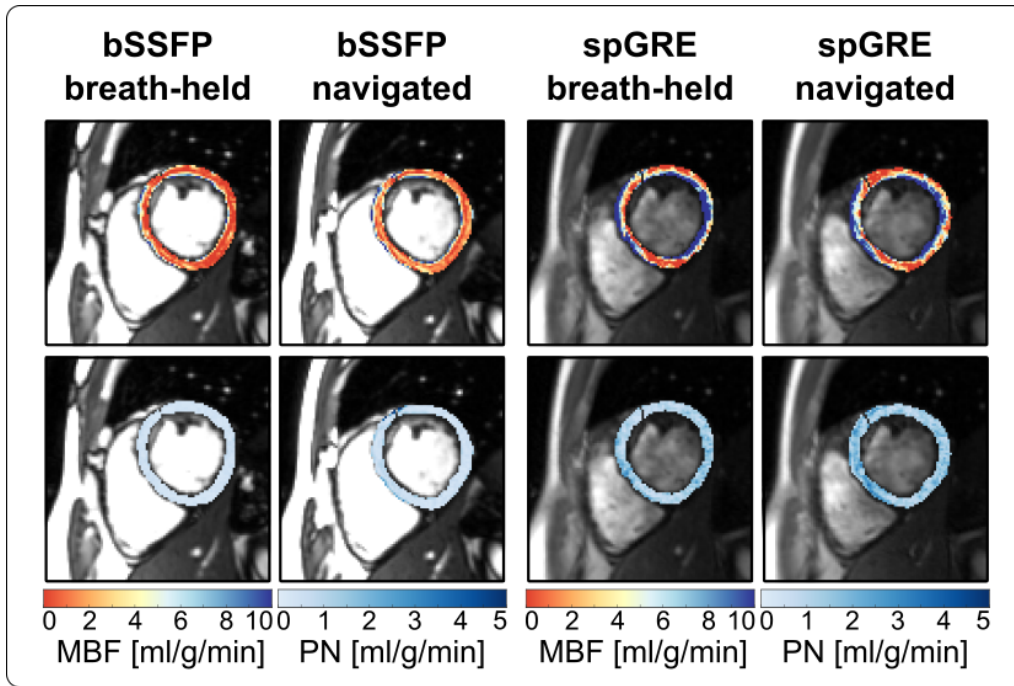


Figure B.4: Representative in vivo perfusion and physiological noise (PN) maps for bSSFP (left) and spGRE (right) images from breath-held and navigated acquisitions. Perfusion maps were reconstructed with polarity correction applied to the images prior to perfusion quantification. The quality of the perfusion maps is comparable for breath-held and navigated acquisitions and MBF values are comparable across all acquisitions.

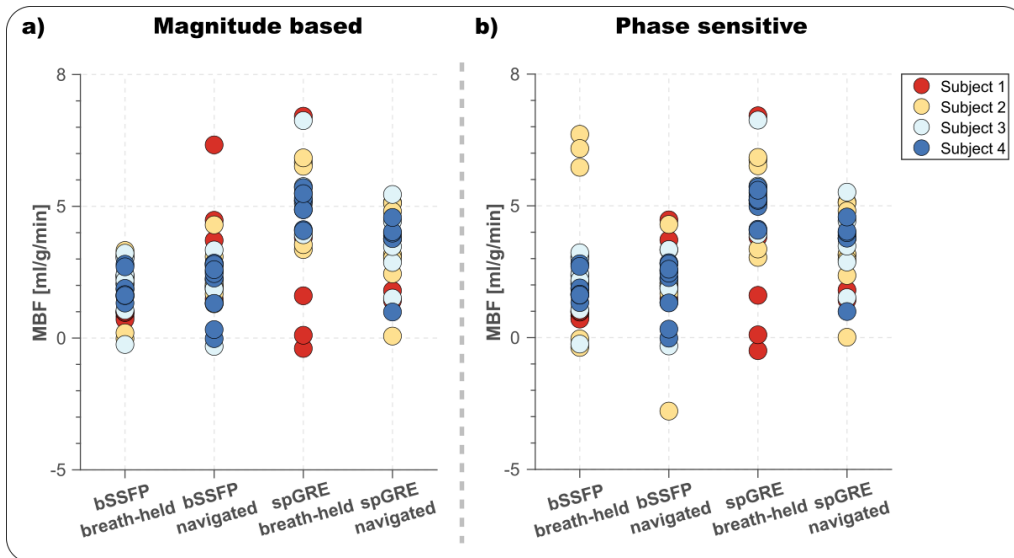


Figure B.5: Plots of all in vivo pair-wise MBF values for each acquisition type and for (a) magnitude and (b) phase-sensitive (PS) reconstruction modes. The four subjects are depicted with different colours. Subjects 1 & 2 had shorter RR intervals, such that shorter inversion times were corrected with PS reconstruction, eventually changing measured MBF. In spGRE readouts, respiratory navigation yielded more realistic MBF values than breath-held. The breathing strategy had less influence on bSSFP-based MBF.

B.1.6 *Conclusion*

Phase-sensitive perfusion reconstruction restores image contrast and may result in more precise MBF values. Free-breathing myoASL was demonstrated with dual-respiratory navigation and double ECG-gating and yields perfusion values comparable to breath-held myoASL. This approach can enable faster contrast-agent-free perfusion mapping with improved patient comfort.

PUBLICATIONS

- [1] Ties O. Tensen, Maša Božić-Iven, Chiara Coletti, and Sebastian Weingärtner. "E-MaRSSim: A Python-based open-source MRI pulse sequence simulation tool." In: *Proceedings of the ESMRMB MRI Together Workshop 2021*. 2021.
- [2] Tefvik F. Ismail, Wendy Strugnell, Chiara Coletti, Maša Božić-Iven, Sebastian Weingärtner, Kerstin Hammernik, Teresa Correia, and Thomas Küstner. "Cardiac MR: From Theory to Practice." In: *Frontiers in Cardiovascular Medicine* 9 (2022).
- [3] Maša Božić-Iven, Stanislas Rapacchi, Iain Pierce, George Thornton, Qian Tao, Lothar R. Schad, Thomas Treibel, and Sebastian Weingärtner. "On the reproducibility in cardiac ASL: T₁ corrected reconstruction for mitigating physiological and acquisition related variability." In: *Proceedings of the 25th Annual Scientific Sessions of the SCMR*. 2022.
- [4] Maša Božić-Iven, Stanislas Rapacchi, Iain Pierce, George Thornton, Qian Tao, Lothar R. Schad, Thomas Treibel, and Sebastian Weingärtner. "Towards reproducible Arterial Spin Labelling in the myocardium: Impact of blood T₁ time and imaging readout parameters." In: *Proceedings of the ISMRM Benelux Chapter Meeting*. 2022.
- [5] Maša Božić-Iven, Stanislas Rapacchi, Iain Pierce, George Thornton, Qian Tao, Lothar R. Schad, Thomas Treibel, and Sebastian Weingärtner. "Towards reproducible Arterial Spin Labelling in the myocardium: Impact of blood T₁ time and imaging readout parameters." In: *Proceedings of the Joint Annual Meeting ISMRM-ESMRMB*. 2022.
- [6] Maša Božić-Iven, Stanislas Rapacchi, Iain Pierce, George Thornton, Qian Tao, Lothar R. Schad, Thomas Treibel, and Sebastian Weingärtner. "Improving reproducibility of cardiac ASL using T₁ and flip angle corrected reconstruction." In: *Proceedings of the Annual Meeting of the SMRA*. 2022.
- [7] Maša Božić-Iven, Stanislas Rapacchi, Qian Tao, Lothar R. Schad, and Sebastian Weingärtner. "Respiratory navigated free-breathing myocardial arterial spin labelling (ASL) with phase sensitive reconstruction." In: *Proceedings of the Annual Meeting of the ISMRM*. 2023.
- [8] Merijn Berendsen, Maša Božić-Iven, Joao Tourais, Chiara Coletti, Ingo Hermann, and Sebastian Weingärtner. "Phase-based T₂ mapping using dual phase-cycled balanced SSFP imaging." In: *Proceedings of the Annual Meeting of the ISMRM*. 2023.
- [9] Maša Božić-Iven, Stanislas Rapacchi, Qian Tao, Iain Pierce, George Thornton, Christian Nitsche, Thomas A. Treibel, Lothar R. Schad, and Sebastian Weingärtner. "Improved reproducibility for myocardial ASL: Impact of physiological and acquisition parameters." In: *Magnetic Reso-*

nance in Medicine 91 (1 Sept. 2024), pp. 118–132. ISSN: 0740-3194. DOI: [10.1002/mrm.29834](https://doi.org/10.1002/mrm.29834).

- [10] Maša Božić-Iven, Yi Zhang, Qian Tao, Stanislas Rapacchi, Lothar R. Schad, and Sebastian Weingärtner. “Myocardium signal suppression with T2-preparations for reduced physiological noise in myocardial ASL.” In: *Proceedings of the SCMR Annual Scientific Sessions*. 2024.
- [11] Maša Božić-Iven, Yi Zhang, Qian Tao, Stanislas Rapacchi, Lothar R. Schad, and Sebastian Weingärtner. “Double Inversion Recovery in Myocardial Arterial Spin Labeling (ASL) for reduced physiological noise.” In: *Proceedings of the Annual Meeting of the ISMRM*. 2024.

BIBLIOGRAPHY

- [1] Isidor Isaac Rabi. "Space quantization in a gyrating magnetic field." In: *Physical Review* 51.8 (1937), p. 652.
- [2] Isidor Isaac Rabi, Jerrold R Zacharias, Sidney Millman, and Polykarp Kusch. "A new method of measuring nuclear magnetic moment." In: *Physical review* 53.4 (1938), p. 318.
- [3] Felix Bloch. "Nuclear induction." In: *Physical review* 70.7-8 (1946), p. 460.
- [4] F. Bloch, W. W. Hansen, and M. Packard. "The nuclear induction experiment." In: *Physical Review* 70.7-8 (1946), pp. 474–485.
- [5] Edward M Purcell, Henry Cutler Torrey, and Robert V Pound. "Resonance absorption by nuclear magnetic moments in a solid." In: *Physical review* 69.1-2 (1946), p. 37.
- [6] Herman Y Carr. "Free Precession Techniques in Nuclear Magnetic Resonance." In: *Ph. D. Thesis* (1953).
- [7] Paul C Lauterbur. "Image formation by induced local interactions: examples employing nuclear magnetic resonance." In: *nature* 242.5394 (1973), pp. 190–191.
- [8] Peter Mansfield and Peter K Grannell. "NMR'diffraction'in solids?" In: *Journal of Physics C: Solid State Physics* 6.22 (1973), p. L422.
- [9] Daniel R Messroghli, James C Moon, Vanessa M Ferreira, Lars Grosse-Wortmann, Taigang He, Peter Kellman, Julia Mascherbauer, Reza Nezafat, Michael Salerno, Erik B Schelbert, et al. "Clinical recommendations for cardiovascular magnetic resonance mapping of T₁, T₂, T₂* and extracellular volume: a consensus statement by the Society for Cardiovascular Magnetic Resonance (SCMR) endorsed by the European Association for Cardiovascular Imaging (EACVI)." In: *Journal of Cardiovascular Magnetic Resonance* 19.1 (2016), p. 75.
- [10] Rohit Bakshi, Alan J Thompson, Maria A Rocca, Daniel Pelletier, Vincent Dousset, Frederik Barkhof, Matilde Inglese, Charles RG Guttman, Mark A Horsfield, and Massimo Filippi. "MRI in multiple sclerosis: current status and future prospects." In: *The Lancet Neurology* 7.7 (2008), pp. 615–625.
- [11] Nadine Berrie Smith and Andrew G. Webb. "Image reconstruction in CT." In: *Introduction to medical imaging: physics, engineering and clinical applications*. 2010, pp. 71–74.
- [12] Bernhard L Gerber, Subha V Raman, Krishna Nayak, Frederick H Epstein, Pedro Ferreira, Leon Axel, and Dara L Kraitchman. "Myocardial first-pass perfusion cardiovascular magnetic resonance: history, theory, and current state of the art." In: *Journal of Cardiovascular Magnetic Resonance* 10.1 (2008), pp. 1–18.

- [13] Denis Le Bihan. "Looking into the functional architecture of the brain with diffusion MRI." In: *Nature reviews neuroscience* 4.6 (2003), pp. 469–480.
- [14] Scott B Reeder, Irene Cruite, Gavin Hamilton, and Claude B Sirlin. "Quantitative assessment of liver fat with magnetic resonance imaging and spectroscopy." In: *Journal of Magnetic Resonance Imaging* 34.4 (2011), pp. 729–749.
- [15] Paul A Bottomley. "Noninvasive study of high-energy phosphate metabolism in human heart by depth-resolved ^{31}P NMR spectroscopy." In: *Science* 229.4715 (1985), pp. 769–772.
- [16] LJ Anderson, S Holden, B Davis, E Prescott, CC Charrier, NH Bunce, DN Firmin, B Wonke, J Porter, JM Walker, et al. "Cardiovascular T2-star (T_2^*) magnetic resonance for the early diagnosis of myocardial iron overload." In: *European Heart Journal* 22.23 (2001), pp. 2171–2179.
- [17] Marianna Fontana, Sanjay M Banyersad, Thomas A Treibel, Viviana Maestrini, Daniel M Sado, Steven K White, Silvia Pica, Silvia Castelletti, Stefan K Piechnik, Matthew D Robson, et al. "Native T1 mapping in transthyretin amyloidosis." In: *JACC: Cardiovascular Imaging* 7.2 (2014), pp. 157–165.
- [18] S Bohnen, UK Radunski, GK Lund, F Ojeda, Y Looft, M Senel, L Radziwolek, M Avanesov, E Tahir, C Stehning, et al. "Tissue characterization by T1 and T2 mapping cardiovascular magnetic resonance imaging to monitor myocardial inflammation in healing myocarditis." In: *European Heart Journal-Cardiovascular Imaging* 18.7 (2017), pp. 744–751.
- [19] Vanessa M Ferreira, Jeanette Schulz-Menger, Godtfred Holmvang, Christopher M Kramer, Iacopo Carbone, Udo Sechtem, Ingrid Kindermann, Matthias Gutberlet, Leslie T Cooper, Peter Liu, et al. "Cardiovascular magnetic resonance in nonischemic myocardial inflammation: expert recommendations." In: *Journal of the American College of Cardiology* 72.24 (2018), pp. 3158–3176.
- [20] World Health Organization. *The top 10 causes of death*. <https://www.who.int/news-room/fact-sheets/detail/the-top-10-causes-of-death>. Accessed: 2024-03-25. 2020.
- [21] Adam Timmis, Panos Vardas, Nick Townsend, Aleksandra Torbica, Hugo Katus, Delphine De Smedt, Chris P Gale, Aldo P Maggioni, Steffen E Petersen, Radu Huculeci, et al. "European Society of Cardiology: cardiovascular disease statistics 2021." In: *European Heart Journal* 43.8 (2022), pp. 716–799.
- [22] Elizabeth Wilkins, L Wilson, Kremlin Wickramasinghe, Prachi Bhatnagar, Jose Leal, Ramon Luengo-Fernandez, R Burns, Mike Rayner, and Nick Townsend. *European Cardiovascular Disease Statistics 2017*. European Heart Network, Feb. 2017.

- [23] Ramon Luengo-Fernandez, Marjan Walli-Attai, Alastair Gray, Aleksandra Torbica, Aldo P Maggioni, Radu Huculeci, Firoozeh Bairami, Victor Aboyans, Adam D Timmis, Panos Vardas, et al. "Economic burden of cardiovascular diseases in the European Union: a population-based cost study." In: *European Heart Journal* 44.45 (2023), pp. 4752–4767.
- [24] Stylianos A Pyxaras, William Wijns, Johan HC Reiber, and Jeroen J Bax. "Invasive assessment of coronary artery disease." In: *Journal of Nuclear Cardiology* 25 (2018), pp. 860–871.
- [25] Hendrik J Harms, Sergey V Nesterov, Chunlei Han, Ibrahim Danad, Remigio Leonora, Pieter G Raijmakers, Adriaan A Lammertsma, Juhani Knuuti, and Paul Knaapen. "Comparison of clinical non-commercial tools for automated quantification of myocardial blood flow using oxygen-15-labelled water PET/CT." In: *European Heart Journal–Cardiovascular Imaging* 15.4 (2014), pp. 431–441.
- [26] A. A. Qayyum and J. Kastrup. "Measuring myocardial perfusion: The role of PET, MRI and CT." In: *Clinical Radiology* 70.6 (2015), pp. 576–584.
- [27] Hanns-Joachim Weinmann, Robert C Brasch, Wolf-R Press, and George E Wesbey. "Characteristics of gadolinium-DTPA complex: a potential NMR contrast agent." In: *American Journal of Roentgenology* 142.3 (1984), pp. 619–624.
- [28] Peter Marckmann, Lone Skov, Kristian Rossen, Anders Dupont, Mette Brimnes Damholt, James Goya Heaf, and Henrik S. Thomsen. "Nephrogenic systemic fibrosis: Suspected causative role of gadodiamide used for contrast-enhanced magnetic resonance imaging." In: *Journal of the American Society of Nephrology* 17.9 (Sept. 2006), pp. 2359–2362.
- [29] L Daftari Besheli, S Aran, K Shaqdan, Jonathan Kay, and H Abujudeh. "Current status of nephrogenic systemic fibrosis." In: *Clinical radiology* 69.7 (2014), pp. 661–668.
- [30] Andreas Kribben, Oliver Witzke, Uwe Hillen, Jörg Barkhausen, Anton E Daul, and Raimund Erbel. "Nephrogenic systemic fibrosis: pathogenesis, diagnosis, and therapy." In: *Journal of the American College of Cardiology* 53.18 (2009), pp. 1621–1628.
- [31] Tomonori Kanda, Kazunari Ishii, Hiroki Kawaguchi, Kazuhiro Kitajima, and Daisuke Takenaka. "High signal intensity in the dentate nucleus and globus pallidus on unenhanced T1-weighted MR images: Relationship with increasing cumulative dose of a gadoliniumbased contrast material." In: *Radiology* 270.3 (2014), pp. 834–841.
- [32] Tomonori Kanda, Yudai Nakai, Hiroshi Oba, Keiko Toyoda, Kazuhiro Kitajima, and Shigeru Furui. "Gadolinium deposition in the brain." In: *Magnetic Resonance Imaging* 34.10 (2016), pp. 1346–1350.
- [33] David C. Alsop et al. "Recommended implementation of arterial spin-labeled Perfusion mri for clinical applications: A consensus of the ISMRM Perfusion Study group and the European consortium for ASL in dementia." In: *Magnetic Resonance in Medicine* 73.1 (2015), pp. 102–116.

- [34] Verónica Aramendía-Vidaurreta, Rebeca Echeverría-Chasco, Marta Vidorreta, Gorka Bastarrika, and María A Fernández-Seara. "Quantification of Myocardial Perfusion With Vasodilation Using Arterial Spin Labeling at 1.5T." In: *Journal of Magnetic Resonance Imaging* n/a.n/a (Oct. 2020).
- [35] Zungho Zun, Padmini Varadarajan, Ramdas G. Pai, Eric C. Wong, and Krishna S. Nayak. "Arterial spin labeled CMR detects clinically relevant increase in myocardial blood flow with vasodilation." In: *JACC: Cardiovascular Imaging* 4.12 (2011), pp. 1253–1261.
- [36] Verónica Aramendía-Vidaurreta, Alejandro García-Osés, Marta Vidorreta, Gorka Bastarrika, and María A. Fernández-Seara. "Optimal repetition time for free breathing myocardial arterial spin labeling." In: *NMR in Biomedicine* 32.5 (2019), e4077.
- [37] Hung Phi Do, Terrence R. Jao, and Krishna S. Nayak. "Myocardial arterial spin labeling perfusion imaging with improved sensitivity." In: *Journal of Cardiovascular Magnetic Resonance* 16.1 (2014), pp. 1–6.
- [38] Frank Kober, Terrence Jao, Thomas Troalen, and Krishna S. Nayak. "Myocardial arterial spin labeling." In: *Journal of Cardiovascular Magnetic Resonance* 18.1 (2016), pp. 1–16.
- [39] Frederick H. Epstein and Craig H. Meyer. "Myocardial perfusion using arterial spin labeling CMR: Promise and challenges." In: *JACC: Cardiovascular Imaging* 4.12 (2011), pp. 1262–1264.
- [40] Zungho Zun, Eric C. Wong, and Krishna S. Nayak. "Assessment of myocardial blood flow (MBF) in humans using arterial spin labeling (ASL): Feasibility and noise analysis." In: *Magnetic Resonance in Medicine* 62.4 (2009), pp. 975–983.
- [41] Maša Božić-Iven, Stanislas Rapacchi, Qian Tao, Iain Pierce, George Thornton, Christian Nitsche, Thomas A Treibel, Lothar R Schad, and Sebastian Weingärtner. "Improved reproducibility for myocardial ASL: Impact of physiological and acquisition parameters." In: *Magnetic Resonance in Medicine* 91.1 (2024), pp. 118–132.
- [42] Maša Božić-Iven, Yi Zhang, Qian Tao, Stanislas Rapacchi, Lothar R. Schad, and Sebastian Weingärtner. "Myocardium signal suppression with T₂-preparations for reduced physiological noise in myocardial ASL." In: *Proceedings of the SCMR Annual Scientific Sessions*. 2024.
- [43] Maša Božić-Iven, Yi Zhang, Qian Tao, Stanislas Rapacchi, Lothar R. Schad, and Sebastian Weingärtner. "Double Inversion Recovery in Myocardial Arterial Spin Labeling (ASL) for reduced physiological noise." In: *Proceedings of the Annual Meeting of the ISMRM*. 2024.
- [44] Markus Henningsson, Carl-Johan Carlhäll, and Johan Kihlberg. "Myocardial arterial spin labeling in systole and diastole using flow-sensitive alternating inversion recovery with parallel imaging and compressed sensing." In: *NMR in Biomedicine* 34.2 (2021), e4436.

- [45] Verónica Aramendía-Vidaurreta, Rebeca Echeverría-Chasco, Marta Vidorreta, Gorka Bastarrika, and María A Fernández-Seara. “Quantification of Myocardial Perfusion With Vasodilation Using Arterial Spin Labeling at 1.5T.” In: *Journal of Magnetic Resonance Imaging* 53.3 (Oct. 2021), pp. 777–788.
- [46] Nadine Kawel-Boehm et al. “Reference ranges (“normal values”) for cardiovascular magnetic resonance (CMR) in adults and children: 2020 update.” In: *Journal of Cardiovascular Magnetic Resonance* 22.1 (Dec. 2020).
- [47] Greg J Stanisz, Ewa E Odrobina, Joseph Pun, Michael Escaravage, Simon J Graham, Michael J Bronskill, and R Mark Henkelman. “T₁, T₂ relaxation and magnetization transfer in tissue at 3T.” In: *Magnetic Resonance in Medicine* 54.3 (2005), pp. 507–512.
- [48] Robert R Edelman, Daisy Chien, and Ducksoo Kim. “Fast selective black blood MR imaging.” In: *Radiology* 181.3 (1991), pp. 655–660.
- [49] Tevfik F Ismail, Wendy Strugnell, Chiara Coletti, Maša Božić-Iven, Sebastian Weingaertner, Kerstin Hammernik, Teresa Correia, and Thomas Kuestner. “Cardiac MR: from theory to practice.” In: *Frontiers in cardiovascular medicine* 9 (2022), p. 826283.
- [50] Joao Tourais, Chiara Coletti, and Sebastian Weingärtner. “Brief Introduction to MRI Physics.” In: *Advances in Magnetic Resonance Technology and Applications*. Vol. 7. Elsevier, 2022, pp. 3–36.
- [51] Jorge Zavala Bojorquez, Stéphanie Bricq, Clement Acquitte, François Brunotte, Paul M Walker, and Alain Lalande. “What are normal relaxation times of tissues at 3 T?” In: *Magnetic resonance imaging* 35 (2017), pp. 69–80.
- [52] Jürgen Hennig. “Echoes—how to generate, recognize, use or avoid them in MR-imaging sequences. Part I: Fundamental and not so fundamental properties of spin echoes.” In: *Concepts in Magnetic Resonance* 3.3 (1991), pp. 125–143.
- [53] Jürgen Hennig. “Echoes—how to generate, recognize, use or avoid them in MR-imaging sequences. Part II: Echoes in imaging sequences.” In: *Concepts in Magnetic Resonance* 3.4 (1991), pp. 179–192.
- [54] Matthias Weigel. “Extended phase graphs: dephasing, RF pulses, and echoes-pure and simple.” In: *Journal of Magnetic Resonance Imaging* 41.2 (2015), pp. 266–295.
- [55] Li Feng, Dan Ma, and Fang Liu. “Rapid MR relaxometry using deep learning: An overview of current techniques and emerging trends.” In: *NMR in Biomedicine* (2020), e4416.
- [56] Mehmet Akcakaya, Mariya Ivanova Doneva, and Claudia Prieto. *Magnetic resonance image reconstruction: theory, methods, and applications*. Academic Press, 2022.
- [57] Bertram J Wilm, Christoph Barmet, Matteo Pavan, and Klaas P Pruessmann. “Higher order reconstruction for MRI in the presence of spatiotemporal field perturbations.” In: *Magnetic Resonance in Medicine* 65.6 (2011), pp. 1690–1701.

- [58] Erwin L Hahn. "Spin echoes." In: *Physical review* 80.4 (1950), p. 580.
- [59] Peter Mansfield and Andrew A Maudsley. "Planar spin imaging by NMR." In: *Journal of Physics C: Solid State Physics* 9.15 (1976), p. L409.
- [60] Kensuke Sekihara. "Steady-state magnetizations in rapid NMR imaging using small flip angles and short repetition intervals." In: *IEEE transactions on medical imaging* 6.2 (1987), pp. 157–164.
- [61] Klaus Scheffler and Stefan Lehnhardt. "Principles and applications of balanced SSFP techniques." In: *European Radiology* 13.11 (2003), pp. 2409–2418.
- [62] Oliver Bieri and Klaus Scheffler. "Fundamentals of balanced steady state free precession MRI." In: *Journal of Magnetic Resonance Imaging* 38.1 (2013), pp. 2–11.
- [63] Graeme M Bydder and Ian R Young. "MR imaging: clinical use of the inversion recovery sequence." In: *J Comput Assist Tomogr* 9.4 (1985), pp. 659–675.
- [64] Malcolm H. Levitt. "Composite pulses." In: *Progress in Nuclear Magnetic Resonance Spectroscopy* 18.2 (1986), pp. 61–122.
- [65] Kâmil Uğurbil, Michael Garwood, and M Robin Bendall. "Amplitude- and frequency-modulated pulses to achieve 90° plane rotations with inhomogeneous B₁ fields." In: *Journal of Magnetic Resonance* 72.1 (1987), pp. 177–185.
- [66] Jean H Brittain, Bob S Hu, Graham A Wright, Craig H Meyer, Albert Mavrovski, and Dwight G Nishimura. "Coronary angiography with magnetization - prepared T₂ contrast." In: *Magnetic Resonance in Medicine* 33.5 (1995), pp. 689–696.
- [67] Warren D Foltz, Osama Al-Kwif, Marshall S Sussman, Jeff A Stainsby, and Graham A Wright. "Optimized spiral imaging for measurement of myocardial T₂ relaxation." In: *Magnetic Resonance in Medicine* 49.6 (2003), pp. 1089–1097.
- [68] Teng-Yi Huang, Yi-Jui Liu, Alto Stemmer, and Brigitte P Poncelet. "T₂ measurement of the human myocardium using a T₂-prepared transient-state TrueFISP sequence." In: *Magnetic Resonance in Medicine* 57.5 (2007), pp. 960–966.
- [69] Shivraman Giri, Yiu-Cho Chung, Ali Merchant, Georgeta Mihai, Sanjay Rajagopalan, Subha V Raman, and Orlando P Simonetti. "T₂ quantification for improved detection of myocardial edema." In: *Journal of Cardiovascular Magnetic Resonance* 11.1 (2009), pp. 1–13.
- [70] Paul A Iaizzo. "General features of the cardiovascular system." In: *Handbook of Cardiac Anatomy, Physiology, and Devices* (2015), pp. 3–12.
- [71] Anthony J Weinhaus and Kenneth P Roberts. "Anatomy of the human heart." In: *Handbook of cardiac anatomy, physiology, and devices* (2005), pp. 51–79.

- [72] Monica Diez-Silva, Ming Dao, Jongyoon Han, Chwee-Teck Lim, and Subra Suresh. "Shape and biomechanical characteristics of human red blood cells in health and disease." In: *MRS Bulletin* 35.5 (2010), pp. 382–388.
- [73] Cleveland Clinic. *Heart*. <https://my.clevelandclinic.org/health/body/21704-heart>. Accessed: 2024-03-30. 2024.
- [74] Adam G Goodwill, Gregory M Dick, Alexander M Kiel, and Johnathan D Tune. "Regulation of coronary blood flow." In: *Comprehensive Physiology* 7.2 (2017), p. 321.
- [75] Sara E Anderson, Ryan Lahm, and Paul A Iaizzo. "The coronary vascular system and associated medical devices." In: *Handbook of Cardiac Anatomy, Physiology, and Devices* (2009), pp. 109–123.
- [76] Monique GJTb van Lier, Elco Oost, Jos AE Spaan, Pepijn van Horssen, Allard C van der Wal, Maria Siebes, Jeroen PHM van den Wijngaard, et al. "Transmural distribution and connectivity of coronary collaterals within the human heart." In: *Cardiovascular Pathology* 25.5 (2016), pp. 405–412.
- [77] Russell S Richardson, David C Poole, Douglas R Knight, Sadi S Kurdak, Michael C Hogan, Bruno Grassi, Emily C Johnson, Keith F Kendrick, B Kipp Erickson, and Peter D Wagner. "High muscle blood flow in man: is maximal O₂ extraction compromised?" In: *Journal of Applied Physiology* 75.4 (1993), pp. 1911–1916.
- [78] Russell S Richardson. "Oxygen transport: air to muscle cell." In: *Medicine and science in sports and exercise* 30.1 (1998), pp. 53–59.
- [79] Arthur H.L. From and Robert J. Bache. "Energy metabolism in the normal and diseased heart." In: *Handbook of Cardiac Anatomy, Physiology, and Devices: Second Edition*. Humana Press, 2005, pp. 297–317.
- [80] Jeanette Schulz-Menger et al. "Standardized image interpretation and post-processing in cardiovascular magnetic resonance - 2020 update: Society for Cardiovascular Magnetic Resonance (SCMR): Board of Trustees Task Force on Standardized Post-Processing." In: *Journal of Cardiovascular Magnetic Resonance* 22.1 (Mar. 2020).
- [81] Marc Dewey et al. "Clinical quantitative cardiac imaging for the assessment of myocardial ischaemia." In: *Nature Reviews Cardiology* 17.7 (July 2020), pp. 427–450.
- [82] Aldo J. Vázquez Mézquita et al. "Clinical quantitative coronary artery stenosis and coronary atherosclerosis imaging: a Consensus Statement from the Quantitative Cardiovascular Imaging Study Group." In: *Nature Reviews Cardiology* 20.10 (Oct. 2023), pp. 696–714.
- [83] Nico HJ Pijls, Bernard de Bruyne, Kathinka Peels, Pepijn H van der Voort, Hans JRM Bonnier, Jozef Bartunek, and Jacques J Koolen. "Measurement of fractional flow reserve to assess the functional severity of coronary-artery stenoses." In: *New England Journal of Medicine* 334.26 (1996), pp. 1703–1708.

- [84] Gilles Montalescot, Udo Sechtem, Stephan Achenbach, Felicita Andreotti, Chris Arden, Andrzej Budaj, Raffaele Bugiardini, Filippo Crea, Thomas Cuisset, et al. "2013 ESC guidelines on the management of stable coronary artery disease." In: *European Heart Journal* 34.38 (2013), pp. 2949–3003.
- [85] Michael Salerno and George A Beller. "Noninvasive assessment of myocardial perfusion." In: *Circulation: Cardiovascular Imaging* 2.5 (2009), pp. 412–424.
- [86] GW Bourne and JM Trifaró. "The gadolinium ion: a potent blocker of calcium channels and catecholamine release from cultured chromaffin cells." In: *Neuroscience* 7.7 (1982), pp. 1615–1622.
- [87] Theresa A McDonagh, Marco Metra, Marianna Adamo, Roy S Gardner, Andreas Baumbach, Michael Böhm, Haran Burri, Javed Butler, Jelena Čelutkienė, Ovidiu Chioncel, et al. "2021 ESC Guidelines for the diagnosis and treatment of acute and chronic heart failure: Developed by the Task Force for the diagnosis and treatment of acute and chronic heart failure of the European Society of Cardiology (ESC) With the special contribution of the Heart Failure Association (HFA) of the ESC." In: *European Heart Journal* 42.36 (2021), pp. 3599–3726.
- [88] Raymond J Kim, Dipan J Shah, and Robert M Judd. "How we perform delayed enhancement imaging: HOW I DO..." In: *Journal of cardiovascular magnetic resonance* 5.3 (2003), pp. 505–514.
- [89] Raymond J Kim, David S Fieno, Todd B Parrish, Kathleen Harris, En-Ling Chen, Orlando Simonetti, Jeffrey Bundy, J Paul Finn, Francis J Klocke, and Robert M Judd. "Relationship of MRI delayed contrast enhancement to irreversible injury, infarct age, and contractile function." In: *Circulation* 100.19 (1999), pp. 1992–2002.
- [90] Heiko Mahrholdt, Anja Wagner, Robert M Judd, Udo Sechtem, and Raymond J Kim. "Delayed enhancement cardiovascular magnetic resonance assessment of non-ischaemic cardiomyopathies." In: *European heart journal* 26.15 (2005), pp. 1461–1474.
- [91] Eva C. Sammut et al. "Prognostic Value of Quantitative Stress Perfusion Cardiac Magnetic Resonance." In: *JACC: Cardiovascular Imaging* 11.5 (May 2018), pp. 686–694.
- [92] Paolo G Camici, Giulia d'Amati, and Ornella Rimoldi. "Coronary microvascular dysfunction: mechanisms and functional assessment." In: *Nature Reviews Cardiology* 12.1 (2015), pp. 48–62.
- [93] G. L. T. F. Hautvast, A. Chiribiri, T. Lockie, M. Breeuwer, E. Nagel, and S. Plein. "Quantitative analysis of transmural gradients in myocardial perfusion magnetic resonance images." In: *Magnetic Resonance in Medicine* 66.5 (2011), pp. 1477–1487.

- [94] Wolfgang Utz, Thoralf Niendorf, Ralf Wassmuth, Daniel Messroghli, Rainer Dietz, and Jeanette Schulz-Menger. "Contrast-dose relation in first-pass myocardial MR perfusion imaging." In: *Journal of Magnetic Resonance Imaging: An Official Journal of the International Society for Magnetic Resonance in Medicine* 25.6 (2007), pp. 1131–1135.
- [95] Timothy F Christian, Anthony H Aletras, and Andrew E Arai. "Estimation of absolute myocardial blood flow during first-pass MR perfusion imaging using a dual-bolus injection technique: Comparison to single-bolus injection method." In: *Journal of Magnetic Resonance Imaging* 27.6 (2008), pp. 1271–1277.
- [96] Peter D Gatehouse, Andrew G Elkington, Nicholas A Ablitt, Guang-Zhong Yang, Dudley J Pennell, and David N Firmin. "Accurate assessment of the arterial input function during high-dose myocardial perfusion cardiovascular magnetic resonance." In: *Journal of Magnetic Resonance Imaging* 20.1 (2004), pp. 39–45.
- [97] Michael Jerosch-Herold. "Quantification of myocardial perfusion by cardiovascular magnetic resonance." In: *Journal of Cardiovascular Magnetic Resonance* 12.1 (2010), p. 57.
- [98] Peter Kellman, Michael S Hansen, Sonia Nielles-Vallespin, Jannike Nickander, Raquel Themudo, Martin Ugander, and Hui Xue. "Myocardial perfusion cardiovascular magnetic resonance: optimized dual sequence and reconstruction for quantification." In: *Journal of Cardiovascular Magnetic Resonance* 19.1 (2017), pp. 1–14.
- [99] Michael Jerosch-Herold, Norbert Wilke, Ying Wang, Guan-Rong Gong, Abdul M Mansoor, Hong Huang, Shota Gurchumelidze, and Arthur E Stillman. "Direct comparison of an intravascular and an extracellular contrast agent for quantification of myocardial perfusion." In: *International Journal of Cardiac Imaging* 15 (1999), pp. 453–456.
- [100] Michael Jerosch-Herold, Cory Swingen, and Ravi Teja Seethamraju. "Myocardial blood flow quantification with MRI by model-independent deconvolution." In: *Medical physics* 29.5 (2002), pp. 886–897.
- [101] Kenneth L Zierler. "Equations for measuring blood flow by external monitoring of radioisotopes." In: *Circulation research* 16.4 (1965), pp. 309–321.
- [102] Gaetano Alfano, Francesco Fontana, Annachiara Ferrari, Andrea Solazzo, Rossella Perrone, Francesco Giaroni, Pietro Torricelli, and Gianni Cappelli. "Incidence of nephrogenic systemic fibrosis after administration of gadoteric acid in patients on renal replacement treatment." In: *Magnetic Resonance Imaging* 70 (2020), pp. 1–4.
- [103] Saroj Vadhan-Raj, David C Ford, Naomi V Dahl, Kristine Bernard, Zhu Li, Lee F Allen, and William E Strauss. "Safety and efficacy of ferumoxytol for the episodic treatment of iron deficiency anemia in patients with a history of unsatisfactory oral iron therapy: results of a phase III, open-label, 6-month extension study." In: *American Journal of Hematology* 91.2 (2016), E3.

- [104] U.S. Food and Drug Administration. *FDA Drug Safety Communication: FDA strengthens warnings and changes prescribing instructions to decrease the risk of serious allergic reactions with anemia drug Ferumoxytol*. <https://www.fda.gov/drugs/drug-safety-and-availability/fda-drug-safety-communication-fda-strengthens-warnings-and-changes-prescribing-instructions-decrease>. Accessed: 2024-03-25. Mar. 2015.
- [105] European Medicines Agency. *Public statement: Rienso (ferumoxytol) - Withdrawal of the marketing authorisation in the European Union*. https://www.ema.europa.eu/en/documents/public-statement/public-statement-rienso-ferumoxytol-withdrawal-marketing-authorisation-european-union_en.pdf. Accessed: 2024-03-25. July 2015.
- [106] Faraz Ahmad, Lee Treanor, Trevor A. McGrath, Daniel Walker, Matthew D.F. McInnes, and Nicola Schieda. "Safety of Off-Label Use of Ferumoxytol as a Contrast Agent for MRI: A Systematic Review and Meta-Analysis of Adverse Events." In: *Journal of Magnetic Resonance Imaging* 53.3 (Mar. 2021), pp. 840–858.
- [107] John A Detre, John S Leigh, Donald S Williams, and Alan P Koretsky. "Perfusion imaging." In: *Magnetic Resonance in Medicine* 23.1 (1992), pp. 37–45.
- [108] Richard B. Buxton, Lawrence R. Frank, Eric C. Wong, Bettina Siewert, Steven Warach, and Robert R. Edelman. "A general kinetic model for quantitative perfusion imaging with arterial spin labeling." In: *Magnetic Resonance in Medicine* 40.3 (1998), pp. 383–396.
- [109] A Courtney Henderson, G Kim Prisk, David L Levin, Susan R Hopkins, and Richard B Buxton. "Characterizing pulmonary blood flow distribution measured using arterial spin labeling." In: *NMR in Biomedicine: An International Journal Devoted to the Development and Application of Magnetic Resonance In vivo* 22.10 (2009), pp. 1025–1035.
- [110] Penny A Gowland, Susan T Francis, Keith R Duncan, Alan J Freeman, Bashar Issa, Rachel J Moore, Richard W Bowtell, Philip N Baker, Ian R Johnson, and Brian S Worthington. "In vivo perfusion measurements in the human placenta using echo planar imaging at 0.5 T." In: *Magnetic Resonance in Medicine* 40.3 (1998), pp. 467–473.
- [111] Xingfeng Shao, Dapeng Liu, Thomas Martin, Teresa Chanlaw, Sherin U Devaskar, Carla Janzen, Aisling M Murphy, Daniel Margolis, Kyunghyun Sung, and Danny JJ Wang. "Measuring human placental blood flow with multidelay 3D GRASE pseudocontinuous arterial spin labeling at 3T." In: *Journal of Magnetic Resonance Imaging* 47.6 (2018), pp. 1667–1676.
- [112] Fabio Nery, Charlotte E Buchanan, Anita A Harteveld, Aghogho Odudu, Octavia Bane, Eleanor F Cox, Katja Derlin, H Michael Gach, Xavier Gollay, Marcel Gutberlet, et al. "Consensus-based technical recommendations for clinical translation of renal ASL MRI." In: *Magnetic Resonance Materials in Physics, Biology and Medicine* 33 (2020), pp. 141–161.

- [113] Manuel Taso et al. "Update on state-of-the-art for arterial spin labeling (ASL) human perfusion imaging outside of the brain." In: *Magnetic Resonance in Medicine* (2023).
- [114] Panithaya Chareonthaitawee, Philipp A Kaufmann, Ornella Rimoldi, and Paolo G Camici. "Heterogeneity of resting and hyperemic myocardial blood flow in healthy humans." In: *Cardiovascular research* 50.1 (2001), pp. 151–161.
- [115] Brigitte P Poncelet, Todd M Koelling, Christopher J Schmidt, Kenneth K Kwong, Timothy G Reese, Patrick Ledden, Howard L Kantor, Thomas J Brady, and Robert M Weisskoff. "Measurement of human myocardial perfusion by double-gated flow alternating inversion recovery EPI." In: *Magnetic Resonance in Medicine* 41.3 (1999), pp. 510–519.
- [116] Danny JJ Wang, Xiaoming Bi, Brian B Avants, Tongbai Meng, Sven Zuehlsdorff, and John A Detre. "Estimation of perfusion and arterial transit time in myocardium using free-breathing myocardial arterial spin labeling with navigator-echo." In: *Magnetic Resonance in Medicine* 64.5 (2010), pp. 1289–1295.
- [117] Markus Henningson, Carl Johan Carlhäll, Tino Ebbers, and Johan Kihlberg. "Non-contrast myocardial perfusion in rest and exercise stress using systolic flow-sensitive alternating inversion recovery." In: *Magnetic Resonance Materials in Physics, Biology and Medicine* 35.5 (Oct. 2022), pp. 711–718.
- [118] Florian Fidler, Christian M. Wacker, Christian Dueren, Matthias Weigel, Peter M. Jakob, Wolfgang R. Bauer, and Axel Haase. "Myocardial perfusion measurements by spin-labeling under different vasodynamic states." In: *Journal of Cardiovascular Magnetic Resonance* 6.2 (2004), pp. 509–516.
- [119] Christian M. Wacker, Michael Bock, Andreas W. Hartlep, Gabriele Beck, Gerhard Van Kaick, Georg Ertl, Wolfgang R. Bauer, and Lothar R. Schad. "Changes in myocardial oxygenation and perfusion under pharmacological stress with dipyridamole: Assessment using T² and T₁ measurements." In: *Magnetic Resonance in Medicine* 41.4 (1999), pp. 686–695.
- [120] Christian M. Wacker, Florian Fidler, Christian Dueren, Stefan Hirn, Peter M. Jakob, Georg Ertl, Axel Haase, and Wolfgang R. Bauer. "Quantitative Assessment of Myocardial Perfusion With a Spin-Labeling Technique: Preliminary Results in Patients with Coronary Artery Disease." In: *Journal of Magnetic Resonance Imaging* 18.5 (2003), pp. 555–560.
- [121] Thibaut Capron, Thomas Troalen, Benjamin Robert, Alexis Jacquier, Monique Bernard, and Frank Kober. "Myocardial perfusion assessment in humans using steady-pulsed arterial spin labeling." In: *Magnetic Resonance in Medicine* 74.4 (2015), pp. 990–998.
- [122] Eric C Wong, Matthew Cronin, Wen-Chau Wu, Ben Inglis, Lawrence R Frank, and Thomas T Liu. "Velocity-selective arterial spin labeling." In: *Magnetic Resonance in Medicine* 55.6 (2006), pp. 1334–1341.

- [123] Qin Qin, David C Alsop, Divya S Bolar, Luis Hernandez-Garcia, James Meakin, Dapeng Liu, Krishna S Nayak, Sophie Schmid, Matthias JP van Osch, Eric C Wong, et al. "Velocity-selective arterial spin labeling perfusion MRI: a review of the state of the art and recommendations for clinical implementation." In: *Magnetic Resonance in Medicine* 88.4 (2022), pp. 1528–1547.
- [124] Terrence R. Jao and Krishna S. Nayak. "Demonstration of velocity selective myocardial arterial spin labeling perfusion imaging in humans." In: *Magnetic Resonance in Medicine* 80.1 (2018), pp. 272–278.
- [125] Vanessa Landes, Ahsan Javed, Terrence Jao, Qin Qin, and Krishna Nayak. "Improved velocity-selective labeling pulses for myocardial ASL." In: *Magnetic Resonance in Medicine* 84.4 (2020), pp. 1909–1918.
- [126] Seong-Gi Kim. "Quantification of relative cerebral blood flow change by flow-sensitive alternating inversion recovery (FAIR) technique: Application to functional mapping." In: *Magnetic Resonance in Medicine* 34.3 (Sept. 1995), pp. 293–301.
- [127] A. Javed and K.S. Nayak. "Single-shot EPI for ASL-CMR." In: *Magnetic Resonance in Medicine* (2020).
- [128] Manuel D. Cerqueira, Neil J. Weissman, Vasken Dilsizian, Alice K. Jacobs, Sanjiv Kaul, Warren K. Laskey, Dudley J. Pennell, John A. Rumberger, Thomas Ryan, and Mario S. Verani. "Standardized myocardial segmentation and nomenclature for tomographic imaging of the heart: A statement for healthcare professionals from the Cardiac Imaging Committee of the Council on Clinical Cardiology of the American Heart Association." In: *Journal of Nuclear Cardiology* 9.2 (2002), pp. 240–245.
- [129] Klaas P Pruessmann, Markus Weiger, Markus B Scheidegger, and Peter Boesiger. "SENSE: sensitivity encoding for fast MRI." In: *Magnetic Resonance in Medicine* 42.5 (1999), pp. 952–962.
- [130] Hung Phi Do, Andrew J. Yoon, Michael W. Fong, Farhood Saremi, Mark L. Barr, and Krishna S. Nayak. "Double-gated myocardial ASL perfusion imaging is robust to heart rate variation." In: *Magnetic Resonance in Medicine* 77.5 (2017), pp. 1975–1980.
- [131] Verónica Aramendía-Vidaurreta, Sergio M Solís-Barquero, Marta Vidurreta, Ana Ezponda, Rebeca Echeverria-Chasco, Gorika Bastarrika, and María A Fernández-Seara. "Comparison of Myocardial Blood Flow Quantification Models for Double ECG Gating Arterial Spin Labeling MRI: Reproducibility Assessment." In: *Journal of Magnetic Resonance Imaging* (2024).
- [132] Scott B Reeder, Michael K Atalay, Elliot R McVeigh, Elias A Zerhouni, and John R Forder. "Quantitative cardiac perfusion: a noninvasive spin-labeling method that exploits coronary vessel geometry." In: *Radiology* 200.1 (1996), pp. 177–184.

- [133] Valérie Belle, Elke Kahler, Christiane Waller, Eberhard Rommel, Sabine Voll, Karl-Heinz Hiller, Wolfgang R Bauer, and Axel Haase. "In vivo quantitative mapping of cardiac perfusion in rats using a noninvasive MR spin-labeling method." In: *Journal of Magnetic Resonance Imaging* 8.6 (1998), pp. 1240–1245.
- [134] Benjamin E. Northrup, Kyle S. McCommis, Haosen Zhang, Shuddhadeb Ray, Pamela K. Woodard, Robert J. Gropler, and Jie Zheng. "Resting myocardial perfusion quantification with CMR arterial spin labeling at 1.5 T and 3.0 T." In: *Journal of Cardiovascular Magnetic Resonance* 10.1 (2008), pp. 1–9.
- [135] David C Look and Donald R Locker. "Time saving in measurement of NMR and EPR relaxation times." In: *Review of scientific instruments* 41.2 (1970), pp. 250–251.
- [136] Daniel R Messroghli, Aleksandra Radjenovic, Sebastian Kozerke, David M Higgins, Mohan U Sivananthan, and John P Ridgway. "Modified Look-Locker inversion recovery (MOLLI) for high-resolution T1 mapping of the heart." In: *Magnetic Resonance in Medicine* 52.1 (2004), pp. 141–146.
- [137] Graeme A. Keith, Christopher T. Rodgers, Michael A. Chappell, and Matthew D. Robson. "A look-locker acquisition scheme for quantitative myocardial perfusion imaging with FAIR arterial spin labeling in humans at 3 tesla." In: *Magnetic Resonance in Medicine* 78.2 (Aug. 2017), pp. 541–549.
- [138] Kyle S McCommis, Thomas A Goldstein, Haosen Zhang, Bernd Miseselwitz, Robert J Gropler, and Jie Zheng. "Quantification of myocardial blood volume during dipyridamole and dobutamine stress: a perfusion CMR study." In: *Journal of Cardiovascular Magnetic Resonance* 9.5 (2007), pp. 785–792.
- [139] SR Bergmann, KA Fox, AL Rand, KD McElvany, MJ Welch, J Markham, and BE Sobel. "Quantification of regional myocardial blood flow in vivo with H₂¹⁵O." In: *Circulation* 70.4 (1984), pp. 724–733.
- [140] Mitsue Miyazaki, Xiangzhi Zhou, Tsutomu Hoshino, Kenichi Yokoyama, Rieko Ishimura, and Toshiaki Nitatori. "Non-contrast myocardial perfusion using a novel 4D magnetic resonance arterial spin labeling technique: initial experience." In: *Microvascular Research* 98 (2015), pp. 94–101.
- [141] DJ Atkinson, D Burstein, and RR Edelman. "First-pass cardiac perfusion: evaluation with ultrafast MR imaging." In: *Radiology* 174.3 (1990), pp. 757–762.
- [142] Jane S Skinner, Liam Smeeth, Jason M Kendall, Philip C Adams, and Adam Timmis. "NICE guidance. Chest pain of recent onset: assessment and diagnosis of recent onset chest pain or discomfort of suspected cardiac origin." In: *Heart* 96.12 (2010), pp. 974–978.

- [143] Juerg Schwitter, Daniel Nanz, Stefan Kneifel, Katharina Bertschinger, M Buchi, PR Knusel, Borut Marincek, TF Luscher, and Gustav K von Schulthess. "Assessment of myocardial perfusion in coronary artery disease by magnetic resonance: a comparison with positron emission tomography and coronary angiography." In: *Circulation* 103.18 (2001), pp. 2230–2235.
- [144] E Kanal, K Maravilla, and HA Rowley. "Gadolinium contrast agents for CNS imaging: current concepts and clinical evidence." In: *American Journal of Neuroradiology* 35.12 (2014), pp. 2215–2226.
- [145] Mark Perazella. "Gadolinium-Contrast Toxicity in Patients with Kidney Disease: Nephrotoxicity and Nephrogenic Systemic Fibrosis." In: *Current Drug Safety* 3.1 (2008), pp. 67–75.
- [146] Donald S Williams, John A Detre, John S Leigh, and Alan P Koretsky. "Magnetic resonance imaging of perfusion using spin inversion of arterial water." In: *Proceedings of the National Academy of Sciences* 89.1 (1992), pp. 212–216.
- [147] Sven Haller, Greg Zaharchuk, David L Thomas, Karl-Olof Lovblad, Fredrik Barkhof, and Xavier Golay. "Arterial spin labeling perfusion of the brain: emerging clinical applications." In: *Radiology* 281.2 (2016), pp. 337–356.
- [148] Luis Hernandez-Garcia, Anish Lahiri, and Jonas Schollenberger. "Recent progress in ASL." In: *Neuroimage* 187 (2019), pp. 3–16.
- [149] Terrence Jao and Krishna Nayak. "Analysis of physiological noise in quantitative cardiac magnetic resonance." In: *Public Library of Science (PLOS) One* 14.8 (2019), e0214566.
- [150] G Heusch. "Heart rate in the pathophysiology of coronary blood flow and myocardial ischaemia: benefit from selective bradycardic agents." In: *British Journal of Pharmacology* 153.8 (2008), pp. 1589–1601.
- [151] Ingo Hermann, Peter Kellman, Omer B Demirel, Mehmet Akçakaya, Lothar R Schad, and Sebastian Weingärtner. "Free-breathing simultaneous T₁, T₂, and T₂* quantification in the myocardium." In: *Magnetic Resonance in Medicine* 86.3 (2021), pp. 1226–1240.
- [152] Sebastian Weingärtner, Nadja M Meßner, Johannes Budjan, Dirk Loßnitzer, Uwe Mattler, Theano Papavassiliu, Frank G Zöllner, and Lothar R Schad. "Myocardial T₁-mapping at 3T using saturation-recovery: reference values, precision and comparison with MOLLI." In: *Journal of Cardiovascular Magnetic Resonance* 18.1 (2017), pp. 1–9.
- [153] Sebastian Weingärtner, Kimberly L Desmond, Nancy A Obuchowski, Bettina Baessler, Yuxin Zhang, Emma Biondetti, Dan Ma, Xavier Golay, Michael A Boss, Jeffrey L Gunter, et al. "Development, validation, qualification, and dissemination of quantitative MR methods: Overview and recommendations by the ISMRM quantitative MR study group." In: *Magnetic Resonance in Medicine* 87.3 (2022), pp. 1184–1206.

- [154] Bernard de Bruyne, Jozef Bartunek, Stanislas U Sys, Nico HJ Pijls, Guy R Heyndrickx, and William Wijns. "Simultaneous coronary pressure and flow velocity measurements in humans: feasibility, reproducibility, and hemodynamic dependence of coronary flow velocity reserve, hyperemic flow versus pressure slope index, and fractional flow reserve." In: *Circulation* 94.8 (1996), pp. 1842–1849.
- [155] Hanzhang Lu, Chekesha Clingman, Xavier Golay, and Peter CM Van Zijl. "Determining the longitudinal relaxation time (T₁) of blood at 3.0 Tesla." In: *Magnetic Resonance in Medicine* 52.3 (2004), pp. 679–682.
- [156] Thomas A Treibel, Marianna Fontana, Viviana Maestrini, Silvia Castelletti, Stefania Rosmini, Joanne Simpson, Arthur Nasis, Anish N Bhuvu, Heerajnarain Bulluck, Amna Abdel-Gadir, et al. "Automatic measurement of the myocardial interstitium: synthetic extracellular volume quantification without hematocrit sampling." In: *JACC: Cardiovascular Imaging* 9.1 (2016), pp. 54–63.
- [157] Daniel M Sado, Viviana Maestrini, Stefan K Piechnik, Sanjay M Banyersad, Steven K White, Andrew S Flett, Matthew D Robson, Stefan Neubauer, Cono Ariti, Andrew Arai, et al. "Noncontrast myocardial T₁ mapping using cardiovascular magnetic resonance for iron overload." In: *Journal of Magnetic Resonance Imaging* 41.6 (2015), pp. 1505–1511.
- [158] John C Wood, Maya Otto-Duessel, Michelle Aguilar, Hanspeter Nick, Marvin D Nelson, Thomas D Coates, Harvey Pollack, and Rex Moats. "Cardiac iron determines cardiac T₂^{*}, T₂, and T₁ in the gerbil model of iron cardiomyopathy." In: *Circulation* 112.4 (2005), pp. 535–543.
- [159] Julian A Luetkens, Marilia Voigt, Anton Faron, Alexander Isaak, Narine Mesropyan, Darius Dabir, Alois M Sprinkart, Claus C Pieper, Johannes Chang, Ulrike Attenberger, et al. "Influence of hydration status on cardiovascular magnetic resonance myocardial T₁ and T₂ relaxation time assessment: an intraindividual study in healthy subjects." In: *Journal of Cardiovascular Magnetic Resonance* 22.1 (2020), pp. 1–9.
- [160] Hyun-Kyung Kim, Soo-Hwan Kim, and Jae-Ki Ryu. "Changes in the blood components caused by water intake." In: *Korean Journal of Clinical Laboratory Science* 49.3 (2017), pp. 227–232.
- [161] Charles H Cunningham, John M Pauly, and Krishna S Nayak. "Saturated double-angle method for rapid B₁⁺ mapping." In: *Magnetic Resonance in Medicine* 55.6 (2006), pp. 1326–1333.
- [162] Sebastian Weingärtner, Fabian Zimmer, Gregory J Metzger, Kâmil Uğurbil, Pierre-Francois Van de Moortele, and Mehmet Akçakaya. "Motion-robust cardiac mapping at 3T using interleaved Bloch-Siegert shifts." In: *Magnetic Resonance in Medicine* 78.2 (2017), pp. 670–677.
- [163] Verónica Aramendía-Vidaurreta, Pedro M. Gordaliza, Marta Vidorreta, Rebeca Echeverría-Chasco, Gorka Bastarrika, Arrate Muñoz-Barrutia, and María A. Fernández-Seara. "Reduction of motion effects in myocardial arterial spin labeling." In: *Magnetic Resonance in Medicine* 87.3 (2022), pp. 1261–1275.

- [164] Christian M Wacker, Frank Wiesmann, Michael Bock, Peter Jakob, Jörn JW Sandstede, Anja Lehning, Georg Ertl, Lothar R Schad, Axel Haase, and Wolfgang R Bauer. "Determination of regional blood volume and intra-extracapillary water exchange in human myocardium using Feruglose: first clinical results in patients with coronary artery disease." In: *Magnetic Resonance in Medicine* 47.5 (2002), pp. 1013–1016.
- [165] Jannike Nickander, Raquel Themudo, Simon Thalén, Andreas Sigfridsson, Hui Xue, Peter Kellman, and Martin Ugander. "The relative contributions of myocardial perfusion, blood volume and extracellular volume to native T₁ and native T₂ at rest and during adenosine stress in normal physiology." In: *Journal of Cardiovascular Magnetic Resonance* 21.1 (2019), pp. 1–10.
- [166] Kei Mizukoshi, Masaaki Takeuchi, Yasufumi Nagata, Karima Addetia, Roberto M Lang, Yoshihiro J Akashi, and Yutaka Otsuji. "Normal values of left ventricular mass index assessed by transthoracic three-dimensional echocardiography." In: *Journal of the American Society of Echocardiography* 29.1 (2016), pp. 51–61.
- [167] Robert J Ogg, RB Kingsley, and June S Taylor. "WET, a T₁-and B₁-insensitive water-suppression method for in vivo localized ¹H NMR spectroscopy." In: *Journal of Magnetic Resonance, Series B* 104.1 (1994), pp. 1–10.
- [168] Sebastian Weingärtner, Mehmet Akçakaya, Tamer Basha, Kraig V Kissinger, Beth Goddu, Sophie Berg, Warren J Manning, and Reza Nezafat. "Combined saturation/inversion recovery sequences for improved evaluation of scar and diffuse fibrosis in patients with arrhythmia or heart rate variability." In: *Magnetic Resonance in Medicine* 71.3 (2014), pp. 1024–1034.
- [169] Qian Tao, Pieter van der Tol, Floris F. Berendsen, Elisabeth H.M. Paiman, Hildo J. Lamb, and Rob J. van der Geest. "Robust motion correction for myocardial T₁ and extracellular volume mapping by principle component analysis-based groupwise image registration." In: *Journal of Magnetic Resonance Imaging* 47.5 (2018), pp. 1397–1405.
- [170] American Heart Association Writing Group on Myocardial Segmentation et al. "Standardized myocardial segmentation and nomenclature for tomographic imaging of the heart: a statement for healthcare professionals from the Cardiac Imaging Committee of the Council on Clinical Cardiology of the American Heart Association." In: *Circulation* 105.4 (2002), pp. 539–542.
- [171] Maolin Qiu, R Paul Maguire, Jagriti Arora, Beata Planeta-Wilson, David Weinzimmer, Jinghua Wang, Yuenan Wang, Hyeonjin Kim, Nallakkandi Rajeevan, Yiyun Huang, et al. "Arterial transit time effects in pulsed arterial spin labeling CBF mapping: insight from a PET and MR study in normal human subjects." In: *Magnetic Resonance in Medicine* 63.2 (2010), pp. 374–384.
- [172] Eric C Wong, Richard B Buxton, and Lawrence R Frank. "Quantitative imaging of perfusion using a single subtraction (QUIPSS and QUIPSS II)." In: *Magnetic Resonance in Medicine* 39.5 (1998), pp. 702–708.

- [173] Thomas Troalen, Thibaut Capron, Patrick J Cozzone, Monique Bernard, and Frank Kober. "Cine-ASL: a steady-pulsed arterial spin labeling method for myocardial perfusion mapping in mice. Part I. Experimental study." In: *Magnetic Resonance in Medicine* 70.5 (2013), pp. 1389–1398.
- [174] Nam G Lee, Ahsan Javed, Terrence R Jao, and Krishna S Nayak. "Numerical approximation to the general kinetic model for ASL quantification." In: *Magnetic Resonance in Medicine* 84.5 (2020), pp. 2846–2857.
- [175] Louise AE Brown, Gaurav S Gulsin, Sebastian C Onciul, David A Broadbent, Jian L Yeo, Alice L Wood, Christopher ED Saunderson, Arka Das, Nicholas Jex, Amrit Chowdhary, et al. "Sex-and age-specific normal values for automated quantitative pixel-wise myocardial perfusion cardiovascular magnetic resonance." In: *European Heart Journal-Cardiovascular Imaging* (2022).
- [176] Kristopher D Knott, Claudia Camaioni, Anantharaman Ramasamy, Joao A Augusto, Anish N Bhuva, Hui Xue, Charlotte Manisty, Rebecca K Hughes, Louise AE Brown, Rajiv Amersey, et al. "Quantitative myocardial perfusion in coronary artery disease: a perfusion mapping study." In: *Journal of Magnetic Resonance Imaging* 50.3 (2019), pp. 756–762.
- [177] K Lance Gould, Nils P Johnson, Timothy M Bateman, Rob S Beanlands, Frank M Bengel, Robert Bober, Paolo G Camici, Manuel D Cerqueira, Benjamin JW Chow, Marcelo F Di Carli, et al. "Anatomic versus physiologic assessment of coronary artery disease: role of coronary flow reserve, fractional flow reserve, and positron emission tomography imaging in revascularization decision-making." In: *Journal of the American College of Cardiology* 62.18 (2013), pp. 1639–1653.
- [178] Pedro F Ferreira, Peter D Gatehouse, Raad H Mohiaddin, and David N Firmin. "Cardiovascular magnetic resonance artefacts." In: *Journal of Cardiovascular Magnetic Resonance* 15.1 (2013), pp. 1–39.
- [179] HF Staffeld, HM Mertens, and U Gleichmann. "Influence of dynamic exercise and training on systolic time intervals in normals and patients with coronary heart disease (author's transl)." In: *Zeitschrift fur Kardiologie* 67.5 (1978), pp. 305–316.
- [180] Sophie Schmid, Eidrees Ghariq, Wouter M Teeuwisse, Andrew Webb, and Matthias JP van Osch. "Acceleration-selective arterial spin labeling." In: *Magnetic Resonance in Medicine* 71.1 (2014), pp. 191–199.
- [181] Haosen Zhang, Steve M Shea, Vivian Park, Debiao Li, Pamela K Woodard, Robert J Gropler, and Jie Zheng. "Accurate myocardial T₁ measurements: toward quantification of myocardial blood flow with arterial spin labeling." In: *Magnetic Resonance in Medicine* 53.5 (2005), pp. 1135–1142.
- [182] Julius F Heidenreich, Andreas M Weng, Julian Donhauser, Andreas Greiser, Kelvin Chow, Peter Nordbeck, Thorsten A Bley, and Herbert Köstler. "T₁-and ECV-mapping in clinical routine at 3 T: differences between MOLLI, ShMOLLI and SASHA." In: *BMC Medical Imaging* 19.1 (2019), pp. 1–9.

- [183] Kelvin Chow, Jacqueline A Flewitt, Jordin D Green, Joseph J Pagano, Matthias G Friedrich, and Richard B Thompson. "Saturation recovery single-shot acquisition (SASHA) for myocardial T₁ mapping." In: *Magnetic Resonance in Medicine* 71.6 (2014), pp. 2082–2095.
- [184] Terrence Jao, Hung Phi Do, and Krishna Nayak. "In Vivo Performance of Myocardial Background Suppression." In: *Proc. Intl. Soc. Mag. Reson. Med.* 21. 2013.
- [185] Z Zun, E C Wong, and K S Nayak. "Background Suppression Does Not Reduce Physiological Noise in Myocardial ASL Perfusion Imaging." In: *Proc. Intl. Soc. Mag. Reson. Med.* 17. 2009.
- [186] Frank Q. Ye, Joseph A. Frank, Daniel R. Weinberger, and Alan C. McLaughlin. "Noise reduction in 3D perfusion imaging by attenuating the static signal in arterial spin tagging (ASSIST)." In: *Magnetic Resonance in Medicine* 44.1 (2000), pp. 92–100.
- [187] Wolfgang G Rehwald, Elizabeth Jenista, Michele A Parker, Han W Kim, Enn-Ling Chen, and Raymond J Kim. "Adiabatic T₂-preparation modules optimized for robustness toward cardiac motion and flow—a comparison with existing techniques at 3 Tesla." In: *Journal of Cardiovascular Magnetic Resonance* 13 (2011), pp. 1–2.
- [188] Sirkku M Pikkujamsa, Timo H Makikallio, KE Juhani Airaksinen, and Heikki V Huikuri. "Determinants and interindividual variation of RR interval dynamics in healthy middle-aged subjects." In: *American Journal of Physiology-Heart and Circulatory Physiology* 280 (2001), pp. 1400–1406.
- [189] David Nunan, Gavin R.H. Sandercock, and David A. Brodie. "A quantitative systematic review of normal values for short-term heart rate variability in healthy adults." In: *Pacing and Clinical Electrophysiology* 33.11 (Nov. 2010), pp. 1407–1417.
- [190] Andreas Voss, Rico Schroeder, Andreas Heitmann, Annette Peters, and Siegfried Perz. "Short-term heart rate variability - Influence of gender and age in healthy subjects." In: *Public Library of Science (PLOS) ONE* 10.3 (Mar. 2015).
- [191] Guillem Pons-Lladó. "Reference normal values for myocardial T₁ and T₂ maps with the MAGNETOM Vida 3T system and case examples from clinical practice." In: *MAGNETOM Flash* 72 (2019), pp. 29–33.
- [192] PA Gowland and MO Leach. "A simple method for the restoration of signal polarity in multi-image inversion recovery sequences for measuring T₁." In: *Magnetic Resonance in Medicine* 18.1 (1991), pp. 224–231.
- [193] Maša Božić-Iven, Stanislas Rapacchi, Qian Tao, Schad Lothar R., and Sebastian Weingärtner. "Respiratory navigated free-breathing myocardial arterial spin labelling (ASL) with phase sensitive reconstruction." In: *Proceedings of the Annual Meeting of the ISMRM*. 2023.

- [194] Martin Ugander, Paul S Bagi, Abiola J Oki, Billy Chen, Li-Yueh Hsu, Anthony H Aletras, Saurabh Shah, Andreas Greiser, Peter Kellman, and Andrew E Arai. "Myocardial edema as detected by pre-contrast T₁ and T₂ CMR delineates area at risk associated with acute myocardial infarction." In: *JACC: Cardiovascular Imaging* 5.6 (2012), pp. 596–603.
- [195] Peter CM Van Zijl, Scott M Eleff, John A Ulatowski, Joni ME Oja, Aziz M Uluğ, Richard J Traystman, and Risto A Kauppinen. "Quantitative assessment of blood flow, blood volume and blood oxygenation effects in functional magnetic resonance imaging." In: *Nature Medicine* 4.2 (1998), pp. 159–167.
- [196] Elizabeth R Jenista, Wolfgang G Rehwald, Enn-Ling Chen, Han W Kim, Igor Klem, Michele A Parker, and Raymond J Kim. "Motion and flow insensitive adiabatic T₂-preparation module for cardiac MR imaging at 3 Tesla." In: *Magnetic Resonance in Medicine* 70.5 (2013), pp. 1360–1368.
- [197] American College of Radiology. "ACR–ASNR Position Statement On the Use of Gadolinium Contrast Agents." In: *ACR manual on contrast media (Version 2023)*. 2023, pp. 82–82.
- [198] Markus Henningsson, Shaihan Malik, Rene Botnar, Daniel Castellanos, Tarique Hussain, and Tim Leiner. "Black-blood contrast in cardiovascular MRI." In: *Journal of Magnetic Resonance Imaging* 55.1 (2022), pp. 61–80.
- [199] Michael Garwood and Lance DelaBarre. "The return of the frequency sweep: designing adiabatic pulses for contemporary NMR." In: *Journal of Magnetic Resonance* 153.2 (2001), pp. 155–177.
- [200] Peter Kellman, Daniel A Herzka, and Michael Schacht Hansen. "Adiabatic inversion pulses for myocardial T₁ mapping." In: *Magnetic Resonance in Medicine* 71.4 (2014), pp. 1428–1434.
- [201] Valentin Fuster et al. "ACC/AHA/ESC 2006 Guidelines for the Management of Patients With Atrial Fibrillation." In: *Circulation* 114.7 (Aug. 2006).
- [202] Connie W Tsao, Aaron W Aday, Zaid I Almarzooq, Cheryl AM Anderson, Pankaj Arora, Christy L Avery, Carissa M Baker-Smith, Andrea Z Beaton, Amelia K Boehme, Alfred E Buxton, et al. "Heart disease and stroke statistics—2023 update: a report from the American Heart Association." In: *Circulation* 147.8 (2023), e93–e621.
- [203] Robert A. Byrne et al. "2023 ESC Guidelines for the management of acute coronary syndromes." In: *European Heart Journal* 44.38 (Oct. 2023), pp. 3720–3826.
- [204] Amit R. Patel, Michael Salerno, Raymond Y. Kwong, Amita Singh, Bobak Heydari, and Christopher M. Kramer. "Stress Cardiac Magnetic Resonance Myocardial Perfusion Imaging: JACC Review Topic of the Week." In: *Journal of the American College of Cardiology* 78.16 (Oct. 2021), pp. 1655–1668.

- [205] Geraint Morton, Amedeo Chiribiri, Masaki Ishida, Shazia T Hussain, Andreas Schuster, Andreas Indermuehle, Divaka Perera, Juhani Knuuti, Stacey Baker, Erik Hedström, et al. "Quantification of absolute myocardial perfusion in patients with coronary artery disease: comparison between cardiovascular magnetic resonance and positron emission tomography." In: *Journal of the American College of Cardiology* 60.16 (2012), pp. 1546–1555.
- [206] Silmara Gusso, Carlo Salvador, Paul Hofman, Wayne Cutfield, James C Baldi, Andrew Taberner, and Poul Nielsen. "Design and testing of an MRI-compatible cycle ergometer for non-invasive cardiac assessments during exercise." In: *Biomedical engineering online* 11 (2012), pp. 1–14.
- [207] Elias H Botvinick. "Current methods of pharmacologic stress testing and the potential advantages of new agents." In: *Journal of Nuclear Medicine Technology* 37.1 (2009), pp. 14–25.
- [208] Christopher M Kramer, Jörg Barkhausen, Chiara Bucciarelli-Ducci, Scott D Flamm, Raymond J Kim, and Eike Nagel. "Standardized cardiovascular magnetic resonance imaging (CMR) protocols: 2020 update." In: *Journal of Cardiovascular Magnetic Resonance* 22.1 (2020), p. 17.
- [209] Matthew J Memmott, Christine M Tonge, Kimberley J Saint, and Parthiban Arumugam. "Impact of pharmacological stress agent on patient motion during rubidium-82 myocardial perfusion PET/CT." In: *Journal of Nuclear Cardiology* 25.4 (2018), pp. 1286–1295.
- [210] Elise J Vleeming, Sergiy V Lazarenko, Friso M van der Zant, Xiao-Bo Pan, Jerome M Declerck, Maurits Wondergem, and Remco JJ Knol. "Cardiac displacement during ¹³N-ammonia myocardial perfusion PET/CT: comparison between adenosine- and regadenoson-induced stress." In: *Journal of Nuclear Medicine Technology* 46.2 (2018), pp. 114–122.
- [211] Stephan D Fihn, Julius M Gardin, Jonathan Abrams, Kathleen Berra, James C Blankenship, Apostolos P Dallas, Pamela S Douglas, JoAnne M Foody, Thomas C Gerber, Alan L Hinderliter, et al. "2012 ACCF/AHA/ACP/AATS/PCNA/SCAI/STS guideline for the diagnosis and management of patients with stable ischemic heart disease: a report of the American College of Cardiology Foundation/American Heart Association task force on practice guidelines, and the American College of Physicians, American Association for Thoracic Surgery, Preventive Cardiovascular Nurses Association, Society for Cardiovascular Angiography and Interventions, and Society of Thoracic Surgeons." In: *Circulation* 126.25 (2012), e354–e471.
- [212] Andrew J. Yoon, Hung Phi Do, Steven Cen, Michael W. Fong, Farhood Saremi, Mark L. Barr, and Krishna S. Nayak. "Assessment of segmental myocardial blood flow and myocardial perfusion reserve by adenosine-stress myocardial arterial spin labeling perfusion imaging." In: *Journal of Magnetic Resonance Imaging* 46.2 (2017), pp. 413–420.
- [213] Emily Aherne, Kelvin Chow, and James Carr. "Cardiac T₁ mapping: Techniques and applications." In: *Journal of Magnetic Resonance Imaging* 51.5 (May 2020), pp. 1336–1356.

- [214] Walter RT Witschey, Gerald A Zsido, Kevin Koomalsingh, Norihiro Kondo, Masahito Minakawa, Takashi Shuto, Jeremy R McGarvey, Melissa M Levack, Francisco Contijoch, James J Pilla, et al. "In vivo chronic myocardial infarction characterization by spin locked cardiovascular magnetic resonance." In: *Journal of Cardiovascular Magnetic Resonance* 14 (2012), pp. 1–9.
- [215] Chiara Coletti, Anastasia Fotaki, Joao Tourais, Yidong Zhao, Christal van de Steeg-Henzen, Mehmet Akçakaya, Qian Tao, Claudia Prieto, and Sebastian Weingärtner. "Robust cardiac mapping at 3T using adiabatic spin-lock preparations." In: *Magnetic Resonance in Medicine* 90.4 (Oct. 2023), pp. 1363–1379.
- [216] Pim AL Tonino et al. "Fractional Flow Reserve versus Angiography for Guiding Percutaneous Coronary Intervention." In: *New England Journal of Medicine* 360.3 (2009).
- [217] Keith R Thulborn, John C Waterton, Paul M Matthews, and George K Radda. "Oxygenation dependence of the transverse relaxation time of water protons in whole blood at high field." In: *Biochimica et Biophysica Acta (BBA)-General Subjects* 714.2 (1982), pp. 265–270.
- [218] Debiao Li, Yi Wang, and David J Waight. "Blood oxygen saturation assessment in vivo using T2* estimation." In: *Magnetic resonance in medicine* 39.5 (1998), pp. 685–690.
- [219] Jie Zheng, Jinghua Wang, Mark Nolte, Debiao Li, Robert J Gropler, and Pamela K Woodard. "Dynamic estimation of the myocardial oxygen extraction ratio during dipyridamole stress by MRI: a preliminary study in canines." In: *Magnetic Resonance in Medicine: An Official Journal of the International Society for Magnetic Resonance in Medicine* 51.4 (2004), pp. 718–726.
- [220] Jayanth R. Arnold et al. "Myocardial oxygenation in coronary artery disease: Insights from blood oxygen level-dependent magnetic resonance imaging at 3 Tesla." In: *Journal of the American College of Cardiology* 59.22 (2012), pp. 1954–1964.
- [221] Theodoros D. Karamitsos et al. "Relationship between regional myocardial oxygenation and perfusion in patients with coronary artery disease insights from cardiovascular magnetic resonance and positron emission tomography." In: *Circulation: Cardiovascular Imaging* 3.1 (2010), pp. 32–40.
- [222] Dan Ma, Vikas Gulani, Nicole Seiberlich, Kecheng Liu, Jeffrey L Sunshine, Jeffrey L Duerk, and Mark A Griswold. "Magnetic resonance fingerprinting." In: *Nature* 495.7440 (2013), pp. 187–192.
- [223] Pan Su, Deng Mao, Peiying Liu, Yang Li, Marco C Pinho, Babu G Welch, and Hanzhang Lu. "Multiparametric estimation of brain hemodynamics with MR fingerprinting ASL." In: *Magnetic Resonance in Medicine* 78.5 (2017), pp. 1812–1823.

- [224] Katherine L Wright, Yun Jiang, Dan Ma, Douglas C Noll, Mark A Griswold, Vikas Gulani, and Luis Hernandez-Garcia. "Estimation of perfusion properties with MR fingerprinting arterial spin labeling." In: *Magnetic resonance imaging* 50 (2018), pp. 68–77.
- [225] Hongli Fan, Pan Su, Doris Da May Lin, Emily B Goldberg, Alexandra Walker, Richard Leigh, Argye E Hillis, and Hanzhang Lu. "Simultaneous hemodynamic and structural imaging of ischemic stroke with magnetic resonance fingerprinting arterial spin labeling." In: *Stroke* 53.6 (2022), pp. 2016–2025.
- [226] Klaus Scheffler. "On the transient phase of balanced SSFP sequences." In: *Magnetic Resonance in Medicine* 49.4 (2003), pp. 781–783.
- [227] Maša Božić-Iven, Stanislas Rapacchi, Iain Pierce, George Thornton, Qian Tao, Lothar R Schad, Thomas Treibel, and Sebastian Weingärtner. "Improving reproducibility of cardiac ASL using T₁ and flip angle corrected reconstruction." In: *Proceedings of the Annual Meeting of the SMRA*. 2022.
- [228] Maša Božić-Iven, Stanislas Rapacchi, Iain Pierce, George Thornton, Qian Tao, Lothar R Schad, Thomas Treibel, and Sebastian Weingärtner. "Towards reproducible Arterial Spin Labelling in the myocardium: Impact of blood T₁ time and imaging readout parameters." In: *Proceedings of the Joint Annual Meeting ISMRM-ESMRMB*. 2022.

DECLARATION

I have only used the sources indicated and have not made unauthorised use of services of a third party. Where the work of others has been quoted or reproduced, the source is always given.

I have not yet presented this thesis or parts thereof to a university as part of an examination or degree.

I am aware of the importance of a sworn affidavit and the criminal prosecution in case of a false or incomplete affidavit.

I affirm that the above is the absolute truth to the best of my knowledge and that I have not concealed anything.

Heidelberg, Germany, 2 April 2024

Maša Božić-Iven